School of Electrical Engineering, Computing and
Mathematical Sciences

Investigating the Low-Frequency Emission Properties of Pulsars with the Murchison Widefield Array

Nicholas Anthony Swainston

This thesis is presented for the Degree of
Doctor of Philosophy
of
Curtin University

28 April 2023

To the best of my knowledge and belief this thesis contains no material previously published by any other person except where due acknowledgement has been made. This thesis contains no material which has been accepted for the award of any other degree or diploma in any university.

Nicholas Anthony Swainston

28 April 2023

Acknowledgements

This work was made possible by the continued support of my supervisors, family, and friends. I would like to first thank my parents, that have been endlessly supportive of the meandering path I took to complete this thesis. Your patience and kindness have allowed me to find my purpose and a career I enjoy. I would like to thank my grandparents for helping raise me, and although it saddens me that they are not alive to see me finish my thesis, I like to think they are still proud of me. I would like to thank Hannah for being by my side and her patience for the things we had to put on hold as I completed this thesis.

I would like to thank my supervisors for their years of guidance; Steven Tremblay, who always offered to help me and made sure I understood what I was doing; Sam McSweeney, who helped improve my writing and allowed me to bounce ideas off him; Ian Morrison, who helped me with my technical skills, including understanding the intricacies of GPUs; and Ramesh Bhat, who was a fountain of knowledge and made sure I never lost sight of the scientific goal of my work. I would like to thank my supervisor panel (James Miller-Jones, Arash Bahramian and Christene Lynch) and my aunt Meg Montague for sharing their experience and advice when my motivation was waning and I was unsure if I could finish my thesis. I would also like to thank the staff and students at CIRA, who were always welcoming, willing to offer advice and share in the joy of my successes.

There were many times when I didn't think I could finish this thesis, so thank you all for helping me get to this point.

Abstract

Pulsars are rapidly rotating neutron stars with strong magnetic and gravitational fields, and they make excellent laboratories for studying high-energy physics. Although pulsars were discovered over five decades ago, their exact mechanism of emitting electromagnetic radiation is far from being understood. In particular, how pulsars produce the observed wide variety of emission phenomena and properties is one of the great mysteries in astrophysics.

One of the key emission properties is the radio frequency flux-density spectrum. For the majority of pulsars, it can be described by a simple power law, at least within the range of commonly observed frequencies, i.e. flux density at frequency ν follows the form $S_\nu \propto \nu^\alpha$. However, if the flux densities are measured over a wide range of frequencies, some pulsars tend to show deviation from a simple power law, often with a low-frequency turn-over and sometimes even a high-frequency cut-off. The low-frequency turn-over is thought to be caused by absorption of the local medium, which may allow us to investigate the surrounding medium of a pulsar. On the other hand, the high-frequency cut-off is possibly caused by a relativistic limit on electron acceleration in the electric field near the stellar surface, which can be used to place constraints on the pulsar emission region.

This thesis attempts to shed light on emission physics by studying the radio spectra of a large sample of pulsars. To achieve this goal, observations obtained from the ongoing Southern-sky MWA Rapid Two-metre (SMART) pulsar survey has been leveraged to make low-frequency detections of a large number of pulsars

and make reliable measurements of their flux densities at frequencies below ∼300 MHz. In order to make the survey data processing computationally tractable, part of this thesis work involved developing an improved beamformer software and a method to mitigate ionospheric refraction offsets in low-frequency observations. The development of the SMART survey and search pipeline also led to the discovery of the first three new pulsars with the MWA and 120 low-frequency flux density measurements of previously known pulsars.

To investigate the pulsar spectra of a large sample of pulsars, the pulsar_spectra repository has been developed. This was motivated by the need to create a pulsar flux density catalogue that will make published measurements more accessible to the astronomical community as well as provide a suite of tools for measuring spectra. A new spectral model called the double turn-over spectrum is proposed, which can be used to fit spectra where both the low-frequency turn-over and the high-frequency cut-off are clearly present. Further, a formalism is extended to include the bandwidth integration method, which allows accurate spectral fits when flux density measurements are made over a large fractional bandwidth. This software has been used to measure the spectra of 893 pulsars, i.e. more than twice what was used in the previous largest study (441 pulsars by Jankowski et al., 2018).

These 893 pulsar spectra are analysed by comparing the resultant spectral fit parameters with pulsars' physical and emission properties to explore possible correlations in an attempt to find useful clues about pulsar emission. The analysis shows that the vast majority of pulsars in the sample (68%) have a simple power law spectrum. When considering the energetics of emission, it is impossible for the power law spectrum to continue to extremely low frequencies as that would imply that the emission reaches infinity as the emission frequency reaches zero. There have been measurements of high-frequency cut-offs, but there are so few measurements at these high frequencies that it is unclear whether this is normal behaviour. This suggests that the majority of pulsars having a simple power law

spectrum is caused by limited flux density data at frequencies below 300 MHz and above 5 GHz. More measurements are needed at these high and low frequencies to improve this sample.

This thesis presents several findings relating to pulsar spectra. An interesting finding is that the spectral distribution of normal pulsars is similar to that of millisecond pulsars, which contradicts previous spectral studies. It was also found that the theoretical estimation of the high-frequency cut-off based on the spin frequency is underestimated. Finally, as pulsars age, both the frequency of the low-frequency turn-over and that of the high-frequency cut-off decrease.

Even with the improvements described in this thesis, it remains that spectral information is available for only less than a third of currently known pulsars, many of which include measurements that have not adequately accounted for the changes in apparent flux densities on month to year time scales due to refractive scintillation, which can be up to a factor of two or more. Some specific suggestions have been made on how to further improve the pulsar spectra sample by improving the number and quality of flux density measurements and ways to make the spectral fitting method even more robust. The spectra of pulsars and how they constrain the pulsar emission mechanism can now be studied in greater detail using the data sets and software tools developed as part of this thesis.

Statement of contribution by others

The content of Chapters 3-5 is my own work, with the following qualifications.

In Chapter 3, the original beamforming software (i.e. the core components and implementation) was initially developed by Steven Tremblay and Stephen Ord, on which I improved under the supervision of Stephen Ord, Samuel McSweeney, Ramesh Bhat and Steven Tremblay. The MWA VCS observations were obtained under an observing project led by Parul Jangal (PhD candidate based at the Indian Institute of Technology, Indore) and were scheduled by Andrew Williams.

In Chapter 4, the follow-up observations with the upgraded GMRT and Parkes telescope were performed and processed by Ramesh Bhat, Sanjay Kudale and Shi Dai, through multiple telescope proposals led by Ramesh Bhat. Marcin Sokolowski processed the MWA data for imaging. Ramesh Bhat performed the timing analysis to obtain the pulsar ephemerides, as well as the analysis of GMRT beamformed data. Sanjay Kudale performed the GMRT imaging analysis, and Shi Dai processed the Parkes data. The analysis of MWA pulsar data was undertaken by myself, under close supervision, and with many suggestions from Ramesh Bhat, Samuel McSweeney, and Ian Morrison. Much of the initial writing of the discovery paper was led by Ramesh Bhat and Samuel McSweeney, and I expanded on that content to form the content for Chapter 4.

In Chapter 5, the bandwidth integration correction method was suggested by the reviewer of the (PASA) manuscript and the mathematical derivation was

performed by Samuel McSweeney. I developed the software for spectral analysis and created the database by collating data from a large number of publications with the help of Christopher Lee.

(Signature of Candidate)

(Signature of Supervisor)

Contents

List of Figures

Chapter 1

Introduction

1.1 Motivation and overview

Pulsars are rapidly rotating neutron stars with very strong magnetic fields that emit radio waves from their magnetic poles, which are observable as periodic pulses. Pulsars are extremely dense, with a typical mass of $\sim$1.4 $M_\odot$ and a diameter of approximately 20 km, and they have strong magnetic fields $\sim 10^{12}$ G. These extreme conditions allow us to study high-energy physics that is impossible to recreate in a terrestrial laboratory.

Although pulsars were discovered in 1967 (Hewish et al., 1968), the exact mechanism by which they emit electromagnetic radiation is far from being understood. The pulsar emission is often described using models that include a plasma-filled magnetosphere that co-rotates with the pulsar (Goldreich & Julian, 1969; Melrose, 2017). However, a model that can satisfactorily explain the observed wide variety of emission phenomena and other properties, such as spectral low-frequency turn-over (Kijak et al., 2007; Rajwade et al., 2016; Jankowski et al., 2018), intermittency (Lyne, 2009; Deneva et al., 2009; Meyers et al., 2018) and pulse drifting (Backer, 1973; Rankin, 1986; Janagal et al., 2023), has not yet been developed.

In this thesis, the primary method used to investigate pulsar emission is

through studying the radio spectra of a large sample of pulsars. Recently, Jankowski et al. (2018) performed an extensive study of pulsar spectra using their observations of 441 pulsars. They found the spectra of the vast majority of their sample (79%) can be described by a simple power law spectrum. While there is currently no clear understanding of what causes pulsars to have different spectral indices, there is some evidence that the beam viewing geometry may be a contributing factor. It has been observed by several authors that pulsars with flatter spectra have relatively narrow pulse widths, which suggests that their lines of sight are probably grazing the edge of the emission's beam (Keith et al., 2008; Dai et al., 2015; Jankowski et al., 2018). Moreover, describing the spectra in the form of a simple power-law may be an oversimplification of the true spectral shape, especially in cases where there is only a limited frequency coverage.

With a sufficiently large frequency range, additional spectral features can be observed, such as a low-frequency turn-over (§1.7.3) and high-frequency cut-off (§1.7.2). The low-frequency turn-over is usually attributed to either synchrotron self-absorption (Izvekova et al., 1981) or thermal free-free absorption (Kijak et al., 2007), which allows the study of the medium surrounding the pulsar. The high-frequency cut-off is thought to be due to a relativistic limit on electron velocity (Kontorovich & Flanchik, 2013) and, therefore, can allow us to study the emission region of the pulsar.

Studying the correlation between spectral features and pulsar properties can provide useful clues to what drives pulsar spectra and, in turn, can help us better constrain pulsar emission models that predict specific spectral features: turnovers, cut-offs, and spectral indices. Once the spectral features have been measured for a large number of pulsars, they can be compared to pulsar parameters such as spin period (P), spin-down luminosity ($\dot{E}$, see §1.6.1) and characteristic age (τ, see §1.6.2). For example, the work of Jankowski et al. (2018) reported correlations between the spectral index and derived parameters such as the spin-down luminosity ($\dot{E} = 4\pi^2 I \dot{P} P^{-3}$) and the magnetic field strength at the light

cylinder ($B_{\rm LC} = 2.9 \times 10^{32} \dot{P}^{0.5} P^{3.5}$). As these derived parameters ($\dot{E}$ and$B_{\rm LC}$) are inferred from their measured period and period derivative (under common assumptions), a certain degree of correlation can be expected.

The distribution of the spectral index from these simple power law spectra is used in pulsar population simulations to ascertain how bright pulsars will likely be at other observing frequencies. The spectral index distribution was initially thought to be normally distributed around a mean value. This mean can be biased by the frequencies of large pulsar surveys (Lorimer et al., 1995; Maron et al., 2000; Bates et al., 2013). More recent work suggests that the spectral index distribution can be more accurately fit by a log-normal distribution (Jankowski et al., 2018). These pulsar population studies and simulations can be used to investigate pulsar birthrates which can then be compared with the theoretical estimates based on core-collapse supernova rates (Keane & Kramer, 2008). This can help estimate how many pulsars will likely be discovered with new generation telescopes and surveys, such as the Square Kilometre Array (SKA) (Keane et al., 2015a) and its low-frequency component, SKA-Low (Xue et al., 2017).

Detailed studies of spectral features of a large pulsar sample require observations made at a range of radio frequencies. Unfortunately, there is currently a paucity of low-frequency pulsar flux density measurements. Of the 3389 currently known pulsars, only 456 have flux density measurements below 300 MHz, according to the ATNF pulsar catalogue (version v1.68; Manchester et al., 2005). The resurgence of low-frequency radio telescopes, such as the Low-Frequency Array (LOFAR) (van Haarlem et al., 2013) and the Murchison Widefield Array (MWA) (Tingay et al., 2013; Wayth et al., 2018), allows the study of low-frequency spectral features. Observing at low frequencies becomes more difficult because of the deleterious effects of the interstellar medium (ISM) (§1.4) and the ionosphere (§1.5) compared to high-frequencies. Developing effective mitigation of these effects is therefore essential for accurate low-frequency science and will lead the way for future science planned with the SKA-Low.

The Southern-sky MWA Rapid Two-metre (SMART) pulsar survey, underway at the MWA (Bhat et al., 2023a), provides an excellent niche for obtaining a large sample of low-frequency flux density measurements for pulsars located in the Southern sky. However, low-frequency aperture array telescopes, such as the MWA, present a myriad of challenges that must be overcome to produce an efficient and sensitive survey. For example, processing pipelines must be developed to deal with the huge data rates and effects such as scintillation and ionospheric offsets must be understood and mitigated. MWA flux density measurements can be integrated with data from the literature to model the spectra of a large number of pulsars. In this work, the spectral fitting method developed by Jankowski et al. (2018) can be further expanded or refined to include new models and yield more accurate spectral fits, particularly in the cases of flux density measurements made over large fractional bandwidths. The spectral properties of these pulsars can then be compared to their pulsar parameters to investigate possible correlations and investigate the causes of pulsar emission. This forms the central theme of this thesis.

1.2 Pulsars

Pulsars are neutron stars typically formed through core-collapse supernovae, but it has been theorised that in some cases, they could also result from accretion-induced collapse within binary systems (Ruiter et al., 2019). They have spin periods ranging from about a millisecond to a few tens of seconds (Backer et al., 1982; Tan et al., 2018a) and strong magnetic fields with a magnetic axis misaligned from their rotation axis. They emit electromagnetic radiation out of their magnetic poles, which we observe as pulses each time the emission beam crosses our line of sight, hence the name pulsars.

Pulsars emit electromagnetic radiation at the expense of their rotational kinetic energy. This loss of energy causes the rotational spin periods P to gradually increase with time. This increase is called the spin-down rate and is defined as the

time derivative of the pulse period, $\dot{P} = \mathrm{d}P/\mathrm{d}t$. Both P and $\dot{P}$ can be obtained to very high precision from pulsar timing measurements. These measurements provide unique insights into the spin evolution and various aspects of pulsar evolution of the different populations of pulsars which can be examined in the "P-$\dot{P}$" diagram (see Figure 1.1).

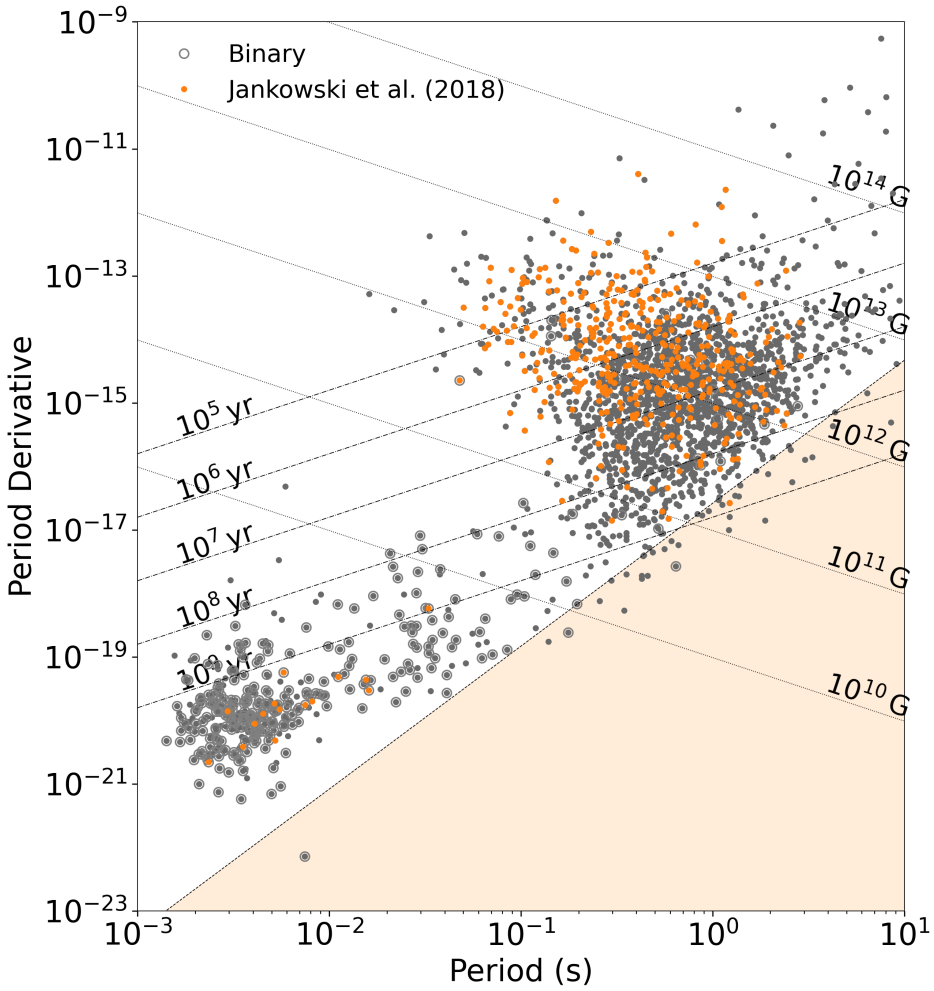

Figure 1.1: The pulsar P-$\dot{P}$ diagram for all known radio pulsars (in grey), binary pulsars (circled) and pulsars with measured pulsar spectra from Jankowski et al. (2018) (in orange). Lines of constant characteristic age τ and magnetic field B are also shown. The death line borders the yellow-shaded region, which depicts the area where pulsars are predicted to no longer produce the electron-positron pairs required for radio emission (Chen & Ruderman, 1993). This death line is not a hard cut-off as it makes several assumptions about the pulsar's magnetic field and mass.

The population of binary Millisecond Pulsars (MSPs) is shown in the bottom left corner of the P-$\dot{P}$ diagram, which is clearly distinct from the isolated slow pulsars in the top left. The formation of MSPs is explained using the recycling model that was introduced in the 1980s (Alpar et al., 1982; Radhakrishnan & Srinivasan, 1982), in which a neutron star is spun up to millisecond spin periods due to the accretion of matter and angular momentum from a binary companion. This model was recently bolstered by the discovery of the first transitional MSP, which was observed to alternate between rotation-powered radio emission and accretion-powered X-ray emission (Archibald et al., 2009; Papitto et al., 2013; Bassa et al., 2014).

Pulsars are often not observed by their individual pulses as they can be too faint to be distinguishable from the noise. To improve the signal-to-noise (S/N) ratio of detections, the time series is partitioned into multiple single-pulse segments according to the pulse period and summed or 'folded' to create an average pulse profile. The emission from pulsars can be observed over a large range of radio frequencies, so the brightness of average pulse profiles can be measured at multiple different frequencies to create a pulsar "spectrum". Over the commonly observed range of frequencies, most pulsars' spectra can be described by a simple power law, $S_\nu \propto \nu^\alpha$, where α is the spectral index and S_ν is the flux density at observing frequency ν. Most pulsars tend to be brighter at lower frequencies, which generally leads to negative spectral indices ($\alpha < 0$).

Recent work suggests that some of the fastest spinning MSPs have the steepest radio spectra ($\alpha < -2.5$) (Kuniyoshi et al., 2015; Kondratiev et al., 2016; Frail et al., 2016). This would make them brighter, and hence easier to detect at frequencies below 300 MHz. This is validated by the recent LOFAR discovery of the fastest-spinning neutron star known in the Galactic field at a central observing frequency of 135 MHz (Bassa et al., 2017b).

1.2.1 Pulsars as astrophysical tools

Pulsars are not only interesting in their own right, but they are also excellent tools for a wide variety of astrophysics. Most notably, they allow us to probe the ionised component of the ISM, and the high rotational stability of MSPs allows them to be used as accurate natural clocks enabling us to test theories of gravity, particularly general relativity.

1.2.1.1 Modelling the Galactic distribution of free electrons

Pulsars are excellent tools for probing the ionised ISM. It is well known that dispersion and scattering measurements of pulsars can be used to model the Galactic distribution of free electrons and the spatial distribution of turbulence. This analysis requires independent distance estimates. These are most commonly acquired using very long baseline interferometry (VLBI), which provides accurate distance measurements of nearby pulsars (e.g. Deller et al., 2009, 2019; Kramer et al., 2021a). When combined with dispersion measurements, this allows us to calibrate distance scales in electron density. This approach has been followed to develop models to describe the large-scale structure of the ISM and has led to steadily refining models to incorporate the spiral arms and a number of other prominent local features (Cordes & Lazio, 2002; Yao et al., 2017). These electron density models can be used to estimate the distances to new pulsars, describe the fluctuations in electron density that causes interstellar scattering, and can be used to explain the scintillation in observations of both Galactic and extragalactic objects (Stinebring et al., 2022; Hancock et al., 2019).

1.2.1.2 Gravitational wave radiation from compact binaries

Pulsars in close binary systems with either a white dwarf or a neutron star as a companion have proven to be excellent tools for testing general relativity (GR) (Taylor, 1975; Kramer et al., 2006). The first such system, the double neutron star binary PSR B1913+16, was discovered using the Arecibo Observatory in

1974 (Hulse & Taylor, 1974). After nearly 20 years of timing observations, it became possible to accurately measure the shift of periastron with extremely high precision. The predicted decay of the periastron due to the emission of gravitational waves (GWs) was in excellent agreement with the measured delay within 0.5% (Taylor & Weisberg, 1989) as shown in Figure 1.2. This remarkable agreement with the predictions of GR won Hulse and Taylor the Nobel Prize in Physics in 1993. Finding more such relativistic systems and using them to conduct further stringent tests of general relativity and other theories of gravity is an important science driver for the SKA and many of its pathfinders (Janssen et al., 2015; Kramer et al., 2021b).

1.2.1.3 Pulsar timing arrays

While measuring the decay of a binary system's periastron provided a solid confirmation of the existence of gravitational waves (and hence indirect confirmation), recent progress and advancements with the Laser Interferometer Gravitational-Wave Observatory (LIGO) led to their direct detection at the high-frequency range ($\approx$ 10 to 250 Hz) (Abbott et al., 2016). Another proposed method is to use pulsar timing arrays (PTAs) to detect ultra low-frequency ($\approx 10^{-9}$ to 10^{-8} Hz) GWs that LIGO-type detectors are not sensitive to. These pulsar timing arrays consist of a set of Galactic MSPs, which are extremely stable natural clocks, to create an array. They can be used to detect deviations in expected pulse arrival times caused by space-time perturbations produced by low-frequency GWs. Current pulsar timing arrays, in particular the combination of efforts under the umbrella of the International Pulsar Timing Array (IPTA) project (e.g. Verbiest et al., 2016; Perera et al., 2019), have the potential to detect GWs by searching for an all-sky signature in the form of a stochastic gravitational-wave background. The detection sensitivity of these PTAs can be improved through the discoveries and addition of more stable MSPs using ongoing and future pulsar surveys (Stovall et al., 2014; Sanidas et al., 2019; Bhat et al., 2023a).

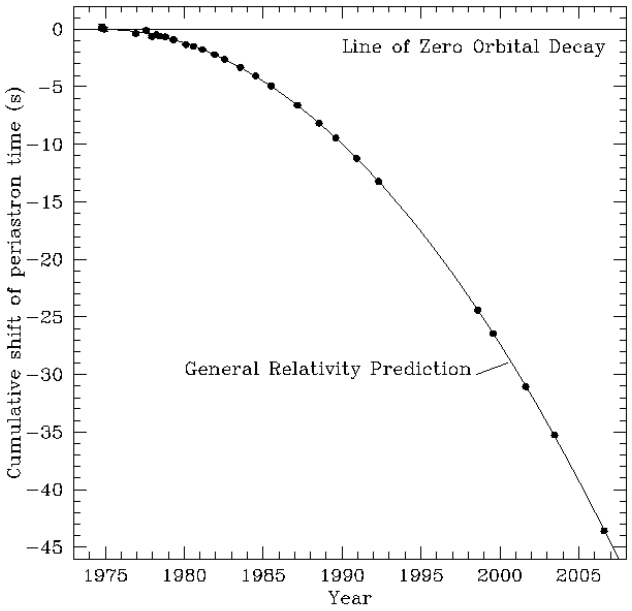

Figure 1.2: Evidence of binary pulsar B1913+16 emitting gravitational radiation. Gravitational waves carry energy away from the binary system causing the orbit to lose energy and the stars to spiral inward towards each other. This orbit can be measured by investigating the pulse times-of-arrival (ToAs), which can be perturbed by a combination of various effects, for example, the different light travel times across the orbit due to the Roemer delay. The dots are measurements of the periastron, while the curve represents the expected behaviour if GWs are carrying energy away from the system at the rate predicted by Einstein's theory of general relativity. The excellent agreement between observation and theory represented the strongest evidence for the existence of gravitational radiation at that time. Image credit: Weisberg & Taylor (2003).

1.3 Pulsar emission mechanism

Despite their discovery more than five decades ago (Hewish et al., 1968) and the substantial progress on both theoretical and observational fronts, it is astonishing that there are still no widely accepted theories that satisfactorily explain the origin of radio emission, in particular, their many observed phenomenologies and features. There are a number of methods to investigate pulsars from an observational perspective, which provide clues to their emission mechanism, such as giant pulses (e.g. Hankins et al., 2003; Oronsaye et al., 2015; Meyers et al., 2017), pulse profile evolution (e.g. Johnston et al., 2008; Dai et al., 2015; Pilia et al.,

2016) and sub-pulse drifting (e.g. Vivekanand & Joshi, 1997; Mcsweeney et al., 2017; Janagal et al., 2021; McSweeney et al., 2022). In this thesis, we focus on a variety of pulsar spectral features as the path toward investigating the pulsar emission mechanism. Ideally, for an emission mechanism model to be widely accepted, it needs to explain a variety of these observed phenomena and properties. Over the past decades, several ideas (and models) for emission mechanisms have been introduced in an attempt to describe some of the observed features. These may serve as the basis for future, and more advanced, models. In this section, we briefly review some of the key ideas that have emerged over the past years that may help better understand the emission mechanism.

To explain the observed radio emission for pulsars, Goldreich & Julian (1969) theorised the necessary existence of a plasma-filled magnetosphere that co-rotates with the pulsar. In this picture, within the magnetosphere, particles travelling at relativistic speeds along the magnetic field lines close to the stellar surface are expected to cause the observed radio emission. However, there are currently no emission models that explain the vast majority of observed pulsar behaviours, essentially leaving pulsar electrodynamics as an unsolved problem (Melrose & Yuen, 2016). Understanding the pulsar emission mechanism will also lead to a greater understanding of the behaviour of relativistic plasma in ultra-strong gravitational and magnetic field regimes.

It is generally assumed that the magnetic axis of a pulsar is offset from its rotational axis (see Figure 1.3). Ruderman & Sutherland (1975) proposed one of the earliest comprehensive theories of pulsar emission, which posited the existence of a region very close to the neutron star surface near the magnetic axis, where there is a relative depletion of charges, called the "vacuum gap". Vacuum gaps are filled with plasma that is less dense than the critical Goldreich-Julian density (Goldreich & Julian, 1969), where the magnetically induced electric field is saturated, and therefore electrons can be accelerated to very high energies. This rotating magnetic field induces an electric field that is strong enough to exceed

the gravitational force by more than 10 orders of magnitude, causing particles to be ripped from the stellar surface (Goldreich & Julian, 1969). Radhakrishnan & Cooke (1969) proposed that electrons trapped and accelerated along the magnetic field lines of the pulsar, emit electromagnetic radiation via the synchrotron-curvature radiation mechanism. This original theory formed the basis of several other, more sophisticated, theories that have emerged over the past decades (e.g. Daugherty & Harding, 1982; Baring, 2004)

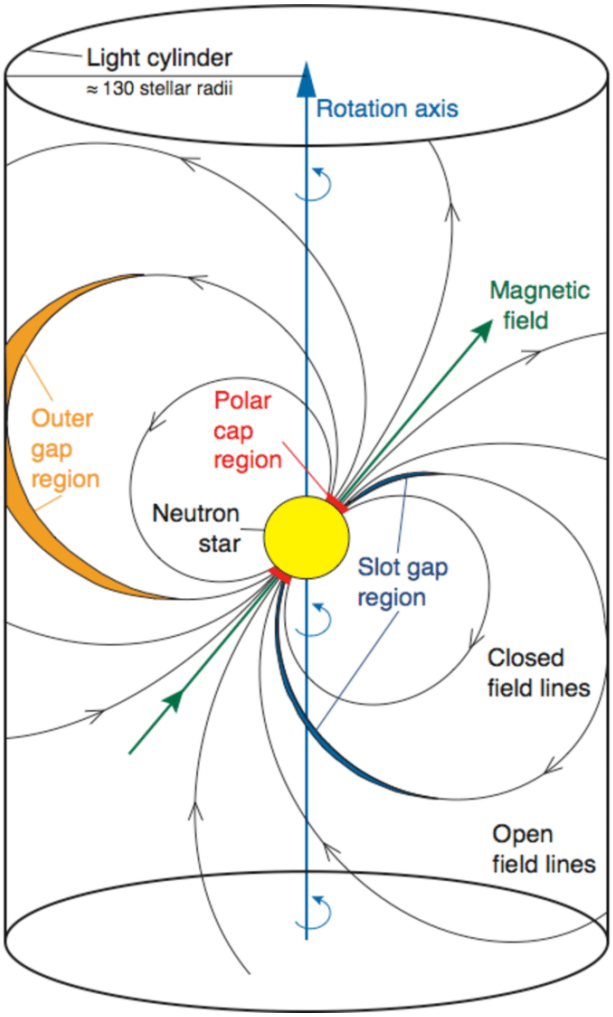

Figure 1.3: A sketch of a pulsar model showing relevant features including the magnetic field (magnetosphere), light cylinder and magnetic field lines. Pulsar emission is thought to originate from the acceleration of charged particles in the magnetosphere. Image credit: (Aliu et al., 2008).

The details of the emission mechanism will likely determine the intrinsic

brightness of the pulsar beam and how it depends on the observing frequency. Thus, if the intrinsic pulsar spectral index can be reliably measured, this can provide useful constraints on the emission mechanism. One complication of measuring the intrinsic spectral form (including the spectral index) is that we only observe a single line of sight cut through the emission beam. Thus, as the pulsar beam shape changes as a function of frequency, this needs to be accounted for when estimating the intrinsic spectral index.

There is some observational evidence that the pulsar beam *does* change as a function of frequency, from the fact that the profile itself changes as a function of observing frequency. A commonly observed trend is that the width of the profile increases at lower frequencies (Cordes, 1978), although there are several exceptions (e.g. B1944+17; Kloumann & Rankin, 2010). This trend is generally taken as evidence that the frequency of emission is a function of the height above the pulsar surface at which it is generated, known as radius-to-frequency mapping (RFM) (Cordes, 1978). The broader profile features at lower frequencies suggest that lower frequencies are emitted at larger heights, where the magnetic field lines make a larger angle to the magnetic axis and therefore have a wider emission beam, while higher frequencies are generated closer to the pulsar surface.

Thus, the observed spectral index can be thought to be comprised primarily of two main frequency-dependent effects: the brightness of the intrinsic beam and the pulse profile evolution as a function of radio frequency. Simultaneously investigating both of these spectral effects can potentially provide us with useful clues to uncover the underlying emission mechanism.

1.4 Effects of the interstellar medium on pulsars

Pulsars are close to perfect point sources due to their small emission region. This, along with the pulsed nature of their radiation (due to lighthouse-like geometry; see Figure 1.3), gives rise to a multitude of ISM effects. Of the prominent ones are dispersion which results in a spread of arrival times when observations are

made at a range of frequencies, and effects such as scattering and scintillation, caused by multipath propagation. These are briefly described below.

1.4.1 Dispersion

The cold, ionised plasma of the ISM causes the electromagnetic radiation that propagates through it to experience a frequency-dependent index of refraction (μ) which can be described by

$$\mu = \sqrt{1 - \left(\frac{\nu_{\rm p}}{\nu}\right)}, \tag{1.1}$$

where ν is the observing freqeuency and the plasma frequency ($\nu_{\rm p}$) is given by

$$\nu_{\rm p} = \sqrt{\frac{e^2 n_{\rm e}}{\pi m_{\rm e}}} \tag{1.2}$$

where $n_{\rm e}$ is the electron number density, while e and $m_{\rm e}$ are the charge and mass of an electron, respectively. Equation 1.1 and 1.2 show that the refraction index increases with the electron density along the line of sight. We define a quantity called the dispersion measure (DM) to characterise this effect, which is given by the equation:

$$\mathrm{DM} = \int_0^d n_{\rm e}(s)\mathrm{d}s \tag{1.3}$$

where d is the distance to the source in parsecs and $n_{\rm e}$ is the electron density in pc cm^{-3}. DM is a useful quantity for studies of the ISM and can also be used to estimate pulsar distances (e.g. NE2001; Cordes & Lazio, 2002). The delay time of a photon compared to a signal of infinite frequency is given by

$$t = 4.15 \times 10^6 \mathrm{ms} \;\; \mathrm{DM}\nu^{-2} \tag{1.4}$$

where ν is the frequency in MHz. This becomes relevant to pulsar detections

when the time delay between the top and bottom frequency bands is considered

$$\Delta t = 4.15 \times 10^6 ms \;\; \mathrm{DM}(\nu_1^{-2} - \nu_2^{-2}) \tag{1.5}$$

where ν_1 is the lower frequency and ν_2 is the higher frequency. If not corrected for, this dispersion delay can substantially broaden the observed pulse, especially at the low frequencies ($\lesssim$300 MHz), sometimes over several pulse periods (see Figure 1.4 for an example pulsar observation with the MWA telescope). The dedispersion methods will be discussed in Chapter 2 (§2.4.1).

1.4.2 Multipath scattering

The distribution of free electrons in the ISM is highly inhomogeneous, which causes observable effects in the form of scattering and scintillation. This radio wave propagation through the inhomogeneous (and turbulent) plasma media is extremely difficult to solve mathematically, so we often make a simplification in the form of a "thin screen model". This was developed by Scheuer (1968), and early observations validating it were made by Lyne & Rickett (1968). The "thin screen model" assumes that the entire scattering medium along the line of sight is represented by a thin screen located between the pulsar and the observer, as shown in Figure 1.5.

While this appears to be an oversimplification of the problem, it still allows us to predict the expected degree of scattering and relate the expectations with some of the observables. The scattered wavefronts are deflected from the pulsar over an angular spectrum of width θ_0, which results in a diffraction pattern for the observer. The multipath scattering will essentially cause the point source to be broadened in the form of a "scattering disk" whose radius θ_d is given by

$$\theta_\mathrm{d} = \theta_0/2 \approx \frac{e^2}{2\pi m_\mathrm{e}} \frac{\Delta n_\mathrm{e}}{\sqrt{a}} \frac{\sqrt{d}}{\nu^2} \tag{1.6}$$

where d is the distance from the screen to the observer, e is the charge of

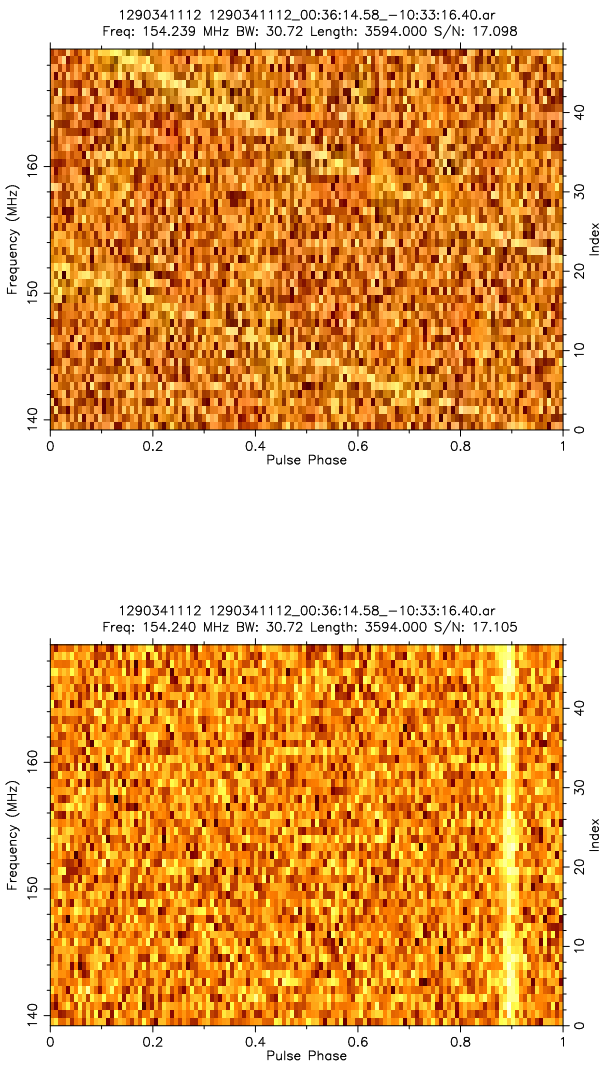

Figure 1.4: The frequency against pulse phase plots of PSR J0036−1033 before (top) and after (bottom) dedispersion. J0036−1033 has a DM of 23 pc cm^{-3} which is enough to smear the pulse profile over two pulse periods without dedispersion.

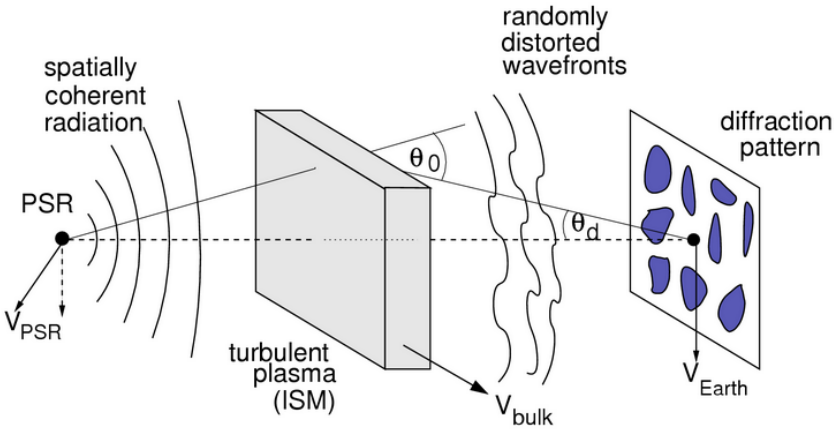

Figure 1.5: The thin screen diffraction/scattering model. The pulsar emits coherent radio waves, which are then distorted by the turbulent ISM, causing a diffraction pattern where θ_0 is the angle that the wave is bent and θ_d is the radius of the scatter-broadened image. The thin screen model can be used to help explain scattering and scintillation. Image credit: Lorimer & Kramer (2005).

an electron, m_e is the mass of an electron, n_e is the electron density, a is the scale size of electron density variations and ν is frequency. Because the scattered wavefronts at larger angles travel a longer geometrical path length (see Figure 1.5), they reach the observer later than the unscattered wavefronts. The equation for the mean scattering delay is given by

$$\tau_\mathrm{d} = \frac{\theta_\mathrm{d}^2 d}{c} = \frac{e^4}{4\pi^2 m_\mathrm{e}^2} \frac{\Delta n_\mathrm{e}^2}{a} d^2 \nu^{-4} \tag{1.7}$$

The longer path length leads to an exponential scattering tail (Williamson, 1972), as seen in MWA observations of the Crab pulsar (Meyers et al., 2017) (see Figure 1.6). The theoretical frequency dependence for the scattering delay (assuming a Kolmogorov type distribution of scattering plasma) is given by $\tau_\mathrm{d} \propto \nu^{-4.4}$ (Lee & Jokipii, 1975). However, observations suggest a somewhat shallower scaling, $\tau_\mathrm{d} \propto \nu^{-4}$ (Bhat et al., 2004). This means, at low frequencies, scattering can be more severe compared to that at ∼1-2 GHz, as shown in Figure 1.6. Even though pulse energy is essentially conserved in scatter-broadening, the peak amplitude of the pulse in observations decreases as the degree of scatter-

ing increases. This reduces the signal-to-noise, which can make detecting distant pulsars at low frequencies ($\lesssim$300 MHz) generally difficult.

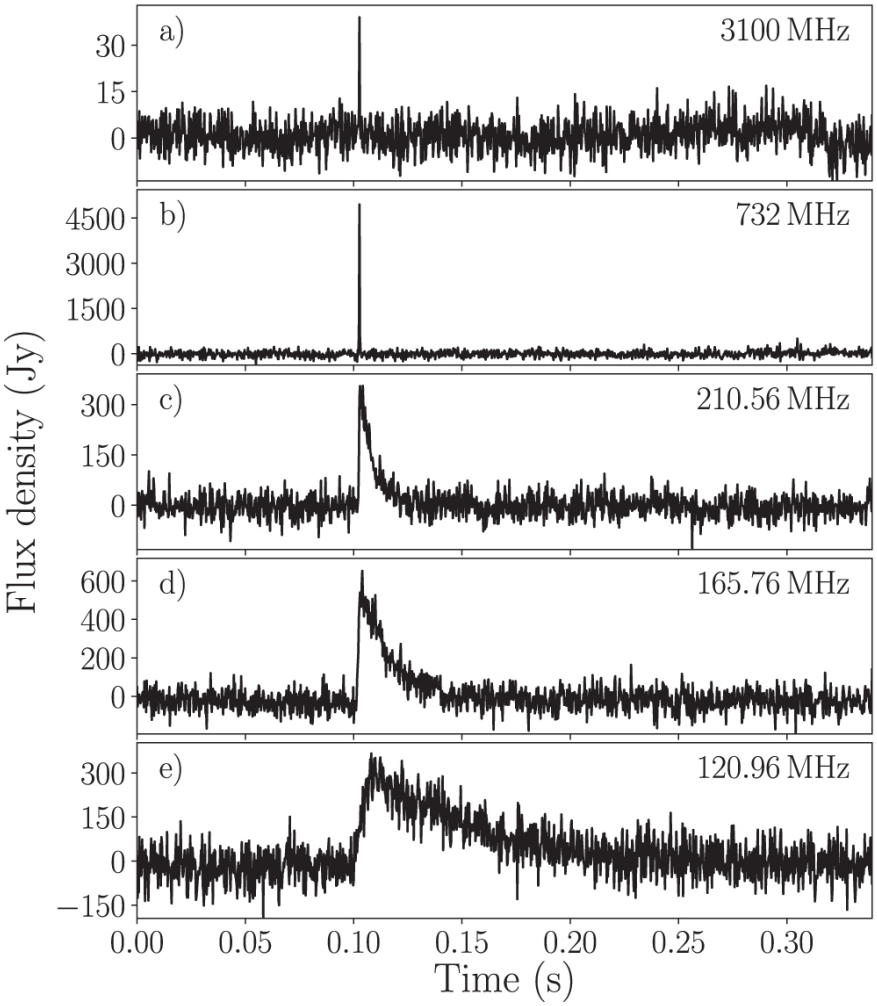

Figure 1.6: Simultaneous giant pulse of the Crab pulsar at five observing bands: (a)3100 MHz,(b) 732 MHz, (c) 210.56 MHz, (d) 165.76 MHz, and (e) 120.96 MHz. Multipath scattering is a strong function of frequency, $\tau_{\rm d} \propto \nu^{-4}$, so its effects are most obvious at MWA frequencies, introducing a significant exponential tail to each giant pulse, while the Parkes pulses are δ functions with the recorded time resolution. Image credit: Meyers et al. (2017).

At the MWA's low frequencies (80-300 MHz), signals from high-DM pulsars are generally strongly affected by scatter broadening. The generally steep flux density spectra of pulsars mean their flux density will typically be higher. This often does not lead to a more sensitive detection as the sky temperature also has a steep spectral index ($T_{\rm sky} \propto \nu^{-2.6}$), so only pulsars with highly steep spectra such

as PSR J0038-2501, which has a spectral index of -2.73 and was detected in the SMART survey (Bhat et al., 2023b), will be detected at a higher S/N. This may partially compensate for the signal degradation caused by scatter broadening's effect. The MWA's high frequency and time resolution (10 kHz and 100 microseconds, respectively) allow scattering tails to be studied in detail (e.g. Kirsten et al., 2019).

1.4.3 Scintillation

Another effect caused by multipath propagation that affects pulsar detections is scintillation. The resultant intensity fluctuations affect pulsar detectability in large pulsars surveys and their apparent flux density. Ideally, a pulsar's scintillation needs to be understood and taken into account to measure its flux density for the purpose of spectral analysis.

Scintillation manifests in observations as short-term fluctuations of intensity in both frequency and time. It is caused by propagation through the turbulent plasma of the ISM. The scattered wavefronts have a range of phases, which give rise to an interference pattern, as shown in Figure 1.5. These interference patterns are most pronounced when the RMS phase of scattered wavefronts is more than one radian. The scintillation bandwidth, also known as the characteristic scale in frequency, ($\nu_{\rm d}$) and the scattering delay ($\tau_{\rm d}$) are related to each other via the following relation,

$$2\pi\nu_{\rm d}\tau_{\rm d} \sim 1, \tag{1.8}$$

where the scintillation bandwidth scales as

$$\nu_{\rm d} \propto \frac{1}{\tau_{\rm d}} \propto \nu^4. \tag{1.9}$$

Scintillation can also be observed as a two-dimensional image of pulse intensity in frequency and time called a dynamic spectrum. A scintle is a region of increased

flux density with a characteristic size $\nu_{\rm d}$ in the frequency domain and $\tau_{\rm diff}$ in the time domain.

In the strong scintillation regime, there are two types of scintillation: Diffractive interstellar scintillation (DISS) and Refractive interstellar scintillation (RISS). The intensity variations due to DISS have approximate scintillation timescales of $\tau_{\rm diff} \sim 600$ s and scintillation bandwidth of $\nu_{\rm d} \sim 1$ MHz at 300 MHz for low-DM pulsars such as B0950+08 and J0437−4715. It should be noted that these quantities are highly frequency, direction, and distance-dependent; e.g., the timescale of the DISS scales as

$$\tau_{\rm diff} \propto \nu^{1.2} d^{-0.6} \tag{1.10}$$

where d is the distance between the Earth and the pulsar. RISS is a consequence of variations in electron density on much larger scales than those responsible for DISS. Such variations have scintillation time scales ($\tau_{\rm ref}$) ranging from days to months and scale as

$$\tau_{\rm ref} \propto \nu^{-2.2} d^{1.6} \tag{1.11}$$

The MWA's high sensitivity allows us to make accurate measurements of such observables using the dynamic spectrum method. For example, Bhat et al. (2016) observed the diffractive and refractive scintillation, including drifts in the scintillation of PSR J0437−4715, as shown in Figure 1.7. From this dynamic spectrum, they obtained $\nu_{\rm d} \sim 1.7$ MHz and $\tau_{\rm diff} \sim 260$ s, at a frequency of 185 MHz.

The observed fluctuations in the dynamic spectrum of PSR J0437−4715, which has a DM of 2.64 pc cm^{-3}, may represent an extreme example, but suggests that the apparent flux density can change by a factor of ∼5-6 for low-DM pulsars ($<\sim$ 10 pc cm^{-}3) (Bhat et al., 2016). As pulsars scintillate down, the S/N ratio decreases, which can result in fainter pulsars being undetectable. Therefore,

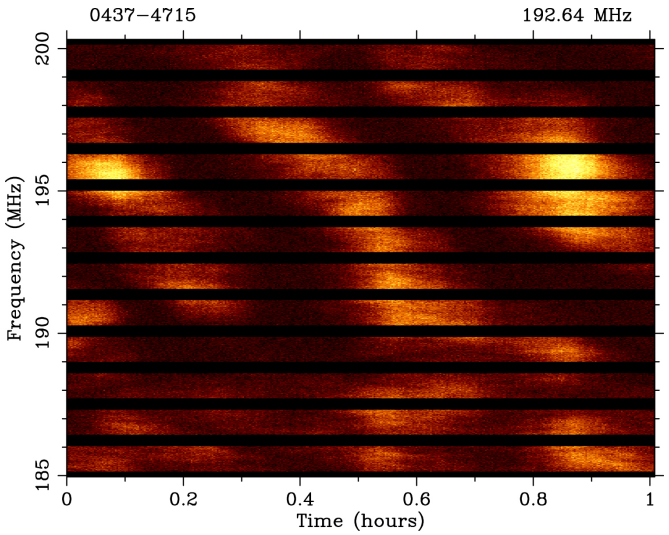

Figure 1.7: Dynamic spectrum of PSR J0437−4715 from MWA observations over a time duration of 1 hr and over a bandwidth of 15.36 MHz centred at a frequency of 192.64 MHz. The gaps in frequency correspond to the edge channels (20 each) on either end of a given coarse (1.28 MHz) channel that was not recorded due to a limitation in data recording in the early days of VCS commissioning. The data resolutions are 10 s in time and 10 kHz in frequency. Image credit: Bhat et al. (2016).

multiple observations over a large time span may be needed in order to increase the detectability of such pulsars.

To make accurate measurements of the flux density to allow robust pulsar spectral analysis, the pulsar must be observed in a way that mitigates both the diffractive and refractive effects of scintillation. If the bandwidth of the observation is several times ($>\sim 5$) larger than the $\nu_{\rm d}$, then the individual fluctuations caused by those scintles will be averaged out over the bandwidth. If there is not sufficient bandwidth, then the pulsar must be observed several times over a time scale greater than $\tau_{\rm diff}$ to average out the scintillation. To negate the effects of refractive scintillation, each frequency will need to be observed several times over a time scale greater than $\tau_{\rm ref}$. Such observing campaigns require a large amount of telescope time, so they can be difficult to schedule.

1.5 The ionosphere

The Earth's ionosphere is the uppermost layer of the atmosphere that is excited by energy from the Sun to form a low-density plasma layer extending up to a few hundred kilometres. The ionosphere can be described by its total electron content (TEC), which is the column density of electrons integrated along a line through the plasma. The spatial variations of the TEC cause incoming radio wavefronts to be refracted and hence give rise to apparent position offsets. The variation of the TEC can be referred to as the slant TEC (STEC), which can be used to calculate the apparent spatial offsets

$$\Delta\theta \simeq -\frac{1}{8\pi^2}\frac{e^2}{\epsilon_0 m_\mathrm{e}}\frac{1}{\nu^2}\nabla\mathrm{STEC[rad]} \tag{1.12}$$

where e is the electron charge, ϵ_0 is the vacuum permittivity and m_e is the electron mass (Jordan et al., 2017). The value of the STEC is direction-dependent and is often larger at lower elevations as there will be a larger amount of the ionosphere along the line of sight. This ionospheric position offset is known to affect low-frequency observations (less than 300 MHz) but has only become a problem with modern telescopes such as the MWA and LOFAR, which have the resolution ($1.1'$ and $4.5'$[1] respectively at 175 MHz) to observe these effects.

These offsets can be categorised into two groups: a "bulk" offset that is caused by a gradient in the TEC across the whole field of view; and a residual offset that is caused by small spatial scale variations in the TEC. The bulk offset is generally easier to calibrate (e.g. using the Real-Time System (RTS), which was designed to calibrate the large FoV of the MWA (Mitchell et al., 2008)), but the residual offsets are more difficult to calibrate. If these offsets are not corrected for, it will cause inaccuracies in position estimates of any pulsar candidates detected in untargeted searches, which makes follow-up more difficult. Offsets will also move the known pulsars to the edge of the tied-array (phased array) beam, which has

[1]This is for the LOFAR core stations which are commonly used to for beamformed pulsar observations.

a typical beamwidth of the order of a few arcminutes at ∼100-200 MHz, for the MWA extended array. This will reduce the S/N ratio of detections, making them more difficult to detect, and reduce the apparent flux density. Work is underway to understand these residual offsets and how quickly they change (e.g. Jordan et al., 2017).

1.6 Derived pulsar parameters

The period and period derivative of a pulsar are measurable properties that can be used to derive other pulsar parameters, such as the magnetic field strength. Among the other basic properties of pulsars are the spin-down luminosity and characteristic ages, which are explained in the following sections.

1.6.1 Spin-down luminosity

For the vast majority of pulsars, the rotation periods tend to increase with time. We call this spin down, and it is caused by the loss of rotational kinetic energy, $E_{\rm rot}$, which represents the total power output by the neutron star. The spin-down luminosity $\dot{E}$ is given by

$$\dot{E} \equiv -\frac{dE_{\rm rot}}{dt} = -\frac{d(I\Omega^2/2)}{dt} = -I\Omega\dot{\Omega} = 4\pi^2 I\dot{P}P^{-3}, \tag{1.13}$$

where $\Omega = 2\pi/P$ is the rotational angular frequency and I is the moment of inertia. If we assume the moment of inertia is the canonical value of $I = 10^{45}$ g cm^2 (i.e. a neutron star of mass ∼1.4 M$_\odot$ and radius ∼10 km (Lorimer & Kramer, 2005)), we find

$$\dot{E} \simeq 3.95 \times 10^{31} \text{erg s}^{-1} \left(\frac{\dot{P}}{10^{15}}\right)\left(\frac{P}{s}\right)^{-3}. \tag{1.14}$$

This rotational energy is converted into several different forms of radiation. The most significant is magnetic dipole radiation, followed by the high-energy

radiation and pulsar wind. Only a tiny, seemingly insignificant, fraction of $\dot{E}$ is converted into radio emission.

Although spin-down luminosity is not a direct indication of the observable radio luminosity, it is a useful parameter for estimating the power output of a pulsar. The spin-down luminosity may influence the emission and, therefore, the pulsars' spectra. For example, both Han et al. (2016a) and Jankowski et al. (2018) found a correlation between the spin-down luminosity and the spectral index.

1.6.2 Characteristic age

As a pulsar spins down, it loses a fraction of its rotational kinetic energy, so its spin frequency $(\tilde{\nu})$[2] changes. This loss of energy is due to the rotating magnetic dipole emitting an electromagnetic wave which will slow its spin frequency. This can be simplified to a power law with the form

$$\dot{\tilde{\nu}} = -K\tilde{\nu}^n, \tag{1.15}$$

where n is the braking index, and K is a constant. The spin-down model of Equation 1.15 can also be expressed in terms of the pulse period (since $\dot{\tilde{\nu}} = 1/P$)

$$\dot{P} = KP^{2-n} \tag{1.16}$$

We can estimate the characteristic age of a pulsar by integrating the above equation by assuming that n is constant with time

$$T = \frac{P}{(n-1)\dot{P}}\left[1 - \left(\frac{P_0}{P}\right)^{n-1}\right] \tag{1.17}$$

where P_0 is the spin period at birth. If we assume the $n = 3$ and that the birth spin period is much shorter than the current value ($P_0 << P$), then the equation for characteristic age simplifies to

[2]In this thesis, $\tilde{\nu}$ is used to denote a pulsar's spin frequency so it is not confused with observing frequency ν.

$$\tau \equiv \frac{P}{2\dot{P}} \simeq 15.8\text{Myr} \left(\frac{P}{\text{s}}\right) \left(\frac{\dot{P}}{10^{-15}}\right)^{-1} \tag{1.18}$$

The possible values of τ are shown in the $P - \dot{P}$ diagram (Figure 1.1). As the pulsar ages, it will move towards the bottom right of the $P - \dot{P}$ diagram and eventually cross the "death line" and no longer produce radio emission. This death line is not a hard cut-off as it makes several assumptions about the pulsar's magnetic field and mass to predict when electron-positron pair production ceases (Chen & Ruderman, 1993).

Due to the assumption that $n = 3$, this does not provide a reliable estimate. It has been shown that due to a decaying inclination angle (a) that the value of n changes throughout a pulsar's life (Johnston & Karastergiou, 2017). There are several cases of pulsars where their ages are independently calculated and where it was found that the characteristic age is inaccurate. One extreme example is PSR J0537+2817 which has a characteristic age of 620 kyr but, based on its proper motion, was born only 30 kyr ago (Kramer et al., 2003b).

Although the characteristic age is unreliable, it can still be useful for investigating the properties of pulsars. Investigating correlations between characteristic age and other pulsar parameters, such as spectra, can help us understand how pulsars evolve. For example, Jankowski et al. (2018) compared the characteristic age to the spectral index and found no significant correlation.

1.7 Pulsar spectral properties

Over the last few decades, considerable effort has been put into measuring the flux density of pulsars at a range of radio frequencies. This effort began in earnest with Sieber (1973) (and publications within), followed by Malofeev (1980) and Izvekova et al. (1981) at low frequencies ($\lesssim$100 MHz). While it has become less fashionable to make routine measurements, some of the large pulsar surveys (e.g. Manchester et al., 2001; Sanidas et al., 2019) often report flux density measure-

ments of redetected pulsars. There are also targeted flux density surveys whose goal is to use their measurements to investigate pulsar spectra (e.g. Jankowski et al., 2018; Spiewak et al., 2022; Kondratiev et al., 2016). These pulsar flux density surveys require a complete understanding of the instrument to make accurate estimates of the apparent flux density. To ensure the effect of scintillation is mitigated, pulsars must be observed multiple times over a period larger than the scintillation timescale, which requires a significant amount of telescope time, and averaged.

Once sufficient flux density measurements are made at a range of frequencies, the spectra of the pulsars can be studied. The spectra of a large number of pulsars have been collated as early as 1995 (Lorimer et al., 1995) using different population sizes and frequency ranges (e.g. Toscano et al., 1998; Malofeev et al., 2000; Maron et al., 2000; Bilous et al., 2016; Han et al., 2016a; Spiewak et al., 2022), see Table 6.4. The largest pulsar spectral analysis to date was performed by Jankowski et al. (2018), who studied the spectral properties of 441 pulsars. This is only a fraction ($\lesssim 20\%$) of the over 3000 known pulsars (see Figure 1.1).

The majority of pulsars' apparent spectra are steep and can be described using a simple power law with spectral index α (see §1.7.1). With a wide enough frequency range of measurements, some pulsars are shown to deviate from the simple power law with a low-frequency turn-over (see §1.7.3) or a high-frequency cut-off (see §1.7.2). These spectral features will be explained in the following sections, and the spectral models used in this thesis will be later explained in §5.4.1.

1.7.1 Spectral index

The spectral index of pulsars is an observed property of the steepness of a spectrum. Currently, we do not understand what causes different pulsars to have varying spectral indices. It has been suggested that the pulse profile evolution as a function of radio frequency (e.g. RFM) contributes to the observed spectral

index. This is likely only a contributing factor to the apparent spectral index that must be accounted for so the brightness of the intrinsic beam as a function of radio frequency can be investigated. One method for understanding the spectral index is to find correlations between it and pulsar properties. Several authors (Jankowski et al., 2018; Han et al., 2016a; Lorimer et al., 1995), have found such a correlation with the spin-down luminosity, which provides us clues to what drives the spectral index emission property.

The measured values of spectral index α vary from ~ -0.2 to ~ -3.0 with a mean of $\langle\alpha\rangle = -1.60 \pm 0.03$ (Jankowski et al., 2018). The spectral index can be an important selection effect in pulsar searches and, therefore, their derived populations. For instance, untargeted searches of large swathes of the sky at high frequencies are more likely to detect pulsars with flatter spectra, while low-frequency searches are more likely to detect steep spectrum pulsars, as discussed in Bates et al. (2013) (see Figure 1.8). It is, therefore, important to search for pulsars at a range of frequencies to develop a complete picture of the pulsar population. For example, Lorimer et al. (1995) proposed that younger pulsars may have flatter spectra, but that may merely be a population bias due to the fact that high-frequency surveys preferentially tend to select younger pulsars along the Galactic plane.

The mean value of the spectral index also seems to be biased by the frequency range that it is measured over, as shown in Table 6.4. For example, publications that only measure the spectral index over a low-frequency range, such as Bilous et al. (2016) and Malofeev et al. (2000), tend to estimate a flatter mean spectral index (-1.4 and -1.47 ± 0.76 respectively) while publications that use a high-frequency range, such as Han et al. (2016a) and Spiewak et al. (2022), estimate a steeper spectrum (-2 and -1.92 ± 0.06 respectively). All other publications that used a large frequency range estimated a spectrum between -1.6 and -1.8 (Lorimer et al., 1995; Toscano et al., 1998; Maron et al., 2000; Jankowski et al., 2018).

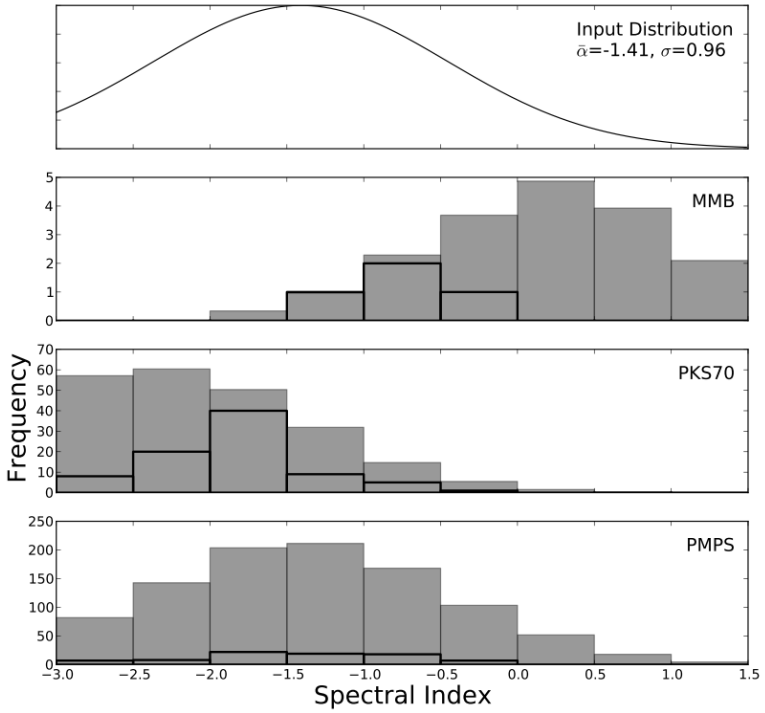

Figure 1.8: Histograms of the spectral index of detected pulsars in a simulation using `PsrPop` done by Bates et al. (2013) (grey; averaged over 100 realisations) and from the pulsar catalogue (black outline). Each panel represents each survey respectively: the Parkes 6.5 GHz multi-beam pulsar survey at 6591 MHz (MMB, (Bates et al., 2011)), the Parkes Southern pulsar survey at 436 MHz (PKS70, (Manchester et al., 1996)), and the Parkes multi-beam pulsar survey at 1352 MHz (PMPS, (Manchester et al., 2001)). The top panel shows the input distribution used to generate a model pulsar population.

The distribution of spectral indices is often used in simulations of the pulsar populations with programs such as `PsrPopPy` (Bates et al., 2014a). The spectral index distribution was initially thought to be normally distributed, but more recent work suggests they are more accurately fit by a log-normal distribution (Jankowski et al., 2018). These simulations and population studies can be used to predict the number of discoveries in future surveys (with the SKA, for example) and to estimate the number of neutron stars in the Galaxy, which can then be compared to the supernova birth rate (e.g. Keane & Kramer, 2008).

1.7.2 High-frequency cut-off

It has been observed by several authors (e.g. Malofeev, 1980; Jankowski et al., 2018) that at high frequencies, pulsars' emission drops to below the telescope detection limit in what is often called a high-frequency hard cut-off. This frequency limit is due to the electron's acceleration in the electric field from the stellar surface, which passes through a maximum and decreases as the electron velocity approaches relativistic speeds ($\gamma \gg 1$). This relativistic limit takes the functional form of the spectra shown in Figure 1.9.

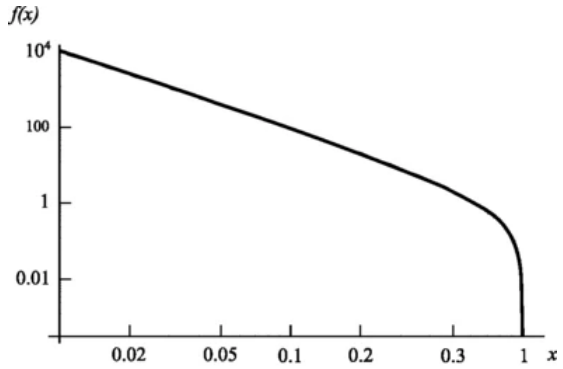

Figure 1.9: Function $f(x) = (1-x)/x^2, x = \omega/\omega_{\rm cf}(0)$ that defines the spectrum of coherent emission of electrons accelerated in the vacuum gap. Image credit: Kontorovich & Flanchik (2013).

This cut-off frequency $\nu_{\rm c}$ has been estimated by Kontorovich & Flanchik (2013) to be

$$\nu_{\rm c} = \sqrt{\frac{eE_{\rm max}}{2m_{\rm e}h}} = \sqrt{\frac{\pi eB}{m_{\rm e}cP}}, \tag{1.19}$$

where $E_{\rm max}$ is the maximum value of the electric field, e is the charge and $m_{\rm e}$ is the mass of the electron, h is Planck's constant, c is the speed of light in a vacuum, B is the magnetic field strength, and P is the spin period. Due to the dependence of the magnetic field on the period, Equation 1.19 can be further simplified to predict the value of $\nu_{\rm c}$

$$\nu_{\rm c} = 1.4{\rm GHz}\left(\frac{P}{s}\right)^{0.46\pm0.18} \tag{1.20}$$

1.7.3 Low-frequency turn-over

For most pulsars, the flux density spectrum turns over at low frequencies (see Figure 1.10 for the spectral shape). There are several similar ways to describe a low-frequency turn-over. The expression used in this thesis is shown in Equation 5.7, which is repeated here for convenience

$$S_\nu = c \left(\frac{\nu}{\nu_0}\right)^{\alpha} \exp\left[\frac{\alpha}{\beta}\left(\frac{\nu}{\nu_{\rm peak}}\right)^{-\beta}\right], \tag{1.21}$$

where α is the spectral index, $\nu_{\rm peak}$ is the turn-over frequency, and $0 < \beta \leq 2.1$ determines the smoothness of the turn-over. A similar expression for low-frequency turn-over was used by Izvekova et al. (1981)

$$S_\nu = c \left(\frac{\nu}{\nu_0}\right)^{\alpha} \exp\left[\frac{-\alpha}{2-5\delta}\left(\frac{\nu}{\nu_{\rm peak}}\right)^{-(2-5\delta)}\right], \tag{1.22}$$

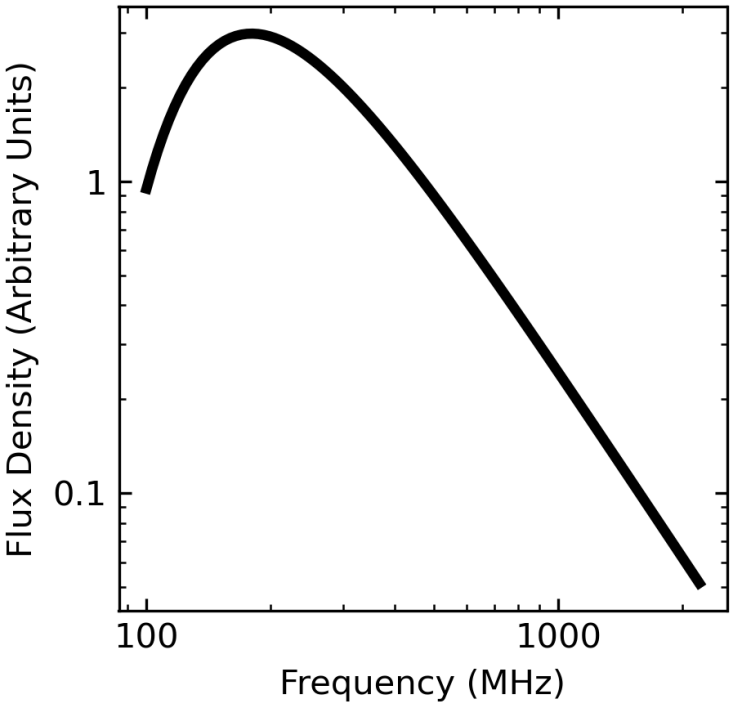

Figure 1.10: The functional form of the low-frequency turn-over spectrum as described by $S_\nu = c \left(\frac{\nu}{\nu_0}\right)^{\alpha} \exp\left[\frac{\alpha}{\beta}\left(\frac{\nu}{\nu_{\rm peak}}\right)^{-\beta}\right]$.

where δ is the turn-over parameter that Izvekova et al. (1981) uses and is equivalent to

$$\beta = -(2 - 5\delta) \tag{1.23}$$

This power law with low-frequency turn-over model can be used to describe synchrotron self-absorption when $\beta < 2.1$ and thermal free-free absorption when $\beta = 2.1$. Since absorption occurs due to the density of matter rather than the total amount along a line of sight, the majority of absorption will occur at the most dense region. It is possible that there is a dense region along the line of sight, such as an H2 region, but for most pulsars, their surrounding medium will be the highest-density region. Investigating these low-frequency turn-overs can potentially give us insights into the medium surrounding pulsars.

It has been observed that normal pulsars' turn-over frequency follows a trend of approximately:

$$\nu_{\rm peak} = 120 \text{ MHz} \left(\frac{\tilde{\nu}}{\text{Hz}} \right)^{0.36}, \tag{1.24}$$

where $\nu_{\rm peak}$ is the turn-over frequency (Malofeev, 1980, 1996). However, MSPs do not seem to follow this trend. Equation 1.24 predicts that MSPs with a period of $P \leq 50$ ms should have a $\nu_{\rm peak} \geq 350$ MHz, but often this is not the case. Early work that involved measurements of 30 MSPs showed no evidence of a turn-over above ∼100 MHz (Kuzmin & Losovsky, 2001). According to Kuzmin & Losovsky (2001), the nature of the turn-over can be interpreted geometrically and the small divergence of the magnetic eld lines may inhibit low-frequency spectral turn-over compared to normal pulsars

1.7.3.1 The optical depth infered from gigahertz-peaked spectra

When convex spectra (power law with low-frequency turn-over or log parabolic spectra) have a maximum flux density at a frequency around 1 GHz, this is classed

as a gigahertz-peaked spectrum pulsar (Kijak et al., 2007, 2011; Dembska et al., 2015; Kijak et al., 2017). It has been proposed by Rajwade et al. (2016) that the high frequency of this turn-over is due to the thermal free-free absorption in a dense surrounding medium; for example, a pulsar wind nebula, molecular cloud, or supernova remnant. Rajwade et al. (2016) proposed a model of the optical depth of the surrounding medium for gigahertz-peaked spectra.

$$S_\nu = c \left(\frac{\nu}{\nu_0}\right)^{\alpha} \exp\left[-\tau_{\rm ref} \left(\frac{\nu}{\nu_{\rm ref}}\right)^{-2.1}\right], \tag{1.25}$$

where $\tau_{\rm ref}$ is the optical depth at a reference frequency ($\nu_{\rm ref}$). To obtain the value of optical depth, we use the expression given in Mezger & Henderson (1967)

$$\tau_{\rm ref} = 0.082\ a\ \nu_{\rm ref}^{-2.1}\ {\rm EM}\ T_{\rm e}^{-1.35}, \tag{1.26}$$

where $T_{\rm e}$ is the electron temperature, a is a correction factor of the order unity for electron temperatures $T_{\rm e} > 20$ K, and EM is the emission measure.

Combining the previous two equations,

$$\nu_{\rm peak} = -0.433\ a^{-0.476}\ {\rm EM}^{0.476}\ T_{\rm e}^{-0.643} \tag{1.27}$$

$$\nu_{\rm peak}^{2.1} = -0.173\ a\ {\rm EM}\ T_{\rm e}^{-1.35} \tag{1.28}$$

and

$$\tau = -0.014 \frac{\nu_{\rm peak}}{\nu}^{2.1} \tag{1.29}$$

Substituting this back into the Equation 1.25,

$$S_\nu = c \left(\frac{\nu}{\nu_0}\right)^{\alpha} \exp\left[0.014 \left(\frac{\nu}{\nu_{\rm peak}}\right)^{-2.1}\right], \tag{1.30}$$

which is equivalent when $\beta = 2.1$ and $\alpha = 0.029$. The restrictive value of α makes it hard to directly compare spectra fit with Equation 1.22 to Equation 1.25.

Equation 1.27 is a three-parameter equation (a can be treated as a constant), so once $\nu_{\rm peak}$ is measured, sometimes the exact values of EM and $T_{\rm e}$ can't be calculated. Rajwade et al. (2016) estimated a reasonable range of values for EM or $T_{\rm e}$ by using common values for the other parameter.

1.8 Pulsar population simulations

Pulsar searches increase the number of known pulsars, and with this known pulsar population, we can extrapolate a pulsar population model. The predicted population of pulsars can be used to test theoretical estimates of supernova rates. Current estimates of the pulsar birth rate are higher than the core-collapse supernova rate (Keane & Kramer, 2008), which suggests there are biases in our pulsar population models or a lack of understanding of the types of pulsars and their evolution.

The most popular software for simulating pulsar populations is `PsrPopPy`[3] (Bates et al., 2014a) which is a `Python` implementation of `PsrPop`[4], the original `Fortran` software. The software is easy to install and run in 'standard' mode, thanks to a set of scripts included with the software. It is also modular enough that other models or methods can be added by writing customised scripts.

We will now summarise the method described in Bates et al. (2014a) and discuss some of the assumptions made that may lead to biases or inaccuracies. The software uses one or more pulsar surveys to describe the number of pulsars that are detected in an area of the sky, given the survey's detection threshold. Pulsars are generated using either the "snapshot" or "evolve" methods until the expected number of pulsars are detected by the survey.

The snapshot method uses the following statistical model distributions to simulate the current Galactic population: pulse period; pulse width; luminosity; spatial; Galactic electrons (DM); scintillation; and spectral index.

[3] https://github.com/samb8s/PsrPopPy
[4] http://psrpop.sourceforge.net

These models allow the creation of simulated pulsars, whose fluxes are scaled from the input pulsar survey frequency (often at ∼1.4 GHz) to different frequencies using a simple spectral index. Because only a simple power law is used to extend the pulsar luminosity to low frequencies, the simulated population that is detectable at low frequencies may be overestimated because it does not take into account low-frequency turn-overs and scattering. To simulate the population more accurately, we must improve our understanding of pulsar spectra at low frequencies so they can be integrated into simulation software.

The evolve method is the other method for simulating a population based on the work of Ridley & Lorimer (2010). It generates pulsars of random characteristic ages and evolves them for the following parameters: magnetic field; rotational alignment; pulsar spin-down; and Galactic position after moving through the Galactic potential. Note that there is no evolution of the pulsar spectra, so any potential correlation between characteristic age and pulsar spectra parameters will not be taken into account using this method.

If, on the other hand, we incorporate more complex pulsar spectra into the simulations, we can more accurately simulate the underlying pulsar population. These simulated populations can help estimate how many pulsars will be discovered in new telescopes and surveys, such as the SKA, and can inform which parameter spaces are most likely to yield the most pulsar discoveries.

1.9 The direction and scope of this thesis

The primary goal of this thesis is to study the spectra of pulsars at low frequencies with the MWA. To achieve this, we will leverage the SMART pulsar survey that is currently underway at the MWA (see Bhat et al. (2023a,b)) as it has the potential to provide hundreds of low-frequency flux density measurements for a large sample of Southern-sky pulsars. These measurements will be used along with the published data (in the literature) to refine pulsar spectra for a large sample of pulsars. However, to achieve this goal, several challenges had to be

overcome.

The MWA has a huge field of view (FoV) of ($\sim$600 deg^2 at 150 MHz), but this comes at the cost of the substantial processing required to create thousands of tied-array beams (explained in Chapter 2, §2.3.1) to tessellate the entire field of view. The feasibility of the SMART survey, and the ultimate success of our program of finding/detecting pulsars and measuring flux densities at low frequencies, depends on developing an efficient pipeline for undertaking this massive processing effort. Chapter 3 describes our method for overcoming one of the major bottlenecks by altering the beamforming algorithm to avoid the redundant reading of data and calibration.

The effects of the ionosphere are more prominent at the low frequencies of MWA (80-300 MHz). In an effort to correct for these ionospheric position offsets, the MWA uses direction-independent calibration for voltage capture system (VCS) observations, unlike most telescopes which use direction-dependent schemes. An investigation of the effectiveness of ionospheric offset calibration and a method for mitigating it was performed in Chapter 3.

Once the MWA beamformer was optimised, the Southern-sky MWA Rapid Two-metre (SMART) initial pass survey (explained in Chapter 2, see §2.5) data processing commenced. This led to a steady increase in the number of detections of known pulsars. Many of these pulsars were detected for the first time at frequencies below 300 MHz, which is not surprising as most of the pulsar surveys in the southern sky were carried out at frequencies above $\sim$400 MHz (Manchester et al., 1978, 1996, 2001; Keith et al., 2010). The development of this survey and search pipeline proved to be a worthwhile investment as it has, to date, discovered five pulsars. This is only with the initial processing (i.e. a shallow survey) from a small fraction ($<$10%) of the data that have been analysed (and scrutinised for pulsar candidates). The discovery, follow-up and spectral analysis of the first pulsar discovered with the MWA are described in Chapter 4 (see also Swainston et al. (2021)). The development of this follow-up method (Swainston et al., 2021)

allowed the spectra of the first pulsar discovery to be included in the final spectral analysis and demonstrates how future discoveries will be included in future work.

The 120 pulsar flux density measurements from the SMART survey (Bhat et al., 2023b) were integrated from measurements reported in the literature. A closer analysis of a large body of accrued measurements suggested that accurate spectral analysis will benefit from developing refined techniques for modelling pulsar flux density data and consistently applying them across the data sets to obtain robust spectral fits. The lack of a dedicated pulsar flux density catalogue or open-source fitting software became apparent at this stage. Even though the ATNF pulsar catalogue (version v1.68 released on November 2022; Manchester et al., 2005)[5] does maintain a large collection of published flux densities, the quoted frequency at which they are measured is sometimes necessarily approximate. This is largely to do with the way the database is structured. Often times this results in each researcher doing their own literature review and manually recording the flux density measurements in their own private databases, which are generally not shared, and as a result, leads to unnecessary duplication of effort. Moreover, the use of different spectral fitting methods and their implementations can also lead to inconsistent spectral results, which makes comparing results between different publications rather tedious, as well as difficult. These considerations motivated the development of a new software package called `pulsar_spectra`, described in Chapter 5. `pulsar_spectra` is intended to be a centralised repository for pulsar flux density measurements with the main goal of making published measurements more accessible to the astronomical community and providing them with a user-friendly suite of tools for accurately modelling spectra.

The development of `pulsar_spectra` allows the spectral analysis of a substantially expanded sample of pulsars and is described in Chapter 6. As discussed in this chapter, the pulsar sample that was used for our analysis is more than

[5] https://www.atnf.csiro.au/research/pulsar/psrcat/

twice that was used in the previous most extensive analysis by Jankowski et al. (2018). The parameters of the spectral fits and the related results are compared to pulsar parameters in order to explore possible correlations that may give clues about pulsar emission. The analysis explores possible biases in the spectral fitting method (§6.3.4), limitations of the data (§6.3.5), correlations that are due to bias (§6.3.6) and correlations that are likely due to an underlying theoretical motivation (§6.3.7).

In Chapter 7, the results of the spectral analysis work are discussed further, as well as the current limitations and potential future work.

Chapter 2

Instrumentation and Methodologies

2.1 Overview of the Murchison Widefield Array

The Murchison Widefield Array (MWA) is located at Inyarrimanha Ilgari Bundara, the CSIRO Murchison Radio-astronomy Observatory (MRO), approximately 315 kilometres northeast of Geraldton in Western Australia's Mid-West region. The MRO is a sparsely populated, radio-quiet zone protected by the Australian Government and therefore has a relatively low level of radio-frequency interference (RFI) caused by broadcast radio, TV and cell phones but can still be affected by aircraft and satellites. The MWA is the low-frequency (80-300 MHz) precursor telescope of the Low-Frequency component of the Square Kilometre Array (SKA-Low), which is being built on the same site.

The Phase I MWA (Tingay et al., 2013) consisted of 128 'tiles' distributed across a ∼3 km diameter region, where each tile is a dipole array composed of 16 dual-polarisation dipole antennas that are arranged in a 4×4 square grid with a ∼1.1 m separation and mounted on a ground screen of steel wire mesh, as shown in Figure 2.1. Signals from the 16 dipoles of a tile are combined by an analog beamformer, where a set of switchable delays (between 0 and 13.5 ns)

Figure 2.1: A photograph of an MWA tile with a corresponding analog beamformer unit (the 'white box') at the MRO site. Each tile consists of 16 equally spaced dual-polarisation dipoles.

are employed to steer the 'tile beam' (or 'primary beam') toward one of the 197 predetermined sky positions (known as 'sweet spots').

The analog signal from each tile is amplified, digitised, and channelised in a receiver box (Prabu et al., 2015). There are 16 receiver boxes deployed at the site, one for every eight tiles, in which 16 streams of dual-polarisation analog signals are filtered to a bandpass of 80−300 MHz. The signal subsequently undergoes two stages of channelisation, both implemented with polyphase filter banks (PFBs), the first stage within the receiver and the second stage within dedicated field programmable gate array (FPGA) hardware. This first stage of channelisation produces 24×1.28 MHz coarse frequency channels with a total bandwidth of 30.72 MHz. In the Phase I system, the signal underwent a second stage of channelisation, producing 128×10 kHz fine channels, resulting in a time resolution of 100 μs (Ord et al., 2015).

Between late 2016 and mid-2017, the MWA underwent a major upgrade from Phase I to Phase II (Wayth et al., 2018). This involved the addition of 128 new

tiles, 72 tiles short baseline tiles, which are used in the compact configuration (see Figure 2.2) and 56 long baseline tiles, which are used in the extended configuration (see Figure 2.3). Although the array now consists of 256 tiles, the signal path and the electronics (receivers and correlator) were not upgraded, so only 128 tiles can be used at once in either the compact or extended array configurations.

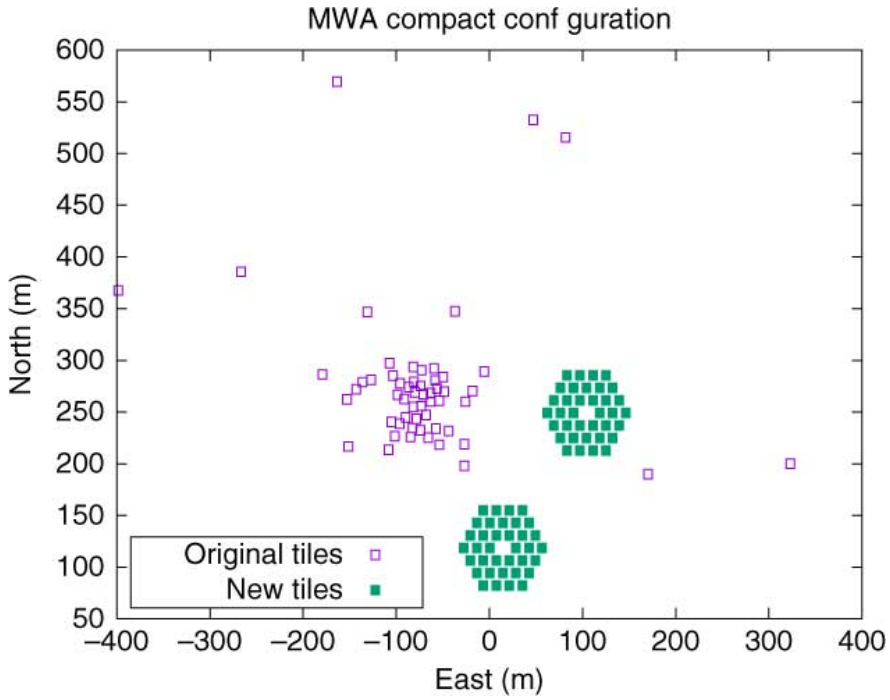

Figure 2.2: The compact configuration includes the 72 new tiles arranged as two regular hexagonal arrays (filled squares) (Wayth et al., 2018).

The compact configuration consists of 56 tiles in the MWA's core and 72 new tiles arranged in two regular hexagonal configurations as shown in figure 2.2. The hexagonal configurations result in a large number of redundant baselines, which enable the recovery of antenna gains during calibration without requiring a sky model (e.g. Li et al., 2018) and boosts the power-spectrum sensitivity, which is ideal for probing the Epoch of Reionization (e.g. Parsons et al., 2012) (one of the MWA's key science goals). The compact configuration's shorter baselines result in a larger Full Width at Half Maximum (FWHM) of the tied array beam, see Table 2.1. This is advantageous for performing pulsar surveys as the FWHM is increased by a factor of 4.5 at 155 MHz, compared to Phase I, which allows

each beam to cover a factor of ∼20 more area of the sky per tied-array beam, as explained in §2.3.1.

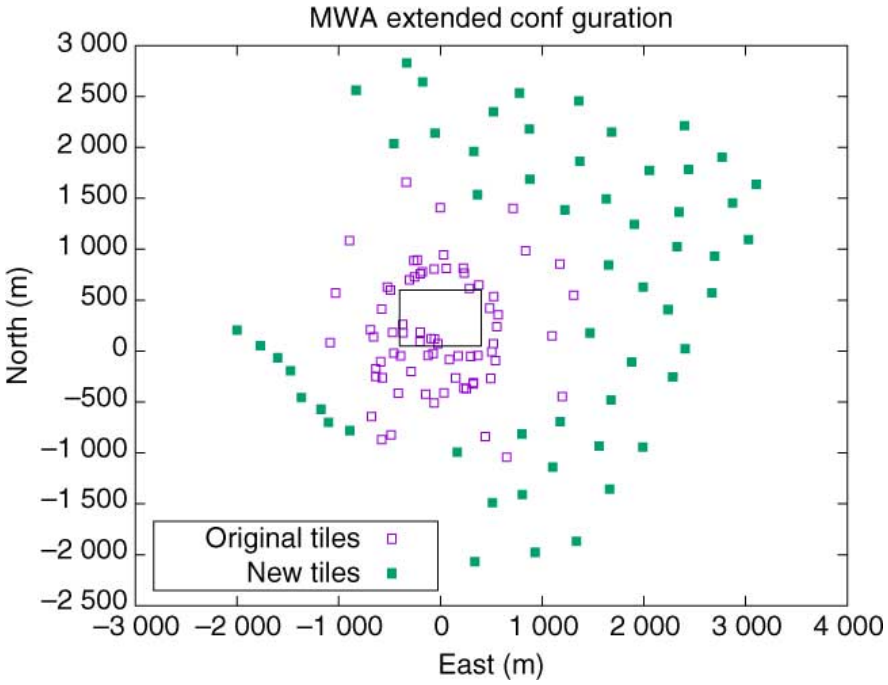

Figure 2.3: The extended configuration includes the 56 new long-baseline tiles (filled squares) (Wayth et al., 2018). The inset rectangle shows the area bounded by Figure 2.2.

The extended configuration uses 56 sparsely-spaced tiles placed within a ∼6 km diameter instead of the 56 closely-spaced core tiles from the Phase I MWA as shown in Figure 2.2. This allows higher resolution imaging (∼ 1.8′ at 155 MHz) and reduces classical confusion by a factor of ∼8, compared to the Phase I MWA (Wayth et al., 2018). The extended configuration is favoured by most radio imaging-based science goals as well as for pulsar candidate follow-up, as the higher resolution allows us to estimate the position of a pulsar more accurately. In order to satisfy the requirements of the MWA's various science goals, the array configuration is switched approximately once a year.

The MWA has been further upgraded to Phase III, which, thanks to the MWAX correlator (Morrison et al., 2023), can use all 256 tiles at once. The Phase II data and the MWAX correlator were not used in this thesis, so all

Array configuration	80 MHz	155 MHz	300 MHz
Phase II compact	42.7	22.1	11.4
Phase I	9.5	4.9	2.5
Phase II extended	3.4	1.8	0.9

Table 2.1: The FWHM of the MWA tied array beam in arc minutes for different array configurations and frequencies.

descriptions of the MWA refer to the "legacy" system.

2.2 The Voltage Capture System

In the legacy system, after analog beamforming and two PFB steps, the media converter servers record the fine channelised data, as seen in Figure 2.4, also known as the VCS archive. These files conserve the complex voltages of each tile with a time and frequency resolution of 100 μs and 10 kHz, respectively, and are archived for further post-processing. This process is explained in more detail in Tremblay et al. (2015).

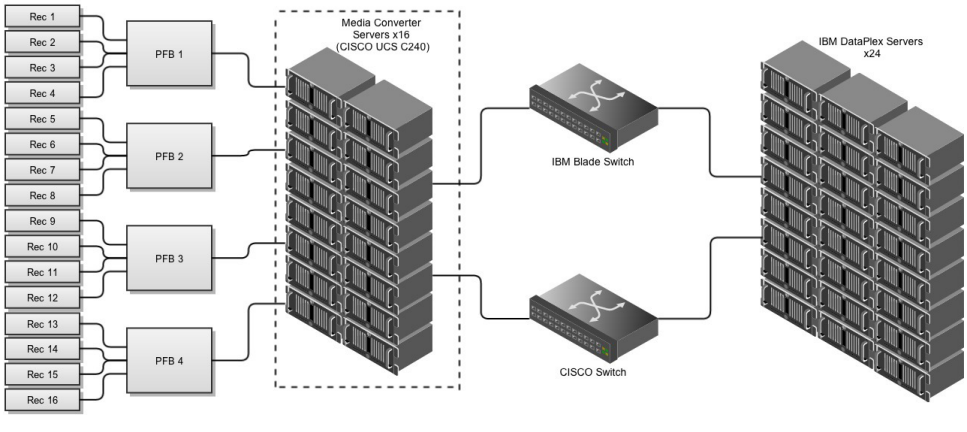

Figure 2.4: A simplified signal path of the MWA legacy system. In VCS mode, the baseband data are written to local RAIDs on the media converter servers (highlighted with the dashed box). This data has 100 μs time resolution and 10 kHz wide channels. Image credit:(Tremblay et al., 2015).

Due to the large number of tiles and high time and frequency resolution, the data rate of the MWA VCS observations is enormous at 27 TB per hour. This data

rate and the size of the VCS archive limit the total dwell time of a VCS observation to 80 minutes. These data are transferred to the Pawsey Supercomputing Centre via a fibre optic cable to be archived. This transfer limits the VCS observations to ∼160 minutes per week. These limitations are made up for by the extreme flexibility of the VCS data, including the ability to create thousands of tied-array beams that can cover the ∼600 deg^2 FoV in post-processing.

2.3 MWA VCS processing

The MWA VCS data can be post-processed in several ways, including creating a sensitive tied-array beam (see §2.3.1); creating an incoherent beam, with reduced sensitivity compared to a tied-array beam but observes the entire FoV (see §2.3.2); and offline correlated, which reduces the time resolution but improves sensitivity so it can be used for radio imaging. A tied-array beam is required to do sensitive pulsar astronomy, so we shall focus on that.

2.3.1 Tied-Array Beamforming

The design philosophy and algorithmic implementation behind tied-array beamforming with the MWA is explained in detail in Ord et al. (2019). In the following sections, we give an overview of these algorithms (§2.3.1.1, 2.3.1.2 and 2.3.1.3).

2.3.1.1 Delay Compensation

We must compensate for the geometric and cable delays Δt to a single reference point to phase up the telescope. The phase correction for a channel, n with centre frequency ν_n of antenna j required to compensate for beam steering and cable delays is

$$\phi_{j,n} = 2\pi \Delta t_j \nu_n \tag{2.1}$$

As the Earth rotates, it alters the array's projected baselines which causes

the interferometer fringe pattern on the sky to change. We can measure how the fringes change with time, known as the fringe rate, to recalculate the delays frequently enough to maximise sensitivity. Given the maximum frequency of 300 MHz and the maximum baseline of 5 km, the maximum fringe rate for the MWA Phase 2 is $\sim$1 rad s^{-1}. Since one radian is enough to de-cohere the beam, the delays will be recalculated every second.

2.3.1.2 Calibration

The gain calibration process is an attempt to determine the instrumental response. Each antenna in the array has a complex gain, imparting a phase turn on the incoming electric field. This phase turn serves to de-cohere the sum of the antenna signals so they must be compensated for, so they are on the same relative, or absolute, amplitude and phase scale.

Due to the antennas' lack of calibrated noise diodes, the antennas cannot be calibrated individually and must be calibrated as an interferometer. The most common method is via a short calibration scan performed on a nearby calibrator field. The raw voltages are correlated to form visibilities from which the calibration solution can be obtained.

These antenna-based complex gains can be described using the Jones matrix formalism (Hamaker et al. 1996; Sault et al. 1996; Hamaker 1996; Hamaker 2000). The Jones matrix J_j for each antenna, j, is the complex gain that affects the incident electric field vector, e, that results in an antenna voltage v_j:

$$v_j = J_j e \tag{2.2}$$

The RTS (Mitchell et al., 2008) is a software calibrator that can be run offline to produce an estimation of the complex gains. This is done by iteratively removing residual visibilities and attempting to correct for ionospheric offsets, starting with the brightest sources. While the RTS can correct for direction-dependent ionospheric offsets, this information is not applicable when the calibrator obser-

vation is in a different part of the sky than the target observation, as is usually the case for VCS observations[1]. For this reason, obtaining a calibration solution from a dedicated observation of a bright source is standard practice. We use this direction-independent calibration solution at low radio frequencies, which incorporates the bulk ionospheric shift into the gain solutions but does not correct for residual ionospheric offsets. The lack of residual ionospheric offset corrections only significantly affects observations at low frequencies ($\lesssim$140 MHz) as the median ionospheric offset is less than 15% of the FWHM above 140 MHz for the Phase II extended array. Since the majority of MWA observations are conducted above 140 MHz, the residual offset does not pose a problem for most MWA science.

2.3.1.3 Beam Formation

The MWA is an aperture array radio telescope. This allows all telescope functions, such as pointing, to be done electronically without moving parts (Bowman et al., 2007; Lonsdale et al., 2009).

The calculation of the detected beam (e') is described by expanding Equation 34 from Ord et al. (2019).

$$e' = \sum_{j}^{N_{\rm A}} v_j J_j^{-1} exp\{-i\phi_{j,n}\} \tag{2.3}$$

where v_j is the complex voltage from each tile, J_j^{-1} is the inverse of the complex gain of the direction independent calibration estimated by the RTS, $exp\{-i\phi_{j,n}\}$ is the direction-dependent delay compensation and $N_{\rm A}$ is the number of tiles (128).

This detected beam is calculated for both polarisations and then transformed to the four Stokes parameters in the following manner:

[1] Although in-field calibration can be attempted using correlated VCS data, it can often fail to converge on a calibration solution, e.g. due to the lack of bright sources in the field.

$$\mathrm{I} = \left[e'_x e'^*_x - \frac{1}{N_\mathrm{A}^2} \sum_j^{N_\mathrm{A}} e'_{j,x} e'^*_{j,x} \right] + \left[e'_y e^*_y - \frac{1}{N_\mathrm{A}^2} \sum_j^{N_\mathrm{A}} e'_{j,y} e'^*_{j,y} \right] \tag{2.4}$$

$$\mathrm{Q} = \left[e'_x e'^*_x - \frac{1}{N_\mathrm{A}^2} \sum_j^{N_\mathrm{A}} e'_{j,x} e'^*_{j,x} \right] - \left[e'_y e^*_y - \frac{1}{N_\mathrm{A}^2} \sum_j^{N_\mathrm{A}} e'_{j,y} e'^*_{j,y} \right] \tag{2.5}$$

$$\mathrm{U} = 2 \times \mathrm{Re} \left[e'_x e^*_y - \frac{1}{N_\mathrm{A}^2} \sum_j^{N_\mathrm{A}} e'_{j,x} e^*_{j,y} \right] \tag{2.6}$$

$$\mathrm{V} = -2 \times \mathrm{Im} \left[e'_x e'^*_y - \frac{1}{N_\mathrm{A}^2} \sum_j^{N_\mathrm{A}} e'_{j,x} e'^*_{j,y} \right] \tag{2.7}$$

The four Stokes parameters can be used to analyse a pulsar's rotation measure and the linearly and circularly polarised components of its pulse profile. Due to this scientific benefit, it is the default to calculate all four Stokes parameters. In cases where a large number of beams are being created, such as a pulsar survey, only Stokes I (Equation 2.4) is calculated as it is sufficient to detect pulsars and reduces the file size by a factor of four.

2.3.2 Incoherent Beam

The incoherent beam squares the complex voltages to create real powers and sums them over each tile, j, (separately for each polarisation of the tile) without calibrating or correcting for the geometric delays as seen in the equation:

$$P_\mathrm{inco} = \sum_{j=1}^{N} v_j^2 \tag{2.8}$$

where v_j is the complex voltage of one of the polarisations of each tile, and N is the number of tiles which is 128. This creates a beam with an FWHM of

$\sim 30^\circ$ at 150 MHz that requires minimal post-processing and is sensitive enough to detect bright pulsars as Xue et al. (2017) has shown by detecting 50 known pulsars. This reduction in sensitivity compared to the tied-array beam is $\propto\sim \sqrt{N}$ and thanks to an increase in processing efficiency of the multi-pixel beamformer (see Chapter 3), the incoherent beam is rarely beneficial.

2.3.3 Flux density measurements

Accurately measuring flux density is essential for inferring pulsar radio luminosities, energetics and spectra but requires extensive knowledge of the telescope to account for antenna temperature, beam shape, etc. The simplest way to measure flux density is to use a semiconductor diode to inject white noise into the receiver system to accurately measure the antenna temperature (e.g. Jodrell Bank and Effelsberg telescopes (Seiradakis et al., 1995; Gould & Lyne, 1998)). Not all telescopes have this ability, so many have to simulate their beam response to estimate their gain (G) and system temperature ($T_{\rm sys}$).

The MWA data presented in this work were processed without absolute flux calibration, with the initial pulse profiles given in arbitrary units. To calculate MWA flux densities, we first model the pulse profile using a combination of sigma-clipping and noise estimation and removal techniques (Stickel, 2010). Based on the model pulse, we divide the profile into on- and off-pulse regions (illustrated in Figure 2.5). The off-pulse region is used to calculate the standard deviation of the noise, which we divide the profile by to express it as a signal-to-noise ratio.

This profile can be converted to flux density units and subsequently averaged to calculate the mean flux density, using the radiometer equation:

$$S_{\rm mean} = \frac{(S/N)T_{\rm sys}}{G\sqrt{n_{\rm p}t_{\rm int}\Delta\nu_{\rm band}}}\sqrt{\frac{W}{P-W}} \tag{2.9}$$

where S/N is the signal-to-noise ratio of the pulse profile, $T_{\rm sys}$ is the system temperature, G is the gain, $n_{\rm p}$ is the number of polarisations, $t_{\rm int}$ is the integration time of the observation, $\Delta\nu_{\rm band}$ is the bandwidth of the observation, W is the

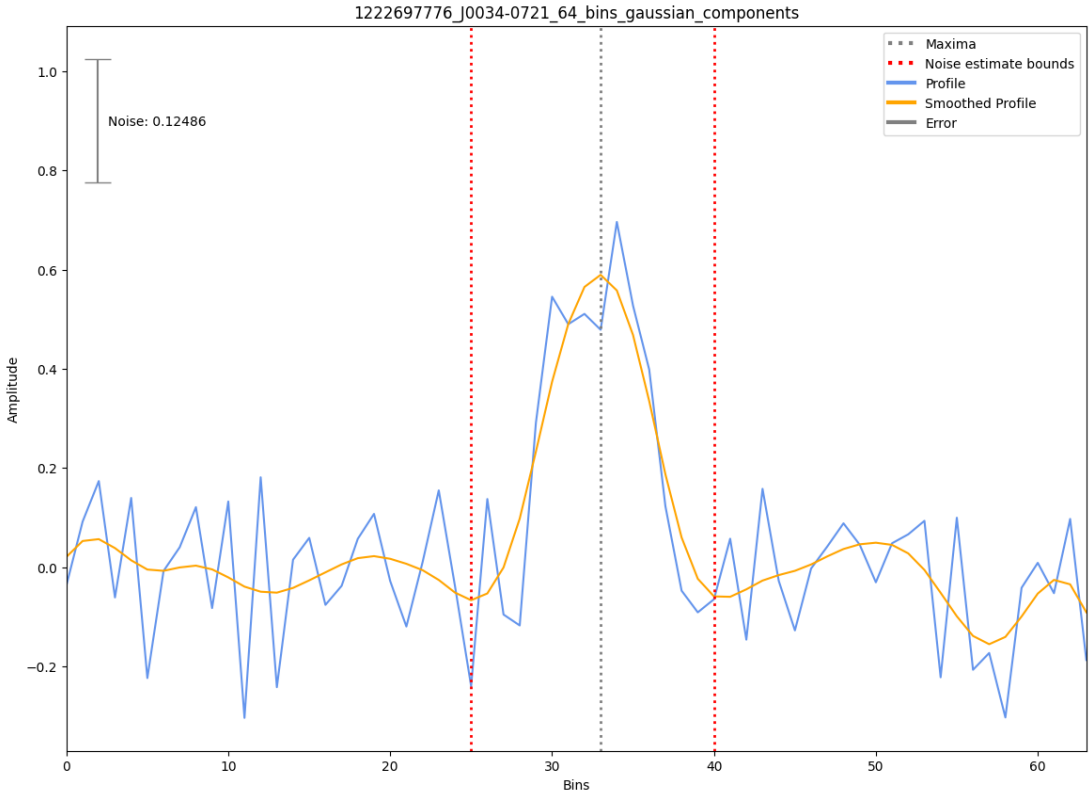

Figure 2.5: An example of the on and off pulse of a profile found using a combination of sigma-clipping and noise estimation and removal techniques (Stickel, 2010).

width of the pulse and P is the period of the pulsar.

If this profile is sufficiently scattered that the scattering tail is close to or longer than the pulse period, this can cause the flux density to be underestimated. This can arise either because the scattering tail causes the noise floor to be artificially raised, or because it becomes likely that part of the scattered tail is incorrectly attributed to the off-pulse region, which leads to an overestimate of the standard deviation of the noise.

Meyers et al. (2017) created a method for simulating the phased array power pattern of an MWA observation over the entire sky, which can be used to estimate the system temperature and gain. In this work, the simulation was automated to allow the calculation of the flux density of the 120 pulsars detected in the SMART survey (Bhat et al., 2023a), see Table A.1. We will now summarise the method developed in Meyers et al. (2017).

The system temperature is a combination of the receiver temperatures ($T_{\rm rec}$), antenna temperatures ($T_{\rm ant}$) and ambient temperature (T_0) and can be calculated as

$$T_{\rm sys} = \eta T_{\rm ant} + (1-\eta)T_0 + T_{\rm rec} \tag{2.10}$$

where η is the array's frequency- and direction-dependent radiation efficiency, which is estimated to be 0.98. The ambient temperature of each receiver is recorded in the metadata of each observation, and the receiver temperature is known for each frequency. The antenna temperature is calculated as a product of the phased array power pattern and the sky temperature map (we use the global sky model of de Oliveira-Costa et al. (2008) and scale it to our frequencies) using convolution.

The solid angle ($\Omega_{\rm A}$) can be determined from the integral of the phased array power pattern. The solid angle can be converted to the effective area, which in turn can be converted to gain

$$G = \frac{2\pi\eta\lambda^2}{k_{\rm B}\Omega_{\rm A}} \tag{2.11}$$

where λ is the observing wavelength and $k_{\rm B}$ is the Boltzmann's constant.

Both G and $T_{\rm sys}$, along with other values of the pulsar observation, can be input into Equation 2.9 to estimate the flux density. To ensure the validity of this method, we compare the flux density estimated via tied-array beamforming to imaging of the same observation, as shown in Table 2.2. All measurements are within three sigma except for that of J1834−0010, which is likely due to source blending increasing the flux in imaging, which can be expected for MWA's resolution. This method has gone on to be used in the publication Bhat et al. (2023a).

Pulsar	Obs ID	Imaging Flux Density (mJy)	Beamforming Flux Density (mJy)	Factor
J1820−0427	1276619416	545(109)	597(74)	1.1
J1825−0935	1276619416	176(35)	440(152)	2.5
J1834−0010	1276619416	107(21)	23(6)	4.7
J1834−0426	1276619416	259(52)	285(32)	1.1
J1849−0636	1276619416	84(17)	140(18)	1.7
J1921+2153	1148063920	908(182)	1082(102)	1.2

Table 2.2: Comparison between the flux density measurements calculated using standard imaging methods and through the new method of simulating a phased array power pattern with the MWA tied-array beam. All measurements are within three sigma except for the J1834−0010, which is likely due to source blending increasing the flux in imaging, which can be expected for MWA's resolution.

2.4 Pulsar search techniques

Using the birthrate of neutron stars, Lorimer et al. (1993) estimated that there are 13000 ± 2000 potentially observable pulsars (luminosity greater than 10 mJy kpc^2 assuming a uniform one steradian beaming angle). If this estimate is correct, then the upcoming SKA telescope could detect over 10000 new pulsars. To discover

these pulsars, one needs to search an area of the sky for pulsars of an unknown period, DM, and orbital parameters. The two most common types of pulsar searches are (1) targeted, where a part of the sky that is likely to contain pulsars, such as a supernova remnant (e.g. Straal & van Leeuwen, 2019; Gupta et al., 2005), is searched and (2) blind, where a large area of the sky is searched (e.g. Manchester et al., 1996; Sanidas et al., 2019). Blind pulsar surveys are the most common and successful in terms of total pulsars discovered, the majority of which are long-period pulsars.

The two most common pulsar search methods are periodicity and single pulse searches. Single pulse searches are used to find individual pulses from pulsars that emit sporadically. Periodic pulsar searches can help detect pulsars even when their individual pulses are too weak to be detectable, and for this reason, they are the most common. Single pulse searches are often used in conjunction with periodic searches because they take minimal computation time and use the already dedispersed data, as shown in Figure 2.6, which illustrates a typical pulsar search pipeline.

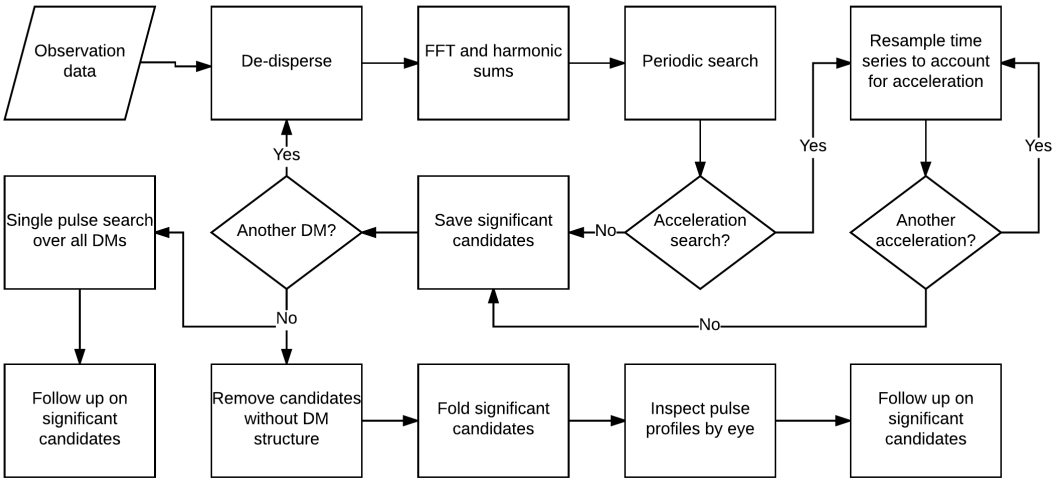

Figure 2.6: A common pulsar search pipeline. Each step is explained in more detail in Section 2.4. Inspired from an image contained in Lorimer & Kramer (2005)

A pulsar search pipeline first dedisperses the data to form a large number of

time series spanning the chosen DM range. Each time series is then searched for periodic signals and single pulses. The most common method is to Fourier transform the time series and search the resulting spectra for significant features after harmonics are summed to improve the signal-to-noise ratio. Another method is the fast folding algorithm which has a higher false positive rate than periodic searches but has received renewed interest due to its increased sensitivity to long-period pulsars (Cameron et al., 2017; Tan et al., 2018a; Morello et al., 2020). The best candidates are then folded and inspected to confirm if the signal is a pulsar. This process is described in more detail in the following sections.

2.4.1 Dedispersion

As explained in §1.4.1, dispersion effects must be corrected to sensitively observe pulsars. The most common method for dedispersion is incoherent, explained in §2.4.1.1, and the choice of dispersion measure steps used for a pulsar search are explained in §2.4.1.2.

2.4.1.1 Incoherent Dedispersion

Incoherent dedispersion is the simple method of shifting each frequency channel in time so that the dispersed signal lines up in time across all frequency channels. Since there may still be some dispersion within the frequency channel, as shown in Figure 2.7, this can lead to what is called dispersion smearing.

For cases where the frequency bandwidth is much smaller than the observing frequency ($\Delta\nu << \nu$), we can simplify Equation 1.5 to

$$t_{\mathrm{DM}} \approx 8.3 \times 10^6 \mathrm{ms} \;\; \mathrm{DM} \frac{\Delta\nu}{\nu^3} \tag{2.12}$$

As this dispersion smearing gets larger than the time resolution, the sensitivity of the pulse profile is decreased. This smearing is considered when deciding on DM step size, see §2.4.1.2.

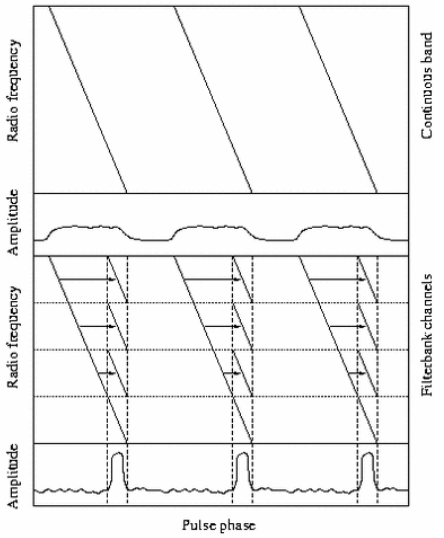

Figure 2.7: This figure helps to illustrate the diagonal DM of a theoretical pulsar. The top panel shows the raw pulsar signal in frequency and time. The second panel shows how folding on this data without correcting for dispersion creates an extremely broadened profile. The third panel illustrates the process of discrete or incoherent dedispersion. Due to finite frequency resolution, there is still some dispersion within each frequency channel. Once this dispersion exceeds the time resolution, the pulse profile appears broadened. Image credit: Lorimer & Kramer (2005).

2.4.1.2 Dispersion Measure Step size

Since the DMs of the pulsars are not known *a priori*, we must search over a range of DM values. The choice of DM trials is a compromise between computational efficiency and search sensitivity. A large number of DM trials becomes computationally expensive as an FFT and a periodic search must be performed for every DM within the chosen range. The number of DM trials must be small enough that a pulsar between two DM trials will not become too broadened and, therefore, less likely to be detectable.

To decide on a DM step ($\mathrm{DM_{step}}$), we must decide what amount of smearing due to a potentially incorrect DM is acceptable. We define this as a smearing factor i_{smear}, which is the number of time bins that is acceptable to have dispersion smearing across. This is explained by the equation:

$$i_{\text{smear}} t_{\text{samp}} = t_{\text{DM}} \tag{2.13}$$

where t_{samp} is the time resolution, t_{DM} is the smearing caused by dispersion. A common value for i_{smear} is three, but this value depends on the expected pulse width of the pulsars one is searching for and the time resolution of the telescope.

The maximum smearing caused by incorrect DM is when the true DM is in the centre of two DM trials (half the size of a DM step). To keep the smearing caused by this incorrect DM less than $i_{\text{smear}} t_{\text{samp}}$, we can calculate the DM_{step} using the equation:

$$\text{DM}_{\text{step}} = 4.15 \times 10^{-6} i_{\text{smear}} t_{\text{samp}} \frac{\nu^3}{\Delta\nu_{\text{band}}} \tag{2.14}$$

where t_{samp} is the time resolution in ms, ν is the central frequency and $\Delta\nu_{\text{band}}$ is the total frequency bandwidth in MHz. As the DM increases, the dispersion smearing within a single channel will be more than the smearing over the bandwidth due to an incorrect DM. This point is called the diagonal DM and can be calculated using the following:

$$\text{DM}_{\text{diag}} = 8.3 \times 10^{-6} i_{\text{smear}} t_{\text{samp}} \frac{\nu^3}{\Delta\nu_{\text{chan}}} \tag{2.15}$$

where $\Delta\nu_{\text{chan}}$ the frequency resolution in MHz. Once DM_{diag} is reached, the t_{samp} is doubled by summing adjacent bins to save on processing time as the dispersion smearing lowers the effective time resolution. This process is repeated with the new t_{samp} to calculate the new DM step and diagonal DM until the desired DM limit is reached. Table 2.3 shows an example of this.

2.4.2 Single Pulse Search Techniques

Several types of pulsars emit too sporadically to be detectable by periodic search techniques. These non-periodic pulsars include Rotating RAdio Transients (RRATs), nullers, intermittent pulsars, and giant pulse emitters. The most famous giant

pulse emitter is the Crab pulsar. A single pulse search runs a matched filter of a boxcar function over each of the dispersed time series to find all pulses and their arrival time, DM and signal-to-noise ratio. These pulses can be examined to find pulses that originate from a single, non-zero DM. An example of this technique is shown in Figure 2.8, where the MWA detected the Crab pulsar (PSR J0534+2200), which was initially discovered by its single pulses (Staelin & Reifenstein, 1968). Single pulse searches of dedispersed time series are computationally inexpensive and, for this reason, are often included in pulsar surveys.

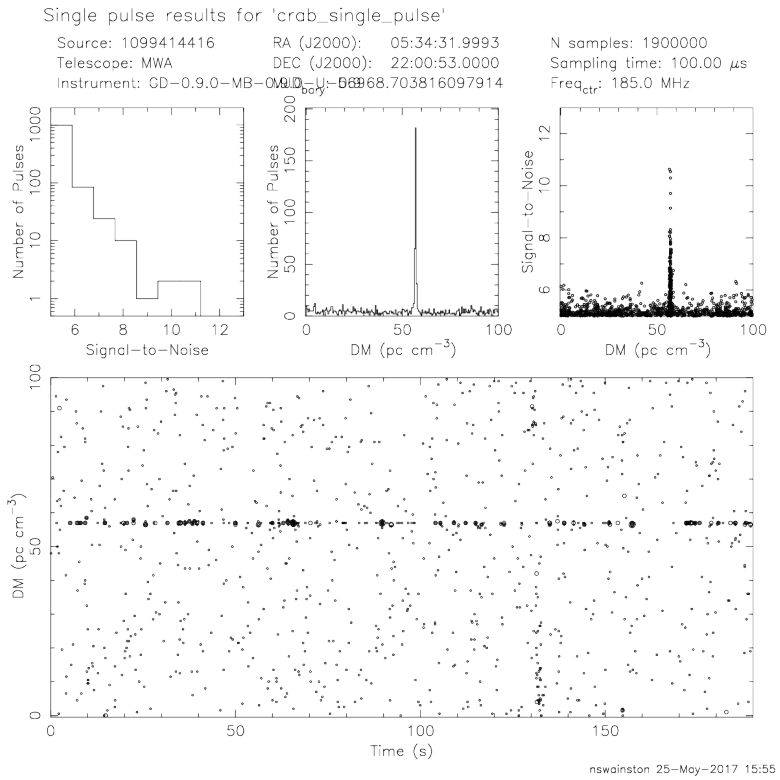

Figure 2.8: The `single_pulse_search.py` output of an MWA observation of the Crab pulsar. The dots in the lower section of the figure represent detected pulses, whereas the pulses with higher signal-to-noise ratios have larger dots. The distribution of the pulses in signal-to-noise, DM and the number of pulses are displayed in the top graphs. Many of these pulses are random noise, but at the DM of 57 pc cm^{-3}, it is clear the repeating pulses are coming from a Galactic source.

2.4.3 The Fourier Transform

To analyse the periodicity of a time series, the most common method is to take the Fourier transform of the time series and examine the Fourier frequency domain. For a dedispersed time series T_j that is a set of N data points, we can compute the discrete Fourier transform (DFT) using the equation:

$$F_k = \sum_{j=0}^{N-1} T_j \exp(-2\pi i j k/N) \tag{2.16}$$

where $i = \sqrt{-1}$. The resulting Fourier frequency series will have bins of width 1/T where T is the length of the observation. The DFT is rarely used in practice as the more computationally efficient Fast Fourier Transform (FFT) is favoured (FFT only uses $N \log N$ operations compared to the DFT's N^2 (Bracewell, 1999)). Due to astronomical data having times series has a large number of samples ($N > 2^{25}$), the observations are often split into smaller chunks to improve the computational efficiency further. One of the exceptions is pulsar surveys which often use the entire time series to maximise the sensitivity of the FFT.

2.4.4 Periodic Search Techniques

Doing a periodic search for a pulsar that is not in a binary system is a simple process of searching for peaks in power in the Fourier space and, for this reason, is not very computationally expensive. It is essential to be sensitive to binary pulsars as they are excellent laboratories for testing general relativity and $\sim 83\%$ contain MSPs (taken from ATNF catalogue version v1.68; Manchester et al., 2005)[2]. For this reason, pulsar search techniques have been developed to be sensitive to binary pulsars and are explained in the following sections.

[2] https://www.atnf.csiro.au/research/pulsar/psrcat/

2.4.4.1 Coherent Acceleration Search for Binary Pulsars

Pulsars in compact binary systems are more difficult to find due to their power smearing into neighbouring frequency bins due to the Doppler effect. To correct the time series to account for binary systems, we resample the time series by:

$$\tau(t) = \tau_0(1 + V_{\rm r}(t)/c) \tag{2.17}$$

where $V_{\rm r}(t)$ is the radial velocity, c is the speed of light, $\tau(t)$ is the time interval in the pulsar frame and τ_0 is used for normalisation. To accurately recover all sensitivity, we would have to create a time series for every possible function of $V_{\rm r}(t)$ set by the Keplerian orbital parameters. This is known as a coherent search, which is rarely used due to the daunting amount of computational processing it requires (Nieder et al., 2020).

2.4.4.2 Acceleration Searches for Binary Pulsars

When the observation time is much smaller than the binary orbital period ($t_{\rm obs} \ll P_{\rm orb}$), we can assume a constant orbital acceleration $a_{\rm r}$ such that $V_{\rm r}(t) = a_{\rm r}t$. This reduces the search parameter space from a five-dimensional coherent search to a one-dimensional acceleration search. Since this will have to be repeated for the thousands of DM steps for each beam, the computation time of an acceleration search becomes the most significant process in a pulsar search pipeline. An example of the potential improvement of an acceleration search is shown in Figure 2.9.

2.4.5 Periodic candidate selection

Once the periodic search process is complete, it will result in a large number of pulsar candidates, on the order of tens of thousands. To test the validity of candidates, it is useful to compare them to the response of purely Gaussian noise. A reasonable maximum deviation of the noise in Fourier space can be converted

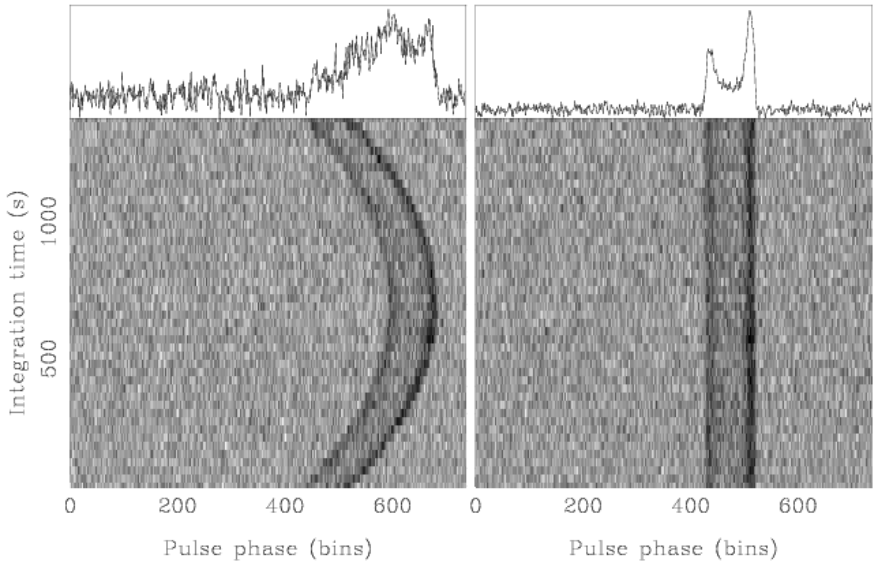

Figure 2.9: Left: A folded pulse profile of binary pulsar PSR B1913+16 from a 22 min observation with Arecibo. Right: The same time series corrected for an orbital acceleration $a_1 = -16$ m s^{-2}. Image credit: (Lorimer & Kramer, 2005).

to signal-to-noise to make a suitable threshold:

$$S/N_{\rm min} = \frac{\sqrt{ln[n_{\rm trials}]} - \sqrt{\pi/4}}{1 - \pi/4} \simeq \frac{\sqrt{ln[n_{\rm trials}]} - 0.88}{0.47} \tag{2.18}$$

For a ten-minute observation with the MWA VCS, $n_{\rm trials} \sim 6{\times}10^6$ so $S/N_{\rm min} \sim 6.5$ so all Fourier powers below 6.5 can be ignored as candidates.

Examining a candidate's DM and the shape of its S/N ratio over adjacent DM bins can help us determine if it is most likely a genuine candidate, random noise or terrestrial radio frequency interference (RFI). If a candidate has a DM of zero, it is likely caused by terrestrial RFI, as it has not had to go through the ISM. Real sources will have a characteristic curved shape when comparing the S/N ratio to DM, which peaks at a non-zero DM. This is due to the loss of sensitivity the further away from the true DM each DM bin is. An example of this characteristic curve is shown in the bottom middle plot of Figure 2.15. A random noise signal will not show this structure over period or DM, so this can be used to filter out more spurious candidates.

Periodic candidates with sufficient S/N and the expected curved characteristic

shape over adjacent DMs are "folded" on. This means folding or averaging the observation over the pulsar's period to add pulses coherently to create a brighter pulse profile. This can lead to a large number of folded candidates that will have to be classified, often with a combination of machine learning (ML) and human classification.

2.4.6 Candidate Follow Up

Once a pulsar candidate with a significant pulse profile is discovered (Figure 2.15 for example), it is not immediately confirmed as a genuine pulsar. The pulsar candidate must be followed up with additional observations to improve the accuracy of estimates of its position and orbital period. Pulsar searches often grid the sky with beams so a candidate may be detected in one or several beams. Suppose it is detected in only one of its beams. In that case, four more observations are taken (as illustrated in Figure 2.10a), or if it is detected in two beams, then only two follow-up observations will be required (Figure 2.10b).

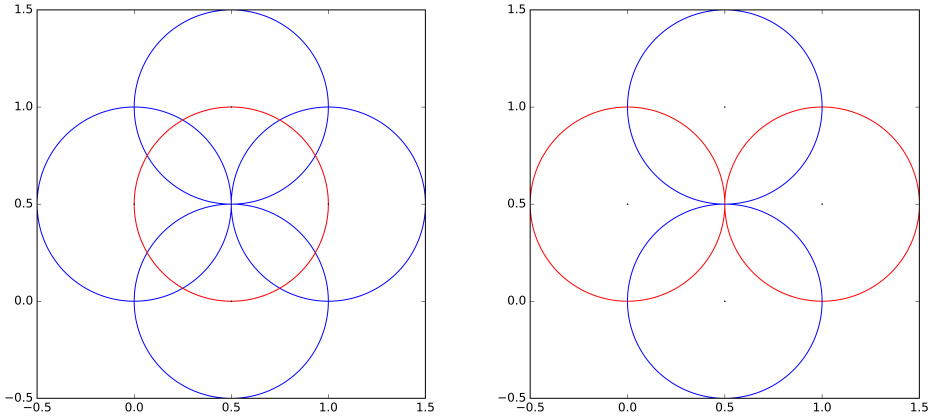

(a) (b)

Figure 2.10: Two examples of pulsar candidate follow-up techniques to increase the position determination accuracy where the red circles represent the original detection beam's FWHM and the blue circles represent the follow-up observation beam's FWHM. Once all observations are taken, the S/N ratios can be compared to calculate the most likely position of the pulsar within ≈ 0.2 FWHM (assuming a Gaussian main beam response). The scale of these images is normalised to the beam's FWHM.

The original and follow-up detections can be used to compare the S/N ratios from each beam and, assuming a Gaussian main beam, estimate an approximate pulsar position accurate to within ≈0.2 FWHM of the beam. These follow-up observations will reduce the survey efficiency and will only give an approximate position due to uncertainties in the beam model, and the time difference in observations may have different scintillation effects that affect the S/N.

2.5 The Southern-sky MWA Rapid Two-metre (SMART) initial pass survey

The Southern-sky MWA Rapid Two-metre (SMART) pulsar survey exploited the Murchison Widefield Array's large field-of-view (FoV) and VCS to observe the sky south of 30° in declination for pulsars and fast transients in the 140-170 MHz band. Observations of 80 minutes were taken at each primary beam pointing. However, to reduce the initial search pass processing time, only the first 10 minutes of each observation were processed, and with coarse DM steps. Processing time was significantly reduced at the expense of a $\sim$ 65 % reduction in search sensitivity.

Figure 2.11 summarises the processing of the SMART survey. The process is explained in more detail in the following sections. We will explain the observing strategy in §2.5.1, observation quality assurance using the pulsar processing pipeline in §2.5.2, the pulsar search pipeline in §2.5.3, candidate classification in §2.5.4 and confirmation and follow-up of candidates in §2.5.5.

2.5.1 Observing Strategy

Thanks to the large FoV of the MWA ($\sim$600 deg^2 at 150 MHz), the entire Southern sky ($< 25°$ declination) was observed with the MWA in only 70 observations. Each of the SMART survey observations has a dwell time of 4800 s which allowed the survey to be completed in less than 100 hours of telescope time. This was a

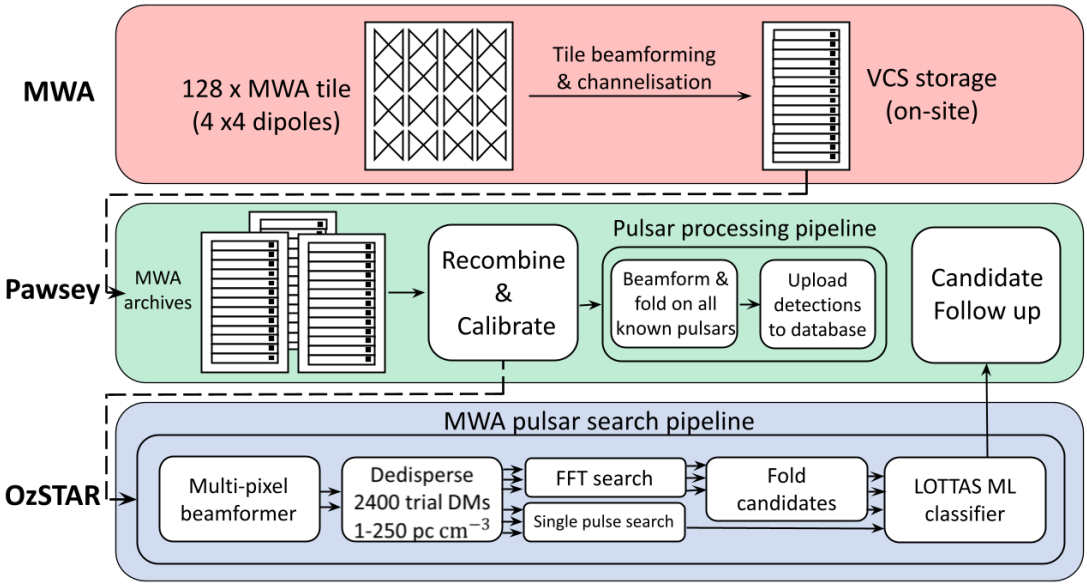

Figure 2.11: An overview of the SMART survey processing and on which supercomputer parts of the processing were performed. Ten minutes of MWA data was downloaded to Pawsey, where it was recombined and calibrated. The data quality was checked using the pulsar processing pipeline (§2.5.2) and then transferred to OzSTAR where it was searched using the MWA search pipeline (§2.5.3). The full 80 minutes of data were downloaded onto Pawsey to perform follow-up of any significant candidates (§2.5.5).

survey speed of $\sim$600 deg^2 hr^{-1}, which is an order of magnitude faster than most telescopes but comes at the cost of an enormous data rate of 27 TB an hour.

Due to the significant data rates of MWA VCS observations, the survey accumulated 2.3 PB of raw observation data, which resulted in data management challenges. One of these challenges included transferring the VCS data off the MWA site to the Pawsey MWA archive, which limited the number of observations to two a week. For this reason, the SMART survey was split into five, each part of which was observed on a different semester, as demonstrated by the different colours in Figure 2.12.

The declinations were chosen based on the tile beam "sweet spots" that were used with great success in the GLEAM survey (Wayth et al., 2015). The number of observations per declination range was chosen to provide a $\sim 8^\circ$ right ascension overlap with adjacent observations. This provided an observation overlap in both

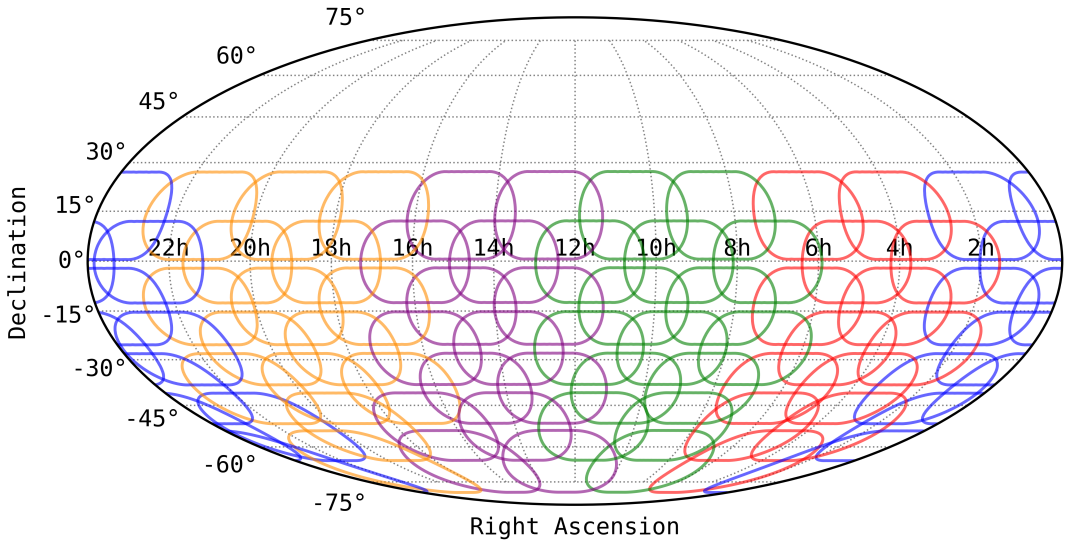

Figure 2.12: The observing plan for the SMART survey where each circle represents the FWHM of each observation, and their colour represents a different semester that the observations were taken.

declination and right ascension to serve as a two-pass strategy. This made it more likely to detect pulsars that we were not sensitive to in the other observations due to their intermittent nature (e.g. a nuller that was "turned off") or they were scintillating down (due to refractive scintillation). The overlap strategy also assisted in candidate follow-up as it ensured another observation of the candidate.

2.5.2 Observation quality assurance

Each SMART observation requires 3.6 TB of storage and took approximately 27 thousand CPU hours to process for the first pass. To ensure these resources were well-spent, we first performed a data quality check using the pulsar processing pipeline, which attempted to detect all known pulsars in the FoV. For the data quality check, we define "in the FoV" to mean all pulsars above 30% of the tile beam's power and above 10% of the tile beam's power for bright pulsars (estimated S/N above 15 from spectral fitting).

The first 10 minutes of the observations were downloaded, and tied-array beams were formed at the positions of all pulsars in the FoV. Each known pulsar

was folded using the ephemeris from the ATNF and PRESTO's `prepfold` command using many period and DM trials to account for possible inaccuracies. A pulsar was classed as detected if it was classified as a pulsar by the LOTAAS ML classifier (explained in §2.5.4.1). If no pulsars were detected in an observation, the observation was classed as unusable and a re-observation was scheduled. If pulsars were detected, they were then examined to determine if significant RFI or noise prevented this pulsar from being detected with the expected sensitivity. Once all observations were of acceptable quality, they were processed with the MWA pulsar search pipeline (see §2.5.3).

All pulsar detections were further processed to assure the best quality detection (highest number of profile bins with an S/N greater than the standard value of 8). The data were further processed to create a polarisation profile and to estimate the rotation measure. These high-quality detections were then used to estimate the flux density of each pulsar (using the method explained in §2.3.3), which was published in Bhat et al. (2023a).

2.5.3 The MWA pulsar search pipeline

The computation requirements of pulsar surveys are infamously large due to each beam requiring hundreds of dispersion measures to be searched for periodic signals. This is exacerbated at low frequencies as more dispersion measure steps are required. The thousands of beams and DM steps required to process an MWA VCS observation required the management of tens of thousands of supercomputing jobs. Initial attempts to create a search processing pipeline using common software languages like `Python` and `Bash` quickly became hard to manage and error-prone.

This led to the development of the MWA pulsar search pipeline using the pipeline software language `Nextflow` (Di Tommaso et al., 2017). The use of `Nextflow` made the pipeline easier to read, maintain and run on multiple super-

computers. The pipeline is contained in the mwa_search[3] repository (Swainston et al., 2023) where it will continue to be developed for the next pass of the survey.

The first pass of the search was primarily performed on the OzSTAR supercomputing cluster. Each of the steps of the pipeline will be described in the following sections.

2.5.3.1 Tied-array beam grid

To cover the $\sim$ 600 deg^2 FoV of the MWA observations, we create a hexagonally tessellated grid of tied-array beams. The distance between the tied-array beams was chosen so that their beam FWHM overlap at all frequencies, as shown in Figure 2.13. This pointing grid was created with the following `mwa_search` command:

```
grid.py -o OBSID -a -b BEGIN -e END
        -d 0.3 -f 0.9 -n 1080
```

The above command line specifies the following behaviour:

- `-o OBSID` is the MWA observation ID
- `-b BEGIN` is the first GPS second of the observation that one will process
- `-e END` is the last GPS second of the observation that one will process
- `-d 0.3` is the estimated FWHM in degrees
- `-f 0.9` is the fraction of the FWHM to separate the beams. This will overlap them for the full frequency range of the SMART observations.
- `-n 1080` makes the script output a different file for every 1080 pointings. Each of these files was given to the pipeline to process the observation in stages to help manage the data rate and the number of files the pipeline creates so they can be deleted before the next stage begins.

[3] https://github.com/CIRA-Pulsars-and-Transients-Group/mwa_search

For the first pass, BEGIN and END will use the first 600 seconds of an observation. The number of beams this will produce varies from ∼6000 to ∼8000 depending on the observation's declination. The different declinations will change the primary beam response and the shape of the tied-array beam, as shown in Figure 2.13.

2.5.3.2 Beamforming

The beamforming was performed with the MWA Multi-Pixel Beamformer (MPB), as explained in §3.3.2. This beamforming is done for 120 beams simultaneously, using GPU being used per coarse channel. Here is an example command:

```
make_beam -o OBISD -b BEGIN -e END -d INPUT_DIR
          -f CHANNEL_ID -J CALIBRATION_SOLUTION
          -P POINTINGS -m META_FILE -p -s -z UTC
```

The above command line specifies the following behaviour:

- `-o OBSID` is the MWA observation ID
- `-b BEGIN` is the first GPS second of the observation that one will process
- `-e END` is the last GPS second of the observation that one will process
- `-d INPUT_DIR` is the directory containing the raw VCS files
- `-f CHANNEL_ID` is the coarse frequency channel ID
- `-J CALIBRATION_SOLUTION` is the RTS calibration solution file
- `-P POINTINGS` is the right ascension and declination of the tied-array beams that will be made
- `-m META_FILE` is the file containing observation metadata
- `-p` will make a PSRFITs format output file

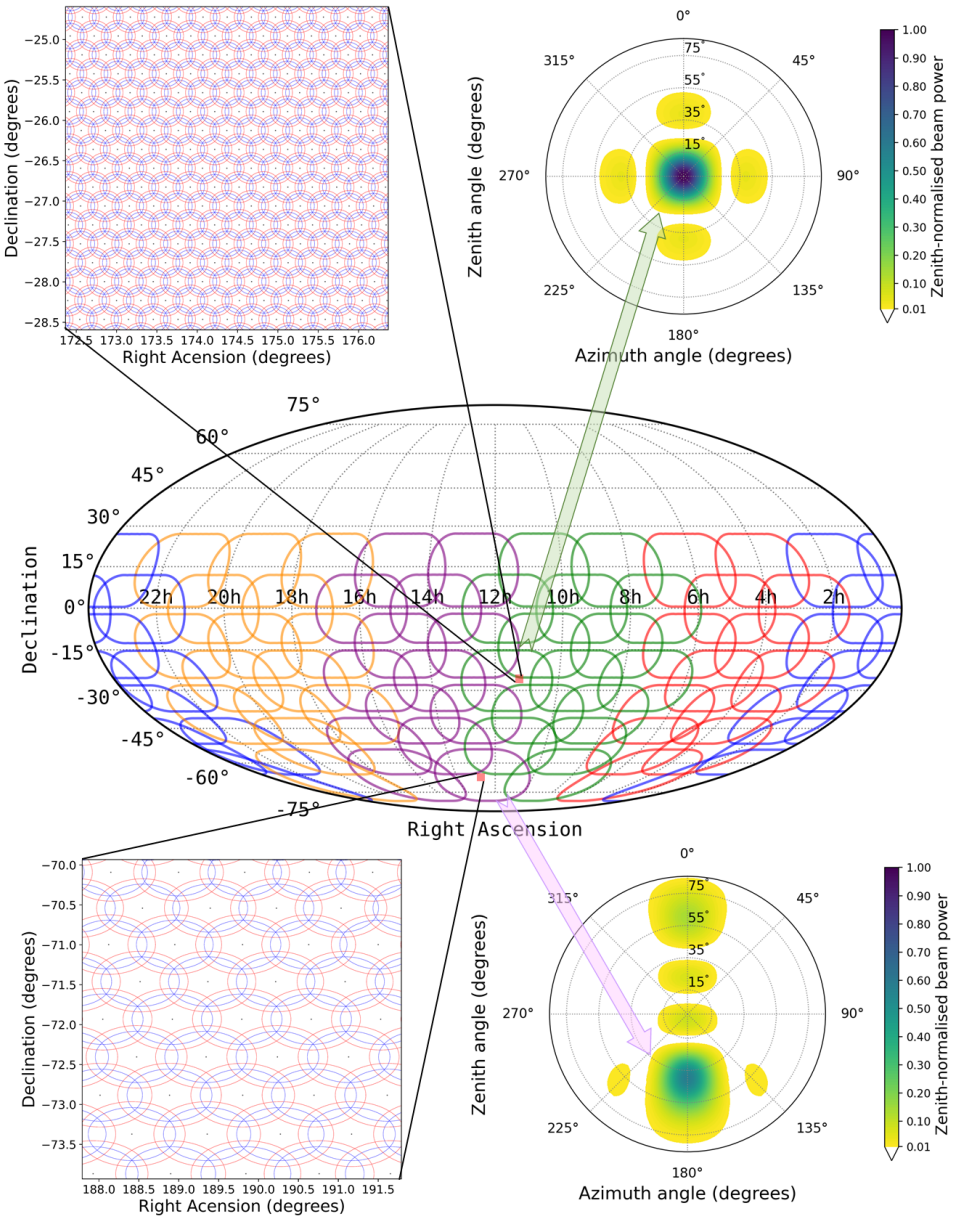

Figure 2.13: Sky tessellation of the SMART survey. The left panels show beam tiling patterns for two select pointings: the top one is a near-zenith pointing ($\delta = -28\,\mathrm{deg}$), and the bottom one is a far southern pointing ($\delta = -70\,\mathrm{deg}$). The number of tied-array beams varies from ∼6000 to ∼8000 from near-zenith to far-zenith pointings, and the beam shape becomes elliptical at large offsets from the zenith. The size of the circle/ellipse indicates half power tied-array beam size; the red and blue circles correspond to the low and high ends of the SMART band (140-170 MHz). The right panels show the primary beam response for the same declination pointings at the central frequency of 155 MHz. Image credit: Bhat et al. (2023a).

- `-s` will make a summed Stokes output which is a fourth of the output size, making search processing easier to handle
- `-z UTC` is the time of the start of the observation in UTC

This outputs one file for each of the 24 coarse channels, which must then be spliced together.

Thanks to the GPU acceleration and the multi-pixel parallelism, beamforming was no longer the bottleneck in the MWA search pipeline. The beamforming is still an extremely input/output (I/O) heavy process which can strain supercomputing cluster resources. To prevent overwhelming OzSTAR's metadata server, we limited the number of simultaneous beamforming jobs to 120 (14,400 beams) and output the files to SSD temporary storage to limit the number of writes to the Lustre file system.

2.5.3.3 Dedispersion

We create a dedispersion plan using the `mwa_search`'s `lfDDplan.py`:

```
lfDDplan.py -f 154.24 -b 30.72 -nf 3072 -t 0.1
            -ld 1 -hd 250 -m 0.2
```

The above command line specifies the following behaviour:

- `-f 154.24` the centre frequency in MHz
- `-b 30.72` the bandwidth in MHz
- `-nf 3072` the number of frequency channels
- `-t 0.1` the time resolution in ms
- `-ld 1` the lowest DM
- `-hd 250` the highest DM

$\mathrm{DM_{min}}$ ($\mathrm{pc\,cm^{-3}}$)	$\mathrm{DM_{max}}$ ($\mathrm{pc\,cm^{-3}}$)	$\mathrm{DM_{step}}$ ($\mathrm{pc\,cm^{-3}}$)	N_{DM}	d_{s}	Δt_{eff}	N_{sub} (ms)
1.0	12.2	0.02	560	1	0.1	4
12.2	24.4	0.03	406	2	0.2	6
24.4	48.8	0.06	406	4	0.4	16
48.8	97.6	0.11	443	8	0.8	32
97.6	195.2	0.23	424	16	1.6	64
195.2	250.0	0.46	119	16	3.2	64

Table 2.3: Dedispersion plan for the first-pass SMART processing where columns 1 and 2 denote the ranges in dispersion measure, between $\mathrm{DM_{min}}$ and $\mathrm{DM_{max}}$, with a DM step-size of $\mathrm{DM_{step}}$, resulting in N_{DM} trial DM values. The downsampling factor is denoted by d_{s}, i.e. the factor by which the temporal resolution is averaged to yield a net resolution Δt_{eff}. N_{sub} is the number of frequency channels to partially shift to a nominal DM before being dedispersed, which results in fewer calculations.

- `-m 0.2` the minimum $\mathrm{DM_{step}}$, picking 0.2 significantly reduces the number of DMs

`lfDDplan.py` assumes a i_{smear} of 3 and the maximum d_{s} of 16 as the time samples (10000 a second) are not divisible by a higher power of two such as 32. The output of `lfDDplan.py` used for the first pass is shown in Table 2.3.

We use PRESTO's `prepsubband` to implement the dedispersion plan for each of the tied-array beams like so:

`prepsubband -lodm` $\mathrm{DM_{min}}$ `-dmstep` $\mathrm{DM_{step}}$ `-numdms` N_{DM}
`-zerodm -nsub` N_{sub} `-downsamp` d_{s}
`-numout 60000/`d_{s} `*.fits`

The above command line specifies the following behaviour:

- `-lodm` $\mathrm{DM_{min}}$ is the minimum DM to dedisperse
- `-dmstep` $\mathrm{DM_{step}}$ is the DM step-size
- `-numdms` N_{DM} is the number of DMs to dedisperse

- `-zerodm` normalises the time series at a DM of zero before dedispersing, which smooths out the power fluctuations that are common at low frequencies
- `-nsub` N_{sub} is the number of frequency channels to partially shift to a nominal DM before being dedispersed, which results in fewer calculations
- `-downsamp` d_{s} is the downsampling factor
- `-numout 60000/`d_{s} is the number of output samples expected which is $60000/d_{\mathrm{s}}$ due to the first pass only using 600 s of data
- `*.fits` defines the input tied-array beam PSRFITs files

2.5.3.4 Single pulse search

To find individual pulses, we search the dedispersed files using a boxcar function using the following command

```
single_pulse_search.py -p -m 0.5 -b *.dat
```

The above command line specifies the following behaviour:

- `-p` looks for pulses without making a plot
- `-m 0.5` sets the maximum downsampling to 0.5 seconds
- `-b` does not check for bad blocks, which prevents giant pulses from being flagged
- `*.dat` defines the dedispersed files

A `.singlepulse` file was output for each DM, which was combined into a single `.SpS` file for the beam. This was put through SpS[4], LOFAR's single pulse classifier (Michilli et al., 2018) which uses ML techniques to differentiate RFI from

[4] https://github.com/danielemichilli/SpS

astrophysical signals, classify interesting signals, and produce diagnostic plots. This software has been adapted to be used for the MWA and its effectiveness was validated by using it to successfully detect two known RRATs, one of which had been previously detected with the MWA (Meyers et al., 2019). Further testing and development will be done in the future.

```
single_pulse_searcher.py -no_store -fits *fits
                         -plot_name NAME.pdf *.SpS
```

The above command line specifies the following behaviour:

- `-no_store` does not store the output into an HDF5 database
- `-fits *fits` defines the input tied-array beam PSRFITs file
- `-plot_name NAME.pdf` defines the output plot name
- `*.SpS` defines a combined input file of all the single pulse files from `single_pulse_search.`

An example of `SpS`'s output is shown in Figure 2.14. The detection of the RRAT PSR J0410−31 demonstrates that `SpS` can detect transient pulsars. The current software is suspected of having a few bugs, such as the pulse profile not being representative of what is expected, so this software will have to be improved before it is used in the next processing pass of the survey.

2.5.3.5 Periodic Search

We perform an FFT on all dedispersed files using PRESTO's `realfft`, then perform a simple periodic search (no acceleration search) using the command:

```
accelsearch -zmax 0 -flo 1000 -fhi 0.533
            -numharm 16 *.fft
```

The above command line specifies the following behaviour:

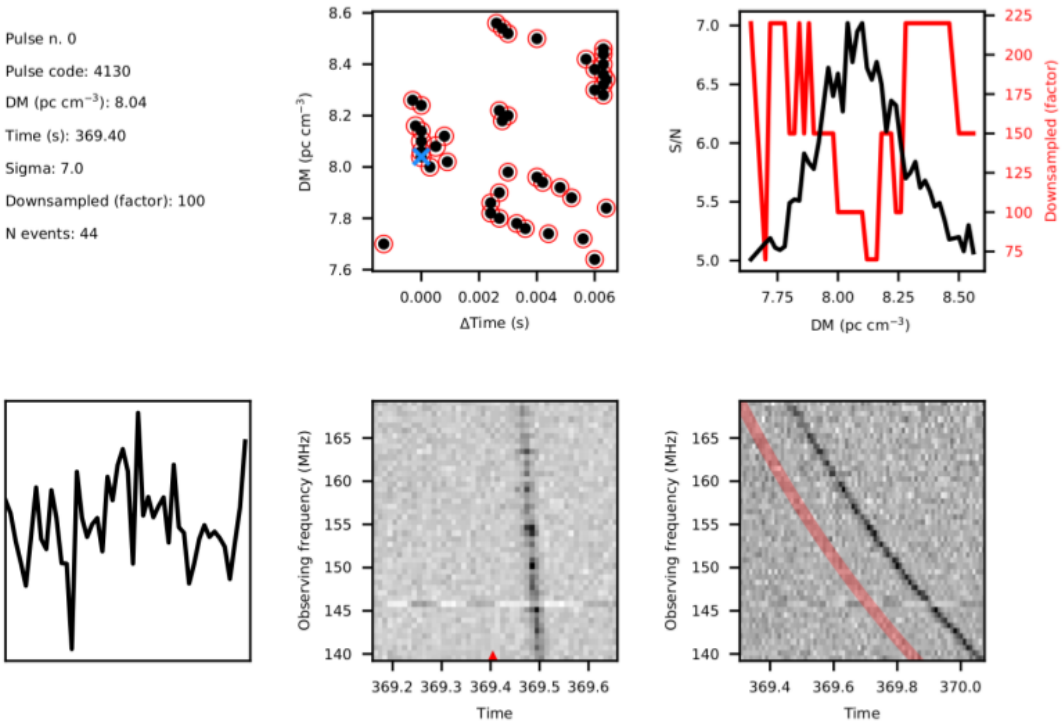

Figure 2.14: Detection of the RRAT PSR J0410−31 using `SpS`. *Top left*: The metadata of the detection. *Top middle*: Local pulses in DM and time to check that the pulses are clustered. *Top right*: The S/N against DM to check for the characteristic curve expected for true candidates. *Bottom left*: The pulse profile, which may be inaccurate due to a residual dispersion sweep, it representing a time window preceding the pulse (indicated by the red arrow in the bottom middle plot) or other software bugs. *Bottom middle*: The dedispersed ν and time plot to check the pulse is detectable throughout the band. *Bottom right*: The ν and time plot before dedispersion with a red line to show the expected dispersion sweep.

- `-zmax 0` is the maximum acceleration to search for, so setting it to zero forgoes a computationally expensive acceleration search
- `-flo 0.533` is the minimum frequency to search for, which encompasses all pulsars in the ATNF catalogue
- `-fhi 1000` is the maximum frequency to search for, which encompasses all pulsars in the ATNF catalogue, including their harmonics
- `-numharm 16` is the number of harmonics to search
- `*.fft` defines the input FFT files

This will output `.ACCEL` and `.cand` files containing the periodic candidates and their harmonics. It has been shown in Sengar et al. (2023) that increasing the number of harmonics to 32 yields more pulsar discoveries, so this increase will be adopted in the next processing pass.

2.5.3.6 Periodic candidate selection

For an MWA observation, there can be millions of periodic candidates. To reduce the number of periodic candidates, we use `PRESTO`'s `ACCEL_sift.py` to filter out candidates without detections in adjacent DMs and low S/N ratios.

```
ACCEL_sift.py -f NAME --r_err 1.1
              --min_num_DMs 8
              --low_DM_cutoff 1.0
              --sigma_threshold 3.0
              --c_pow_threshold 10.0
              --short_period 0.0005
              --long_period 15.0
              --harm_pow_cutoff 3.0
```

The above command line specifies the following behaviour:

- `-f NAME` is the filename to be used for the output file cand_<NAME>.txt
- `--r_err 1.1` how close a candidate has to be to another candidate to consider it the same candidate (in Fourier bins)
- `--min_num_DMs 8` how many DMs a candidate must be detected in to be considered "good"
- `--low_DM_cutoff 1.0` lowest DM to consider as a "real" pulsar (not RFI)
- `--sigma_threshold 3.0` ignore candidates with a sigma (from incoherent power summation) less than this

- `--c_pow_threshold 10.0` ignore candidates with a coherent power less than this
- `--short_period 0.0005` shortest period candidates to consider (s)
- `--long_period 15.0` longest period candidates to consider (s)
- `--harm_pow_cutoff 3.0` ignore any candidates where at least one harmonic does exceed this power

This significantly reduces the number of periodic candidates. Equation 2.18 suggests that `--sigma_threshold` should be 6.5 instead of 3 so our current value was likely too conservative. Now that a large number of pulsars have been detected with the MWA, there is sufficient test data to attempt to raise this value without missing true candidates for the next processing pass.

2.5.3.7 Candidate fold

Each of the significant periodic candidates from `ACCEL_sift.py` was then folded (also known as pulse stacking) to increase the S/N of the individual pulses. This was done with `PRESTO`'s `prepfold` command.

```
prepfold -o NAME -dm DM
         -accelfile NAME.cand -accelcand CAND_ID
         -n NBINS
         -npart N_TIME_CHUNK
         -dmstep DM_foldstep
         -npfact PERIOD_SEARCH_N
         -ndmfact N_DM_FACT
         -pstep 1 -pdstep 2 -noxwin -noclip
         -runavg -nsub 256 *.fits
```

The above command line specifies the following behaviour:

- `-o NAME` the base output name of the plot and binary files
- `-accelfile NAME.cand` the output file from `accelsearch`
- `-accelcand CAND_ID` the ID of the candidate as the `NAME.cand` may have several candidates
- `-n N_BINS` number of profile bins
- `-npart N_TIME_CHUNK` number of chunks to split the time window into
- `-dmstep` $\mathrm{DM}_{\mathrm{foldstep}}$ the minimum DM stepsize over the observation in profile bins
- `-npfact PERIOD_SEARCH_N` which will be used to search N periods and p-dots will be searched where $N = 2 * \mathrm{PERIOD\_SEARCH\_N} * proflen + 1$
- `-ndmfact` N_{DMfact} where N DMs will be searched where $N = 2 * N_{DMfact} * proflen + 1$
- `-pstep 1` the minimum period stepsize over the observation in profile bins
- `-pdstep 2` the minimum $\dot{P}$ stepsize over the observation in profile bins
- `-noxwin` do not show the result plots on-screen, only make postscript files
- `-noclip` do not clip the data to ensure giant pulses are not removed
- `-runavg` subtract each block average as it is read to avoid power fluctuations
- `-nsub 256` the number of sub-bands to use for the DM search
- `*.fits` defines the input tied-array beam PSRFITs file

The values for `N_BINS`, `N_TIME_CHUNK`, $\mathrm{DM}_{\mathrm{foldstep}}$ and `PERIOD_SEARCH_N` is dependent on if the pulsar has a period less than 10 ms. If the period is greater than 10 ms, then the values were `N_BINS`=100, `N_TIME_CHUNK`=120, $\mathrm{DM}_{\mathrm{foldstep}}$=1 and `PERIOD_SEARCH_N`=1 which is what the LOTTAAS ML researchers found to be

the best `prepfold` values to make the ML sensitive to pulsars (Tan et al., 2018b). If the period was less than 10 ms, then `N_BINS` was reduced to 50 so the profile bins were not less than the time resolution, `N_TIME_CHUNK` was reduced to 40, so it is more likely to see the fainter MSP emission in the time plot, $\mathrm{DM}_{\mathrm{foldstep}}$ was increased to 3 to search a more reasonable number of bins and `PERIOD_SEARCH_N` is increased to 2 to search for more periods.

By default, `prepfold` would often search an unreasonable range of DMs (up to ±100). To avoid this we calculated the value of N_{DMfact} to only search ±2 DM using:

$$N_{\mathrm{DMfact}} = \left\lceil \frac{1}{4.677 \mathrm{DM}_{\mathrm{foldstep}} P} \right\rceil \tag{2.19}$$

where $\lceil\rceil$ represents round up to the nearest integer.

An example of `prepfold`'s output is shown in Figure 2.15. This detection of PSR J1002−2036 is an excellent example of what we look for in pulsar candidates. It has a strong pulse profile, the pulsar can be seen throughout the time and frequency series (unlike noise or RFI, which would not appear throughout), and the characteristic curve around its true value can be seen in the DM, period and period derivative series, and there is a single peak in the period vs period derivative plot.

2.5.4 Candidate classification

Each MWA observation in the first pass search results in ∼60000 folded candidates. The classification of these candidates is done in two stages, first through ML, which reduces the number of candidates to ∼6000, and then goes through a stage of human classification.

2.5.4.1 Machine learning classification

The candidates were first classified with ML, for which we use the LOTAAS ensemble candidate classifier (Tan et al., 2018b). The LOTAAS classifier has

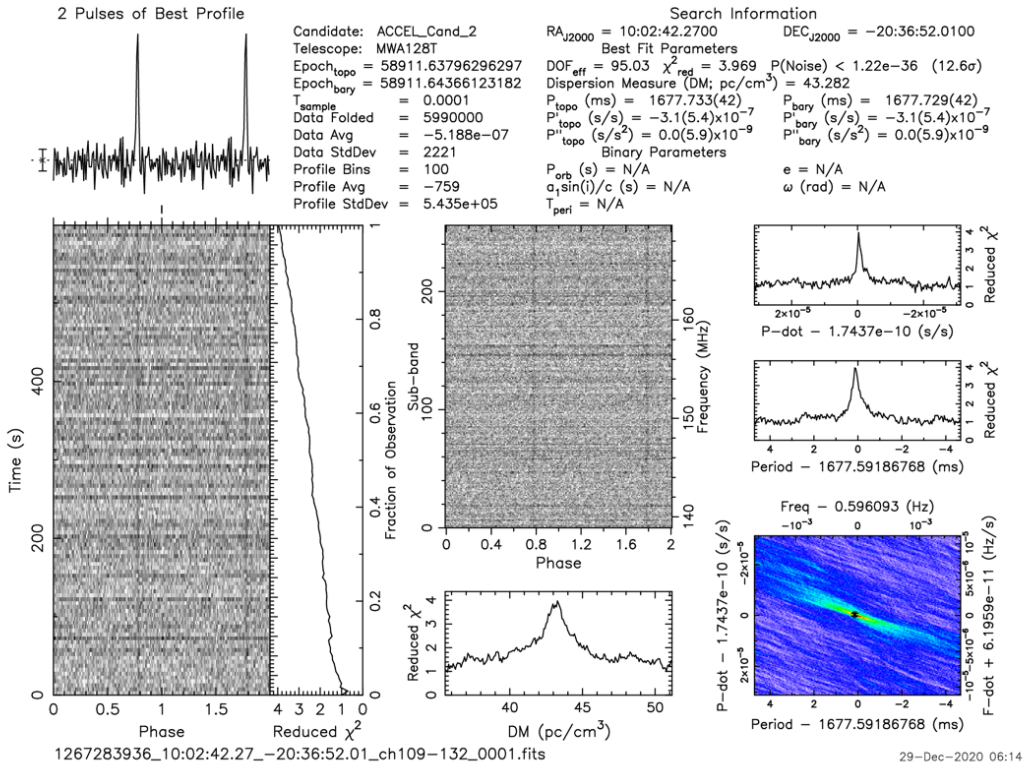

Figure 2.15: The third pulsar discovered with the MWA pulsar search pipeline, PSR J1002−2036 (Bhat et al., 2023b). *Top left*: The average of all pulses, repeated twice. *Top right*: The metadata of the detection. *Bottom left*: The dedispersed time series. *Middle middle*: The dedispersed frequency series. *Bottom middle*: The DM curve where the reduced χ^2 measures the pulse profile with respect to a flat line and is similar to an S/N rather than the usual quantitative statistical value of goodness. *Middle right*: The period and period derivative series. *Bottom right*: The period vs period derivative plot.

yet to be trained on MWA candidates but still performs well, with a recall rate of 83% (Bhat et al., 2023a), reducing the number of candidates by an order of magnitude.

This is done by first extracting features from the `prepfold`'s PFD files with the `PulsarFeatureLab`[5] repository Lyon et al. (2016).

```
PulsarFeatureLab.py -d DIR -t 6 -c 3 --arff --meta
                    -f feature_extraction.arff
```

The above command line specifies the following behaviour:

- `-d DIR` the directory containing candidates
- `-t 6` generate the 8 pulsar features from Lyon et al. (2016)
- `-c 3` defines the input as PRESTO's PFD file format
- `--arff` writes feature output in the WEKA ARFF file format
- `--meta` includes meta-information in the ARFF file
- `-f feature_extraction.arff` the file to output the candidates to

Each of these pulsar feature files is then put through the ensemble classifier using the `LOTAASClassifier`[6] repository Tan et al. (2018b). We do this for each of the five models and define a positive classification if it is positively classified by at least three of the models.

```
for i in {1..5}; do
    java -jar LOTAASClassifier.jar -m ${i}.model
                                   -p ARRF -a 1
done
```

The above command line specifies the following behaviour:

[5] https://github.com/scienceguyrob/PulsarFeatureLab/tree/V1.3.2
[6] https://github.com/scienceguyrob/LOTAASClassifier

- `-m ${i}.model` one of the five input model files
- `-p ARRF` the ARRF file from `PulsarFeatureLab.py`
- `-a 1` uses the J48 decision tree algorithm

2.5.4.2 Human classification

The ∼6000 candidates per observation is a daunting task for human classification. Initial attempts at manually classifying them (moving candidates into different directories based on their ratings) were found to be time-consuming and challenging to keep organised. For this reason, we enlisted the help of the Astronomy Data And Computing Services (ADACS) and Optical Data Central to develop The SMART Pulsar Database.

The primary purpose of The SMART Pulsar Database is to make it easier for a large number of researchers to classify the tens of thousands of candidates as efficiently as possible so the most promising candidates can be found and followed up quickly. Researchers can log onto the website and were shown a candidate, as shown in Figure 2.16, and given as much information as possible so they can determine if it is noise, RFI, a known pulsar or a promising new candidate. All candidates, if they are known pulsars or not, are given a ranking from one to five where the following are the grades:

1. Noise
2. A very weak candidate that could be a fluctuation of the noise
3. A weak possible candidate
4. Likely a pulsar but not extremely bright
5. A bright, excellent candidate that is worth following up

[7] https://apps.datacentral.org.au/smart/

Figure 2.16: An example of the candidate rating page on The SMART Pulsar Database [7]for PSR J2330−2005. *Top left*: The image of the candidate. *Bottom left*: The metadata of the candidate. *Top middle*: Where users can put their rating, label it if it is a known pulsar and any other notes. *Middle middle*: Which known pulsar the candidate likely is, based on position, period and DM. *Bottom middle*: Will give the same rating to other nearby candidates with similar periods and DMs if their box is ticked. *Top right*: Parameters to search for similar candidates. *Middle right*: The location of similar candidates. *Bottom right*: The images and metadata of all similar candidates (more will be shown below).

Once multiple researchers have classified a candidate, and if it has been given an average rating greater than three and confirmed that it is not a known pulsar; it is deemed worthy of follow-up. All but the first pulsar discovery with the MWA was classified with the help of the SMART database.

2.5.5 Confirmation and follow-up of candidates

To confirm that a candidate is real, we download the full 80 minutes of the observation to enhance the sensitivity of the detection. This significantly increased the sensitivity of PSR J1002−2036, as shown in Figure 2.17, compared to the original detection, as shown in Figure 2.15. Since this is a very strong detection, we can be confident that this is a genuine new pulsar. To be thorough, it should still be confirmed with multiple detections with multiple telescopes.

To improve the position estimate of the candidate, traditionally, other telescopes would need to re-observe at different locations, as shown in Figure 2.10. With the MWA, we do not have to re-observe because we can create a hexagon of tied-array beams around the candidate in post-processing. We then compare the S/N ratio of the detections as shown on the left of Figure 4.2. We then look for archival observations of the candidates using `vcstools`'s `find_pulsar_in_obs.py` command.

```
find_pulsar_in_obs.py -c hh:mm:ss.ss_+dd:mm:ss.ss
                      --obs_for_source
```

The above command line specifies the following behaviour:

- `-c hh:mm:ss.ss_+dd:mm:ss.ss` the coordinate to look for in right ascension and declination
- `--obs_for_source` tells the script to look for all observations that contain a source instead of its default which is to find all sources in an observation

This command will output a file that lists all MWA VCS observations the

candidate is in, how long for and with what tile power. To improve our position estimate, we first find Phase 1 observations and then Phase 2 extended array observations to slowly improve the resolution of the tied-array beams (see Table 2.1). If a Phase 1 observation is available, we cover the Phase 2 compact position estimate with a grid of 37 beams to improve it further, as shown in the middle of Figure 4.2. Phase 2 extended array observations were used to improve this estimate further, as shown on the right of Figure 4.2, which will be the final tied-array beam estimate. The MWA position estimate can only be further improved by creating a radio image of the pulsar, but this is only sensitive to extremely bright pulsars. The position is further improved through observations with high-frequency telescopes such as Parkes and GMRT, as shown in Figure 4.3.

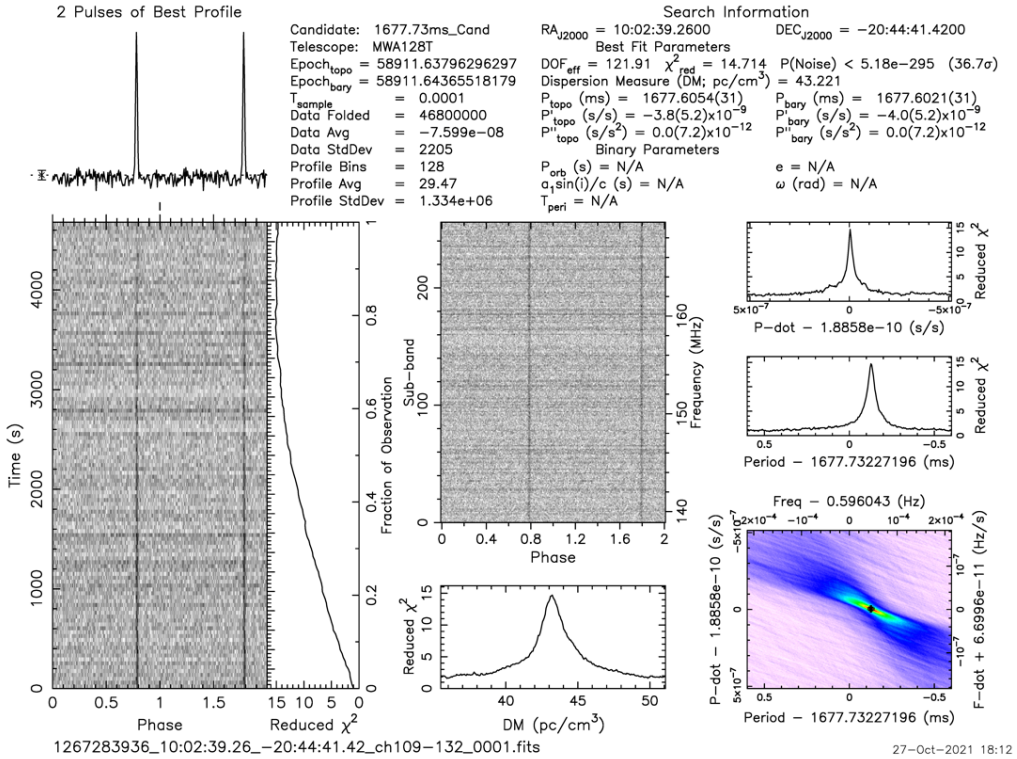

Figure 2.17: The third pulsar discovered with the MWA pulsar search pipeline, PSR J1002−2036 (Bhat et al., 2023b). This uses the full 80 minutes of data instead of the 10 minutes used in Figure 2.15.

To improve the timing solution of the pulsar, follow-up observations were scheduled at an exponential cadence. As each observation is added to the timing solution, the period's accuracy is increased, allowing observations from a larger time span to be added without missing an entire pulse period. Once sufficiently accurate, these timing solutions can be published so the pulsar is easily detectable by other telescopes.

Chapter 3

A Multi-Pixel Beamformer for Pulsar Surveys and Ionospheric Corrected Localisation

This chapter describes the solutions to two problems preventing efficient and accurate low-frequency pulsar surveys with the MWA. The multi-pixel beamformer improves processing efficiency so that large-scale surveys are feasible, and the ionospheric correction method ensures that flux density measurements are not affected by incorrect offset calibrations. This chapter is a faithful reproduction of the author's publication Swainston et al. (2022a), which has the full title "MWA Tied-Array Processing IV: A Multi-Pixel Beamformer for Pulsar Surveys and Ionospheric Corrected Localisation", as per Curtin University's policy. In both this and subsequent chapters, the end matter (Acknowledgements, References) of the original papers have been shifted to the relevant sections of this thesis. The sections "2.1.1 Calibration" and "2.1.2 Beam formation" from the original have been moved to §2.3.1.2 and 2.3.1.3 respectively and expanded to prevent duplication. It also differs from the original in other minor respects, including the formatting of both the text and the images and the numbering of the equations and figures.

3.1 Abstract

The Murchison Widefield Array (MWA) is a low-frequency aperture array capable of high-time and frequency resolution astronomy applications such as pulsar studies. The large field-of-view of the MWA (hundreds of square degrees) can also be exploited to attain fast survey speeds for all-sky pulsar search applications, but to maximise sensitivity requires forming thousands of tied-array beams from each voltage-capture observation. The necessity of using calibration solutions that are separated from the target observation both temporally and spatially makes pulsar observations vulnerable to uncorrected, frequency-dependent positional offsets due to the ionosphere. These offsets may be large enough to move the source away from the centre of the tied-array beam, incurring sensitivity drops of ∼30-50% in Phase II extended array configuration (maximum baseline of 5 km) during some of the worst ionospheric conditions. We analyse these offsets in pulsar observations and develop a method for mitigating them, improving both the source position accuracy and the sensitivity. This analysis prompted the development of a multi-pixel beamforming functionality that can generate dozens of tied-array beams simultaneously, which runs a factor of ten times faster compared to the original single-pixel version. This enhancement makes it feasible to observe multiple pulsars within the vast field of view of the MWA and supports the ongoing large-scale pulsar survey efforts with the MWA. We explore the extent to which ionospheric offset correction will be necessary for the MWA Phase III and the low-frequency Square Kilometre Array (SKA-Low).

3.2 Introduction

The Murchison Widefield Array (MWA) was initially built as a low-frequency connected element interferometer of 128 aperture array 'tiles' consisting of 16 dual-polarisation dipole antennas (Tingay et al., 2013). This Phase I MWA was designed to be an imaging telescope to support a wide range of science, from

continuum imaging of Galactic and extragalactic radio sources to detecting the epoch of re-ionisation (Bowman & Collaboration, 2015). One of the significant strengths of the MWA is its huge field-of-view (FoV); each tile (i.e. 4 x 4 array of dual-polarisation antennas) provides an FoV in the range from ∼300 to ∼1000 square degrees depending on the observing frequency within its 70-300 MHz operating range. This large FoV makes the MWA a highly efficient survey instrument.

As the coarse 0.5 second time resolution achievable with the MWA's hybrid correlator (Ord et al. 2015) was not adequate to support pulsar observations, a new functionality called the Voltage Capture System (VCS, Tremblay et al. (2015)) was developed. It allows recording channelised voltage data after the second stage of the polyphase filter bank in the MWA's signal path, providing a native time resolution of 100 μs and a frequency resolution of 10 kHz. However, recording these voltages results in very high data rates, $\sim$ 27 TB per hour, limiting the maximum possible observing time to 90 minutes due to available disk storage. These raw antenna voltages can then be calibrated and combined into a single, channelised, dual-polarisation voltage, tied-array, *pencil beam* through software beamforming, as detailed in Ord et al. (2019). This tied-array beamforming is essential to support high-sensitivity pulsar and fast transient science with the MWA.

The combination of the VCS and the software beamformer have been leveraged to conduct low-frequency pulsar science (Meyers et al., 2017; Bhat et al., 2018; Mcsweeney et al., 2017). This is, in part, due to the constant development of the beamformer, such as the polarimetric verification performed by Xue et al. (2019). In McSweeney et al. (2020) a polyphase synthesis filter was implemented to recover some of the time resolution at the expense of frequency resolution ($\sim 0.8\mu$s and 1.28 MHz). This enabled the low-frequency range of the MWA to be exploited to obtain accurate dispersion measure measurements of millisecond pulsars (Kaur et al., 2019).

The MWA was upgraded with a further 128 tiles, extending its maximum baseline to ∼6 km (Wayth et al., 2018). However, the signal path remains the same, and as a result, only data from 128 of the 256 tiles can be correlated or recorded in the VCS mode at a given time. This "Phase II" MWA (Wayth et al., 2018) can be configured either as a compact array with baselines within ∼300 metres or as an extended array with baselines up to ∼6 km. The compact array configuration, which provides a sensitivity equivalent to that of Phase I MWA for tied-array beam processing, has a much broader beam size (a FWHM of $\sim 23'$ at 155 MHz), almost a factor of ∼6 times larger than the Phase I array and hence a beam area that is ∼40 times larger. The larger beam size of the compact array means a smaller number of beams are needed to cover a given area within the FoV, which is more appealing for large scale pulsar surveys.

The Phase II extended array's ∼6 km maximum baseline is ideal for localising pulsar candidates (see Bhat et al. (2023a)) but, at the low frequencies of the MWA, the smaller tied-array beam size can become comparable to positional offsets due to the refractive ionosphere. This refraction is due to spatial variations of the total electron content (TEC), the lowest order of which is a slope across the FoV whose net effect on the apparent source positions can be described by a single "bulk offset". The positional offsets remaining after the bulk offset has been removed (e.g. during calibration) are due to higher-order variations in the TEC and are termed "residual offsets" in this work. Any offset not corrected for during calibration can potentially degrade the sensitivity of a detection if the offset is an appreciable fraction of the size of the tied-array beam.

Calibration of MWA VCS data typically involves an observation of a bright source and the *Real Time System* (RTS, Mitchell et al. 2008) to create a direction independent calibration solution which is subsequently applied to the target observation. If the bulk offset is correctly accounted for, the median residual offsets are less than 0.13 $'$ for 50% of observations and less than 0.29 $'$ for 90% of observations at 200 MHz (Jordan et al., 2017; Kassim et al., 2007). Figure 3.1

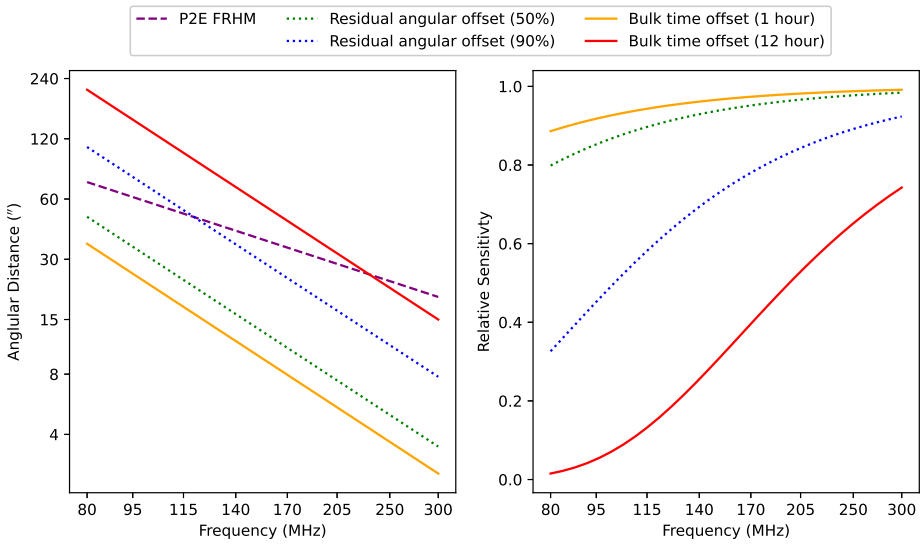

Figure 3.1: *Left*: how the MWA Phase II extended array (P2E) tied-array beam's half-width half-maximum (HWHM) scales with frequency assuming a Gaussian beam shape compared to different ionospheric offset estimates. *Right*: how these offsets would affect the relative sensitivity of an observation. The ionospheric offset estimates include: Residual angular offset (50%), the median residual offset for the 50th percentile of the observations (Jordan et al., 2017); Residual angular offset (90%), as above but for the 90th percentile; Bulk time offset (1 hour), the maximum change in the bulk offset over 1 hour seen in the work of Arora et al. (2015); Bulk time offset (12 hours), as above but over a 12 hour period.

illustrates how the size of the residual offsets scales with frequency compared to the Half Width Half Maximum (HWHM). This suggests that the residuals only significantly affect sensitivity at low frequencies ($\lesssim$140 MHz), due to the offsets of the order of the beam size, for $\sim$10% of our observations.

For the majority of MWA observations, the best calibration source is in a different part of the sky and observed at a different time than the target observation. That is, the calibration and target observations generally sample different ionospheres. Thus, the bulk offset determined during calibration can differ from the bulk offset present in the target observation. Using GPS satellites to probe the ionosphere above the MWA, Arora et al. (2015) observed the bulk offset change by up to $\sim 0.17'$ (at 150 MHz) in an hour or up to $\sim 1'$ (at 150 MHz) over 12 hours. It is standard practice to have at least one calibration observation

within an hour of the target observation. However, sometimes these calibration solutions fail to converge, and we are obliged to use calibration observations up to 48 hours away. In these cases, the bulk offset has likely changed, as illustrated by the 12-hour angular distance offset in Figure 3.1. For example, if applying the correction for an incorrect bulk offset moves a source to the half-power point of our tied-array beam, it would require observing for four times as long to recover the lost sensitivity. To prevent this, we must understand this bulk offset error and develop a method for mitigating it.

We must correct for these offsets to efficiently perform high-sensitivity pulsar and transient science in the extended array configuration and with the upcoming MWA Phase III. Our strategy for measuring and correcting positional offsets is conceptually simple: we form multiple beams around the target position and measure the strength of the detection as a function of the pointing position. Even for the compact configuration, surveys of known pulsars may require forming up to hundreds of beams, while blind surveys require thousands of beams to tile the entire FoV, creating a processing bottleneck. These use cases have prompted the development of new functionality that allows processing VCS data for generating multiple beams efficiently to overcome the problems associated with the VCS's high data rates. This new multi-pixel beamformer functionality will allow us to exploit the enhanced sensitivity achieved via a tied-array beam as well as the large FoV.

Similar multi-pixel beamformers have been developed to support pulsar science using other low-frequency radio telescopes such as the Giant Metrewave Radio Telescope (GMRT) (Roy et al., 2012) and the Low-Frequency Array (LOFAR) (Broekema et al., 2018; Sanidas et al., 2019), both of which perform real-time processing of antenna voltages to generate ∼10-100 beams. The MWA beamformer, on the other hand, is conceptually different in design (Ord et al. 2019) and employs post-processing offline to generate tied-array beams. The multi-pixel beamformer functionality presented in this paper can output hundreds of tied-

array beams simultaneously to make large scale pulsar surveys computationally feasible, allowing us to study and correct for ionospheric offsets.

The remainder of this paper is organised as follows. We first discuss the implementation of the MWA tied-array beamforming in §3.3.1, and its upgrade to the multi-pixel beamformer in §3.3.2. Then in §3.3.3, we benchmark the improvement in processing efficiency compared to the previous beamformer using multiple supercomputers. In §3.4 we demonstrate the multi-pixel beamformer's capability to correct for ionospheric offsets and perform a pulsar census. Finally, In §3.5 we discuss the implications for MWA Phase III and low-frequency Square Kilometre Array (SKA-Low).

3.3 Implementation and Benchmarking

3.3.1 Tied-Array Beamforming with the MWA

The design philosophy and algorithmic implementation behind tied-array beamforming with the MWA are explained in detail in Ord et al. (2019) and §3.3.1. In the following sections, we give an overview of the software implementation in its current production version (§3.3.2) that was not explained in Ord et al. (2019).

3.3.2 Multi-Pixel Beamforming Functionality

To form multiple beams, a naive approach would be simply to repeat the calculation of Equation (2.3) for each desired pointing in the FoV. This is computationally expensive due to the large size of the voltages, v_j, requiring significant read time, see Figure 3.2. Once these voltages have been calibrated, they can be used to beamform anywhere within the FoV. This suggests a strategy for forming multiple beams efficiently since the only quantity that changes for different tied-array beam pointings is the geometric delay. The geometric delay changes at a rate of 1.0 rad s^{-1} which equates to a 1% S/N drop if calculated once per

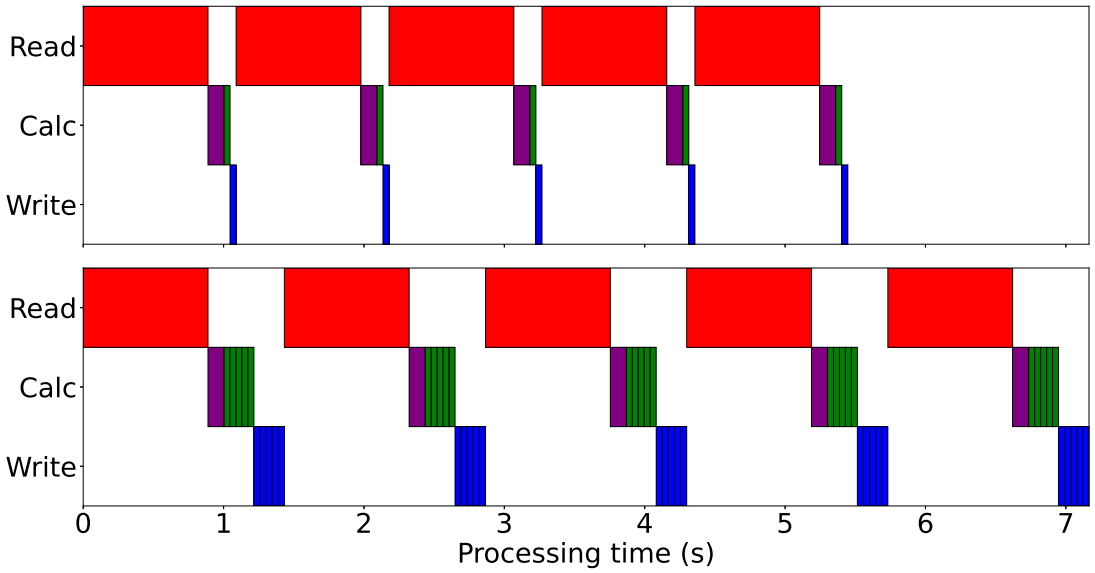

Figure 3.2: A comparison of the processing time and workflow of the single-pixel beamformer (top panel) processing a single beam and the multi-pixel beamformer (bottom panel) processing five beams. Each block represents the processing time required to read in a second of data (red), apply the calibration solution (purple), perform the delay compensation and tile summation (green) and write out the results (blue).

second. One can therefore compute the quantities

$$e_j = J_j^{-1} v_j \tag{3.1}$$

just once per second of data, leaving only the summation over tiles,

$$e' = \sum_{j}^{N_{\rm A}} e_j \exp\{-i\phi_j\}, \tag{3.2}$$

to be performed for each desired pointing.

The complete set of computational steps required for an efficient multi-pixel beamformer would therefore be as follows (the colours listed for each step refer to the diagram shown in Figure 3.2):

1. Reading in the raw MWA complex voltages (red)

2. Applying the calibration solution and primary beam correction as per Equation (3.1) (purple)

3. Correcting for the geometric and cable delays as per Equation (3.2), flattening the bandpass, and converting to Stokes parameters (green)

4. Writing the beamformed data to disk (blue)

Further optimisation by means of overlapping read/write tasks will be explored in the future.

We use an MWA antenna beam model to compensate for the dipole response as part of the gain compensation. The original beamformer used an analytical beam model (described briefly in Ord et al. (2019)), but since version 2.3 the multi-pixel beamformer has used the Full Embedded Element (FEE) primary beam model for both calibration and beamforming (Sokolowski et al., 2017). The FEE beam model simulates every dipole in the MWA tile (4×4 bow-tie dipoles) separately, taking into account all mutual coupling, ground screen and soil effects, and has been tested empirically by various authors (e.g. Line et al., 2018; Chokshi et al., 2021). Dead dipoles, which also affect the beam response, are also taken into account during beamforming.

3.3.2.1 Implementation

The MWA beamformer has been developed as part of the `vcstools`[1] repository (Swainston et al., 2020). The beamformer processes one second of data at a time, recalculating the geometric delays at the same cadence. Each second of MWA VCS data has 10,000 time samples, 3,072 frequency channels, 128 tiles and two polarisations, which equates to 8 million independent calculations of $v_j J_j^{-1} exp\{-i\phi_{j,n}\}$ per second per tied-array beam. This computation is spread over 24 Graphics Processing Units (GPUs), one for each of the 24 coarse frequency

[1] https://github.com/CIRA-Pulsars-and-Transients-Group/vcstools

channels. Per second of observation, this lowers the size of the input baseband voltages to 313 MB and the number of calculations to 325,000 per GPU.

The large size of the raw voltages is not only a problem for processing efficiency: if running a large number of beamforming jobs, the significant demands on file I/O can affect the health of supercomputing clusters' metadata servers. These metadata servers can only handle a certain transfer rate from the file system (e.g. Lustre, which is often used on supercomputing clusters) to memory which becomes a limiting factor for large scale beamforming jobs and another reason to process as many simultaneous beams as possible with the multi-pixel beamformer.

The original single-pixel implementation of the beamformer involved a GPU kernel for each beam involving the calculation shown in Equation (2.3). This kernel was split in two so that the calculation in Equation (3.1) can be performed only once per run, after which a kernel for calculating Equation (3.2) can be performed for each beam. Storing these intermittent products (calibrated voltages) on the GPU device may exhaust the available device memory. To prevent the GPU from running out of device memory, the beamformer automatically calculates the largest fraction of a second that can be accommodated on the GPU and processes the data in batches. Asynchronous streams were implemented to ensure that each chunk of data was moved onto the GPU and processed as soon as possible. With the above implementation in place, the only limit on the number of beams that can be processed at once is the maximum job wall time imposed by supercomputing clusters. If requested, the Stokes parameters are calculated, and the bandpass of each frequency channel flattened to account for the frequency-dependent sensitivity of the receivers. Finally, the Stokes parameters are moved off GPU memory to an output buffer.

The Stokes parameters are written to disk in either the PSRFITS (Hotan et al., 2004) or VDIF (Whitney et al., 2009) formats. For PSRFITS (the format used in our search pipeline), the beamformer outputs Stokes parameters to one

output file per pencil beam. As the number of beams increases, opening and writing to a large number of files place an extra burden on the file system as it puts strain on the metadata servers. To prevent this, it is recommended to use Solid State Drives (SSDs), if available, to ensure writing the files does not become a bottleneck.

Blind pulsar searches using traditional search algorithms only use Stokes I. Writing only Stokes I reduces the output by a factor of 4 and can improve the efficiency of the beamformer even more than implied by the benchmarks presented in the following sections. Any pulsar candidates found using Stokes I can be re-beamformed at a later date using the full Stokes parameters for polarisation analysis.

3.3.3 Benchmarking

The processing requirements of an all-sky pulsar search are notoriously massive and often take several years. For this reason, it is crucial to understand the beamforming bottlenecks so we can choose the supercomputer clusters that can most efficiently process the data.

3.3.3.1 Relative speed improvements

The following equation can model the efficiency improvement of the multi-pixel beamformer over the single-pixel beamformer:

$$R = \frac{N_{\mathrm{B}}(t_{\mathrm{R}} + t_{\mathrm{C}} + t_{\mathrm{B}} + t_{\mathrm{W}})}{t_{\mathrm{R}} + t_{\mathrm{C}} + N_{\mathrm{B}}(t_{\mathrm{B}} + t_{\mathrm{W}})}, \tag{3.3}$$

where N_{B} is the number of tied-array beams calculated at once, t_{R} is the time it takes to read in data, t_{C} is the time to transfer data onto the GPU and apply the complex gains, t_{B} is the time to form the beam and calculate the Stokes parameters, and t_{W} is the time to write the data to disk. This theoretical prediction of the improvement is compared to the benchmarked improvement in Table 3.1 and

illustrated in Figure 3.3.

3.3.3.2 Supercomputer platforms

To ensure the processing load of a pulsar survey can be spread between multiple supercomputers and that all collaborators can process VCS data, we made our software portable enough to be easily installed on multiple supercomputing clusters through containerisation, see the `vcstools DockerHub`[2].

The beamformer was initially installed and developed on the Pawsey Supercomputing Centre's Galaxy supercomputer[3], which is used to support Australian Square Kilometre Array Pathfinder (ASKAP) and the MWA's radio astronomy processing. However, all MWA processing at Pawsey has since been migrated to the new Garrawarla cluster[4], and the beamformer software is now installed and running on that system. To spread the processing load, we additionally installed our beamforming software on Swinburne University's OzSTAR supercomputer[5] and China SKA Regional Centre's (CSRC) prototype supercomputer. Benchmarks are presented for all three systems.

3.3.3.3 Benchmarking method

The read/input and write/output speeds can fluctuate due to how much strain the supercomputer's metadata server is under at any given time. To account for this fluctuation, the multi-pixel beamformer was benchmarked by running 24 10-minute instances using 1 to 20 simultaneous beams and compared to the single-pixel beamformer. This fluctuation still exists, leaving a $\sim$10% variability on all read and write benchmarks. The improvement is illustrated in Figure 3.3 and agrees with our improvement prediction.

[2] https://hub.docker.com/repository/docker/cirapulsarsandtransients/vcstools

[3] https://support.pawsey.org.au/documentation/display/US/HPC+Systems#HPCSystems-Galaxy(CrayXC30)

[4] https://support.pawsey.org.au/documentation/display/US/Garrawarla+Documentation

[5] https://supercomputing.swin.edu.au/ozstar/

Super computer	GPU	TFLOP	N_{GPU}	t_R (ms)	t_C (ms)	t_B (ms)	t_W (ms)	F_T	F_B
Garrawarla	NVIDIA V100 PCIE	7.0	78	677	80	33	20	8.9	7.7
OzSTAR	NVIDIA P100 PCIe	4.7	214	266	117	42	42	8.0	10.4
CSRC	NVIDIA V100 SXM	7.8	16	1329	36	54	32	9.3	8.4

Table 3.1: The benchmarks of each part of the MWA multi-pixel beamformer on three supercomputers where GPU is the brand/model of graphics card, TFLOPS (TeraFlops) is the peak performance for double precision of the graphics card, N_{GPU} is the total number of GPUs available on the supercomputer. The following are estimates of the time required to process a second of data at each step where t_R is the time spent reading in data, t_C is the time spent transferring data onto the GPU and applying the complex gains, t_B is the time spent forming the beam and calculating the Stokes parameters and t_W is the time spent writing the data to disk. There are also factors of improved processing efficiency for 20 beams where F_T is the theoretical improvement using Equation 3.3 and F_B is the measured improvement from benchmarking.

At 20 simultaneous beams, the improvement of the multi-pixel beamformer is a factor of 7.7, 10.4 and 8.4 compared to the single-pixel beamformer for Garrawarla, OzSTAR and the CSRC prototype, respectively (see Table 3.2). Once $t_R < NB \times (t_B + T_W)$, the beamformer is no longer limited by the time spent reading in the data, and the new limiting factor becomes the time spent on the GPU and writing to disk. Thus, technological improvements such as faster GPUs and the use of SSDs can significantly improve the beamformer's processing rate.

In Table 3.1 we compare the processing required to tile a 10-minute observation with (MWA Phase II compact array) tied-array beams for both the single and multi-pixel beamformers. Performing a pulsar search with the MWA requires a large number of dispersion trials to maintain sensitivity due to the increased dispersion effect at our low-frequency range. Therefore to do even a simple periodic pulsar search on the 6000 beams would require approximately 20 thousand CPU hours, which is similar to the GPU hours required by the single-pixel beamformer, see Table 3.2. The multi-pixel beamformer only takes a tenth of the processing time, meaning beamforming is no longer a bottleneck, and a blind pulsar search with the MWA is feasible.

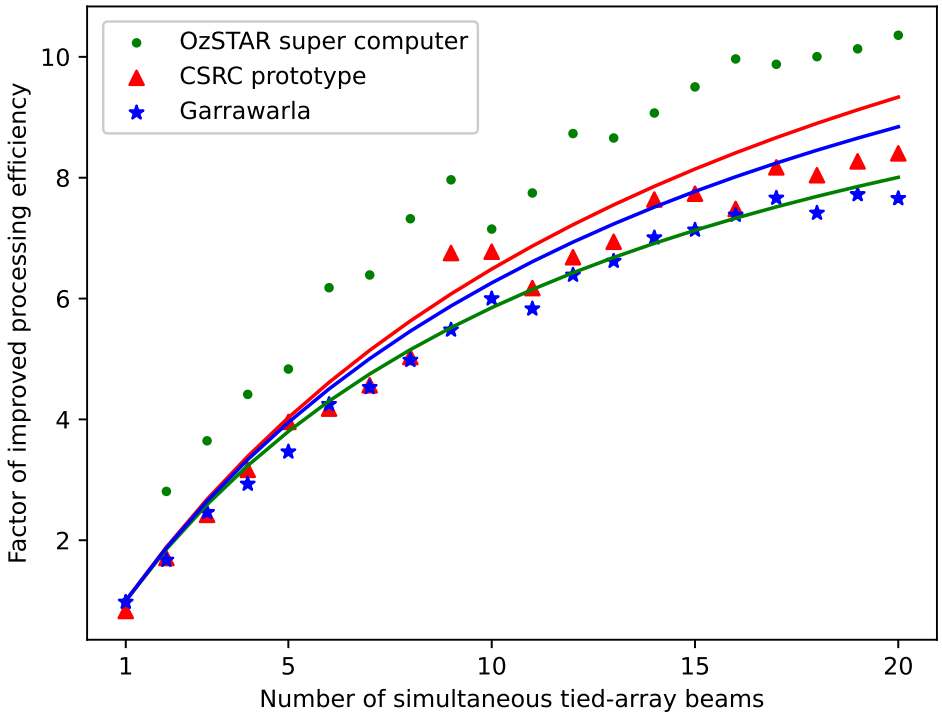

Figure 3.3: A comparison of the processing efficiency improvement of the multi-pixel beamformer for a given number of beams on the OzSTAR (green), China SKA Regional Centre's prototype (red) and Garrawarla (blue) supercomputers. The processing efficiency per tied-array beam is an increasing function of the number of simultaneously calculated beams for the multi-pixel beamformer.

3.4 Applications

The improved efficiency of the multi-pixel beamformer makes large scale processing such as pulsar surveys and candidate localisation (Swainston et al., 2021) computationally feasible. Unlike other telescopes, the MWA VCS can beamform in post-processing and create a grid of pointings to estimate the position of the source without the need for re-observation. This allows the MWA to quickly localise candidates for follow up and since the beams are simultaneous, they are in the same RFI environment, so the signal-to-noise ratios of the detections can be used as a reliable proxy for comparative sensitivity. We use the localisation

Super Computer	Software version	1B (s)	20B (s)	6000 Beams (kSU)
Garrawarla	SPB	479	479	19.1
Garrawarla	MPB	490	63	2.5
OzSTAR	SPB	973	973	38.8
OzSTAR	MPB	999	94	3.7
CSRC	SPB	884	884	35.4
CSRC	MPB	1064	105	4.2

Table 3.2: A comparison of the original single-pixel beamformer (SPB) and the multi-pixel beamformer (MPB) processing times in seconds per tied-array beam per coarse frequency channel for a 10-minute MWA observation where 1 B and 20 B represent calculating 1 beam or 20 beams simultaneously. "6000 Beams" indicates the processing time in kSU (thousand service units) to process the ∼6000 tied-array beams required to tile the entire FoV of a 10-minute MWA Phase II compact array observation.

method as described in Bannister et al. (2017) and shown in Figure 3.4. This method provides a beam localisation uncertainty $\sigma_{\mathrm{L}} = 14''$, but this does not take into account any errors in calibration and residual ionospheric offsets. The method for minimising the calibration errors is explained in the following sections.

3.4.1 Testing the validity of calibration solutions and ionospheric corrections

At 155 MHz, the ionosphere can move the apparent position of sources by ∼15″ in typical conditions or up to ∼50″ in the worst conditions. When the MWA is in the extended array configuration, the FWHM (∼1.26′ at 155 MHz) of the tied-array beams is small enough to affect detection sensitivity when the ionosphere moves the apparent position of sources. The RTS will attempt to correct for the bulk ionospheric offset estimated by the calibration solution. If the calibration source is observed at a different time and in a different part of the sky, the ionosphere may change, leading to a different bulk offset (see Figure 3.1).

We used the 18 pulsars detected in observation 1276619416 (taken on MJD 59019; as part of the G0071 project to study pulsar emission physics) to inves-

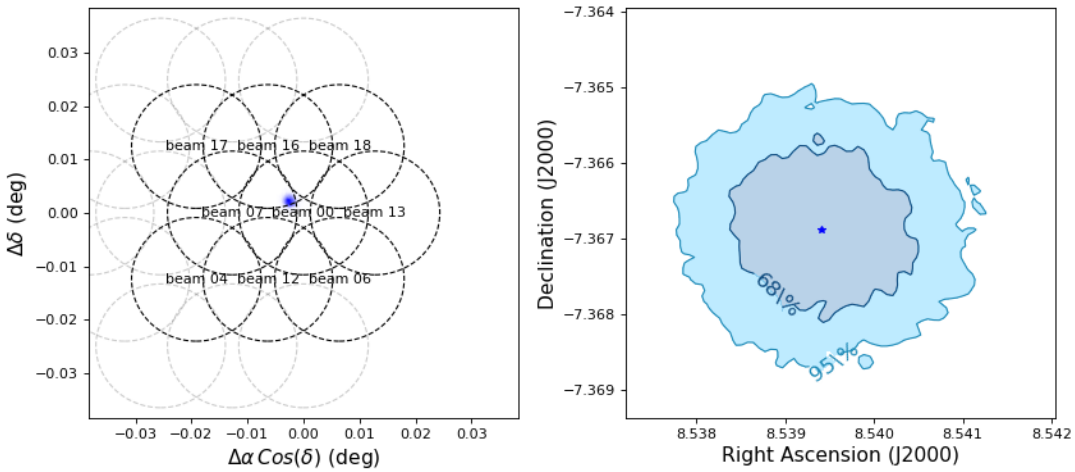

Figure 3.4: The localisation of PSR J0036−1033 (Swainston et al., 2021) in observation 1292933216. The observation is centred at 155 MHz and the tied-array beam has a FWHM of ∼1.26′. The localisation method is as described in Bannister et al. (2017) and estimates the position to within 14″. *Left*: the dashed lines represent the FWHM of each of the tied-array beams. The faint grey dashed lines are beams that are more than a beam width away and therefore not included in the localisation calculation. *Right*: the first (dark blue) and second (light blue) confidence intervals of the localisation.

tigate the offsets that the ionosphere causes. These offsets were calculated by making a grid of pointings around the catalogue positions, as shown in Figure 3.4, and estimating its position based on the measured signal-to-noise ratios. The left plot of Figure 3.5 shows that offsets cause the sources to appear ∼30 ″ away in a single direction that is independent of where they are in the FoV. We, therefore, believe this offset is caused by incorrectly accounting for the bulk offset, which caused a ∼ 40% S/N degradation, as shown in the right plot of 3.5.

We compared this to the theoretical degradation in the signal-to-noise ratio that would arise due to the offsets placing the targets significantly far from the centre of the tied-array beam. The applied beamforming operation (Ord et al., 2019) is equivalent to summing each baseline with equal weighting. In imaging parlance, this is the same as applying a "natural" weighting. We estimated the beam response with the naturally weighted point spread function, generated by

taking the Fourier transform of the projected baselines, which in this case was produced when imaging the data with the WSCLEAN software (Offringa et al., 2014). Taking a 1D (horizontal) cut through the point spread function produces a theoretical sensitivity curve as a function of offset, which is shown in the right plot of Figure 3.5. There is good agreement between the measured and theoretical signal-to-noise ratio degradation, but the slightly steeper slope of the measured points suggests that our beam has more sensitivity close to the centre of the beam, leading to a sharper fall-off.

If such an offset is not corrected for, an observation's duration would have to increase by a factor of $\sim$3 to recover the $\sim$40% loss in sensitivity. Because there are often hundreds of known pulsars in an observation's FoV, it is inefficient to create a grid of tied-array beams around every pulsar to correct for any offsets. Instead, we have developed an efficient method for measuring and correcting for an incorrect bulk offset which is explained in the next section. After correcting the bulk ionospheric offset, the residual ionospheric offsets will remain, which cannot be corrected without direction-dependent calibration on the same field. As the residual offsets are typically $< 10''$ (Jordan et al., 2017), they only cause $< 5\%$ reduction in detection sensitivity, which is factored into our position estimate uncertainties.

3.4.1.1 Correcting for incorrect bulk ionospheric offsets

Any residual bulk ionospheric offsets must be measured and removed to ensure maximum sensitivity and accuracy of pulsar position estimates. To measure the offset, we choose at least three bright pulsars (with a signal-to-noise ratio above 20) within the FoV, and form a grid of pointings around them to estimate each pulsar's apparent position (see Figure 3.4). To ensure that the average of the measured offsets most accurately reflects the bulk offset (instead of a localised ionospheric disturbance), we preferentially choose pulsars that are spread as widely as possible across the FoV. If three suitable pulsars cannot be found

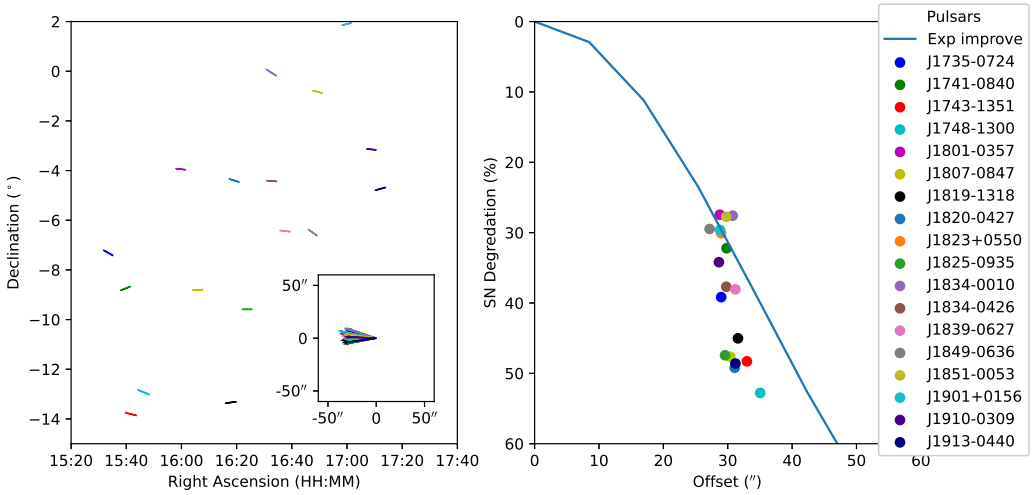

Figure 3.5: The results of position estimation using a grid of pointings around the 18 pulsars in observation 1276619416. *left inset*: The difference between the position estimated using the method shown in Figure 3.4 and the known position from the ATNF pulsar catalogue. *left*: The offsets of each pulsar increased by a factor of 100, so they are visible for each pulsar's position to show that after subtracting the bulk offset, there does not appear to be any obvious correlation between the direction of the residual offsets and sky position. *right*: The degradation in the signal-to-noise ratio (S/N) of the pulsar due to its incorrect position and its total offset. The blue line represents the expected degradation using the naturally weighted point spread function generated by taking the Fourier transform of the projected baselines.

within the FoV, pulsars with a lower S/N can also be used. The offset between the apparent and true pulsar positions is averaged for the three pulsars, and this average becomes our estimate for the bulk offset. This bulk offset is subtracted from the position of subsequent pulsar detections in that observation to derive position estimates.

After removing the bulk offset, the uncertainty of the derived position will be dominated by the residual offsets σ_{R}. Although the bulk offset derived in this way will only be an approximation of the true bulk offset, the uncertainty of the bulk offset σ_{B} will be significantly smaller than the average residual offsets as long as the selected pulsars sample spatially independent ionospheric shifts. However, as noted above, this assumption can fail if the chosen pulsars are too close to each

other on the sky, or if there are large scale spatial structures in the ionosphere across the primary beam. For the purposes of estimating the positional errors, we assume that the measured ionospheric shifts are not biased in this way. Thus, the position uncertainty, σ_{P}, is the quadrature sum of the standard deviation of the magnitudes of the residual offsets, σ_{R}, and the localisation uncertainty σ_{L}:

$$\sigma_{\mathrm{P}} = \sqrt{\sigma_{\mathrm{R}}^2 + \sigma_{\mathrm{L}}^2}. \tag{3.4}$$

3.4.2 Detection of known pulsars within a field-of-view

The MWA has already performed a pulsar census (Xue et al., 2017) using the incoherent beam, which preserves the entire single tile FoV ($\sim$610 deg^2 at 150 MHz) but is a factor of $\sim$10 less sensitive than the tied-array beam. To perform an MWA tied-array beam pulsar census, we must create a tied-array beam on each known pulsar with a dispersion measure below 250 pc cm^{-3} within the field-of-view. Because there are often hundreds of known pulsars in an observation's FoV, we use the bulk offset correction method described in §3.4.1.1 to efficiently ensure the maximum sensitivity.

To demonstrate the effectiveness of the multi-pixel beamformer and the bulk offset correction method, we beamformed on the 256 pulsars in the FoV of observation 1276619416 and detected 18 pulsars (see Figure 3.5). Observation 1276619416 is in Phase II extended array configuration, has a centre frequency of 184.96 MHz and a tied-array beam FWHM of 1.05′. Thanks to the bulk offset correction method, the signal-to-noise ratio of these detections improved by $\sim$30-50%.

The original single-pixel beamformer was then used to reprocess all the pulsar detections in observation 1276619416 to compare the signal-to-noise ratio with the multi-pixel beamformer detections. The difference in signal-to-noise ratio is, on average, less than 1% and is likely due to floating-point rounding errors. These results validate that a multi-pixel beamformer is required to process obser-

vations efficiently and can do so with equal sensitivity to the original single-pixel beamformer.

3.5 Discussion

3.5.1 Survey feasibility

The required GPU time to create tied-array beams for the entire FoV for a 10-minute observation using the Garrawarla, OzSTAR and CSRC supercomputers are shown in Table 3.1. Using OzSTAR benchmarks from Table 3.2 and assuming an average of 16 GPUs are available for our use, we can approximate how much wall time it would take to process each 10-minute observation. This comes to about 14 weeks for the single-pixel beamformer but only 22 days with the multi-pixel beamformer. This equates to 19 years of processing to create the ∼700,000 tied-array beams required to cover the Southern Sky with the single-pixel beamformer but only ∼1.8 years with the multi-pixel beamformer. This enhancement dramatically improves the feasibility of performing a Southern Sky survey with the MWA.

3.5.2 Implications for MWA Phase III and SKA-Low

The Phase II MWA extended array has a maximum baseline of 6 km and a tied-array beam HWHM of $\sim 40''$ (at 155 MHz), which is small enough to be potentially affected by the ionospheric effects described in this paper. The imminent upgrade of the MWA to Phase III will allow all 256 tiles to be correlated and recorded simultaneously. This will include the same 6 km baselines of the Phase II extended array, so all future observations will have to consider minimising or mitigating these ionospheric offsets. The ionospheric residual offsets will begin to cause sensitivity loss for observations below $\sim$ 140 MHz when there is high ionospheric turbulence, as indicated in Figure 3.1.

The stochastic nature of the ionosphere means we cannot predict, even to

first order, how variations will behave over time or in different parts of the sky. The effect this turbulence has on the bulk offset over time was observed in Arora et al. (2015) and shown to change by up to $\sim 0.17'$ (at 150 MHz) in an hour with no observable patterns. How the ionosphere behaves in different parts of the sky and during different parts of the solar cycle has not been studied, but we can assume that there could be variations of $\sim 0.5'$. Since we frequently use calibration observations over 50 degrees away from the target observation, we may be correcting for a different bulk offset. However, we cannot predict which calibration observations will cause an incorrect bulk offset correction as there is no clear correlation with time from observation or distance from the target observation position. For example, one calibration solution obtained from an observation separated by 31 hours yielded no significant bulk offset when applied to the target observation. On the other hand, the example shown in Figure 3.5 uses a calibration observation with in an hour and demonstrates a $\sim 30''$ offset which led to a $\sim 40\%$ reduction in sensitivity. Therefore, using the bulk offset correction method for all observations with calibration solutions more than an hour away is recommended.

This has implications for real-time beamforming systems, which are desirable given the increased data rate of the Phase III high-time resolution (HTR) observing mode. The current VCS delivers (4+4)-bit complex samples for 128 dual-polarisation tiles at a $\sim$ 28 TB/hour data rate. In contrast, Phase III (Wayth et al., 2018) will deliver (8+8)-bit complex samples for 256 tiles, which will quadruple the data rate to $\sim$ 112 TB/hour. This increased data rate will make real-time beamforming more desirable as these tile voltages will not have to be stored or transferred for post-processing. However, these ionospheric offsets are more problematic for real-time beamforming since they cannot be corrected in post-processing.

Besides the MWA, both LOFAR and uGMRT are two other prominent low-frequency facilities that operate in the $\sim$100-200 MHz band (and beyond), with

baselines extending out to ∼10 km or longer. When beamforming, LOFAR uses its core stations primarily situated within a ∼1 km radius, with a maximum baseline of ∼2 km. Phased-array observations with the uGMRT may need to employ antennas located well outside the central square for higher sensitivity. Even though the uGMRT Band 2 (120-240 MHz) is not the most preferred observing band due to RFI considerations, it is still an order of magnitude more sensitive compared to the Phase 3 MWA, provided the signals from far-arm antennas (up to ∼25 km baselines) can be coherently combined. While the sub-array capabilities of the uGMRT can be exploited for mitigating potential ionospheric offsets and the consequent sensitivity degradation, suitable consideration of maximum baselines and the expected ionospheric offsets, can help to make more optimal (effective) use of the full uGMRT for sensitive pulsar observations within its Band 2 range.

Beyond the currently operational low-frequency facilities, the upcoming SKA-Low will also necessarily benefit from such considerations. A significant subset of pulsar science planned with the SKA (in particular those involving timing or single-pulse studies) rely on sub-arraying, and hence involve sub-grouping of stations extending out to baselines of ∼10 km. While the much higher sensitivity offered by SKA-Low will readily allow optimal sub-grouping of stations, considerations along the lines discussed here will likely become important for maximising achievable sensitivity, especially for beamformed observations at frequencies $\lesssim$ 150 MHz. For instance, high-sensitivity observations in this lower SKA-Low band are likely to benefit from sub-grouping of stations within an extent of $\lesssim$ 1-2 km, which may not be possible for stations located in the outer parts of the array. For these outer core stations, suitable sub-grouping within $\lesssim$2-3 km may help mitigate the ionospheric effects, while any sub-grouping involving stations with $\gtrsim$5 km baselines may require mitigation schemes similar to those discussed here, especially given that SKA-Low is to be built at the same site as the MWA, and so ionospheric effects will be quite similar and less than sites like uGMRT

where the TEC fluctuations are known to be more significant due to its proximity to the magnetic equator.

3.6 Summary

The multi-pixel beamformer is a factor ∼10 more efficient than previous MWA beamformer iterations without affecting the sensitivity of pulsar detections. The portability of the software has been proven by installing it on three supercomputers, which can share the processing load of large-scale surveys between multiple institutions. These improvements make it feasible to perform large scale pulsar surveys with the MWA.

We investigated the ionosphere's effect on MWA VCS observations and characterised them as the bulk and residual offsets. The ionospheric residual offsets only affect sensitivity below 140 MHz when the ionosphere is very turbulent. The bulk ionospheric offsets can be as large as $\sim 35''$ and can reduce sensitivity by up to $\sim 50\%$ when the bulk offset differs between the calibration and target observation, as illustrated in Figure 3.5. This bulk offset error can be measured and corrected using the method described in §3.4.1.1. Correcting this bulk offset makes our pulsar candidate position estimates more accurate, and our improved understanding of the ionosphere provides more realistic position uncertainties. Mitigating the ionospheric offsets will become more important for MWA Phase III and should be considered in the design of SKA-Low.

Chapter 4

Discovery of a steep-spectrum low-luminosity pulsar with the Murchison Widefield Array

This chapter describes the first pulsar discovered with the MWA, its follow-up and spectral analysis. This discovery validates the effectiveness of the search pipeline and demonstrates the method for follow-up for MWA discoveries that will provide spectra. This chapter is based on the author's publication Swainston et al. (2021), as per Curtin University's policy. Since the publication of Swainston et al. (2021), the flux density calculation method explained in §2.3.3 has been automated and validated. This has allowed the MWA flux density values to be calculated and incorporated into updated versions of Figure 4.5 and 4.6. The new section §4.5.7 explains the updated variability plot (Figure 4.7) and spectral fit (Figure 4.6) which uses the `pulsar_spectra` fitting software. This update found a consistent spectral index value of $\alpha = -2.2 \pm 0.1$ compared to the original $\alpha = -2.0 \pm 0.2$. It also differs from the original in other minor respects, including the formatting of both the text and the images and the numbering of the equations and figures.

4.1 Abstract

We report the discovery of the first new pulsar with the Murchison Widefield Array (MWA), PSR J0036−1033, a long-period (0.9 s) non-recycled pulsar with a dispersion measure (DM) of 23.123 pc cm^{-3}. It was found after processing only a small fraction (∼1%) of data from an ongoing all-sky pulsar survey. Follow-up observations have been made with the MWA, the upgraded Giant Metrewave Radio Telescope (uGMRT), and the Parkes 64-m telescopes, spanning a frequency range from ∼150 MHz to 4 GHz. The pulsar is relatively faint, with an estimated spectral index $\alpha = -2.2 \pm 0.1$. The DM-derived distance implies that it is also a low-luminosity source (∼ 0.1 mJy kpc^2 at 1400 MHz). The analysis of archival MWA observations reveals that the pulsar's mean flux density varies by up to a factor of ∼5-6 on timescales of several weeks to months, which is possibly due to extrinsic propagation effects. Despite less than a year of timing observations, we have used a combination of MWA and uGMRT data to determine the pulsar's position to a precision of a few arcseconds. We also report on polarization properties detected in the MWA and Parkes bands. The pulsar's non-detection in previous pulsar and continuum imaging surveys, the observed high variability, and its detection from a small fraction of the survey data searched to date, all hint at a larger population of pulsars that await discovery in the southern hemisphere, with the MWA and the future low-frequency Square Kilometre Array.

4.2 Introduction

Scanning large swathes of the sky to discover new pulsars has been an integral part of pulsar astronomy over its history. Over the past decades, multiple surveys that exploited new telescopes and/or instrumentation have led to substantial progress in understanding the pulsar population, and have uncovered a variety of exotic objects including millisecond pulsars (MSPs), sporadic emitters like rotating radio transients (RRATs), and magnetars (e.g. Manchester et al., 2001;

Cordes et al., 2006; Keith et al., 2010). These discoveries have significantly advanced our understanding of the Galactic population of pulsars, besides enabling wide-ranging astrophysical studies using these objects (e.g. Lorimer et al., 2006; Levin et al., 2013).

The advent of next-generation radio telescopes presents new avenues to explore the Universe. With their wide fields of view and software-defined instrumentation, they allow us to consider novel approaches for pulsar surveys, potentially probing hitherto unexplored parts of the pulsar population parameter space. Some of these new telescopes are also important precursors or pathfinders for the upcoming Square Kilometre Array (SKA) telescope, including its low frequency (50−350 MHz) component (SKA-Low).

Over the past decade, the resurgence of low-frequency pulsar astronomy has led to new surveys undertaken by the Low Frequency Array (LOFAR), the Giant Metrewave Radio Telescope (GMRT), the Green Bank Telescope, and the Canadian Hydrogen Intensity Mapping Experiment (Sanidas et al., 2019; Bhattacharyya et al., 2016; Stovall et al., 2014; Good et al., 2021). These searches at frequencies below 400 MHz have already uncovered over 200 new pulsars including the fastest- and slowest-spinning Galactic field pulsars known (Bassa et al., 2017a; Tan et al., 2018a), and have yielded a number of potentially promising pulsars for high-precision timing projects such as pulsar timing arrays. These low-frequency searches appear to be most effective in uncovering more local objects, but they require substantial computational resources to circumvent the large dispersive delays inherent at lower radio frequencies.

Despite its modest sensitivity compared to most northern facilities such as LOFAR, the combination of a large field of view (FoV) and a superb radio-quiet environment makes the Murchison Widefield Array (MWA; Tingay et al., 2013; Wayth et al., 2018) a promising facility to undertake pulsar searches in the southern hemisphere at frequencies below 300 MHz. The original array of 128 tiles with maximum ∼3-km baseline (Phase 1) was upgraded to provide longer

baselines and a flexible reconfiguration arrangement between compact (300 m) and extended arrays (Phase 2).

Although not originally conceived or designed for pulsar science, the development of a voltage capture system (VCS; Tremblay et al., 2015) and associated software instrumentation (Ord et al., 2019; McSweeney et al., 2022) has geared this telescope for useful pulsar work. Over the past few years the MWA has been exploited for wide-ranging pulsar science, from studies of millisecond pulsars to sporadic emission from pulsars, and from investigating the pulsar emission physics to studying propagation effects caused by the interstellar medium (ISM; e.g. Bhat et al., 2016; McSweeney et al., 2022; Meyers et al., 2018; Kaur et al., 2019). This progress on both scientific and technical fronts to date has also paved the way to initiate a large southern-sky survey for pulsars, which will complement ongoing efforts around the world, in both sky and frequency coverage.

Multi-path propagation effects, in particular temporal broadening that becomes highly prominent at low radio frequencies, limit the detectability of short-period and distant pulsars to a few kiloparsecs in the Galactic plane (e.g. Bhat et al., 2004). Despite this, pulsar surveys at low frequencies tend to benefit from inherently larger fields of view (hence increased survey speeds). In addition, pulsars with a steep spectrum ($\lesssim$ -2.0) are often easier to detect at low frequencies despite the sky background often having a steeper spectrum of $\alpha = -2.6$ (e.g. Maron et al., 2000; Jankowski et al., 2018). Moreover, the much larger variability in flux densities expected at low frequencies (on timescales of weeks to months), due to refractive scintillation effects, also increases the chances of benefiting from episodes of potential scintillation brightening, boosting the prospect of detecting relatively faint pulsars that are otherwise below the detection threshold. A better understanding of these spectral and propagation effects may help to ascertain the detectability of pulsars with future large low-frequency facilities such as SKA-Low (Keane et al., 2015b; Xue et al., 2017).

In this paper, we report on the discovery of a new pulsar with the MWA,

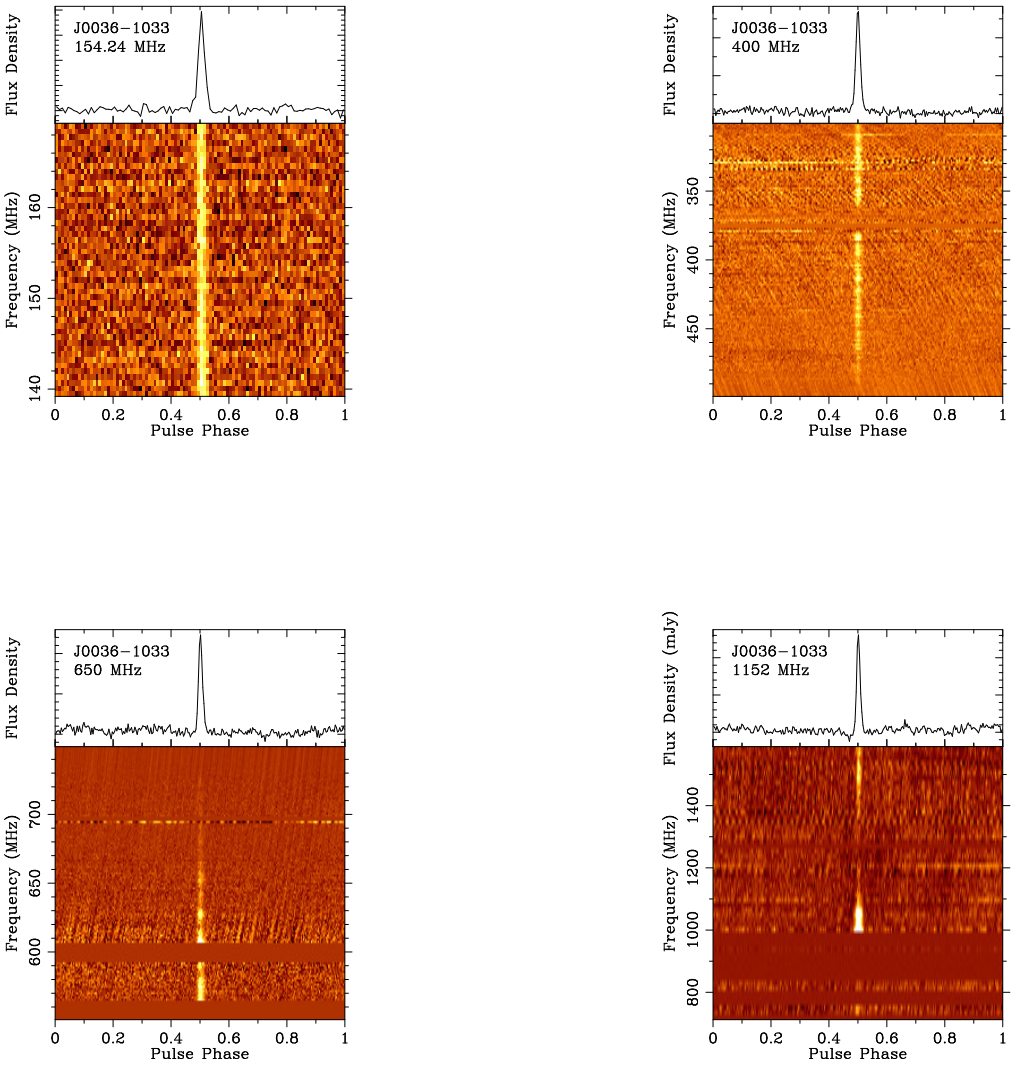

Figure 4.1: Detection plots of PSR J0036−1033 with the MWA (top left panel), uGMRT (top right and bottom left panels) and Parkes (bottom right panel) telescopes, spanning a frequency range from 140 to 1600 MHz: the top panel is the integrated pulse profile and the waterfall plot below shows the pulse strength vs. pulse phase and frequency. MWA observations were made with the Phase 2 compact configuration of the array, whereas those with the uGMRT made use of the 200-MHz mode of phased-array beamformer comprised of 11-13 antennas located within the central square. Parkes observations were made using the ultra-wideband low-frequency receiver (700-4032 MHz), however the pulsar is too weak for a clear detection at $\gtrsim 1.5$ GHz.

PSR J0036−1033, a non-recycled pulsar with a period of 0.9 s and a DM of 23.123 pc cm^{-3}. It was found in the initial processing of a very small fraction (∼1%) of data from an ongoing large survey of the southern hemisphere in the 140-170 MHz band. In § 4.3 and § 4.4, we summarize observational details and data processing related to the discovery and confirmation. Our analysis of the multifrequency data is presented in § 4.5, including evidence that the pulsar is a rare low-luminosity object. In § 4.6, we comment on future prospects for pulsar searches with the MWA and those planned with SKA-Low, and a brief summary of the key results is given in § 4.7.

4.3 The SMART pulsar survey

The combination of the MWA's voltage-capture mode and its recent upgrade, with a compact configuration of 128 tiles within ∼300 metres, allows high-survey-speed pulsar searches of the southern hemisphere at low frequencies. To take advantage of this, an all-sky pulsar search project has been initiated with the eventual goal of surveying the entire sky south of +30° in declination for pulsars in the 140-170 MHz band. This Southern-sky MWA Rapid Two-metre (SMART) pulsar survey is currently in its early stages. It exploits the newly-developed multi-pixel functionality of the MWA's software beamformer, whereby dozens of tied-array beams are formed simultaneously (Swainston et al., 2022a). Further details of the survey design, science goals, observing strategies, and processing pipelines are described in Bhat et al. (2023a).

Considering the substantial processing requirements of searching at the low frequencies of the MWA due to large dispersion delays and the need to form thousands of beams from recorded voltage data survey data processing is being undertaken in multiple stages: in the first pass, 10 minutes of data from each VCS observation (80 minutes) are processed and searched for pulsars, to attain a sensitivity approximately $\sqrt{10/80} \sim 1/3$ of that which would be eventually attainable, a strategy designed to boost the prospects of early discoveries. Each

10-minute observation is processed to generate ∼6300 beams that tessellate the $\sim 500\,\mathrm{deg}^2$ field of view at ∼ 150 MHz. Each tied-array beam (at 100-μs/10-kHz resolutions) is searched out to a DM of 250 $\mathrm{pc\,cm^{-3}}$, in 2358 DM trials, with down sampling by up to a factor of 16 (i.e. time resolution of 0.1 to 1.6 ms). At this stage, our pulsar-detection algorithms are limited to periodicity and single-pulse searches. The search part of the processing chain makes use of the standard suite of tools in the PRESTO software package (Ransom, 2001) and the machine learning classifier that was developed for the LOFAR pulsar survey (Tan et al., 2018b). The calibration performance, data quality, and analysis pipeline are verified via the detection of known pulsars in the field. The software is run on Swinburne's OzSTAR supercomputer.

Telescope/Receiver	Frequency range (MHz)	MJD range	No. of spectral channels	Time resolution (μs)	No. of epochs
MWA VCS	140 - 170	57366 - 59178	3072	100	16
uGMRT Band 3	300 - 500	59158 - 59184	2048	655.36	3
uGMRT Band 4	550 - 750	59159 - 59188	2048	655.36	2
Parkes UWL	704 - 4032	59132 - 59171	3328	256	6

Table 4.1: Summary of follow-up observations

4.4 Discovery and Followup Observations

PSR J0036−1033 is the first new pulsar discovered during our ongoing processing. It has a period of 0.9 s and a DM of 23.123 $\mathrm{pc\,cm^{-3}}$, and was first detected with a signal-to-noise ratio (S/N) ∼ 10-12 in observations taken on MJD 58774. Subsequently the full 80-minute observation (42 TB) was processed and re-searched to yield a much improved detection with S/N ∼36, thereby providing unambiguous initial confirmation of the candidate (Figure 4.1). The fact that the raw voltage data were recorded (instead of the more common filterbank data typically employed in most pulsar searches), along with access to archival VCS data and the suite of available *post hoc* interferometric/tied-array processing options, allowed a multitude of important follow-up analyses to: (1) confirm the discovery;

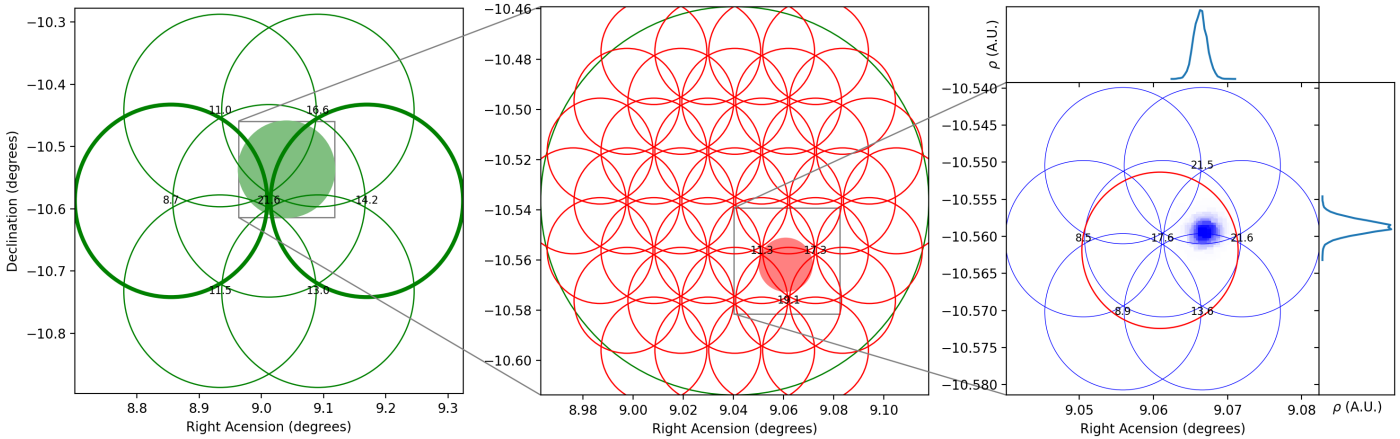

Figure 4.2: Positional determination of the pulsar via tied-array beam localization by re-processing VCS observations. The pulsar was first detected in two compact array beams ($\sim$20$'$; thick green circles), the sky region around which was subsequently covered with a hexagonal grid of beams (thinner green circles). A denser grid was subsequently made with the Phase 1 array beams ($\sim$2$'$; red circles), the best position from which (the red circle on the right panel) was then subjected to a dense hexagonal grid using data from the Phase 2 extended configuration ($\sim$1$'$; blue circles). These latter detections were subjected to the method in Bannister et al. (2017) to derive a probabilistic distribution (the blueish region on the right panel), where the positional uncertainties are $\sim$12$''$, approximately one tenth of the tied-array beam size at 140-170 MHz, with the extended configuration.

(2) obtain a precise sky localization; and (3) undertake initial polarimetric and variability studies of the pulsar. Subsequently, new observations commenced in June 2020 for timing and imaging follow-ups, the analysis and results of which are summarised in the following sections.

4.4.1 Follow-up observations

Besides the MWA, follow-up observations were also made using the uGMRT and Parkes telescopes, the details of which are summarised in Table 4.1. The pulsar was detected at 2-3 epochs, separated by ∼1-3 weeks with both the uGMRT and Parkes, and a total of 16 detections were made with the MWA over a time span of five months.

4.4.1.1 The MWA

Follow-up observations for timing and imaging with the MWA were initiated in June 2020 when the pulsar became a night-time object and the proximity to the Sun was no longer a concern. The MWA operated in the extended configuration from May 2020, and VCS data were recorded with a duration ranging from 20 to 60 minutes. An initial phase-connected timing solution was achieved from the observations taken in June-July 2020, yielding a barycentric period of 0.9000046(5) s (at MJD = 58774) and a marginal (2-σ) estimate for period derivative. Since July 2020, approximately monthly observations have been recorded.

4.4.1.2 The uGMRT

Observations with the upgraded GMRT (uGMRT) were made concurrently in the imaging and phased-array modes, i.e. running the wide-band correlator (Reddy et al., 2017) in conjunction with the phased-array backend that generates beam formed (and channelised) data. These observations were made in both Band 3 (300-500 MHz) and Band 4 (550-750 MHz) of the uGMRT (uGMRT; Gupta et al., 2017). Due to $\sim 1'$ positional uncertainty from the initial localization that

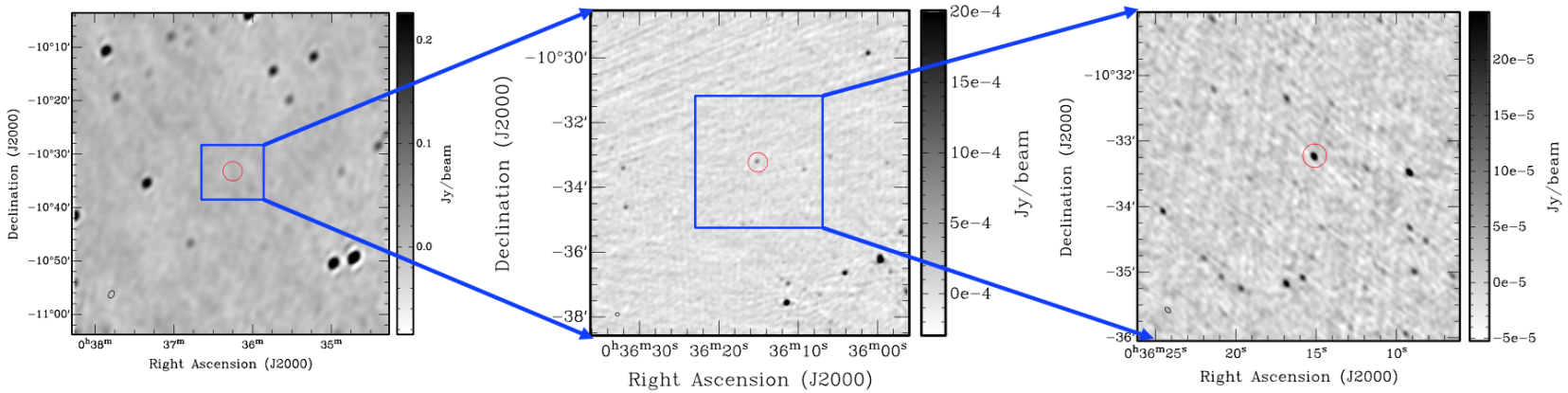

Figure 4.3: *Left:* MWA Stokes I image of the $1 \times 1\,\mathrm{deg}^2$ field (at 154.88 MHz) with the position of the target pulsar in the center (indicated by a circle of the radius ≈5 times the position error of ≈12 arcsec); the rms sensitivity is ≈8 mJy/beam. *Middle:* uGMRT image in Band 3 (300-500 MHz) where the rms sensitivity is ≈156 μJy/beam, yielding a clear ∼6-σ detection of the pulsar. *Right:* uGMRT image in Band 4 (550-750 MHz), where a much higher sensitivity of ≈15 μJy/beam was achieved, resulting in a ∼35-σ detection of the pulsar. The detections in both images are marked by dark circles. The estimated positions have about ∼1 arcsecond uncertainties and they differ by approximately 4 arcseconds, which may arise from residual errors from the ionospheric calibration.

was achieved via MWA tied-array beams (cf. § 4.5.1), two phased-array beams were formed: Beam 1 consisted of antennas located within the central square (typically ∼12), whereas two additional antennas from each of the three arms were added to all working antennas from the central square to form Beam 2. These data were recorded in a traditional filterbank format, generating a 2048-channel spectrum every 655.36 μs. Examples of phased-array beam detections (Bands 3 and 4) are shown in the middle two panels of Figure 4.1. The nearby bright pulsar J0034−0721 was used for testing the setup and phased-array beam sensitivity prior to recording data on the target pulsar.

The visibility data were recorded at the standard 2.68-second resolution. Each observation of the target pulsar was preceded by observations of the phase calibrator 0025−260, which is sufficiently close to the target pulsar and bright enough (S_{325} $\sim$ 20 Jy) to perform bandpass calibration. Prior to starting each cycle of target observation, the array was re-phased, and hence, two observations of the phase calibrator (i.e. immediately preceding and following the scan) were available for calibration purposes. An automated imaging pipeline (Kudale et al. in prep.), composed of flagcal (Chengalur 2013; Prasad & Chengalur, 2012), PyBDSM (Mohan & Rafferty, 2015), and the Common Astronomy Software Applications package (CASA), was used for continuum analysis. In total, three self-calibration and imaging cycles (two phase only, and one amplitude and phase) were carried out. These self-calibrated visibility data were then imaged, in four sub-bands that span the 200-MHz bandwidth, by choosing an appropriate range of channels that span approximately 48 MHz per sub-band.

4.4.1.3 Parkes

Parkes observations used the Medusa backend, in conjunction with the ultra-wideband low-frequency (UWL) receiver, which provides instantaneous radio-frequency coverage from 704 to 4032 MHz (for details, see Hobbs et al., 2020). Data were recorded with 2-bit sampling every 256 μs in each of the 1 MHz wide

frequency channels (3328 channels in total). With the spin period and DM determined by MWA observations, Parkes data were folded using the DSPSR (van Straten & Bailes, 2011) software package with a sub-integration length of 30 s. We manually excised data affected by narrowband and impulsive radio-frequency interference for each subintegration. The best detection from our Parkes observations to date is shown in Figure 4.1. We also observed a pulsed noise signal injected into the signal path before each observation, which provides a reference brightness for each observation and is used to measure the differential gains between the signal paths of the two voltage probes (Hobbs et al., 2020). Polarization and flux density calibration were carried out using PSRCHIVE (Hotan et al., 2004) and followed procedures described in Dai et al. (2020).

4.5 Analysis and Results

4.5.1 Localization

The positional uncertainty of the original detection was $\sim 20'$ (the size of the Phase 2 compact tied-array beam). However, precise localization of the pulsar's position to the level of a few arcseconds (i.e. more than two orders of magnitude improvement) was possible thanks to the subsequent detection of the pulsar in archival MWA data spanning Phase 1, Phase 2 compact, and Phase 2 extended configurations, coupled with the re-processing flexibility afforded by the VCS. The essential methodology is depicted in Figure 4.2, and briefly summarised below. Subsequent resolution of systematic errors present in the MWA localization measurements was achieved via high-resolution imaging of the pulsar field with the uGMRT.

4.5.1.1 Tied-array beamforming with the MWA

Following the original detection using the Phase 2 compact array observations made on MJD 58774, VCS observations containing the pulsar were reprocessed

to make a hexagonal grid of six pointings around the beam in which the pulsar was detected. These detections (corresponding S/Ns) were then used to estimate a maximum likelihood position by assuming Gaussian-shaped beam patterns (with full width at half maximum, FWHM $\sim 19\farcm5$) for the central part of the main lobe of the tied-array beam pattern. An archival VCS observation that covered the pulsar position (on MJD 57406 using the Phase 1 array) was then reprocessed to make a denser grid of three hexagonal rings around the revised position. The resulting detections were then used to obtain a much-improved maximum likelihood position estimate, made possible by the substantially narrower tied-array beams (FWHM $\sim 2\farcm5$). This was then further improved to sub-arcminute precision using new observations taken in the extended configuration, which were processed to make a hexagonal grid of six pointings (Figure 4.2), where tied-array beams are even smaller (FWHM $\sim 1\farcm2$) owing to longer baselines.

These detections were also analyzed using the localization strategy routinely used for initial fast radio burst localization with Australian Square Kilometre Array Pathfinder (Bannister et al., 2017; Shannon et al., 2018), to obtain a more robust position, where statistical uncertainties are $\sim 12''$ (in both RA and DEC). For this final step, we employed a more accurate beam size, based on the point spread function obtained from imaging of the corresponding VCS data. The best position from MWA data (J2000) was RA = 00:36:16, DEC = −10:33:32. However, applying this method to multiple observations revealed a positional wandering of $\sim$ 30-40$''$, which was confirmed via astrometric verification of known pulsars and continuum sources in the field, and is possibly due to a combination of ionospheric and calibration effects. Accurate localization was ultimately achieved via uGMRT high-resolution imaging.

4.5.1.2 High-resolution imaging with the uGMRT

Following the initial localization via the MWA tied-array beam processing, sensitive high-resolution imaging analysis was undertaken with uGMRT Band 3 and

Band 4 observations. Images of the fields around the pulsar position are shown in Figure 4.3, where $\sim 8' \times 8'$ and $\sim 5' \times 5'$ regions around the pulsar position are shown. With $\sim$ 25-km maximum baselines, the size of the PSF is approximately $10''$ and $5''$ respectively in Bands 3 and 4, thus enabling high-resolution imaging of the field. The high sensitivity of the uGMRT enabled sub-band imaging (wherein the 200 MHz observing band was split into 4×50 MHz chunks). The rms varied from $\sim$71 to 223 μJy/beam across Band 3, while Band 4 imaging reached a much lower rms of $\sim$40 to 65 μJy/beam. The best image (from Band 4 imaging on 4 December 2020) reached an rms of $\sim$15 μJy/beam at 650 MHz, resulting in a high-fidelity image of the field and a $\sim$35-σ detection of the pulsar. The resultant positions are: RA = 00:36:15.15 and DEC = $-$10:33:11.9 (Band 3), and RA = 00:36:14.97 and DEC = $-$10:33:16.02 (Band 4), with uncertainties $\sim 0.5''$ and $\sim 0.1''$ in Bands 3 and 4, respectively. The $\approx 4''$ discrepancy in the positions can be attributed to residual errors from ionospheric calibration, which impacts Band 3 calibration more, and we therefore quote a mean position with $\sim 5''$ uncertainties, i.e. RA = 00:36:15.1, DEC = $-$10:33:14, which correspond to Galactic coordinates $l = 112.3°$ and $b = -72.9°$.

4.5.2 Imaging with the MWA

The recorded VCS data can also be correlated offline and imaged. Co-adding the initial two $\sim$20-30 minute observations achieved only a sensitivity of $\sim$6-8 mJy/beam for Stokes I, yielding a non-detection of any source near the expected position. Later co-adding a further four more observations yielded only a marginal improvement in sensitivity. There appears to be a tantalising source near the uGMRT localised position (Figure 4.3), with a flux density $\sim$16 mJy, however the significance is too low ($\sim 2\sigma$) to claim a confident positive detection.

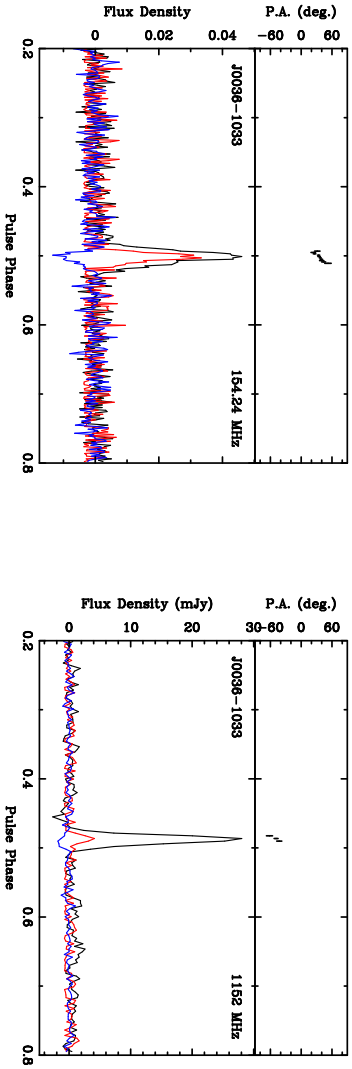

Figure 4.4: Polarimetric profiles of PSR J0036−1033 at MWA 155 MHz (left) and at Parkes 1.1 GHz (right). The black, red, and blue curves in the lower panels show the total intensity, linear, and circular polarization respectively. An analysis of the PA curve (MWA) yields $d\psi/d\phi = \sin\alpha/\sin\beta = 3.8$, constraints that are limited by the data quality and time resolution. The pulsar is weakly polarized at the higher frequency; our analysis (using the RM synthesis technique) yields RM $= -8.1 \pm 0.7$ rad m^{-2} (from MWA observations). Absolute flux density calibration is not possible for MWA data, where the flux density scale is in arbitrary units.

Parameter	Value
Right ascension (J2000)	$00^h36^m15^s.01(4)$
Declination (J2000)	$-10^o33'14''.2(9)$
Galactic longitude (l)	112.3°
Galactic latitude (b)	-72.9°
Epoch (MJD)	58774
Spin period (P)	$0.900009289(3)\,\mathrm{s}$
Period derivative ($\dot{P}$)	$2.131(3) \times 10^{-16}\,\mathrm{s\,s^{-1}}$
Dispersion measure (DM)	$23.1 \pm 0.2\,\mathrm{pc\,cm^{-3}}$
Flux density at 400 MHz	1 mJy
Rotation measure (RM)	$-8.1 \pm 0.7\,\mathrm{rad\ m^{-2}}$
Surface magnetic field (B)	$4.4 \times 10^{11}\,\mathrm{G}$
Characteristic age (τ_c)	67 Myr

Table 4.2: Parameter Summary of PSR J0036−1033

4.5.3 Timing

Timing analysis of recent data (MJD = 59000 - 59150) yielded an initial solution for the basic parameters, i.e. the spin frequency and its first derivative, which were subsequently refined with the addition of times of arrival from past observations (Fig. 4.5). We used the GMRT-determined position as an initial estimate, and then progressively improved the timing solution, with the gradual addition of data from the past years. The timing solution from this 5-yr time span is in Table 4.2. An inferred magnetic field of $B \sim 4.4 \times 10^{11}\,\mathrm{G}$ and a characteristic age, $\tau_c \sim 67\,\mathrm{Myr}$ confirms that it is a nonrecycled pulsar.

4.5.4 Polarimetry

Polarimetric data were available for both the MWA and Parkes observations. The beamformed MWA data were obtained by the system described in Ord et al. (2019) and Xue et al. (2019). The Faraday rotation measure synthesis technique (Brentjens & de Bruyn, 2005) was applied to one of the brightest MWA (MJD 58774.6) detections, yielding an estimated rotation measure (RM) of $-8.1 \pm 0.7\,\mathrm{rad\ m^{-2}}$.

After correcting for Faraday rotation, linear and circular polarization was detected, with the fractional polarization being higher at the lower frequency (Figure 4.4). The Parkes system, which employs noise diodes for polarimetric calibration, has been well tested and verified to yield accurate measurements (e.g. Hobbs et al., 2020). The qualitative agreement between the profiles at the two frequencies (the slope of the position angle, PA, and the sign of the circular) indicates that the MWA polarimetric profiles are at least approximately correct (see Xue, 2019), while the decrease in the fractional linear polarization at higher frequencies is a common feature of pulsar emission (Manchester et al., 1973).

We attempted to fit the rotating vector model (Radhakrishnan & Cooke, 1969) to the PA of the linear polarization across the on-pulse window, in order to constrain the viewing geometry, (α, β), where α is the angle between the magnetic and rotation axes and β is the impact angle of the magnetic axis on the line of sight. In the absence of relativistic effects, the PA curve is expected to be steepest in the centre of the pulse profile, with slope $d\psi/d\phi = \sin\alpha/\sin\beta$, where ψ is the PA at phase ϕ. Across all observations for which there was sufficiently high S/N, the measured slope was consistent with a value of $d\psi/d\phi \sim 3.8\,^\circ/^\circ$. Further constraints on the viewing geometry by this method are unlikely unless the PA can be measured over a wider range of phases (for example, if a broader profile is measured at even lower frequencies).

4.5.5 Archival detections

The fortuitous availability of multiple archival VCS observations that covered the pulsar position and the MWA's operational strategy to archive VCS data for future processing have also enabled multiple (∼10) re-detections of the pulsar in archival data. Many of these are a result of coincidental proximity to the well-known sub-pulse drifting pulsar J0034−0721, which has been the subject of a recent study using the MWA (Mcsweeney et al., 2017; McSweeney et al., 2019). A few observations were made with the original Phase 1 array, most

with the compact Phase 2 array and just one with the extended (Phase 2) array. The amount of time for which J0036−1033 was in the primary beam for these observations varied from ∼10 to ∼80 minutes, and the pulsar position offset from the primary beam centre from ∼3° to ∼12°. The data were processed to generate tied-array beams at the best-determined position as described in § 4.5.1, resulting in positive detections of the pulsar in nearly all observations. Almost all these detections have S/N ∼10-20, which makes the discovery observation (on MJD 58774), where S/N exceeded ∼30, an exceptional one. Nearly half of these detections were at ∼8-10° offset from the primary beam center, i.e. near half power points of the primary beam, thus incurring a loss of S/N by a factor of two.

A summary of these detections is shown in Figure 4.5, along with those from new observations made with the extended configuration in which the MWA has been operating since May 2020. The flux density values were calculated for each detection using the method described in §2.3.3. As evident from the figure, the pulsar displays significant variability by a factor as much as ∼5-6 over a ∼4 yr time span, further discussion of which is deferred to § 4.6.

4.5.6 Flux densities and spectral index

The spectral index α, defined as $S \propto \nu^{\alpha}$, where S denotes the flux density at frequency ν, is estimated from MWA, uGMRT and Parkes measurements that span a frequency range from ∼150 to 1500 MHz. For uGMRT data, $S(\nu)$ was estimated by fitting a 2D Gaussian to the pulsar image using the `imfit` task in CASA, and the uncertainties were estimated as the rms near the pulsar location using the `imstat` task in CASA. For Parkes data, observations of Hydra A, along with those of the pulsed noise signal, were used to derive flux density scales, using the procedure described in Dai et al. (2020).

Figure 4.6 shows a summary of the related measurements and analysis. For the uGMRT bands, which span 300-750 MHz, two independent observations sep-

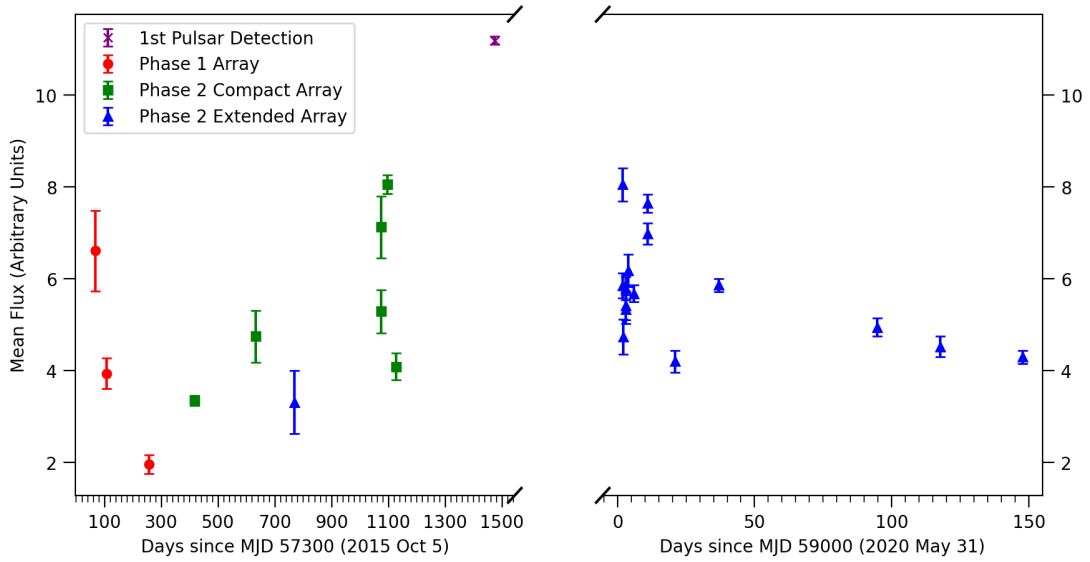

Figure 4.5: Variability in mean flux density of PSR J0036−1033, over a 4-year time span. No absolute flux calibration was attempted, so the reported intensities are given in normalised units. The quantity plotted is indicative of the mean flux density of the pulsar, after applying corrections for the primary beam, and normalised to the zenith gain, and fixed integration (20 min) and 30 MHz bandwidth. The data shown on the left are from archival observations dating back to 2016, whereas those on the right segment are from new observations made (since June 2020) with the extended configuration of the array.

arated by ∼3 weeks were used, thus providing reasonable values for mean flux densities that account for variability arising from scintillation effects. Parkes detections are however from observations separated by a few days, where the main source of uncertainty is the substantial spectral modulation seen in one of our observations (Figure 4.1). Furthermore, with the large fractional bandwidths (50% in uGMRT Band 3, 30% in Band 4, and 70% in Parkes UWL), we are able to make multiple measurements within each of the bands, which were split into a suitable number of sub-bands based on the expected values for the scintillation bandwidth ($\nu_{\rm d}$).

The estimates of $\nu_{\rm d}$ are ∼10 kHz in the MWA band (150 MHz), and ∼0.5 MHz and ∼7 MHz, respectively, in the uGMRT bands centred at 400 and 650 MHz, whereas a much larger value of ∼110 MHz may be expected at Parkes ∼1.2 GHz. Since the pulsar is too weak for scintillation analysis, these are first order estimates based on our MWA observations of PSR J0437−4715 (Bhat et al., 2018), a relatively high Galactic latitude pulsar with a low DM (2.65 $\rm pc\,cm^{-3}$), and assuming the theoretical scaling in DM for the scintillation bandwidth ($\nu_{\rm d} \propto {\rm DM}^{-2.2}$; Cordes et al., 1985). We therefore split the uGMRT 200 MHz range into 4×50 MHz sub-bands, whereas the Parkes band was split up into three uneven bands of 200, 300 and 400 MHz to cover the 900 MHz range (700-1600 MHz) in which the pulsar detection was made. Clearly, relatively smaller values of $\nu_{\rm d}$ (and hence several too many scintles) mean short-term (diffractive) scintillation effects are sufficiently averaged over in both the uGMRT bands, albeit to a lesser extent in the Parkes band. Within the constraints and quality of these measurements, we estimate a spectral index of $\alpha = -2.2 \pm 0.1$ (see Figure 4.6).

4.5.7 Updated MWA flux density results

Since the publication of Swainston et al. (2021), the flux density calculation method developed by Meyers et al. (2017) (see §2.3.3 for explanation) has been automated and validated. This allowed the MWA detections shown in Figure 4.5

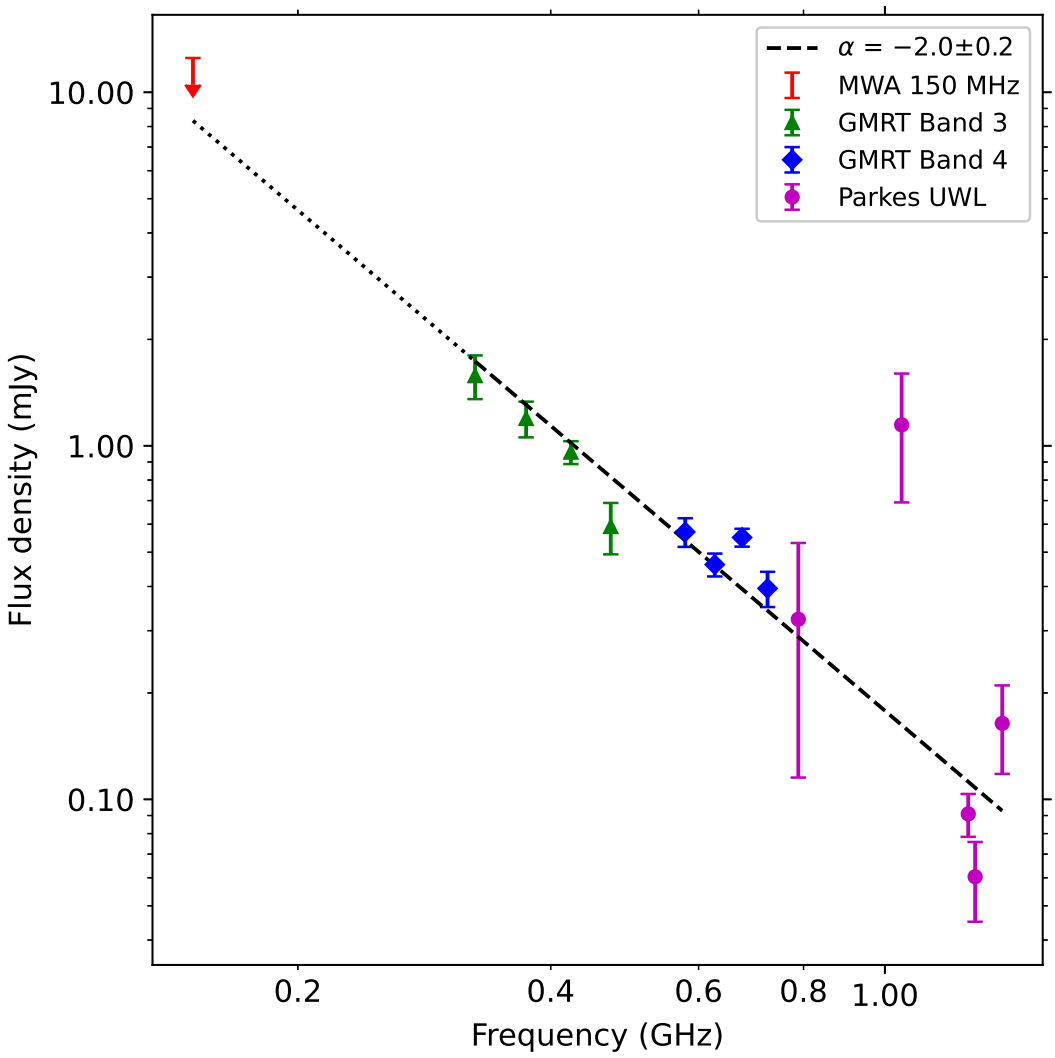

Figure 4.6: Flux density measurements of PSR J0036−1033 over a decadal frequency range from ∼150 to ∼1500 MHz. For uGMRT measurements (300-750 MHz) the uncertainties are dominated by variability between the observing epochs, whereas for Parkes the dominant source of uncertainty is the large spectral modulation seen across the 900 MHz band. A weighted least squares fit yields $\alpha = -2.0 \pm 0.2$. Excluding the apparent outlier measurement at 1.1 GHz (where the pulsar was unusually bright; cf. Fig. 4.1) makes negligible difference to the fit. No detection was made in continuum imaging with the MWA, however the resultant limit is consistent with the estimated spectral slope.

to be reprocessed to provide accurate flux density values. The MWA detections were made with 22 and 3 tied-array beam observations at centre frequencies of 154.24 and 184.96 MHz, respectively, thus providing sufficient observations to account for scintillation variability.

The variability plot (Figure 4.5) has been updated to use the more accurate flux density measurements, as shown in Figure 4.7. It can now be seen that the original detection ("1st Pulsar Detection") was the second brightest detection of PSR J0036−1033, instead of the brightest. This shows that, due to the complexity of the MWA beam, the flux density estimates can't be easily normalised.

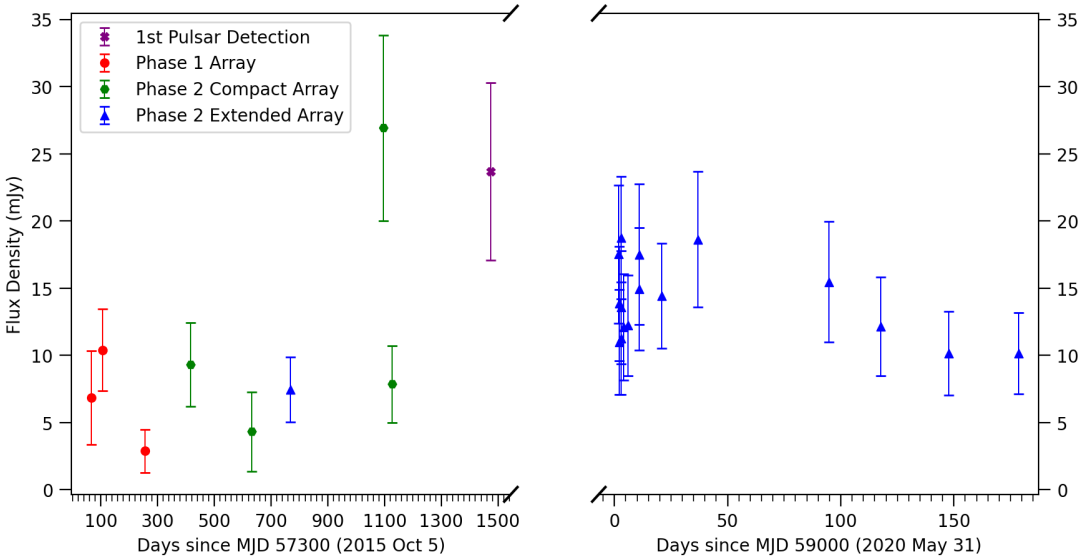

Figure 4.7: Variability in mean flux density of PSR J0036−1033, over a 4-year time span. The data shown on the left are from archival observations dating back to 2016, whereas those on the right segment are from new observations made (since June 2020) with the extended configuration of the array.

The average of the MWA flux density measurements was used to refit the pulsar spectra with the `pulsar_spectra` software suite, see Figure 4.8. The spectral fit uses a more robust method than the weighted least squares fit in Figure 4.6, which includes the integration of the model over the bandwidth of each flux density measurement, see Chapter 5 for an explanation. The updated spectral fit found a steeper spectral index of $\alpha = -2.2 \pm 0.1$ compared to the

original estimate of $\alpha = -2.0 \pm 0.2$.

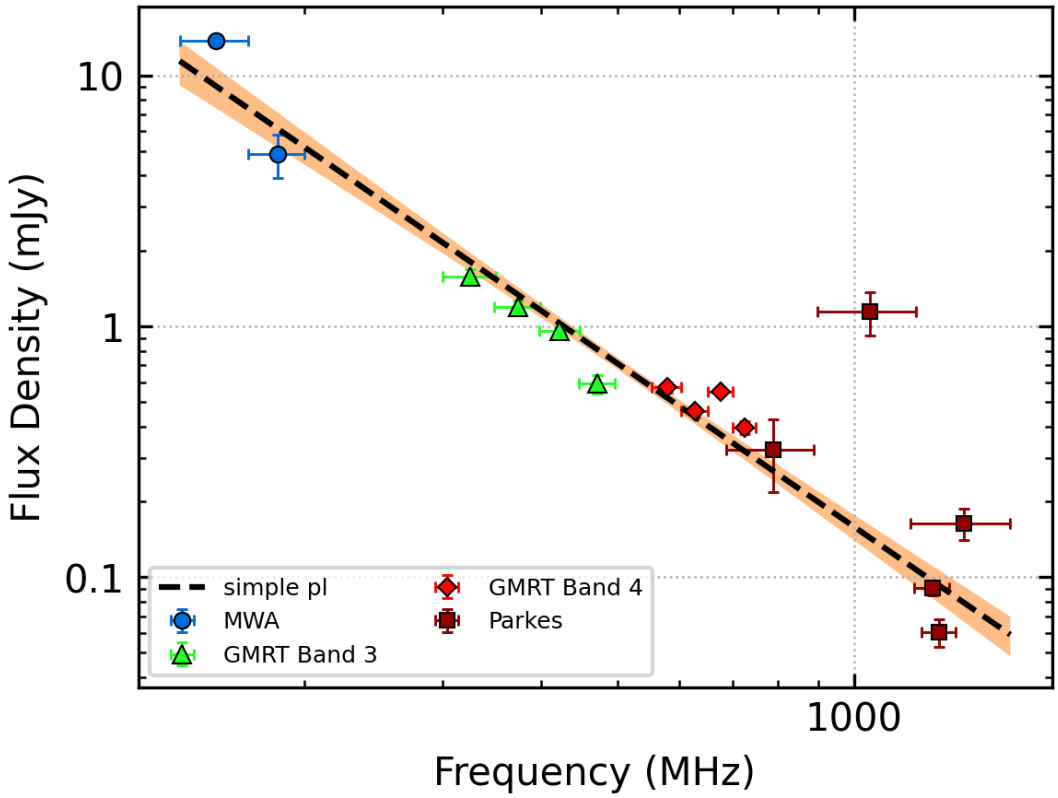

Figure 4.8: Updated spectral fit (compared to Figure 4.6) of PSR J0036−1033 which now includes the flux density measurements from MWA detections. The spectral fit was performed with the `pulsar_spectra` software (see Chapter 5), which found a simple power law spectrum with a spectral index of $\alpha = -2.2 \pm 0.1$ to be the best fit.

4.6 Discussion

A striking aspect of the new pulsar is the indication of a spectrum steeper than most long-period pulsars (Figure 4.8), consistent with the average spectral index of 21 pulsars discovered with LOFAR (Tan et al., 2020). However, in light of the substantial variability observed for this pulsar (Figure 4.7), it is possible that our current estimates of mean flux densities, and hence the spectral index, may depart from their true values.

The spectral fit (Figure 4.8), coupled with a distance estimate of 1.06 kpc (based on the NE2001 model; Cordes & Lazio, 2002)[1], implies a luminosity L_{1400} $\sim$0.1 mJy kpc^2 at 1400 MHz. With only $\sim$40 pulsars (out of 2900) known with L_{1400} below this value, this places J0036−1033 in the lowermost $\sim$2% of the currently known population of long-period pulsars.

The steep spectrum and low luminosity, along with the pulsar's intrinsic variability, likely prevented the detection of the pulsar in previous pulsar and continuum imaging surveys. The pulsar was well below the limiting sensitivities of both the Parkes high time resolution universe survey ($\sim 0.3 - 0.6$ mJy at 1400 MHz; Keith et al., 2010) and the Parkes southern pulsar survey ($\sim$ 3 mJy at 430 MHz; Manchester et al., 1996), towards high Galactic latitudes. The pulsar was also not detected in the TIFR GMRT Sky Survey (Intema et al., 2017) that scanned the entire sky at declination $\delta > -53^\circ$ at 150 MHz, down to a sensitivity of $\sim$2-3 mJy/beam, i.e. over an order-of-magnitude deeper than the MWA GLEAM survey (Hurley-Walker et al., 2017). On the other hand, the original MWA discovery was likely facilitated by the pulsar's high variability. As evident in Figure 4.7, the pulsar was several times brighter than its average when the first detection was made on MJD 58774, with S/N $\sim$10 in the initial search. The detection is thus an excellent demonstration of the efficacy of surveying at low radio frequencies using overlapping observations, separated by more than the refractive scintillation timescale, where scintillation brightening can potentially result in the detectability of objects that are otherwise well below the sensitivity limits of searches.

As such, this discovery heralds a potentially rich harvest of new pulsar discoveries to be made in the remaining shallow pass of the SMART survey, as well as the planned deep survey. To estimate this yield, we have attempted first-order simulations of the survey, using the formalism outlined in Xue et al. (2017), based on the simulation software `PsrPopPy` (Bates et al., 2014b). With the caveat that

[1]The YMW16 model (Yao et al., 2017) is unable to constrain the pulsar distance, as DM saturates at 20.36 pc cm^{-3} toward the pulsar's line of sight ($b = -72.9^\circ$).

our understanding of the pulsar luminosity function and beaming fraction is limited, we project the deep survey to reach a limiting sensitivity of ∼2-3 mJy, with a potential net yield of 310 ± 100 new pulsars. This projection applies to the population of long-period pulsars and does not account for other classes of pulsars such as sporadic emitters (e.g. RRATs), or millisecond and binary pulsars, whose populations are hard to model or simulate. Indeed, the detection of millisecond and binary classes also require high-sensitivity and acceleration searches, which are currently outside the scope of our initial processing.

Assuming an isotropic distribution of our simulated local pulsar population (DM$\lesssim 250$ pc cm^{-3}), and scaling for the current search sensitivity (one-third of the full search sensitivity) and the sky coverage of observations searched to date (∼5% of the sky visible to the MWA), we expect ∼1-2 pulsars from this initial shallow search. The detection of one new pulsar is thus in line with this general expectation. While this may seem fortuitous, we argue that the unique advantages of an MWA pulsar survey, especially from a southern hemisphere, radio-quiet environment, along with our survey parameters (e.g. long dwell times), offer excellent prospects of new pulsar discoveries, despite the MWA's modest sensitivity and substantial processing challenges.

The analysis presented in this paper also demonstrates several benefits of our pulsar survey. The most distinct feature of the SMART pulsar survey, details of which are presented in Bhat et al. (2023a), is the use of the VCS, which records the raw voltage data from individual tiles. While such a strategy poses considerable computational challenges and overheads, it also offers several unique benefits; most notably, the flexibility to reprocess the full observation to confirm the candidate, perform an initial polarimetric analysis, and re-detect the pulsar in archival observations spanning several years, as far back as 2016, when early science was undertaken using the VCS capability. Without this latter ability, the highly variable nature of the pulsar, on timescales of several weeks to months, would not have been apparent.

Furthermore, access to data from all three different array configurations of the MWA (i.e. Phase 1, Phase 2 compact and Phase 2 extended) has allowed us to attain a progressively improved localization, from an initial $\sim 20'$ (the size of the tied-array beam with the compact configuration) to $\sim 10''$ (using the extended array for re-gridding and beamforming), more than two orders of magnitude improvement. This enabled detailed follow-ups with more sensitive telescopes such as uGMRT and Parkes at higher frequencies, which in turn helped establish the steep-spectrum, low-luminosity nature of the pulsar. It also highlights the fact that even telescopes of modest sensitivity (such as the MWA) can be meaningfully leveraged with more sensitive facilities with common sky visibility, for pulsar searching applications. Since the MWA is also a precursor for SKA-Low, this also demonstrates the excellent prospects of using SKA1-Low in conjunction with SKA1-Mid or other sensitive high-frequency telescopes in order to undertake detailed follow-up studies of new pulsar discoveries that are forecast at the low frequencies of SKA-Low.

4.7 Summary and Conclusions

With the discovery of a new pulsar, PSR J0036−1033, from searching a mere ∼1% of the survey data collected to date (i.e. effectively ∼0.5% of the search volume accessible with the current sensitivity of the MWA), we have demonstrated both the efficacy and relevance of low-frequency pulsar searches in the southern hemisphere. This marks an important milestone for pulsar searches with the MWA, notwithstanding its modest sensitivity and numerous processing and data management challenges that arise from non-traditional pulsar instrumentation. The pulsar is seemingly unremarkable in terms of its profile and emission characteristics, but appears have a relatively steep spectrum ($\alpha \approx -2.2$) and low luminosity ($L_{1400} \sim 0.1\,\mathrm{mJy\ kpc^2}$), and exhibits substantial variability in flux density. It reaffirms the importance of low-frequency pulsar surveys for probing the low-luminosity population of pulsars, whereas a non-detection in previous continuum

imaging and pulsar surveys underscores the benefits of exploring new parameter space as well as opportunistic discoveries facilitated by favourable episodes of scintillation brightening.

The pulsar was promptly followed up with more sensitive telescopes such as the uGMRT and Parkes, besides the MWA. This demonstrates how instruments with common-sky visibilities can be fruitfully leveraged for detailed characterization of new pulsars, including improved positional determination and broadband high-frequency follow-ups. For the first time, the archival voltage (VCS) data from the MWA was extensively exploited for confirmation and localization of a new pulsar, and to investigate its time variability. A notable highlight is the progression from initial $\sim 20'$ uncertainty in sky localization to $\sim 10''$ through suitable reprocessing of archival data, and eventually to a few arcsecond precision via high-resolution imaging with the uGMRT. This may also potentially facilitate a faster convergence to its full coherent timing solution, observations for which are currently underway at MWA and Parkes. This discovery also hints at a promising future for pulsar searches with the MWA, as the processing pipelines mature over time, and a potential niche for future low-frequency pulsar surveys planned with SKA-Low.

Chapter 5

pulsar_spectra: A pulsar flux density catalogue and spectrum fitting repository

This chapter describes pulsar_spectra, a centralised repository for pulsar flux density measurements and spectral fitting. This chapter is a faithful reproduction of the author's publication Swainston et al. (2022b), as per Curtin University's policy. Since the publication of Swainston et al. (2022b) the fitting method of pulsar_spectra has been further improved. To describe these improvements, two new sections have been added to this chapter, §5.4.1.6, which describes the new double turn-over spectrum model, and §5.4.2, which describes the new bandwidth integration method. Figure 5.1, Figure 5.2 and Listing 5.1 have also been updated to reflect the new model and method. It also differs from the original in other minor respects, including the formatting of both the text and the images and the numbering of the equations and figures.

5.1 Abstract

We present the pulsar_spectra software repository, an open-source pulsar flux density catalogue and automated spectral fitting software that finds the best spectral model and produces publication-quality plots. The PYTHON-based software includes features that enable users in the astronomical community to add newly published spectral measurements to the catalogue as they become available. The spectral fitting software is an implementation of the method described in Jankowski et al. (2018) which uses robust statistical methods to decide on the best-fitting model for individual pulsar spectra. pulsar_spectra is motivated by the need for a centralised repository for pulsar flux density measurements to make published measurements more accessible to the astronomical community and provide a suite of tools for measuring spectra.

5.2 Introduction

Although pulsars were discovered in 1967 (Hewish et al., 1968), the exact mechanism by which they emit electromagnetic radiation is far from being understood. The pulsar emission mechanism is often described using models that include a plasma-filled magnetosphere that co-rotates with the pulsar (Goldreich & Julian, 1969). However, an emission mechanism that can successfully explain all pulsar emission characteristics, including spectral turn-over and nulling, has not yet been advanced. Radio spectra of pulsars provide important clues, but accurate spectral data are lacking for the majority of pulsars.

Measurements of flux densities are important for inferring pulsar radio luminosities and energetics, as well as for detailed spectral analysis. However, producing accurate pulsar flux densities is challenging for several reasons. Firstly, pulsars scintillate due to the interstellar medium (see §1.4.3); long-term fluctuations due to refractive scintillation can give rise to apparent flux density changes of a factor of ∼2-3 or more depending on their Galactic latitude and the choice of

instrumental parameters (e.g. observing bandwidth and time duration), on time scales up to weeks and months (e.g. Swainston et al., 2021; Bhat et al., 2018; Bell et al., 2016). Obtaining flux measurements, therefore, requires observing campaigns much longer than the scintillation time scale. Secondly, flux density measurements require extensive knowledge of the telescope to account for antenna temperature, beam shape, etc. Furthermore, in the case of pulsars with severely broadened pulse profiles (due to temporal broadening resulting from multipath scattering), reliable measurements may require imaging rather than time-domain techniques. Despite these difficulties, many accurate flux density measurements have been taken over the last several decades (e.g. Izvekova et al., 1981; Taylor et al., 1993; Lorimer et al., 1995; Malofeev et al., 2000; Hobbs et al., 2004b; Bilous et al., 2016; Han et al., 2016b; Johnston & Kerr, 2018; Jankowski et al., 2019; Sanidas et al., 2019). However, there is currently no catalogue designed to record pulsar flux density measurements at arbitrary frequencies. Researchers are obliged to do extensive literature reviews, find the publications that contain flux density measurements of pulsars they are interested in and extract the information from them. This exercise is a time-consuming task that is prone to error.

There is no complete theoretical model for pulsar spectra. For this reason, we use several empirical models as no single model can accurately fit the variety of pulsars' spectra. Deciding which models to use and which is best for each pulsar requires sophisticated statistical techniques. Jankowski et al. (2018) has detailed a method for deciding on the best model using the Akaike information criterion (AIC), which measures the information each model retains without overfitting. This is applied to various spectral models used throughout the literature (see §5.4.1). Their choice of method and implementation can result in different results compared to other researchers with the same data.

We have implemented the methodology of Jankowski et al. (2018) in `pulsar_spectra`[1],

[1] https://github.com/NickSwainston/pulsar_spectra

a fully-featured spectral fitting PYTHON software package. It includes all five models listed above and can be easily extended to include others. pulsar_spectra also contains a catalogue of flux density measurements from several publications. pulsar_spectra is open-source; researchers can upload measurements from new publications into the catalogue, which are then available to all. The software has already been used in Lee et al. (2022).

The remainder of this paper is organised as follows. We will first explain the implementation of the catalogue and its benefits in §5.3. Then in §5.4, we discuss the method used to determine the best spectral fit. Finally, in §5.5 we demonstrate how to use the software.

5.3 Catalogue

There is currently no pulsar catalogue exclusively for flux density measurements. The ATNF pulsar catalogue (version v1.67; Manchester et al., 2005) does maintain a large collection of published flux densities, but the frequency at which they are measured is not always accurate. Flux densities measured at frequencies other than a set of pre-selected frequencies (currently 26, ranging from 30 MHz to 150 GHz) are typically recorded at the nearest listed frequency, which can lead to inaccurate spectral fits if the frequency and flux density values in the catalogue are taken at face value. Moreover, the catalogue's design prohibits multiple measurements at the same or similar frequencies, with only the most recent measurement recorded at any given (approximate) frequency.

Researchers are currently obliged to conduct their own extensive literature reviews to find the publications that contain flux density measurements of pulsars they are interested in and extract the relevant information from them. This is a time-consuming task and, because there is no central place to store this information, it is duplicated effort by each researcher.

To allow researchers to acquire accurate flux density measurements with minimal effort, we have created an open-source catalogue within pulsar_spectra.

The catalogue consists of dictionaries in the form of a YAML file for each included publication. These YAML files contain all the flux density measurements and their uncertainty in mJy and their frequencies in MHz for each pulsar. If the original authors gave no flux density uncertainty, we assumed a conservative relative uncertainty of 50%, following earlier work (Sieber, 1973; Jankowski et al., 2018). This catalogue can easily be collected using a PYTHON function and combined with new results to produce a pulsar spectral fit (as demonstrated in §5.5).

When using the flux density values from the ATNF to fit a pulsar, most researchers know that the values are inaccurate due to the select frequencies of the ATNF (see the left plots in Figure 5.1). They would then extract the publications' true flux density and frequency values to create a more accurate fit. With `pulsar_spectra` this is rarely required as our catalogue can use any frequency value (see the right plots in Figure 5.1). This frequency flexibility also allows us to include papers, such as Murphy et al. (2017) and Johnston et al. (2006), which have flux density measurements at many frequencies. The four pulsars in Figure 5.1 are examples of a different and more accurate fit using `pulsar_spectra` without manually extracting values from the publications.

5.3.1 Currently included and future publications

The catalogue is designed to be a community-maintained, open-source catalogue that prevents duplicated effort. We have currently added 34 publications to the database, which are shown in Table 5.1. This is not a complete list of pulsar flux density publications and is likely to favour Southern-sky (declination $\delta < 0$) pulsars. As researchers use this catalogue, they can add new flux density measurements (or historical ones that are not already included), which can then be made available for other researchers.

To make it easier for other researchers to include new publications in the catalogue, we have created a script to convert a simple CSV into the required

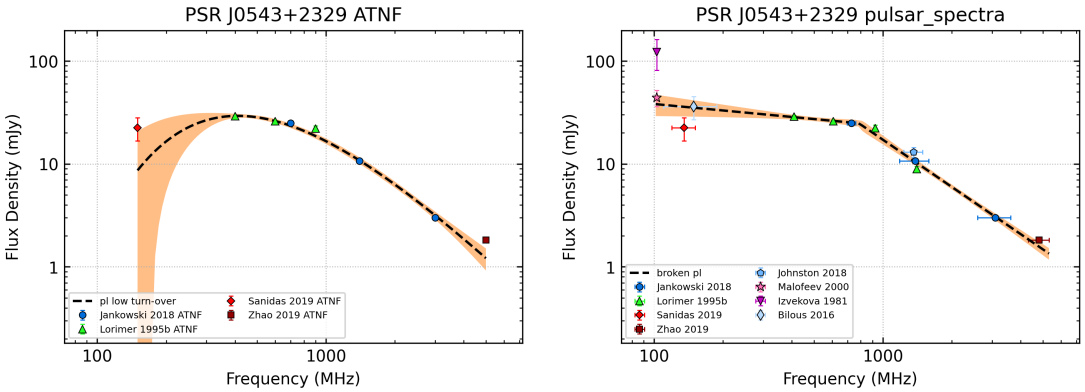

(a) J0543+2329

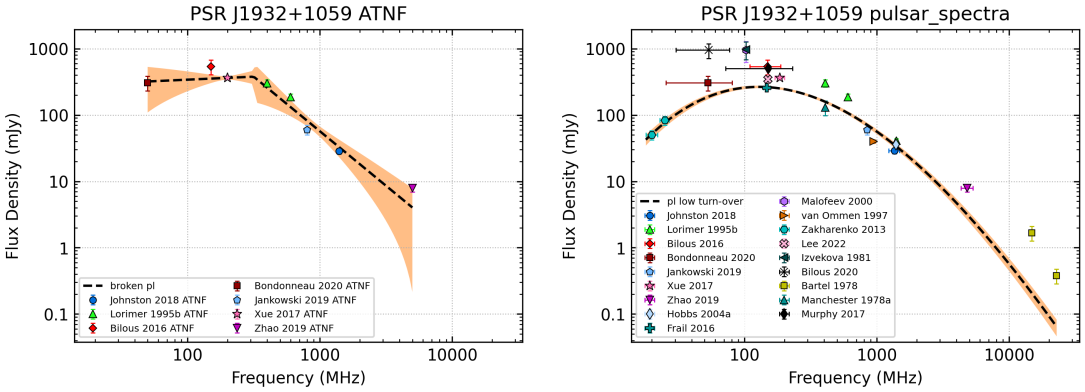

(b) J1932+1059

Figure 5.1: *Left*: A spectral fit using only the flux density values from the ATNF pulsar catalogue. *Right*: A spectral fit using only the flux density values from the `pulsar_spectra` catalogue. As demonstrated through these examples, the `pulsar_spectra` catalogue is able to accommodate many more flux density values than those available in the ATNF pulsar catalogue and hence can yield more accurate spectral fits.

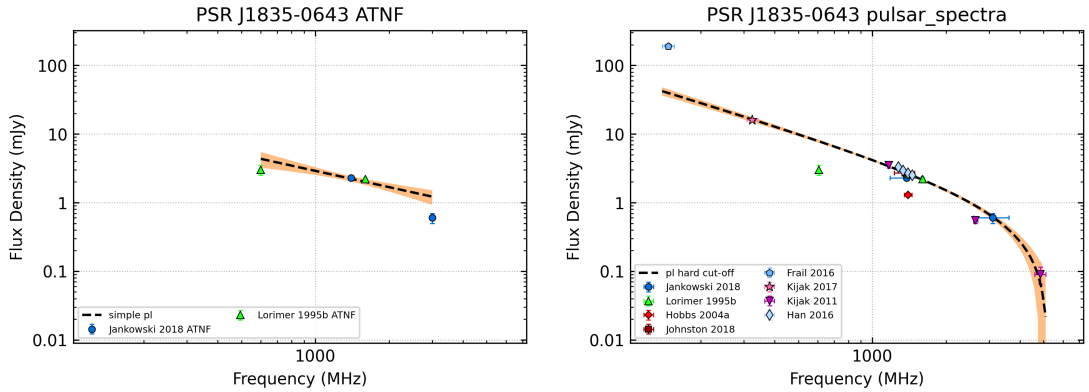

(c) J1835-0643

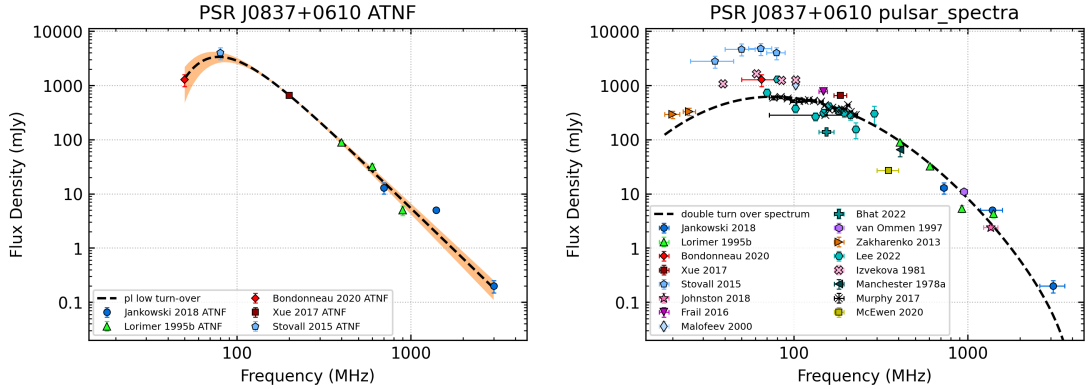

(d) J0837+0610

Figure 5.1: *Left*: A spectral fit using only the flux density values from the ATNF pulsar catalogue. *Right*: A spectral fit using only the flux density values from the `pulsar_spectra` catalogue. As demonstrated through these examples, the `pulsar_spectra` catalogue is able to accommodate many more flux density values than those available in the ATNF pulsar catalogue and hence can yield more accurate spectral fits.

YAML format that the catalogue requires, as explained in our documentation[2]. They can use this to make a pull request, and this publication will be included in the next release of `pulsar_spectra`. We will keep an up-to-date table of publications[3] to make it easier to cite the data and to encourage authors to upload their own published results.

[2] https://pulsar-spectra.readthedocs.io/en/latest/catalogue.html#adding-to-the-catalogue

[3] https://pulsar-spectra.readthedocs.io/en/latest/catalogue.html#papers-included-in-our-catalogue

Publication	#	ν (MHz)
ATNF pulsar catalogue	2827	40-150000
Sieber (1973)	27	38-10690
Bartel et al. (1978)	18	14800-22700
Manchester et al. (1978)	224	408-408
Izvekova et al. (1981)	86	39-102
Dewey et al. (1985)	34	390-390
McConnell et al. (1991)	4	610-610
Johnston et al. (1992)	100	640-1500
Wolszczan & Frail (1992)	1	430-1400
Johnston et al. (1993)	1	430-2360
Manchester et al. (1993)	1	640-640
Taylor et al. (1993)	639	400-1400
Camilo & Nice (1995)	29	430-430
Lundgren et al. (1995)	1	430-1400
Nicastro et al. (1995)	1	400-1400
Guojun et al. (1995)	61	600-1500
Robinson et al. (1995)	2	436-640
Lorimer et al. (1995)	280	408-1606
Manchester et al. (1996)	55	436-436
Zepka et al. (1996)	1	430-1400
van Ommen et al. (1997)	82	800-960
Malofeev et al. (2000)	212	102-102
Kramer et al. (2003a)	200	1400-1400
Hobbs et al. (2004a)	453	1400-1400
Karastergiou et al. (2005)	48	1400-3100
Johnston et al. (2006)	31	8400-8400
Lorimer et al. (2006)	142	1400-1400
Kijak et al. (2007)	11	325-1060
Stappers et al. (2008)	13	147-147
Bates et al. (2011)	34	1400-6500
Keith et al. (2011)	9	17000-24000
Kijak et al. (2011)	15	610-4850
Zakharenko et al. (2013)	40	20-25
Dembska et al. (2014)	19	610-8450
Dai et al. (2015)	24	730-3100
Stovall et al. (2015)	36	35-79
Basu et al. (2016)	1	325-1280
Bell et al. (2016)	17	154-154
Bilous et al. (2016)	158	149-149
Han et al. (2016b)	204	1274-1466
Kijak et al. (2017)	12	325-610
Mignani et al. (2017)	1	97500-343500
Murphy et al. (2017)	60	76-227
Xue et al. (2017)	50	185-185
Jankowski et al. (2018)	441	728-3100
Johnston & Kerr (2018)	586	1400-1400
Jankowski et al. (2019)	205	843-843
Sanidas et al. (2019)	290	135-135
Xie et al. (2019)	32	300-3000
Zhao et al. (2019)	71	4820-5124
Bilous et al. (2020)	43	53-63
Bondonneau et al. (2020)	64	53-65
McEwen et al. (2020)	670	350-350
Han et al. (2021)	201	1250-1250
Johnston et al. (2021)	44	1400-1400

Table 5.1: The publications included in version 2.0 of `pulsar_spectra` where # is the number of pulsars and ν (MHz) is the frequency range. For an up to date table see the documentation

Source	# pulsars
Only ANTF	812
Both catalogues	581
Only pulsar_spectra	1385
Neither catalogues	541

Table 5.2: This table compares the current progress of our catalogue compared to the ATNF. As users continue to add publications the catalogue will grow.

When comparing the current state of the catalogue to the ATNF catalogue (see Table 5.2), the `pulsar_spectra` catalogue already contains a larger sample of pulsar flux density measurements. We hope that the open-source nature of our catalogue and the ease of uploading new publications' flux density measurements will allow our catalogue to grow rapidly in the coming years.

5.4 Pulsar Spectral Fitting

Flux density measurements obtained using different telescopes are subject to different systematic errors due to the telescope's observing setup and varying levels of reliability of the calibration procedures. These systematic errors make robust modelling of spectral fits complicated. Jankowski et al. (2018) developed a method of modelling and objectively classifying spectra which are composed of disparate data from the literature, and our approach is adapted from this work. We now summarise the Jankowski et al. (2018) method used in our software.

To reduce the effect of underestimated uncertainties on outlier points in a given fit, the least-squares function is modified from the regular quadratic loss to a linear loss once the residuals exceed a pre-chosen threshold. In this way, outlier data are penalised, and as a result any measurements that are less reliable are less likely to skew the model fit. In `pulsar_spectra`, we implement this using

the Huber loss function, defined as

$$\rho = \begin{cases} \frac{1}{2}t^2 & \text{if } |t| < k \\ k|t| - \frac{1}{2}k^2 & \text{if } |t| \geq k \end{cases}, \tag{5.1}$$

where t is a residual (i.e. the difference between the model and the measurement) and k is the threshold that defines which points are considered outliers (Huber, 1964). We use a value of $k = 1.345$, for which Huber has shown to be 95% as efficient at parameter estimation as an ordinary least squares estimator operating on data from a Gaussian distribution. We hence define a robust cost function

$$\beta = \sum_i^N \begin{cases} \frac{1}{2}\left(\frac{f_i - y_i}{\sigma_{y,i}}\right)^2 & \text{if } \left|\frac{f_i - y_i}{\sigma_{y,i}}\right| < k \\ k\left|\frac{f_i - y_i}{\sigma_{y,i}}\right| - \frac{1}{2}k^2 & \text{otherwise} \end{cases}, \tag{5.2}$$

where f_i are the values of the model function at the frequencies of the measured flux densities y_i, and $\sigma_{y,i}$ are the corresponding uncertainties of the flux densities.

The cost function is minimised using MIGRAD, a robust minimisation algorithm implemented in the MINUIT C++ library (as described in James & Roos, 1975) which is accessible through the PYTHON interface IMINUIT[4]. MIGRAD uses a combination of Newton steps and gradient descents to converge to a local minimum. The Estimated Distance to Minimum (EDM) is used to define a convergence criterion in terms of a specified tolerance (which must be met for the minimisation to be considered successful), which is set to a value of 5×10^{-6}. The uncertainties are computed at the 1σ level from the diagonal elements of the parameter covariance matrix using the HESSE error calculator.

[4] https://github.com/iminuit/iminuit

5.4.1 Spectral models

We have currently implemented the five spectral models that have distinct spectral shapes from Jankowski et al. (2018). While these five models are sufficient for describing the spectra for the vast majority of pulsars, our software is flexible enough to allow the addition of more spectral models easily, as explained here[5].

The choice of the reference frequency, ν_0, in the following models can affect the spectral fits as the data closer to the reference frequency are given more weight. To make the weighting of the fit as even as possible, we select ν_0 as the geometric average (average in log-space) of the minimum and maximum frequencies in the spectral fit ($\nu_{\rm min}$ and $\nu_{\rm max}$, respectively):

$$\log_{10}\nu_0 = \frac{1}{2}\left(\log_{10}\nu_{\rm min} + \log_{10}\nu_{\rm max}\right). \tag{5.3}$$

This method has also been adopted in previous work (e.g. Bilous et al., 2016). We define the scaling constant in the following spectral models as c.

We shall now describe the spectral models and provide example pulsars that are best fit by each of these models as of `pulsar_spectra` version 2.0.

5.4.1.1 Simple power law

The simple power law is linear in log-space and the most common spectral model. Some examples of this include PSRs J0040+5716 (see Figure 5.2), J1328−4357, and J0955−5304. The model takes the form:

$$S_\nu = c\left(\frac{\nu}{\nu_0}\right)^\alpha, \tag{5.4}$$

where α is the spectral index. The fit parameters are α and c.

[5] https://pulsar-spectra.readthedocs.io/en/latest/spectral_fit.html#models

5.4.1.2 Broken power law

The broken power law is the equivalent of two simple power laws that differ at a spectral break frequency. Variations on this model have been applied in other fields of astrophysics, such as the smoothly broken power-law, which is characterised by an additional parameter describing the width of the transition (e.g. Ryde, 1999). Pulsar spectra are traditionally fit with sharply broken power laws, characterised by only four free parameters (e.g. Sieber, 1973; Murphy et al., 2017). Some examples of broken power-law fits include PSRs J0543+2329 (see Figure 5.1), J0452−1759 and J0820−1350. The model takes the form:

$$S_\nu = c \begin{cases} \left(\frac{\nu}{\nu_0}\right)^{\alpha_1} & \text{if } \nu \leq \nu_\mathrm{b} \\ \left(\frac{\nu}{\nu_0}\right)^{\alpha_2} \left(\frac{\nu_\mathrm{b}}{\nu_0}\right)^{\alpha_1 - \alpha_2} & \text{otherwise} \end{cases}, \tag{5.5}$$

where ν_b is the frequency of the spectral break, α_1 the spectral index before and α_2 the one after the break. The fit parameters are α_1, α_2, ν_b, and c.

5.4.1.3 Log-parabolic spectrum

This model has been used to describe the spectra of radio galaxies (e.g. Baars et al., 1977) and curved pulsar spectra (Bates et al., 2013; Dembska et al., 2014). The model takes the form:

$$\log_{10} S_\nu = a \left[\log_{10}\left(\frac{\nu}{\nu_0}\right)\right]^2 + b \log_{10}\left(\frac{\nu}{\nu_0}\right) + c \tag{5.6}$$

where a is the curvature parameter and b is the spectral index for $a = 0$. The fit parameters are a, b, and c. Since the double turn-over spectrum (see §5.4.1.6) is more related to pulsar theory, the log-parabolic spectrum is no longer used by default.

5.4.1.4 Power law with low-frequency turn-over

This model exhibits a power law at high frequencies with a turn-over at low frequencies. The curve of this turn-over can give us clues about the nature of the pulsar emission mechanism (Izvekova et al., 1981; Kijak et al., 2007). Some examples of this include PSRs J1932+1059 (see Figure 5.1), J1543+0929 and J0034−0721. The model takes the form:

$$S_\nu = c \left(\frac{\nu}{\nu_0}\right)^{\alpha} \exp\left[\frac{\alpha}{\beta}\left(\frac{\nu}{\nu_{\rm peak}}\right)^{-\beta}\right], \tag{5.7}$$

where α is the spectral index, $\nu_{\rm peak}$ is the turn-over frequency, and $0 < \beta \leq 2.1$ determines the smoothness of the turn-over. The fit parameters are α, $\nu_{\rm peak}$, β and c.

5.4.1.5 Power law with high-frequency cut-off

This model, also known as the hard cut-off model, is based on the coherent emission model developed by Kontorovich & Flanchik (2013). At high frequencies, its flux quickly trends towards zero before a cut-off frequency. An example of this is PSR J1835−0643 (see Figure 5.1). The model takes the form:

$$S_\nu = c \left(\frac{\nu}{\nu_0}\right)^{\alpha} \left(1 - \frac{\nu}{\nu_{\rm c}}\right), \qquad \nu < \nu_{\rm c}, \tag{5.8}$$

where α is the spectral index and $\nu_{\rm c}$ is the cut-off frequency. The fit parameters are α, $\nu_{\rm c}$ and c.

5.4.1.6 Double turn-over spectrum

This model exhibits a turn-over at low frequencies and a hard cut-off at high frequencies with an underlying power law. This is a combination of the power law with high-frequency cut-off and the power law with low-frequency turn-over. A large number of fit parameters means this spectrum will rarely be chosen as the best model. However, it is superior to the log parabolic model because it

is physically motivated and has common parameters as other models. Some examples of this include PSRs J0837+0610 (see Figure 5.1) and J2113+2754. The model takes the form:

$$S_\nu = c\left(\frac{\nu}{\nu_0}\right)^{\alpha} \exp\left[\frac{\alpha}{\beta}\left(\frac{\nu}{\nu_{\rm peak}}\right)^{-\beta}\right]\left(1-\frac{\nu}{\nu_{\rm c}}\right), \qquad \nu < \nu_{\rm c}, \tag{5.9}$$

where α is the spectral index, $\nu_{\rm peak}$ is the turn-over frequency, $\nu_{\rm c}$ is the cut-off frequency and $0 < \beta \leq 2.1$ determines the smoothness of the turn-over. The fit parameters are α, $\nu_{\rm c}$, $\nu_{\rm peak}$, β and c.

5.4.2 Bandwidth integration correction

Pulsar spectral fitting often assumes that the reported average flux densities can be treated as the flux density at one specific (usually central) frequency, whereas in reality, they are averaged over some finite bandwidth. This assumption is becoming increasingly inaccurate as telescopes are now often observing with large fractional bandwidths. For this reason, the `pulsar_spectra` fitting method has been improved to include the bandwidth of all detections and expanded our equations to model the integrated flux density across the band.

If a flux density measurement is reported along with a bandwidth, then the correct way to fit a spectral model is to find the expected mean flux density across the band,

$$S_{\rm avg} = \frac{1}{\rm BW}\int_{\nu_{\rm min}}^{\nu_{\rm max}} S_\nu \, {\rm d}\nu, \tag{5.10}$$

where $\rm BW = \nu_{max} - \nu_{min}$. The evaluation of this expression for the simple power law is given below

$$S_\nu = c\left(\frac{\nu}{\nu_0}\right)^\alpha, \tag{5.11}$$

$$S_{\text{avg}} = \frac{1}{\text{BW}}\int_{\nu_{\min}}^{\nu_{\max}} c\left(\frac{\nu}{\nu_0}\right)^\alpha \,\mathrm{d}\nu, \tag{5.12}$$

$$= \frac{\nu_0}{\text{BW}}\left[\frac{c}{\alpha+1}\left(\frac{\nu}{\nu_0}\right)^{\alpha+1}\right]_{\nu_{\min}}^{\nu_{\max}} \tag{5.13}$$

$$= \frac{\nu_0}{\text{BW}}\frac{c}{\alpha+1}\left(\left(\frac{\nu_{\max}}{\nu_0}\right)^{\alpha+1} - \left(\frac{\nu_{\min}}{\nu_0}\right)^{\alpha+1}\right) \tag{5.14}$$

$$= \frac{c({\nu_{\max}}^{\alpha+1} - {\nu_{\min}}^{\alpha+1})}{\text{BW}\,\nu_0^\alpha(\alpha+1)}. \tag{5.15}$$

The derivations for other models are given in the `pulsar_spectra` documentation[6].

5.4.3 Comparing models

To compare five models (described in §5.4.1), we require a comparison metric that accounts for a different number of fit parameters. We use the Akaike information criterion (AIC), which is a measure of how much information the model retains about the data without over-fitting. In other words, a model with more fit parameters is only rated better if the fit is sufficiently improved. It was implemented as

$$\text{AIC} = 2\beta_{\min} + 2K + \frac{2K(K+1)}{N-K-1}, \tag{5.16}$$

where $\beta_{\min}$ is the minimised robust cost function, K is the number of free parameters, and N is the number of data points in the fit. The last term is the correction for finite sample sizes, which goes to zero as the sample size gets sufficiently large.

The model which results in the lowest AIC is the most likely to be the model that most accurately describes the pulsar's spectrum.

[6] https://pulsar-spectra.readthedocs.io/en/latest/bandwidth_intergration.html#integration-of-the-model-functions

5.5 How to use the software

pulsar_spectra is written in PYTHON and is easily installed using `pip install pulsar_spectra`. The complete documentation of the code can be found here[7]. To demonstrate how easy it is to use, we present a simple example for PSR J0040+5716. The code in Listing 5.1 shows how to add a custom set of flux density measurements to those already in the catalogue and find the best spectra fit. The result is shown in Figure 5.2.

Listing 5.1: An example of how to add new flux density measurement to the values from the literature and find the best spectra fit.

```
from pulsar_spectra.catalogue import collect_catalogue_fluxes
from pulsar_spectra.spectral_fit import find_best_spectral_fit

cat_list = collect_catalogue_fluxes()
pulsar = 'J0040+5716'
freqs, bands, fluxs, flux_errs, refs = cat_list[pulsar]
freqs += [300.]
bands += [10.]
fluxs += [10.]
flux_errs += [1.]
refs += ["Your Work"]
find_best_spectral_fit(pulsar, freqs, bands, fluxs, flux_errs,
    refs, plot_best=True)
```

5.5.1 Future plans

One of the benefits of having an open source repository is that we can continue to add models and features as pulsar spectral theory improves. One example is the implicit assumption that the reported flux density can be treated as the

[7] https://pulsar-spectra.readthedocs.io/en/latest/index.html

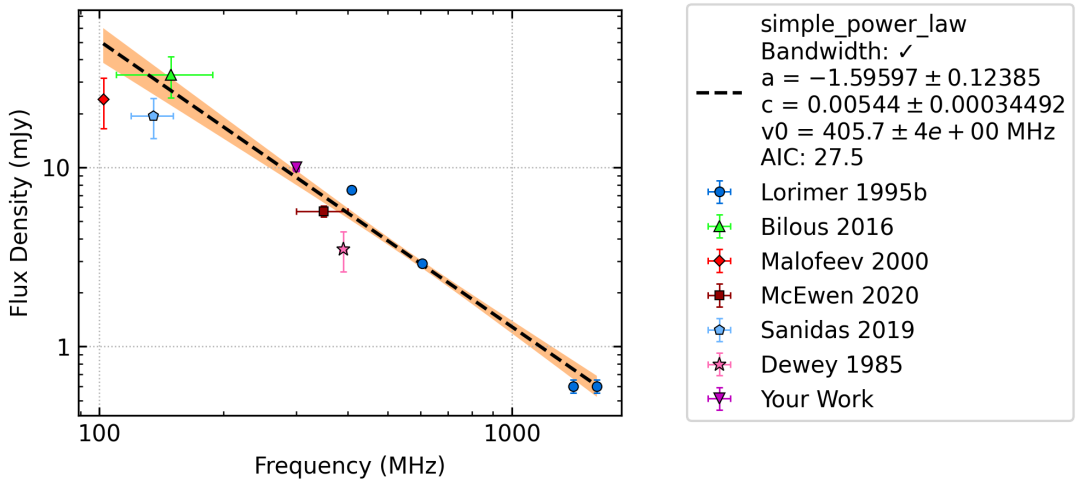

Figure 5.2: The spectral fit to the flux density measurements of PSR J0040+5716 created using the `pulsar_spectra` software and only the 12 lines of code shown in Listing 5.1.

flux density at one specific frequency (usually the central frequency of the observing band). Such an approximation becomes increasingly inaccurate for wider and wider bandwidths. We will expand the catalogue's database to include the bandwidth, of all measurements where this information has been recorded, and expand our equations to model the integrated flux across the band.

5.6 Summary

We have introduced `pulsar_spectra`, a software repository to make pulsar flux density measurements more accessible to the community and make the investigation of pulsar spectra easier by automating pulsar spectral analyses via several standard functional forms. The open-source pulsar flux density catalogue is designed to be extendable, allowing the community to include new publications in the catalogue and cite the work of others. The analysis of spectra for a large body of pulsars can provide valuable clues to the nature of the pulsar emission mechanism and will help refine the knowledge of the detectable pulsar population. Future work may be able to use this spectral analysis (for example the

low-frequency turn-over) to investigate the intervening medium.

Chapter 6

Spectral Analysis of 893 Pulsars

Although pulsars have been studied for almost 50 years, the exact nature of their emission mechanism is far from being understood. Spectral analysis can potentially provide clues about pulsar emission. The study of pulsar spectra is currently limited by the lack of flux density measurements, leading to a lack of accurate spectral data. In this chapter, we use the largest number of spectral measurements to date to investigate what properties of the pulsars cause their spectra.

The 120 pulsars detected in the SMART survey (Bhat et al., 2023a) have been integrated into version 2.0 of the `pulsar_spectra` database, resulting in 893 pulsars with at least four flux density measurements. This data set is over twice as large as the previous pulsar spectra record (441 pulsars in Jankowski et al. (2018)).

The spectral fitting of the pulsars uses the method described in `pulsar_spectra` (Swainston et al., 2022b) and is described in the `all_pulsar_spectra`[1] repository (Swainston, 2022). For convenience, the spectral models used in this analysis and their acronyms are summarised in Table 6.1.

The `all_pulsar_spectra` repository has instructions for how to run the automated spectral fitting so that all the following analyses can be regularly re-

[1] https://github.com/NickSwainston/all_pulsar_spectra

Acronym	Model	Equation	Parameters	#
SPL	simple power law	5.4	c, α	2
BPL	broken power law	5.5	$c, \alpha_1, \alpha_2, \nu_\mathrm{b}$	4
LFTO	power law with low-frequency turn-over	5.7	$c, \alpha, \nu_\mathrm{peak}, \beta$	4
HFCO	power law with high-frequency cut-off	5.8	$c, \alpha, \nu_\mathrm{c}$	3
DTOS	double turn-over spectrum	5.9	$c, \alpha, \nu_\mathrm{peak}, \nu_\mathrm{c}, \beta$	5

Table 6.1: This table summarises the spectral models used in this analysis, including their acronym, equation reference, fit parameters and the number of fit parameters.

produced as the flux density database expands and spectral fitting techniques evolve. The spectral fits and analyses can be viewed on the `all_pulsar_spectra results page`[2]. The results page is versioned (the previous link is v2.0.0) so that researchers can compare spectral results of previous `pulsar_spectra` versions so the `all_pulsar_spectra` repository can be treated as a pulsar spectra database.

This chapter is organised as follows. We will first investigate the effect of the additional flux density measurements from the SMART survey on the spectral fits in §6.1. Then in §6.2, we discuss the results of all 893 spectral fits and their distribution. Finally, in §6.3, we investigate correlations between the spectral fit results and the intrinsic properties of the pulsars.

6.1 Addition of low-frequency flux density measurements from the SMART pulsar survey

The SMART pulsar survey (Bhat et al., 2023a) has nearly completed its first pass of the processing, the shallow survey (see §2.5). During this first pass, 120 known pulsars were detected. The flux densities of these pulsars are shown in Table A.1 and were calculated using the tied-array beam simulation method developed by Meyers et al. (2017) and explained in §2.3.3. Many of these flux density values are from a single observation, so they have not been scintillation averaged. These flux

[2] https://all-pulsar-spectra.readthedocs.io/en/2.0.0/

density measurements provide the lowest frequency measurements for 28 pulsars in the pulsar_spectra database (see bold "Min Freq" values in Table 6.2).

To investigate the effect of the new flux density measurements on the pulsars' spectra, we compare the best spectral model before and after the addition of the SMART flux density measurements in Table 6.2. Of the 120 pulsars, 102 had sufficient flux density measurements to make spectral fits before the SMART measurements, four had enough to make a spectral fit only once the SMART measurements were included, and 14 did not have sufficient data to make a spectral fit. The lack of flux measurement data for these 14 pulsars shows the need for more flux density survey programs. The MWA is well placed to assist this effort due to its large FoV, which allows the observation of pulsars that are often missed (due to lack of telescope time) or that other high-frequency telescopes may not be sensitive to.

23 pulsars changed spectral models after the addition of the SMART measurements, and they are shown in bold in Table 6.2 and the plots of the differences are in Appendix B. A total of six pulsars' spectral model complexity (number of fit parameters) was reduced. Two pulsars, J0729−1836 and J1455−330, changed from power law with low-frequency turn-over to simple power law after the SMART data invalidated low-frequency spectral turn-overs, assuming they are not scintillating up. Two other pulsars' spectra, J1034−3224 and J1041−1942, reverted from power law with high-frequency cut-off to simple power law after reducing the certainty that the high-frequency cut-off was anything more than an inaccurate flux density measurement. Two pulsars, J0525+1115 and J1320−5359, changed from broken power law to power law with high-frequency cut-off, which is an improvement as power law with high-frequency cut-off has a firmer theoretical basis (Kontorovich & Flanchik, 2013) and fewer fit parameters.

The other 17 pulsars changed models to equally or more complex models. The 23 pulsars had an average change to the number of fit parameters of 0.3, demonstrating that we can fit more complex and theoretically motivated models

as we include more data.

6.2 Spectral Properties

The distribution of the best spectral model for each pulsar and their fit parameters can give us insights into the pulsars' properties and the limits of our current spectral sample. The distribution of the spectral models is shown in Table 6.3 for all pulsars, MSPs and slow pulsars. 68% of our sample is a simple power law, which is 11% less than the 79% quoted by Jankowski et al. (2018), suggesting the frequency range in our data set is becoming wide enough to be sensitive to low- and high-frequency spectral features.

6.2.1 Spectral Index

As explained in §1.7.1, the spectral index is an observed property of pulsar spectra that currently has no commonly accepted theoretical explanation, only observed correlations that suggest which parameters determine the spectral index (e.g. Jankowski et al., 2018; Han et al., 2016a). The study of spectral indices and their distribution leads to more accurate pulsar population simulations, which will assist future surveys, and may lead to an understanding of the cause of the varying spectral indices of pulsars.

6.2.1.1 The potential bias of the spectral index

All spectral models contain a single spectral index parameter except for the broken power law, which contains two (see Table 6.1). In the simple power law model, the power law is measured over the entire spectrum leading to an accurate spectral index measurement. Other models, however, may be dominated by non-power-law components across the frequency range where measurements are available. This can affect the accuracy of the power-law component whenever the power-law component is significantly correlated with the other components.

PSR Jname	N flux	Original Model	New Model	Min Freq (MHz)
J0030+0451	12	LFTO	LFTO	50
J0034−0534	33	DTOS	DTOS	50
J0034−0721	45	DTOS	DTOS	20
J0038−2501	1	-	-	**350**
J0051+0423	6	SPL	SPL	25
J0133−6957	3	**-**	**SPL**	**400**
J0134−2937	4	SPL	SPL	**350**
J0151−0635	10	BPL	BPL	25
J0152−1637	20	LFTO	LFTO	35
J0206−4028	12	HFCO	HFCO	107
J0255−5304	5	SPL	SPL	**400**
J0304+1932	16	LFTO	LFTO	24
J0401−7608	9	SPL	SPL	**400**
J0418−4154	3	**-**	**SPL**	**185**
J0437−4715	43	BPL	BPL	76
J0450−1248	9	HFCO	HFCO	102
J0452−1759	23	HFCO	HFCO	102
J0459−0210	6	SPL	SPL	102
J0514−4408	1	-	-	**300**
J0520−2553	4	SPL	SPL	**350**
J0525+1115	15	**BPL**	**HFCO**	61
J0528+2200	19	**LFTO**	**BPL**	39
J0534+2200	8	**LFTO**	**BPL**	102
J0600−5756	2	-	-	**400**
J0601−0527	12	**BPL**	**LFTO**	102
J0614+2229	13	LFTO	LFTO	85
J0624−0424	9	SPL	SPL	102
J0630−2834	48	DTOS	DTOS	35
J0636−4549	1	-	-	**1360**
J0729−−1448	6	SPL	SPL	**350**
J0729−1836	13	**LFTO**	**SPL**	**350**
J0737−3039A	19	BPL	BPL	99
J0742−2822	19	BPL	BPL	102
J0758−1528	12	SPL	SPL	102
J0820−1350	49	BPL	BPL	58
J0820−-3921	7	SPL	SPL	**350**
J0820−4114	28	**LFTO**	**BPL**	76
J0823+0159	13	SPL	SPL	102
J0826+2637	40	BPL	BPL	20
J0835−4510	47	BPL	BPL	76
J0837+0610	57	DTOS	DTOS	20
J0837−4135	15	LFTO	LFTO	147
J0842−4851	7	SPL	SPL	147
J0855−3331	11	LFTO	LFTO	147
J0856−6137	7	SPL	SPL	151
J0902−6325	3	**-**	**SPL**	**400**
J0904−7459	7	SPL	SPL	**400**
J0905−6019	1	-	-	**1360**
J0907−5157	14	**LFTO**	**BPL**	147
J0908−1739	18	LFTO	LFTO	49
J0922+0638	24	LFTO	LFTO	20
J0924−5302	10	SPL	SPL	151
J0924−5814	8	SPL	SPL	**400**
J0942−5552	14	**BPL**	**LFTO**	151
J0942−5657	11	SPL	SPL	151
J0943+1631	12	LFTO	LFTO	25
J0944−1354	7	SPL	SPL	102
J0946+0951	13	DTOS	DTOS	20
J0953+0755	42	LFTO	LFTO	20
J0955−5304	6	HFCO	HFCO	**400**
J0959−4809	8	SPL	SPL	147
J1003−4747	8	HFCO	HFCO	**300**
J1012−2337	5	SPL	SPL	151
J1018−1642	9	**SPL**	**HFCO**	102
J1022+1001	18	**BPL**	**DTOS**	50
J1034−3224	8	**HFCO**	**SPL**	147
J1041−1942	8	**HFCO**	**SPL**	**350**
J1057−5226	10	**SPL**	**BPL**	151
J1059−5742	11	**SPL**	**BPL**	**400**
J1112−6926	7	SPL	SPL	**185**
J1116−4122	13	HFCO	HFCO	147
J1121−5444	9	SPL	SPL	151
J1123−4844	5	SPL	SPL	**400**
J1123−6651	7	SPL	SPL	**400**
J1136+1551	33	BPL	BPL	20
J1136−5525	6	**SPL**	**HFCO**	**400**
J1141−6545	6	HFCO	HFCO	**185**
J1146−6030	10	**SPL**	**BPL**	**400**
J1202−5820	9	SPL	SPL	**400**
J1224−6407	10	**SPL**	**BPL**	**400**
J1225−5556	2	-	-	**436**
J1239−6832	6	SPL	SPL	**400**
J1240−4124	4	SPL	SPL	**300**
J1257−1027	8	SPL	SPL	102
J1300+1240	12	LFTO	LFTO	50
J1311−1228	6	SPL	SPL	102
J1312−5402	6	SPL	SPL	**400**
J1313+0931	6	HFCO	HFCO	57
J1320−5359	9	**BPL**	**HFCO**	**300**
J1328−4357	4	SPL	SPL	**400**
J1332−3032	4	SPL	SPL	**350**
J1335−3642	3	**-**	**SPL**	**350**
J1340−6456	4	SPL	SPL	**400**
J1355−5153	5	**SPL**	**HFCO**	147
J1358−2533	3	**-**	**SPL**	**350**
J1418−3921	5	SPL	SPL	147
J1430−6623	11	LFTO	LFTO	151
J1440−6344	5	**SPL**	**HFCO**	**185**
J1453−6413	25	LFTO	LFTO	102
J1455−3330	8	**LFTO**	**SPL**	**350**
J1456−6843	18	**BPL**	**LFTO**	102
J1507−4352	6	SPL	SPL	147
J1510−4422	2	-	-	**400**
J1527−3931	4	SPL	SPL	**350**
J1534−5334	10	SPL	SPL	154
J1543+0929	14	DTOS	DTOS	53
J1543−0620	14	DTOS	DTOS	25
J2048−1616	20	LFTO	LFTO	102
J2108−3429	4	SPL	SPL	**350**
J2145−0750	31	DTOS	DTOS	50
J2155v3118	11	HFCO	HFCO	147
J2222−0137	6	SPL	SPL	135
J2234+2114	7	SPL	SPL	100
J2241−5236	22	**SPL**	**BPL**	81
J2317+2149	12	LFTO	LFTO	25
J2324−6054	6	SPL	SPL	**400**
J2325−0530	2	-	-	24
J2330−2005	16	LFTO	LFTO	35
J2336−01	1	-	-	24
J2354−22	1	-	-	**350**

Table 6.2: This table displays the spectral fits of the 120 SMART pulsars before and after the additions of the SMART flux density measurements where N flux is the number of flux density measurements not including the SMART data, Min Freq is the minimum frequency of flux density measurements not including the SMART data, Original Model is the spectral model without the SMART data and New Model is with the SMART data where SPL is simple power law, BPL is broken power law, LFTO is power law with low-frequency turn-over, HFCO is power law with high-frequency cut-off and DTOS is double turn-over spectrum.

Model	Total		MSP		Slow	
	#	%	#	%	#	%
SPL	611	68.4	53	61.6	558	69.1
BPL	54	6.0	7	8.1	47	5.8
HFCO	107	12.0	8	9.3	99	12.3
LFTO	105	11.8	12	14.0	93	11.5
DTOS	16	1.8	6	7.0	10	1.2
Total	893	100.0	86	100.0	807	100.0

Table 6.3: The distribution of the spectral models of all pulsars, MSPs ($P < 30$ ms) and slow pulsars.

Spectral index measurements affected in this way can be significantly biased.

This bias becomes evident in Figure 6.1, which shows the distribution of spectral index values for different spectral models. Figure 6.1 (b) shows the expected Gaussian distribution for the simple power law model. The distribution of the other models (Figure 6.1 (c,d,e)) depart from the Gaussian distribution and, as the spectral index should be standard for all models, indicates there is a bias for these models.

The spectral index distribution of the power law with high-frequency cut-off is shown in Figure 6.1 (c) with all measured spectral indices > -2, which is much flatter than the simple power law distribution. This bias towards flat spectral indexes is likely due to some spectra being dominated by the cut-off curve, so there is not enough power-law-dominated spectra to accurately fit the spectral index. Figure 6.2 is an example of this, which measured the spectral index as 0.0, the maximum limit set by `pulsar_spectra` for the power law with high-frequency cut-off model.

The spectral index distribution of the power law with low-frequency turn-over is shown in Figure 6.1 (d) and has several extremely steep (< -4) spectral index measurements. This bias towards steep spectral indexes is due to some spectra being dominated by the turn-over curve, see Figure 6.3 for example, so there is not enough of the power-law-dominated spectra to accurately fit the spectral index. The measured spectral index is -8.0 with a large uncertainty, the maximum limit

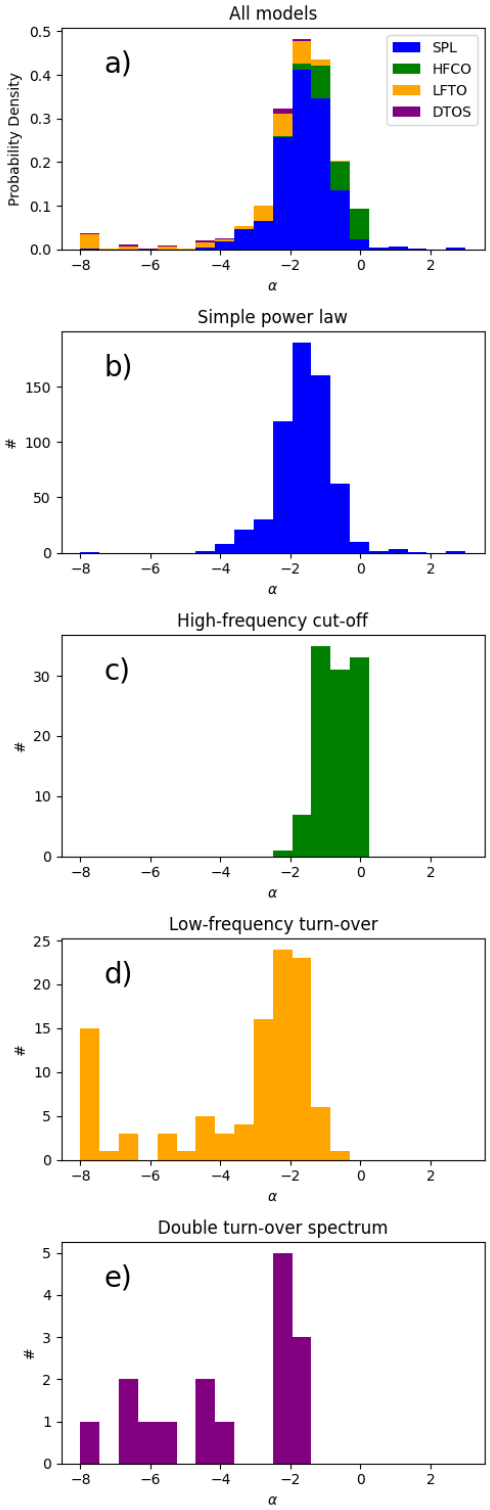

Figure 6.1: Histogram of the distribution of spectral index values for different spectral models.

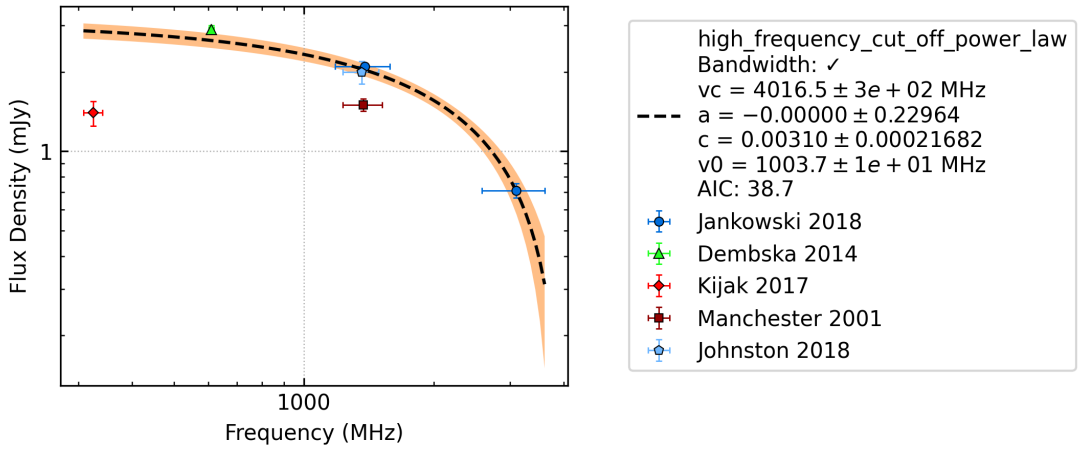

Figure 6.2: The spectrum of PSR J0024−7204C, an example of the power law with high-frequency cut-off spectrum being dominated by the cut-off curve causing an inaccurate spectral index measurement.

set by `pulsar_spectra` for the power law with low-frequency turn-over model.

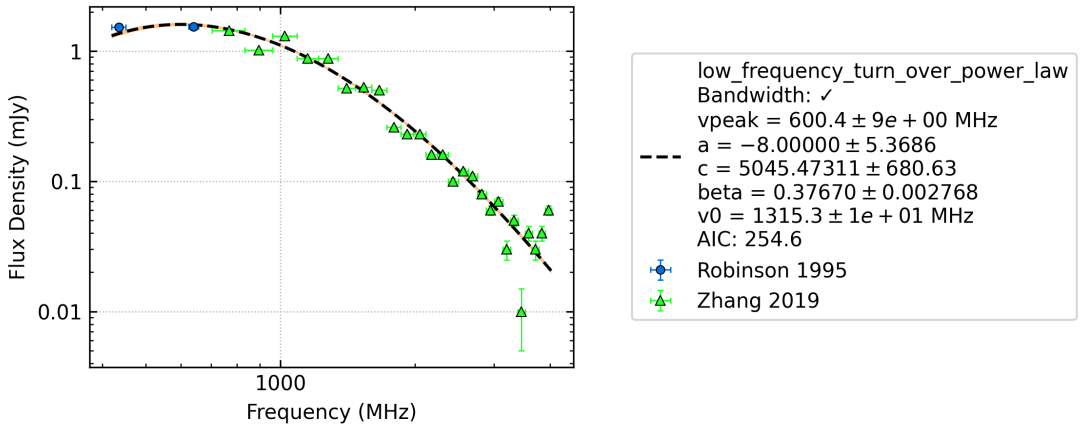

Figure 6.3: The spectrum of PSR J0024−7204C, an example of the power law with low-frequency turn-over spectrum being dominated by the turn-over curve causing an inaccurate spectral index measurement.

The inaccuracy of the spectral index in these more complex models also suggests that the spectral index is not necessary for describing pulsars' spectra when a wide enough frequency range is measured. When considering the energetics of pulsar emission, it is impossible for a simple power law spectrum to continue indefinitely to low-frequencies. This implies that the spectral index is only valid within a restricted range of frequencies. Due to these uncertainties, only the

spectral index values from simple power law fits will be used for all following analyses.

6.2.1.2 Comparison with previous publications

Previous publications have calculated the mean spectral index of different subsets of the pulsar population. We have compared our result of -1.61 ± 0.03 for the simple power law pulsars with other publications in Table 6.4.

Publications that only measure the spectral index over the low-frequency range, such as Bilous et al. (2016) and Malofeev et al. (2000), tend to estimate a flatter mean spectral index (-1.4 and -1.47 ± 0.76 respectively). Han et al. (2016a) used a narrow frequency range of around 1.4 GHz and found a steep spectrum of -2. Spiewak et al. (2022) only measured the spectra of MSPs from 0.58 to 1.67 GHz and found a steep spectrum of -1.92 ± 0.06. All other publications used a large frequency range and estimated a spectrum between -1.6 and -1.8, which agrees with our work. Our mean is very similar to Jankowski et al. (2018) with over twice the number of pulsars, so this could indicate that we are getting close to an unbiased mean spectral index.

Publication	#pulsars	Frequency (GHz)	α
This work	611	0.02 – 343.50	-1.61 ± 0.03
Spiewak et al. (2022)	189	0.58 – 1.67	-1.92 ± 0.06
Jankowski et al. (2018)	276	0.72 – 3.10	-1.60 ± 0.03
Han et al. (2016a)	228	1.20 – 1.50	-2
Bilous et al. (2016)	48	0.11 – 0.18	-1.4
Maron et al. (2000)	263	0.40 – 23.00	-1.80 ± 0.20
Malofeev et al. (2000)	175	0.10 – 0.40	-1.47 ± 0.76
Toscano et al. (1998)	216	0.43 – 1.66	-1.72 ± 0.04
Lorimer et al. (1995)	279	0.40 – 1.40	-1.6

Table 6.4: Comparison of the mean spectral index and their standard error for pulsars fit with simple power law spectra.

6.3 Spectral Correlations with Pulsar Properties

This section will investigate the correlations between spectral features and pulsar properties. Significant correlations help us understand what properties of the pulsars influence pulsar spectra and give us a greater understanding of the pulsar emission process.

6.3.1 Method

We investigated three spectral properties, the spectral index α of the simple power law, the peak frequency $\nu_{\rm peak}$ of the power law with low-frequency turn-over and double turn-over spectrum, and the cut-off frequency $\nu_{\rm c}$ of the power law with high-frequency cut-off. We investigated correlations between the $\log_{10}$ of the following pulsar properties:

1. spin frequency $\tilde{\nu}$,
2. spin-down rate $\left|\dot{\tilde{\nu}}\right|$,
3. period derivative $\dot{P}$,
4. dispersion measure DM,
5. magnetic field at the light cylinder radius $B_{\rm LC}$,
6. characteristic age τ,
7. spin-down luminosity $\dot{E}$,
8. luminosity at 400 MHz L_{400} and
9. luminosity at 1400 MHz L_{1400}.

Each correlation was calculated for the following pulsar populations: all pulsars, pulsars in a binary, isolated pulsars (not in a binary), MSPs and slow (normal) pulsars.

We calculated the Spearman correlation coefficient for each combination of spectral property, pulsar property and pulsar population type, which can be seen in Table 6.5. Such a large number of correlations (105) increases the probability of incorrectly rejecting the null hypothesis. This is known as the multiple testing problem. To prevent the multiple testing problem from causing erroneous inferences, we use the Bonferroni correction method to counteract this:

$$\rho_{\mathrm{B}} = \frac{\rho_{\mathrm{d}}}{m} \tag{6.1}$$

where ρ_{d} is the desired confidence interval, m is the number of hypotheses and ρ_{B} is the Bonferroni corrected confidence interval. The correction reduces the ρ value we check for from 0.01 to 0.000095238. A correlation is significant if the coefficient is above 0.4 and the ρ is less than 0.000095238, which are marked in bold in Table 6.5,

As previously mentioned, we only use α values from simple power law models. We also only use values between 0 and -4 to remove outliers and poorly sampled parts of the population. For ν_{c}, we only use power law with high-frequency cut-off as the double turn-over spectrum ν_{c} is not reliable whenever there are insufficient high-frequency measurements sampling the cut-off. We also removed low luminosity pulsars ($L_{400} < 3$ and $L_{1400} < 0.1$) as that population is not well sampled.

6.3.2 Correlation with all pulsar parameters

The results of our investigations into the correlations between the spectral properties (spectral index α, the peak frequency ν_{peak}, and the cut-off frequency ν_{c}) and pulsars' parameters can be seen in Table 6.5. The significant correlations are shown in bold and discussed in either §6.3.6 if they are likely due to a selection

bias or §6.3.7 if they are likely theoretically motivated.

α Correlation Coefficient

set	all	in binary	isolated	MSP	slow
#pulsars	611	52	559	53	558
$log_{10}(x)$	$r_s(p, N)$	$r_s(p, N)$	$r_s(p, N)$	$r_s(p, N)$	$r_s(p, N)$
$\tilde{\nu}$	0.15 (2.0e-04, 595)	−0.16 (2.6e-01, 51)	0.19 (6.4e-06, 544)	−0.15 (2.9e-01, 52)	0.21 (1.4e-06, 543)
$\lvert\dot{\tilde{\nu}}\rvert$	0.13 (1.4e-03, 589)	−0.20 (1.7e-01, 51)	0.16 (1.4e-04, 538)	−0.28 (4.6e-02, 52)	0.16 (1.6e-04, 537)
$\dot{P}$	0.08 (4.8e-02, 588)	0.04 (7.9e-01, 51)	0.09 (3.6e-02, 537)	−0.21 (1.4e-01, 51)	0.08 (5.5e-02, 537)
DM	−0.12 (2.8e-03, 595)	−0.12 (3.8e-01, 51)	−0.13 (1.6e-03, 544)	−0.26 (6.4e-02, 52)	−0.14 (1.1e-03, 543)
B_{LC}	−0.13 (1.6e-03, 588)	0.16 (2.5e-01, 51)	−0.16 (1.2e-04, 537)	0.12 (4.0e-01, 51)	−0.17 (5.2e-05, 537)
τ	−0.12 (3.3e-03, 588)	0.01 (9.5e-01, 51)	−0.14 (1.2e-03, 537)	0.28 (4.3e-02, 51)	−0.13 (2.0e-03, 537)
$\dot{E}$	0.16 (6.4e-05, 588)	−0.17 (2.3e-01, 51)	0.19 (1.0e-05, 537)	−0.26 (6.7e-02, 51)	0.18 (1.9e-05, 537)
L_{400}	−0.39 (3.0e-21, 550)	−0.16 (3.3e-01, 41)	**−0.44** (2.2e-25, 509)	−0.27 (8.8e-02, 40)	**−0.44** (3.5e-25, 510)
L_{1400}	0.02 (6.6e-01, 574)	0.15 (3.1e-01, 48)	−0.00 (9.8e-01, 526)	−0.00 (9.9e-01, 50)	0.01 (8.0e-01, 524)

Low-frequency turnover frequency (MHz) Correlation Coefficient

set	all	in binary	isolated	MSP	slow
#pulsars	121	12	109	18	103
$log_{10}(x)$	$r_s(p, N)$	$r_s(p, N)$	$r_s(p, N)$	$r_s(p, N)$	$r_s(p, N)$
$\tilde{\nu}$	0.33 (2.3e-04, 121)	0.13 (7.0e-01, 12)	0.36 (1.1e-04, 109)	0.12 (6.4e-01, 18)	0.40 (3.0e-05, 103)
$\lvert\dot{\tilde{\nu}}\rvert$	0.38 (1.9e-05, 121)	−0.01 (9.8e-01, 12)	**0.42** (4.6e-06, 109)	−0.16 (5.2e-01, 18)	**0.52** (1.5e-08, 103)
$\dot{P}$	0.32 (3.9e-04, 118)	−0.13 (7.1e-01, 11)	0.40 (2.5e-05, 107)	−0.38 (1.6e-01, 15)	**0.41** (1.6e-05, 103)
DM	**0.56** (1.6e-11, 121)	0.67 (1.7e-02, 12)	**0.58** (3.5e-11, 109)	0.29 (2.4e-01, 18)	**0.66** (2.0e-14, 103)
B_{LC}	−0.20 (2.6e-02, 118)	−0.06 (8.5e-01, 11)	−0.23 (1.8e-02, 107)	−0.07 (8.1e-01, 15)	−0.28 (4.8e-03, 103)
τ	−0.39 (1.3e-05, 118)	0.15 (6.5e-01, 11)	**−0.47** (4.1e-07, 107)	0.29 (3.0e-01, 15)	**−0.49** (1.1e-07, 103)
$\dot{E}$	**0.46** (1.3e-07, 118)	−0.21 (5.4e-01, 11)	**0.48** (1.8e-07, 107)	−0.19 (4.9e-01, 15)	**0.53** (1.2e-08, 103)
L_{400}	−0.00 (9.7e-01, 106)	−0.10 (8.2e-01, 8)	0.02 (8.2e-01, 98)	−0.36 (3.1e-01, 10)	0.09 (4.1e-01, 96)
L_{1400}	0.34 (2.1e-04, 112)	0.28 (4.6e-01, 9)	0.38 (6.6e-05, 103)	0.20 (5.2e-01, 13)	**0.45** (3.0e-06, 99)

High-frequency cut off frequency (MHz) Correlation Coefficient

set	all	in binary	isolated	MSP	slow
#pulsars	123	10	113	14	109
$log_{10}(x)$	$r_s(p, N)$	$r_s(p, N)$	$r_s(p, N)$	$r_s(p, N)$	$r_s(p, N)$
$\tilde{\nu}$	0.39 (4.1e-05, 106)	−0.04 (9.4e-01, 7)	**0.40** (4.0e-05, 99)	−0.10 (8.2e-01, 8)	**0.40** (3.7e-05, 98)
$\lvert\dot{\tilde{\nu}}\rvert$	**0.40** (1.8e-05, 106)	0.14 (7.6e-01, 7)	**0.47** (1.1e-06, 99)	−0.12 (7.8e-01, 8)	**0.52** (4.9e-08, 98)
$\dot{P}$	0.24 (1.5e-02, 106)	−0.46 (2.9e-01, 7)	0.29 (3.8e-03, 99)	−0.52 (1.8e-01, 8)	0.35 (4.8e-04, 98)
DM	0.37 (9.4e-05, 106)	−0.21 (6.4e-01, 7)	**0.43** (7.0e-06, 99)	−0.19 (6.5e-01, 8)	**0.45** (2.8e-06, 98)
B_{LC}	−0.28 (4.3e-03, 106)	0.04 (9.4e-01, 7)	−0.27 (6.1e-03, 99)	0.05 (9.1e-01, 8)	−0.27 (6.9e-03, 98)
τ	−0.34 (3.0e-04, 106)	0.21 (6.4e-01, 7)	−0.39 (5.7e-05, 99)	0.29 (4.9e-01, 8)	**−0.47** (8.7e-07, 98)
$\dot{E}$	**0.50** (6.9e-08, 106)	0.29 (5.3e-01, 7)	**0.51** (9.4e-08, 99)	−0.12 (7.8e-01, 8)	**0.51** (7.4e-08, 98)
L_{400}	−0.02 (8.0e-01, 102)	−0.26 (6.2e-01, 6)	0.02 (8.4e-01, 96)	−0.21 (6.4e-01, 7)	0.01 (8.9e-01, 95)
L_{1400}	0.26 (8.5e-03, 103)	0.04 (9.4e-01, 7)	0.31 (1.9e-03, 96)	0.14 (7.4e-01, 8)	0.31 (2.6e-03, 95)

Table 6.5: The correlations between the spectral properties (spectral index α, the peak frequency ν_{peak}, and the cut-off frequency ν_c) and pulsars' parameters. r_s is the Spearman correlation coefficient, p is the confidence interval and N is the number of pulsars. A correlation is considered significant if $r_s > 0.4$ and $p < 0.000095238$, these are shown in bold.

6.3.3 Comparison with Jankowski et al. (2018)

Our spectral fitting and correlation method are similar to that used in Jankowski et al. (2018). Hence, any deviations are likely due to the improvement of our

catalogue in both the number of pulsars and the number of flux density measurements. When comparing Table 11 of Jankowski et al. (2018) to Table 6.5, we see none of the significant correlations from Jankowski et al. (2018).

To investigate if the correlations that Jankowski et al. (2018) were biased by the pulsars they selected, we have created Table 6.6 using only the 441 pulsars used by Jankowski et al. (2018). The only significant correlation in Table 6.6 is with $\dot{E}$, which is only just on the threshold we set of 0.4. This reduction in correlation coefficients is likely due to the increase in the number and frequency range of the flux density measurements in the `pulsar_spectra` catalogue, leading to a less biased result.

	α Correlation Coefficient				
set	all	in binary	isolated	MSP	slow
#pulsars	248	8	240	7	241
$log_{10}(x)$	$r_s(p, N)$	$r_s(p, N)$	$r_s(p, N)$	$r_s(p, N)$	$r_s(p, N)$
$\tilde{\nu}$	0.37 (3.9e-09, 245)	-0.21 (6.1e-01, 8)	0.37 (2.6e-09, 237)	-0.11 (8.2e-01, 7)	0.37 (3.4e-09, 238)
$\lvert\dot{\tilde{\nu}}\rvert$	0.36 (1.2e-08, 243)	0.62 (1.0e-01, 8)	0.39 (7.9e-10, 235)	0.43 (3.4e-01, 7)	0.38 (1.1e-09, 236)
$\dot{P}$	0.22 (5.6e-04, 243)	0.36 (3.9e-01, 8)	0.25 (1.1e-04, 235)	0.39 (3.8e-01, 7)	0.25 (1.4e-04, 236)
$B_{\rm LC}$	-0.29 (5.3e-06, 243)	0.36 (3.9e-01, 8)	-0.29 (6.1e-06, 235)	0.29 (5.3e-01, 7)	-0.29 (6.3e-06, 236)
τ	-0.31 (8.7e-07, 243)	-0.55 (1.6e-01, 8)	-0.34 (5.9e-08, 235)	-0.50 (2.5e-01, 7)	-0.34 (8.5e-08, 236)
$\dot{E}$	**0.40** (8.5e-11, 243)	0.29 (4.9e-01, 8)	**0.41** (6.5e-11, 235)	0.39 (3.8e-01, 7)	**0.40** (1.4e-10, 236)

Table 6.6: Correlation Coefficients of spectral index power law fits of the 248 of the 441 pulsars from Jankowski et al. (2018).

6.3.4 Lack of high-frequency data causing underestimation of ν_c

As shown in Figure 6.4, there is a bimodal distribution of ν_c. The lack of ν_c at $\sim$3.2 GHz could be due to 1$-$3 GHz being a favoured frequency for telescopes such as Parkes.

To confirm this is an observational bias, all pulsars with a ν_c value greater than 3 GHz were refit with all flux density measurements about 3 GHz removed. Many returned to SPL fits as expected, but several remained HFCO fits with significantly lower ν_c values, as shown in Figure 6.5. This suggests that ν_c can be underestimated and should be confirmed with high-frequency non-detections.

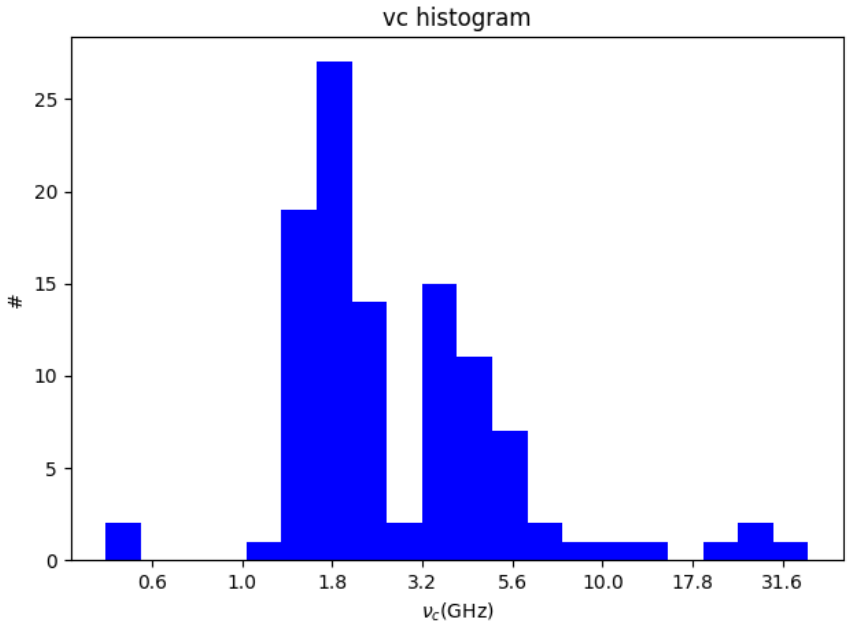

Figure 6.4: Histogram of the distribution of high-frequency cut-off (ν_c) values for power law with high-frequency cut-off model fits. The lack of values at ∼3.2 GHz suggests a bias in the current method.

Currently, `pulsar_spectra` does not include non-detections in the catalogue or the spectral fitting, but this feature will likely be implemented in the future.

6.3.5 Potential causes of low-frequency turn-over other than absorption

The expected cause of the low-frequency turn-over in the power law with low-frequency turn-over model we use (Equation 5.7) is synchrotron self or thermal free-free absorption of the medium surrounding the pulsar. This is not the only cause of an apparent low-frequency turn-over, and our current method's ability to separate them is limited.

One cause of an apparent low-frequency turn-over is scintillation when flux density measurements are calculated using only a single observation, so the apparent flux density varies. This can be corrected by averaging several measurements over a period longer than the scintillation timescale. Since our database does not

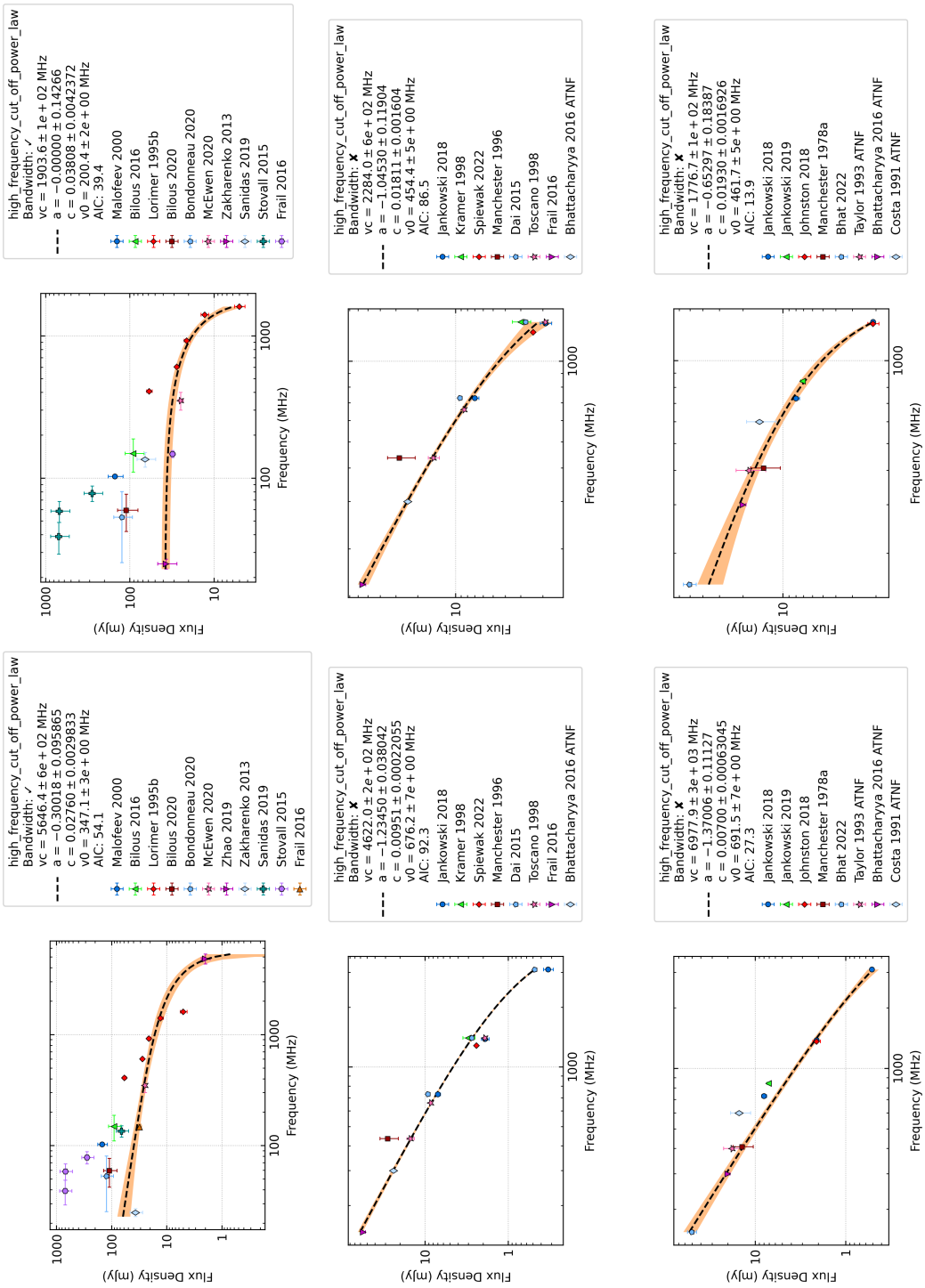

Figure 6.5: On the left are the original fits of J0454+5543, J1045−4509 and J1320−5359, respectively and on the right are refits with all flux density measurements above 3 GHz removed.

include if this scintillation averaging has been performed, we can not rule out scintillation causing the best fit spectral model to be incorrect. If the low-frequency flux density values are scintillating down it causes an apparent low-frequency turn-over model to be fit or if the values are scintillating up it causes an apparent simple power law to be fit.

Multi-path scattering can cause a scattering tail longer than the pulsar's period, which can artificially raise the noise baseline, lowering the apparent flux density and possibly causing an apparent low-frequency turn-over (Bhat et al., 2004; Lewandowski et al., 2015). One example of this effect is shown in Figure 6.6a, which has a scattering tail much longer than the pulse period at MWA frequencies. This causes the flux density to be underestimated by an order of magnitude compared to flux densities at similar frequencies, as shown in Figure 6.6b. If this was the only measurement at low frequencies, the spectra could have been incorrectly modelled as having a low-frequency turn-over. Although it is easy to tell if the apparent flux density has been lowered by scattering by investigating the pulse profile, this is not included in our database, so it can't be ruled out automatically.

Other theoretical models can explain low-frequency turn-overs (e.g. Löhmer et al., 2008), so our current method needs to be revised as it can not separate these potential causes of a low-frequency turn-over.

6.3.6 Apparently significant individual correlations due to observational bias

This section will discuss each significant correlation, as shown in Table 6.5, that is likely due to observational bias rather than an underlying theoretical motivation.

6.3.6.1 α with L_{400}

There is a correlation coefficient of -0.44 for isolated slow pulsars between their L_{400} and α (see Figure 6.7). This suggests that brighter pulsars have steeper

spectral indexes. Because there is no such correlation (0.02) between L_{1400} and α, this is not correlated with the pulsar's total luminosity. This is, therefore, likely a selection effect caused by steep spectrum pulsars being brighter at low frequencies. Regardless, this demonstrates that a range of frequencies is required to accurately investigate pulsars' luminosity distribution.

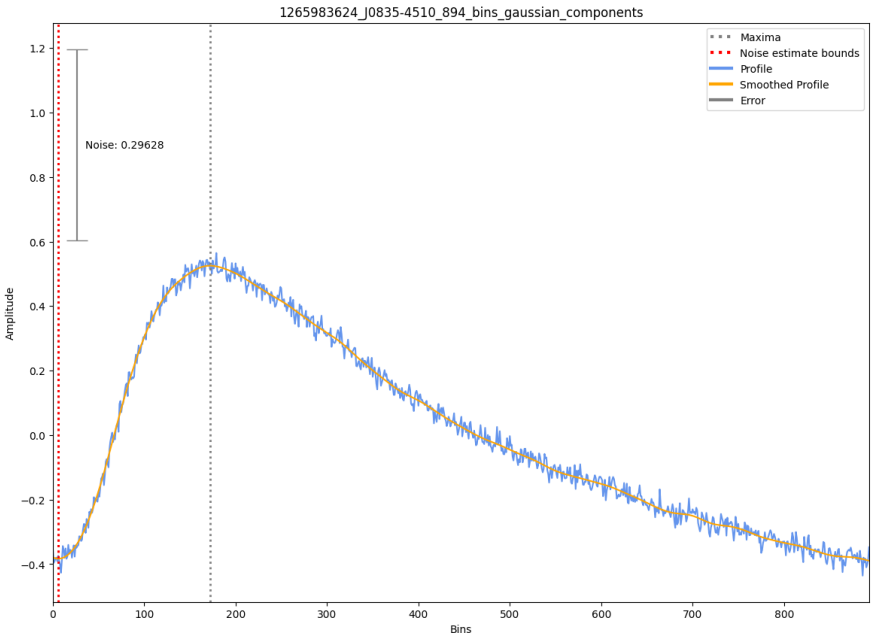

(a) The pulse profile of an MWA detection of PSR J0835−4510. The scattering tail is longer than the pulse period, which causes the noise baseline to be overestimated and the flux density to be underestimated.

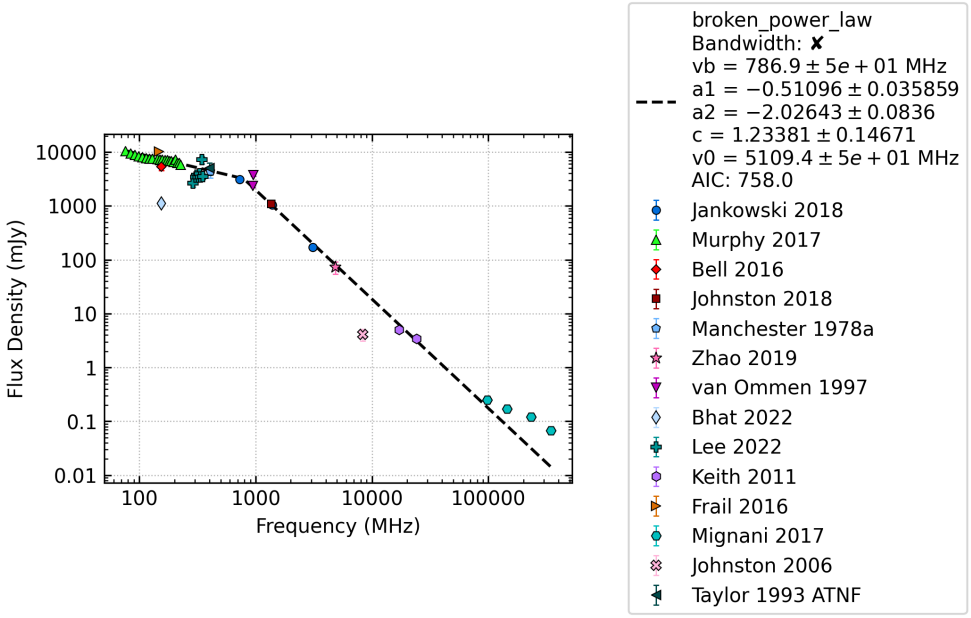

(b) The spectral fit of PSR J0835−4510. The flux density of the MWA detection (Bhat_2022) is underestimated by an order of magnitude compared to the flux densities at similar frequencies.

Figure 6.6: A detection of PSR J0835−4510 with the MWA as an example of how multipath scattering can reduce the apparent flux density estimation.

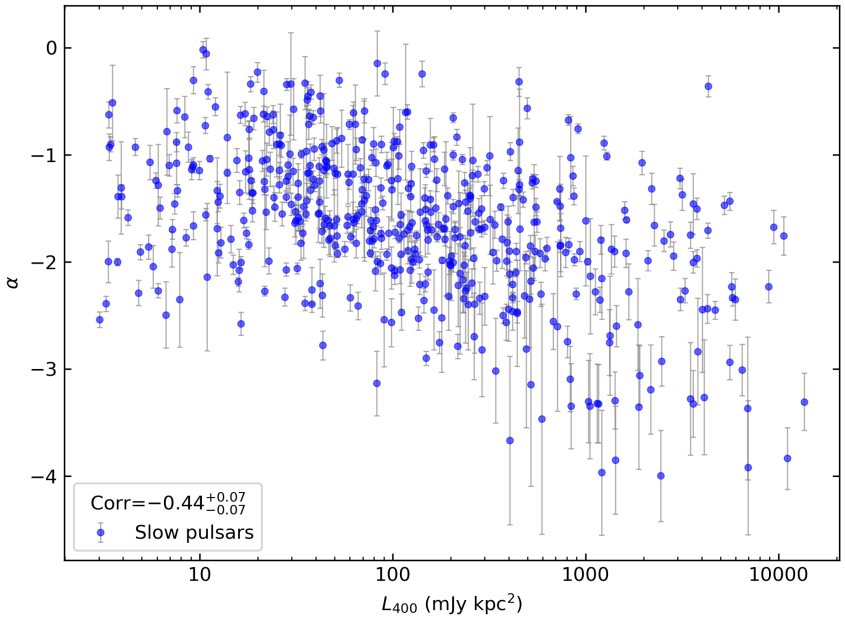

Figure 6.7: The correlation between α and L_{400} for slow pulsars.

6.3.6.2 $\nu_{\rm peak}$ with L_{1400}

There is a correlation coefficient of 0.45 for slow pulsars between their $\nu_{\rm peak}$ and L_{1400}, see Figure 6.8. Similar to §6.3.6.1, there is no correlation with L_{400} and $\nu_{\rm peak}$, so this is no correlation with the total luminosity. This correlation is likely a selection bias caused by the higher $\nu_{\rm peak}$ means the luminosity is more likely to peak at a high frequency such as 1.4GHz.

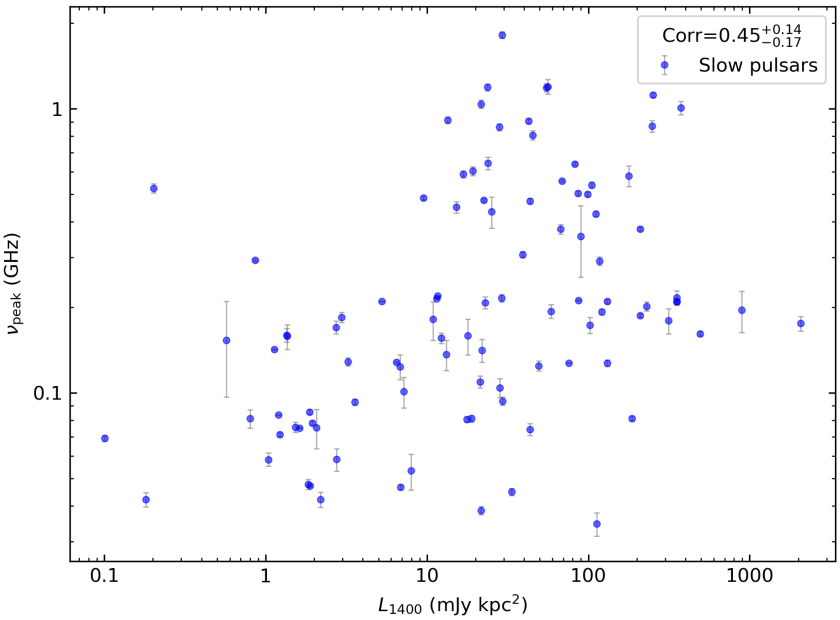

Figure 6.8: The correlation between $\nu_{\rm peak}$ and L_{1400} for slow pulsars.

6.3.6.3 $\nu_{\rm peak}$ and $\nu_{\rm c}$ with DM

For slow pulsars, there is a correlation coefficient of 0.66 between $\nu_{\rm peak}$ and DM (see Figure 6.9a) and 0.45 between $\nu_{\rm c}$ and DM (see Figure 6.9b).

The low-frequency turn-over at $\nu_{\rm peak}$ is caused by absorption and thus could be due to an increased density of the surrounding medium. A denser surrounding medium would affect the DM, but it would be near insignificant (<1%), so this correlation is unlikely due to the surrounding medium. There can not be an actual correlation between $\nu_{\rm c}$ and DM. Therefore, it must be a selection bias such as the bimodal distribution of $\nu_{\rm c}$ (see §6.3.4).

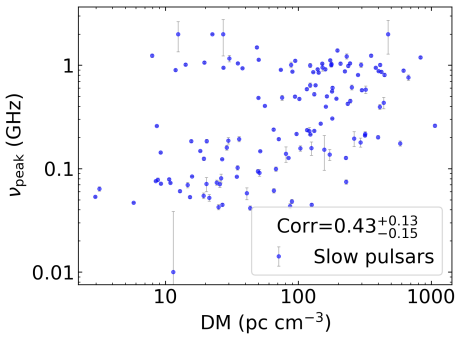

(a) The correlation between ν_{peak} and DM for slow pulsars.

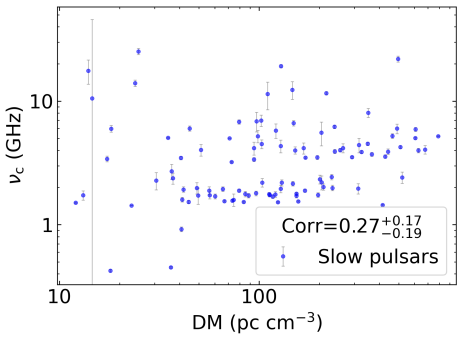

(b) The correlation between ν_c and DM for slow pulsars.

Figure 6.9: The correlations of DM for slow pulsars.

High DM pulsars are often found at higher frequencies (due to the reduced effects of dispersion smearing and scattering), and low DM pulsars are often found at low frequencies as their surveys spend longer dwell times above the Galactic plane than high-frequency surveys. The peak of a pulsar's emission is likely to peak near the frequency it was discovered, which can lead to a selection bias in both ν_{peak} and ν_c.

The lack of pulsars in the bottom right quadrant of Figure 6.9a is likely due to the difficulty of detecting low-frequency turn-overs at high DMs. The effects of dispersion smearing and scattering will significantly lower the sensitivity of low-frequency telescopes, making them unable to make flux density measurements as the spectrum starts to turn over. The lack of low-frequency flux density measurements causes the spectrum to appear to be a simple power law, making ν_{peak} measurements impossible.

There is no reason for the lack of pulsars in the top left of Figure 6.9a as there is no dispersion caused sensitivity loss for ν_{peak} at high frequencies. Therefore, this selection bias is caused by high-frequency surveys spending insufficient time away from the galactic plane to find low DM pulsars. To find high-frequency ν_{peak} for low-DM pulsars, they must be discovered at high frequencies as it is unlikely that low-frequency surveys would be sensitive enough to find a pulsar that has

already turned over. This bias should be considered when planning new surveys and performing pulsar population synthesis.

Alternatively, the pulsars in the top right quadrant of Figure 6.9a could be overestimating their $\nu_{\rm peak}$ due to scattering. For example, PSR J1818−1422 already shows a long scattering tail at 1.4 GHz (Johnston & Kerr, 2018), so the $\nu_{\rm peak}$ at 868 MHz could be due to multi-path scattering instead of absorption leading to a nugatory correlation as it consists of two different effects.

6.3.6.4 $\nu_{\rm peak}$ and $\nu_{\rm c}$ with $\left|\dot{\tilde{\nu}}\right|$

For slow pulsars, there is a correlation coefficient of 0.52 between $\nu_{\rm peak}$ and $\left|\dot{\tilde{\nu}}\right|$ (see Figure 6.11a) and 0.52 between $\nu_{\rm c}$ and $\left|\dot{\tilde{\nu}}\right|$ (see Figure 6.11b). These figures look very similar to Figure 6.13, so to investigate we substitute the equation $\dot{P} = -\nu P^2$ into Equation 1.14 to get

$$\dot{E} \simeq 3.95 \times 10^{31} \frac{\dot{\nu}}{P}. \tag{6.2}$$

Figure 6.10 shows the inverse correlation between $\dot{\nu}$, which is spread over ≈ 7 orders of magnitude, and P, which is spread over ≈ 3 orders of magnitude, for slow pulsars. Since the value of $\dot{E}$ is dominated by $\dot{\nu}$, the correlation plots for $\dot{E}$ (Figure 6.13) and $\left|\dot{\tilde{\nu}}\right|$ (Figure 6.11) appear to be very similar. Because $\dot{E}$ is more indicative of underlying pulsar properties, we conclude that the correlation $\nu_{\rm peak}$ and $\left|\dot{\tilde{\nu}}\right|$ is caused by the correlation between $\left|\dot{\tilde{\nu}}\right|$ and $\dot{E}$ and is, therefore, a selection bias.

6.3.7 Significant individual correlations with theoretical motivations

This section will discuss each significant correlation, as shown in Table 6.5, that is likely due to an underlying theoretical motivation.

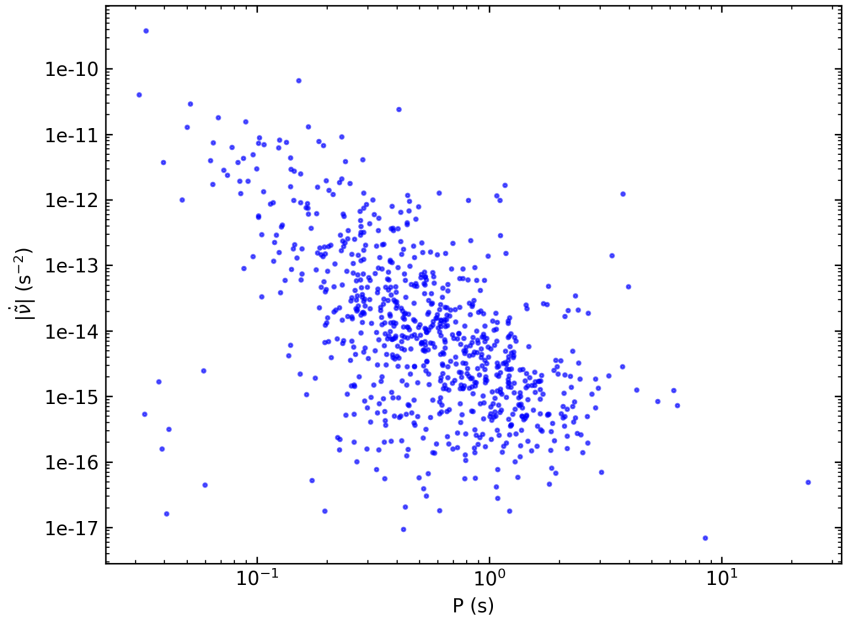

Figure 6.10: The correlation between $\left|\dot{\tilde{\nu}}\right|$ and period for slow pulsars, essentially the inverse of the $P - \dot{P}$ diagram.

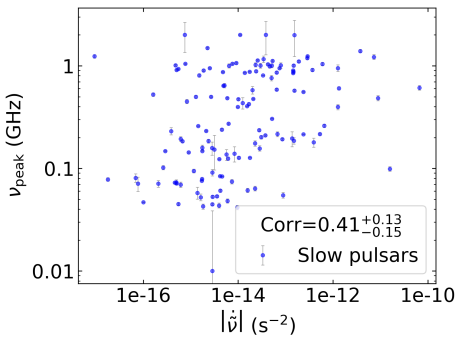

(a) The correlation between ν_{peak} and $\left|\dot{\tilde{\nu}}\right|$ for slow pulsars.

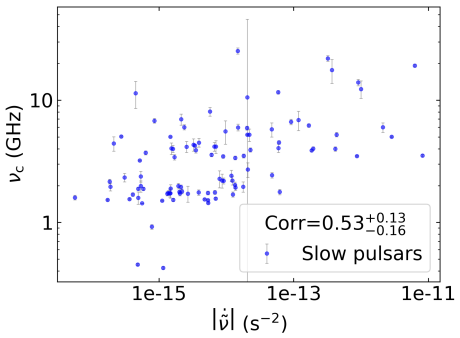

(b) The correlation between ν_{c} and $\left|\dot{\tilde{\nu}}\right|$ for slow pulsars.

Figure 6.11: The correlations of $\left|\dot{\tilde{\nu}}\right|$ for slow pulsars.

6.3.7.1 ν_c with $\tilde{\nu}$

For slow pulsars, there is a correlation coefficient of 0.4 between ν_c and $\tilde{\nu}$ (see Figure 6.12), which was predicted by Kontorovich & Flanchik (2013). The predicted trend, Equation 1.20, has been plotted in purple in Figure 6.12. Our results follow the prediction for slow pulsars but diverge for MSPs. Since the theory makes assumptions about the magnetic field, it follows that MSPs diverge as they are known for having differing/weaker magnetic fields.

Equation 1.20 appears to underestimate the value of ν_c and given the possible underestimation of our values of ν_c, see §6.3.4, this difference could be even more significant. This suggests that the maximum electric field in the polar gap is underestimated. There is also a large spread in the measured values of ν_c compared to the uncertainties based on theory. The measured spread could be due to assumptions in the theoretical prediction and inaccuracies in the high-frequency cut-off measurement caused by the cut-off curve often only being constrained by a single flux density measurement.

6.3.7.2 ν_c and ν_{peak} with $\dot{E}$

Spin-down luminosity has a strong correlation with ν_{peak} and ν_c with slow pulsars, as shown in Figure 6.13. This indicates that the peak emission region of the pulsar is at higher frequencies for pulsars with higher spin-down luminosity.

Using Equation 1.20 and Equation 1.14, we can show that spin-down luminosity is inversely proportional to theoretically predicted ν_c based on the spin frequency:

$$\dot{E} \propto \tilde{\nu}^3 \propto \nu_c^{-6.52}. \tag{6.3}$$

This contradicts the trend shown in Figure 6.13b, which suggests this trend is not caused by the relativistic limits in the pulsar's polar gap.

In a broad sense, this is logical as higher power (spin-down luminosity) often

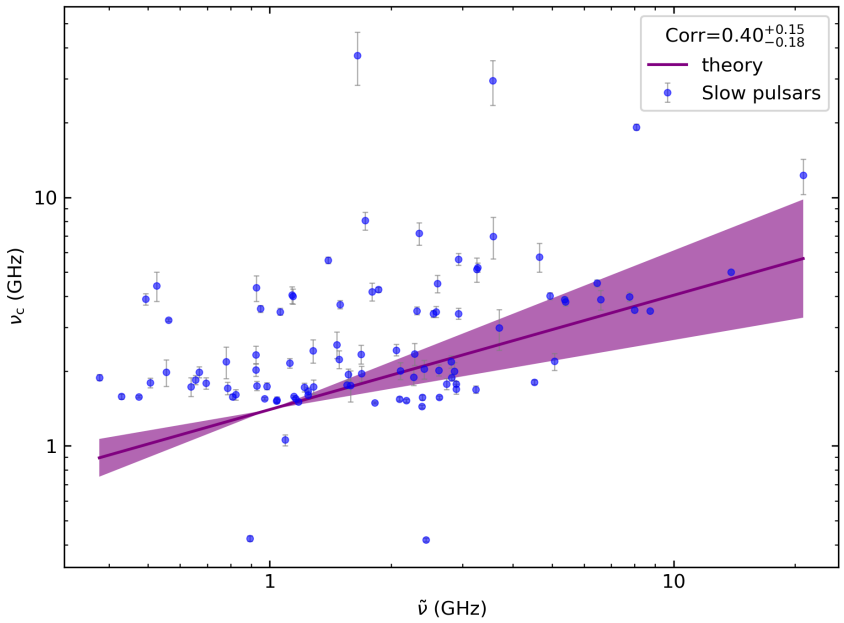

Figure 6.12: The correlation between ν_c and $\tilde{\nu}$ for slow pulsars. The theoretical relation predicted by Kontorovich & Flanchik (2013) ($\nu_c = 1.4\text{GHz}\left(\frac{P}{s}\right)^{0.46\pm0.18}$) is shown in purple. The deviation from theory is likely due to underestimating the maximum electric field in the polar gap, the assumptions made in $\nu_c = 1.4\text{GHz}\left(\frac{P}{s}\right)^{0.46\pm0.18}$ and the inaccuracy of ν_c measurements.

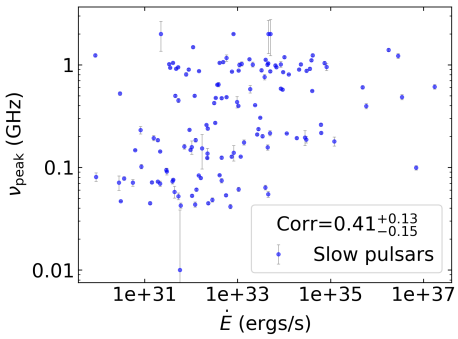

(a) The correlation between ν_{peak} and $\dot{E}$ for slow pulsars.

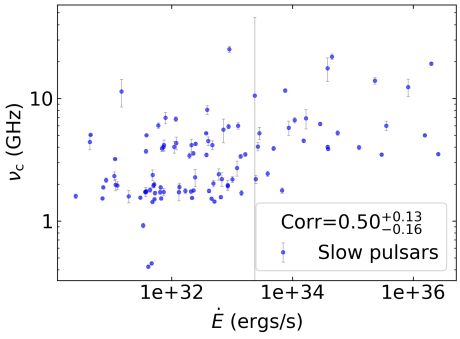

(b) The correlation between ν_c and $\dot{E}$ for slow pulsars.

Figure 6.13: The correlations of $\dot{E}$ for slow pulsars.

leads to higher frequency emission. Because this power is emitted as a combination of high-energy radiation, magnetic dipole radiation, pulsar wind and radio emission, it is difficult to determine its actual cause. Although it is unlikely that the cause is magnetic dipole radiation due to there being no correlation between ν_c and magnetic field.

6.3.7.3 ν_{peak} and ν_c with τ

Both ν_{peak} and ν_c have a strong negative correlation with τ, see Figure 6.14. This implies that as pulsars age, their emission occurs at lower frequencies. This correlation is not seen in MSPs, but this is expected since τ is an approximation for slow pulsars, not MSPs that have gone through accretion. This also agrees with §6.3.7.2 as spin-down luminosity decreases as pulsar age.

This demonstrates the importance of pulsar surveys at various frequencies to detect pulsars of various ages. This evolution of pulsar spectra should also be included in pulsar population simulations to accurately account for our sensitivity to pulsars of different ages.

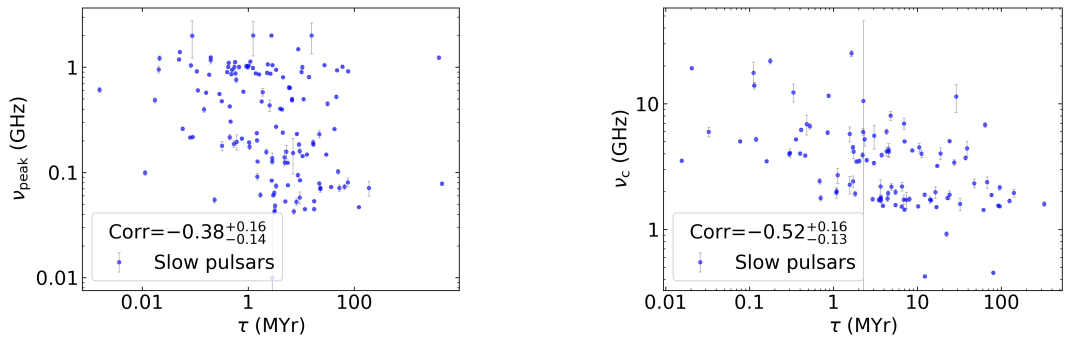

(a) ν_{peak} and τ (b) ν_c and τ

Figure 6.14: The correlations of τ for slow pulsars.

6.4 The spectra of millisecond pulsars

The differing evolution of MSPs and slow pulsars means they should be treated as different populations of pulsars. The differences in their spectra allow us to study the difference between the two populations.

As seen in Table 6.3, the distribution of spectral models between MSPs and slow pulsars is similar (within 8%). This suggests that the type of spectra does not change when evolving into an MSP, although the values of their spectral parameters might.

6.4.1 The spectral index of millisecond pulsars

The spectral index of MSPs has historically been believed to be steeper than slow pulsars. For example, (Toscano et al., 1998) stated that slow pulsars have a mean spectral index of -1.7 and MSPs have -1.9. In Table 6.7, we compare the mean spectral index of slow pulsars to MSPs and find that MSPs are only slightly steeper and within their uncertainty range. There is a significant difference between the mean spectral index that Spiewak et al. (2022); Dai et al. (2015); Toscano et al. (1998) found and our work.

This difference may be due to the high-frequency range ($>$ 400 MHz) that Spiewak et al. (2022); Dai et al. (2015); Toscano et al. (1998) used, as only using high-frequency flux measurements favours steep spectral index measurements (e.g. Maron et al., 2000; Toscano et al., 1998). The full Spiewak et al. (2022) data set should be included in the `pulsar_spectra` catalogue to test this difference more robustly, but this still needs to be done.

Our mean spectral index agrees with Kramer et al. (1999), but this may be due to the low number of MSPs and flux density measurements. Both our work and Kramer et al. (1999) suggest that MSPs do not have significantly steeper spectra than slow pulsars, which suggests that the apparent steeper spectra of MSPs are a selection bias caused by favouring high-frequency measurements.

[3]Dai et al. (2015) made measurements at three bands and calculated the two spectral indices,

Publication	Frequency (GHz)	Slow #	Slow α	MSP #	MSP α
This work	0.02 – 343.50	611	-1.61 ± 0.03	53	-1.69 ± 0.05
Spiewak et al. (2022)	0.58 – 1.67	-	-	189	-1.92 ± 0.06
Dai et al. (2015)	0.70 – 3.60	-	-	24	-1.79 ± 0.02[3]
Kramer et al. (1999)	2.70 – 4.90	-	-	16	-1.6 ± 0.1
Toscano et al. (1998)	0.42 – 1.62	216	1.72 ± 0.04	19	-1.9 ± 0.1

Table 6.7: Comparison of the mean spectral index and for the slow pulsars and MSPs of our sample and other publications.

The distributions of spectral indices of the MSPs and slow pulsars are compared in Figure 6.15. It can be seen that they are both approximately Gaussian, centred at ~ -1.65 and are not skewed. The slow pulsars appear to have a wider spread of spectral indices, but that is likely due to their larger population. This is consistent with there being no significant difference between MSP and slow pulsar spectra.

6.4.2 The low-frequency turn-over of millisecond pulsars

Kuzmin & Losovsky (2001) suggested that MSPs have no low-frequency turn-over after measuring 30 MSPs and finding no turn-over above 102 MHz. However, the algorithm used in `pulsar_spectra` identifies power law with low-frequency turn-over's as the preferred model for 12 MSPs in our sample, 10 of which have turn-over frequencies above 102 MHz. On the face of these results, this would invalidate Kuzmin & Losovsky (2001)'s claim. However, on closer inspection, there are possible reasons to doubt the validity of our results for almost all of our fits, see Figure 6.17. In some cases (PSRs J0024−7204J, J0621+1002 and J0711−6830), the fit measures a low-frequency flattening but does not measure enough low-frequency points below $\nu_{\rm peak}$ to be confident of a low-frequency turn-over. In other cases (PSRs J0030+0451, J1300+1240 and J0613−0200) where the fit appears

one between the highest and centre band ($\alpha_1 = 1.76 \pm 0.01$) and the other between the centre and lowest band ($\alpha_2 = 1.81 \pm 0.01$), so we averaged these values.

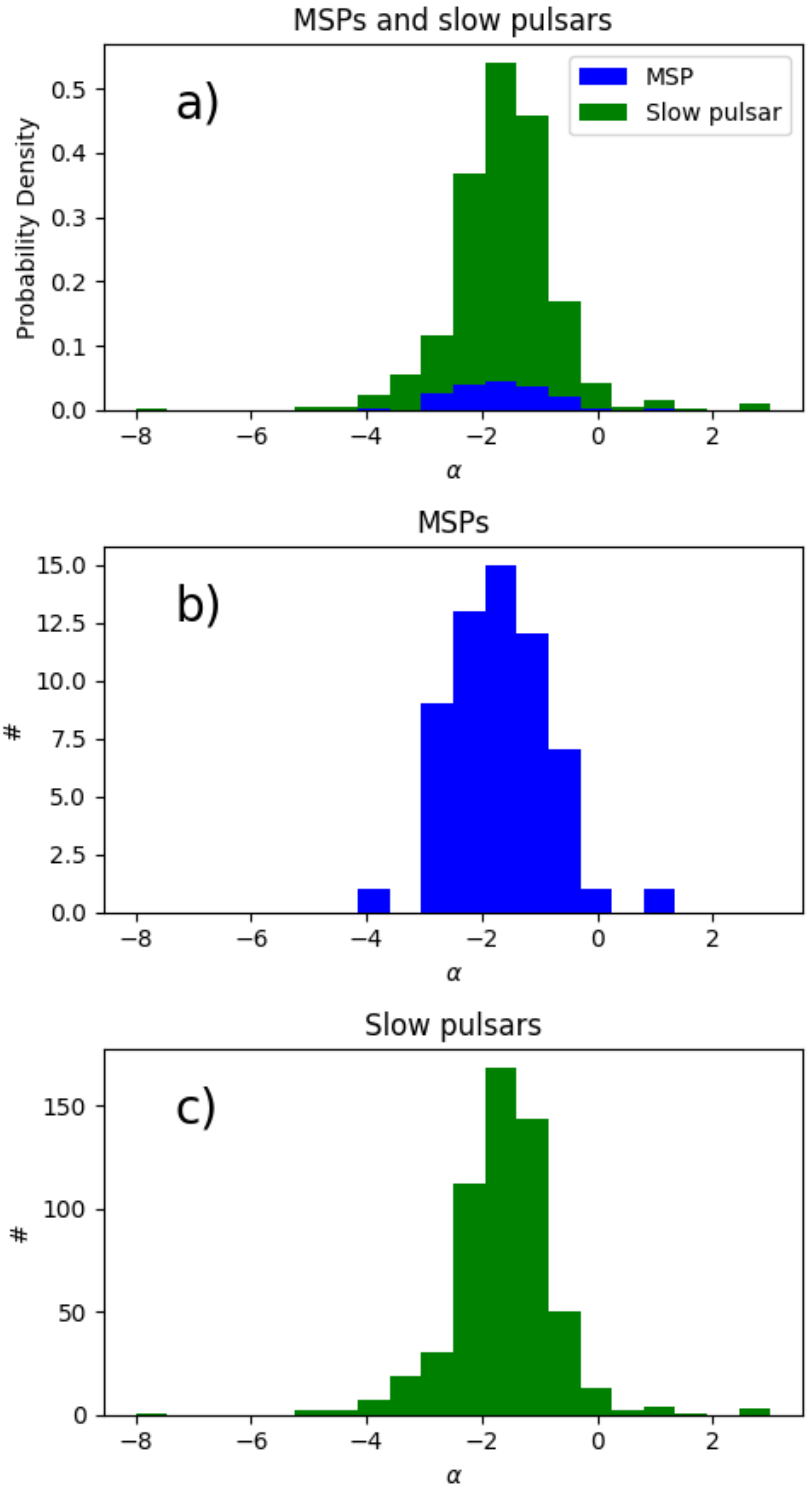

Figure 6.15: Comparison of the spectral index distributions of the MSP and slow pulsar samples.

to overestimate the steepness of the turn-over when there are sizeable fractional bandwidth measurements. There are also cases (PSRs J1600−3053, J1623−2631 and J1603−7202), the algorithm is clearly down-weighting the lowest-frequency point more than seems reasonable. These potential inaccuracies are further discussed in §6.4.2.1. Kuzmin & Losovsky (2001) suggested that MSPs' different magnetic field structures can explain the apparent absence of turn-over. However, as the turn-over can be due to thermal absorption of the surrounding medium, we believe Kuzmin & Losovsky (2001)'s explanation is incomplete.

It has been observed by (Malofeev, 1996) that normal pulsars' turn-over frequency follows the trend shown in Equation 1.24. This has already been shown to overestimate $\nu_{\rm peak}$ by Kuzmin & Losovsky (2001) as they found no turn-over above 102 MHz when MSPs with a period of $P \leq 50$ ms are predicted to turn over at $\nu_{\rm peak} \geq 350$ MHz. Figure 6.16 confirms that Equation 1.24 is not valid for MSPs.

6.4.2.1 The potential inaccuracies in low-frequency turn-over fit

Although 12 pulsars were found to have a low-frequency turn-over, our data and method still need to be improved to be confident with all 12, as shown in Figure 6.17. While we are confident in some fits, like PSRs J0024−7204, J0214+5222 and J2124−3358 (see Figure 6.17 (a) and (b)), exhibit at least a low-frequency flattening if not a low-frequency turn over, the other MSPs are examples of potentially inaccurate spectral fits.

PSRs J0024−7204J, J0621+1002 and J0711−6830 (see Figure 6.17 (c) and (d) for example) have spectra that have begun to turn over, but since we have no flux density measurements lower than $\nu_{\rm peak}$, we can not be confident that this is a low-frequency turn-over. This demonstrates the need for more low-frequency measurements of MSPs

PSRs J0030+0451, J1300+1240 and J0613−0200 (see Figure 6.17 (e) and (f) for example) have flux density measurements with large fractional bandwidths

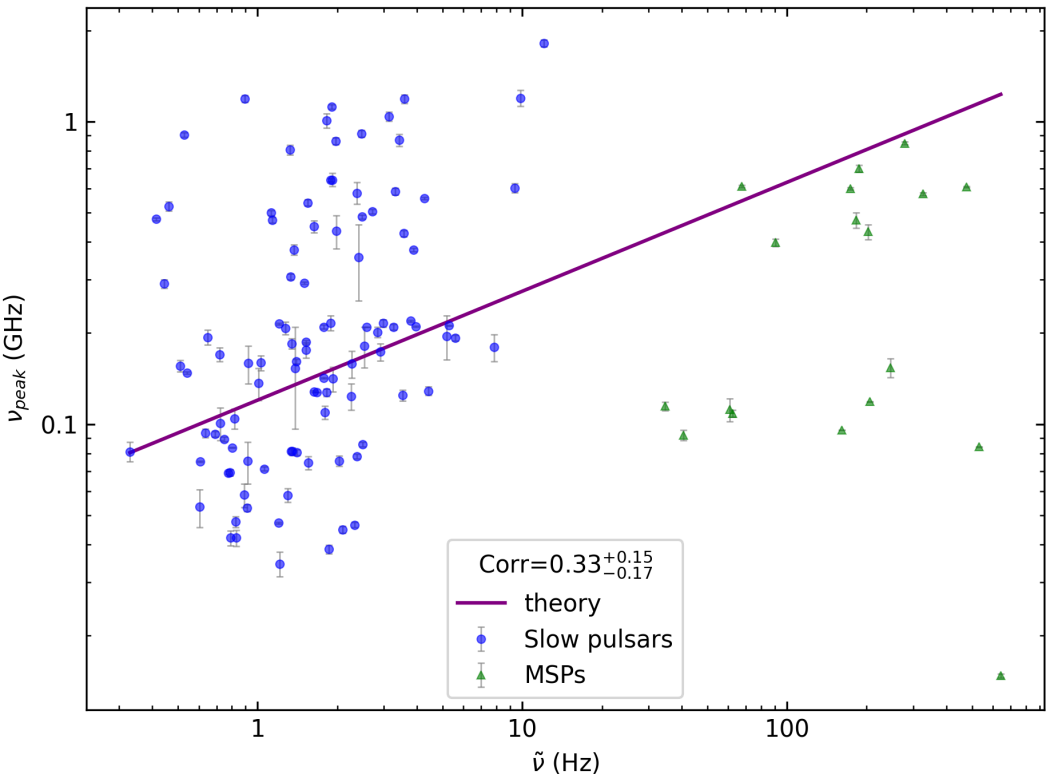

Figure 6.16: The correlation between $\nu_{\rm peak}$ and $\tilde{\nu}$ for all pulsars and the theoretical correlation suggested by Malofeev (1996) in Equation 1.24.

that dominate the low-frequency turn-over. The current bandwidth integration method does not appear to accurately fit the low-frequency end of the curve, causing a potential overestimation of $\nu_{\rm peak}$. The current implementation uses a Taylor series expansion to approximate the bandwidth integral of the model, and this may need to be improved in the future. The best fit may also be improved by the inclusions of other spectral models, such as the flicker noise model (Löhmer et al., 2008), which flattens at low frequencies.

PSRs J1600−3053, J1623−2631 and J1603−7202 (see Figure 6.17 (g) and (h) for example) have spectra that are potentially skewed by an underestimated uncertainty causing a low-frequency value above the curve to be effectively ignored. This uncertainty underestimation may be due to scintillation not being averaged out over several observations. The database could be improved by noting if flux

density measurements are scintillation averaged and, if they are not, increase their uncertainty accordingly. It should also be noted that the log scale of Figure 6.17 (g) and (h) make the lowest-frequency point appear 5 and 16 sigmas, respectively, off from the fit line when in truth, they are only 3 sigmas off.

6.4.3 Lack of correlations of millisecond pulsars

As shown in Table 6.5, we found no correlations between spectral features and pulsar properties for MSPs. The lack of correlations may be due to a lack of data (there are only 18 values of $\nu_{\rm peak}$ and 14 values $\nu_{\rm c}$), which may not be enough to discern a correlation for MSPs. Alternatively, the pulsar parameters may no longer significantly affect MSP spectra due to differing properties, such as the magnetic field strength, and the assumptions made in pulsar parameter derivations not applying to MSPs, such as characteristic age.

6.5 Summary

This chapter presents the spectral analysis of the most significant pulsar spectral sample to date. This is thanks to the implementation of the `pulsar_spectra` repository that not only enabled the most extensive collection of pulsar flux densities but also provides open-source software for the future growth of the catalogue and development of spectral fitting techniques. The new low-frequency flux density measurements from the SMART survey (Bhat et al., 2023a) were used to expand the catalogue at low radio frequencies. The distribution of the spectral index measurements was analysed, compared to previous publications and used to discover biases in the method. We investigated correlations between spectral parameters and pulsar properties to reveal the bias in our pulsar data and clues to pulsar emission. Our conclusions are the following:

(i) The vast majority of pulsars (68%) have a simple power law spectrum, which is 11% fewer than Jankowski et al. (2018) estimated. This suggests that

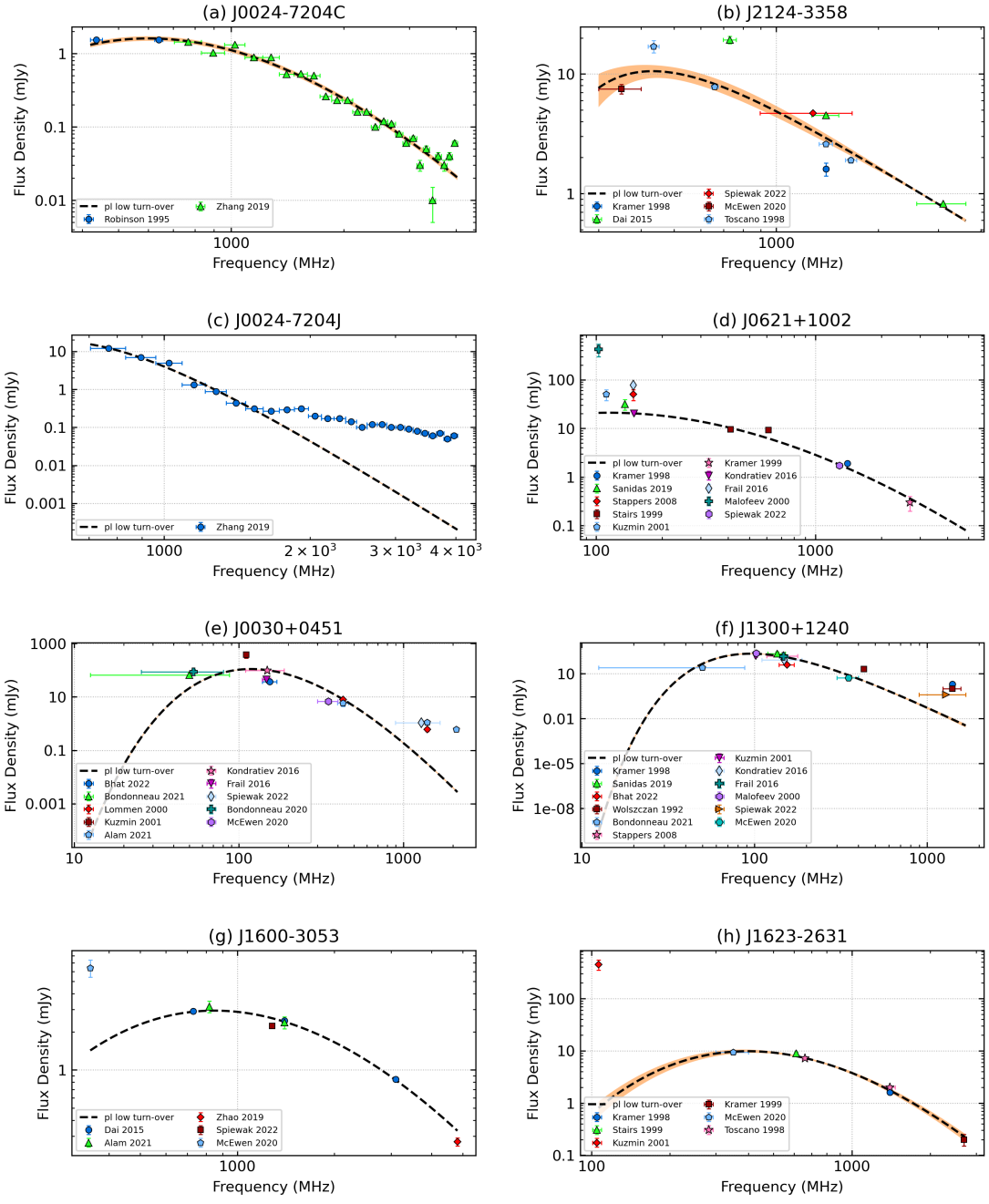

Figure 6.17: Eight examples of power law with low-frequency turn-over in MSPs. The first two plots, (a) and (b), are spectral fits that were are confident are showing low-frequency turn-over or at least low-frequency flattening. The other plots are spectral fits that we are not confident with for the reasons explained in the text.

the frequency range of our data is becoming wide enough to be sensitive to more low- and high-frequency spectral features.

(ii) We found a mean spectral index of -1.61 ± 0.03 which is consistent with previous works (e.g. Jankowski et al., 2018).

(iii) The spectral model distribution and mean spectral index of normal pulsars and MSPs appear to be similar, which contradicts previous publications that suggest MSPs have a steeper spectrum (e.g. Toscano et al., 1998; Spiewak et al., 2022).

(iv) There are several limitations with the current spectral fitting method, which include a lack of high-frequency data causing underestimation of the high-frequency cut-off $\nu_{\rm c}$ and apparent low-frequency turn-overs due to causes other than thermal absorption in the surrounding medium.

(v) The apparent correlation between DM and both $\nu_{\rm peak}$ and $\nu_{\rm c}$ is likely due to either scattering causing $\nu_{\rm peak}$ to be overestimated at high DMs or high-frequency pulsar surveys spending insufficient time at high Galactic latitudes to find high DM pulsars causing a population bias.

(vi) The correlation between $\nu_{\rm c}$ and $\tilde{\nu}$ agrees with the theory predicted by Kontorovich & Flanchik (2013). The theoretical values for $\nu_{\rm c}$ are underestimated, which suggests the maximum electric field in the polar gap is underestimated.

(vii) The emission region (both $\nu_{\rm peak}$ and $\nu_{\rm c}$) is correlated with the spin-down luminosity and negatively correlated with the characteristic age. This implies that as pulsars age and their spin-down luminosity decrease, they emit at lower frequencies. This validates the need to search for pulsars at a wide range of frequencies.

Chapter 7

Discussion and Conclusions

7.1 Summary

The primary goal of this research was to study the spectra of pulsars at low frequencies with the MWA. This was one of the primary goals of the SMART survey, which to date, has provided flux density measurements of 120 pulsars at low frequencies. 50 of these pulsars were observed at least twice (33 with two observations, 12 with three observations and 5 with four observations) which currently is not enough to meaningfully quantify their variability. Future work will include more observations that will allow us to quantify their variability. These were combined with data from the literature to investigate the spectra of 893 pulsars. The increase in the population of pulsars with measured spectra can be seen by comparing Figure 7.1 with Figure 1.1.

Processing SMART survey data is computationally expensive, owing to the MWA's large FoV and the fact that tied-array beams are computed offline. To meet this challenge, the multi-pixel beamformer was developed, which improved the efficiency of beamforming many beams by a factor of 10. This new capability allowed us to investigate the effectiveness of SMART's chosen calibration procedure, and implement an efficient method for mitigating inaccurate calibration due to ionospheric shifts. Furthermore, a method was developed to ensure

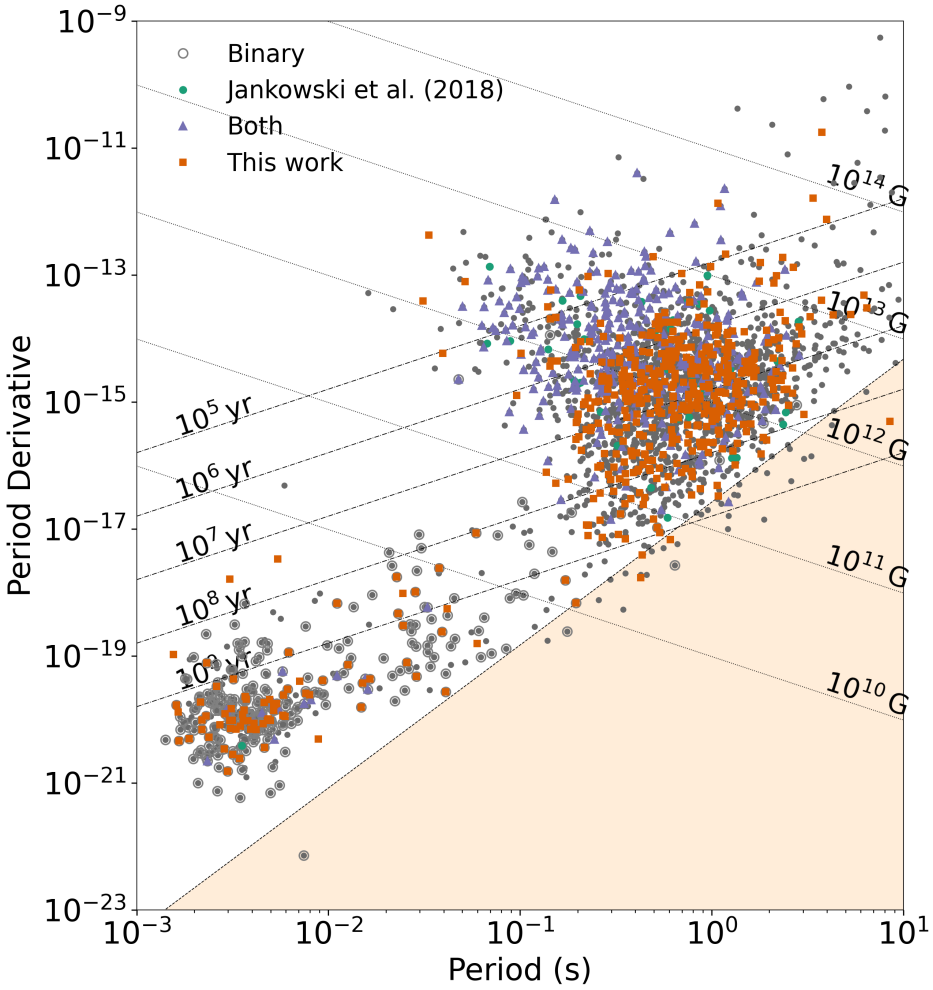

Figure 7.1: The pulsar P-$\dot{P}$ diagram for all known radio pulsars (in grey), binary pulsars (circled), pulsars with measured spectra from Jankowski et al. (2018) (green circles), pulsars with measured spectra from this work (magenta triangles) and pulsars from both Jankowski et al. (2018) and this work (orange squares). Lines of constant characteristic age τ and magnetic field B are also shown. The yellow-shaded region shows the region where pulsars are predicted not to exist.

the accuracy of flux density and candidate position measurements (see Chapter 3). These developments not only made the SMART survey tractable but also provided insights for ionospheric calibration with the SKA.

The development of the SMART survey and search pipeline led to the discovery of the first new pulsars with the MWA. The method used to follow up this pulsar and analyse spectra can be used in future SMART pulsar discoveries to increase the number of spectra of pulsars discovered at low frequencies (see Chapter 4). The automation of the MWA flux density simulation method allowed the calculation of 120 pulsar flux density measurements from the SMART survey (Bhat et al., 2023b), many of which were their first detections at low frequencies.

The lack of a dedicated pulsar flux density catalogue or open-source fitting software necessitated the creation of `pulsar_spectra`. `pulsar_spectra` is a centralised repository for pulsar flux density measurements to make published measurements more accessible to the astronomical community and provide a suite of tools for measuring spectra. `pulsar_spectra` implements a new spectral model called the double turn-over spectrum, which, with a wide enough frequency range, can measure a low-frequency turn-over and a high-frequency cut-off, and the bandwidth integration method, which accurately models how flux density measurements with large fractional bandwidths will be integrated over a spectral model (see Chapter 5).

The development of `pulsar_spectra` allows the spectral analysis of 893 pulsars (see Chapter 6), which is twice as many as the previous most extensive analysis of 441 pulsars by Jankowski et al. (2018). The parameters of the spectral fit results were compared to pulsar parameters to investigate possible correlations that may give clues about pulsar emission. The most robust findings from the resulting analysis include: the majority of pulsars (68%) have a simple power law spectrum with a mean spectral index of -1.61 ± 0.03; the spectral model distribution and mean spectral index of normal pulsars and MSPs appear to be similar; the correlation between ν_c and $\tilde{\nu}$ agrees with the theory predicted by Kontorovich

& Flanchik (2013); and as pulsars age they emit at lower frequencies.

7.2 Future improvements to flux density data

7.2.1 Insufficient data

While this work has dramatically improved the number of pulsars with measured spectra, over two-thirds of known pulsars are still without spectra due to insufficient flux density measurements. This lack of measurements in the current pulsar_spectra catalogue can be improved by including more publications and increasing the number and scale of flux density observing campaigns.

Extracting the flux density information from a publication and converting it to the format required by pulsar_spectra is a time-consuming process that no single researcher can perform for all current or future publications. The development of pulsar_spectra reduces, but does not solve, this problem by making it easier to upload data to the catalogue. We have already had some success sharing this load as one researcher[1] has already added a large number of publications to the catalogue.

We must also continue to include data from future publications, which would ideally be most efficiently input by the authors themselves. While pulsar_spectra has provided a list of publications[2] included in the catalogue, this may not be enough to motivate authors to include their publications as data is not always cited. It is increasingly common for authors to publish their data online (e.g. Ochsenbein F., 2019) so it is more accessible. Insofar as pulsar_spectra continues to be the largest catalogue of pulsar flux density measurements, uploading their data to pulsar_spectra will be the best option to make their data accessible.

[1] https://github.com/NickSwainston/pulsar_spectra/pull/73

[2] https://pulsar-spectra.readthedocs.io/en/latest/catalogue.html#papers-included-in-our-catalogue

7.2.1.1 Recommended pulsar flux density campaigns

The lack of flux density data is not only due to publications not included in the catalogue but also due to the large telescope observing time required for flux density observing campaigns. This work has shown the benefit of spectral analysis even with limited data. More flux density data is required to improve this work further. In this section, we suggest pulsars that, as a part of a flux density measurement campaign, will likely improve our understanding of spectral features.

The spectral fits of the 893 Pulsars from Chapter 6 can be used to estimate flux density at a range of frequencies. This and the `pulsar_spectra` flux density catalogue can be used to estimate which pulsars are detectable at frequencies that have yet to be observed. The tables resulting from this analysis have been deferred to Appendix C. Updated versions of these tables will be maintained online[3] and include CSVs of the table data.

For a flux density campaign performed with a low-frequency telescope, we recommend the 391 pulsars in Table C.1 as they have no flux density measurements below 300 MHz and an estimated flux density of greater than 1 mJy at both 150 or 300 MHz. The best spectral model for these pulsars are simple power law or power law with high-frequency cut-off, so their spectral turn-over has yet to be discovered and would benefit from further investigation at low frequencies. As the SMART survey moves on to its next survey pass, it is poised to detect some of these southern pulsars.

For a flux density campaign performed with a high-frequency telescope, we recommend the 524 pulsars in Table C.2 as they have no flux density measurements above 5 GHz and an estimated flux density of greater than 0.01 mJy at both 5 and 10 GHz. The best spectral model for these pulsars are simple power law or power law with low-frequency turn-over, so their spectral cut-off has yet to be discovered and could benefit from further investigation at high frequencies.

[3] https://all-pulsar-spectra.readthedocs.io/en/latest/suggested_campaigns.html

The large number of pulsars in both these potential campaigns and those that currently do not have sufficient flux density measurements to determine a spectrum shows considerable potential for extending the collective knowledge of pulsar spectra.

7.2.2 Record scintillation averaging or epoch in the flux density database

Scintillation will cause the apparent flux to vary by an amount that depends on the frequency and bandwidth of the observation. One example of this is the scintle at ∼1 GHz in Figure 4.8, which is almost an order of magnitude brighter than nearby measurements. Accurate spectral measurements can only be made by averaging out these scintillation effects or at least accounting for them in their flux density uncertainties.

The simplest way to correct this is to take several measurements over a period longer than the scintillation timescale and average them. Our current catalogue has no information about which publications averaged out the effects of scintillation or if they attempted to adjust their uncertainties to account for it. This lack of information may cause a measurement experiencing significant scintillation to be given the same weight in the fit as a measurement that has sufficiently mitigated the scintillation.

A more robust method would be only to record each individual flux density measurement made of the pulsar and its epoch. With both the bandwidth and epoch information, we can estimate if the effects of both diffractive and refractive scintillation have been averaged out at each measurement frequency. We can then adjust the uncertainty of any measurement that has not been averaged out to be weighted lower in the spectral fit. Such measurements are likely available in pulsar timing projects and could be an excellent resource if integrated into a single database. Such data will allow us to study the effects of scintillation and make more accurate spectral measurements.

7.2.3 Record scattering in the flux density database

Multi-path scattering can cause a scattering tail longer than the pulsar's period, lowering the apparent flux density (measured using a pulse profile instead of imaging) and causing inaccurate measurements. This is due to the scattering tail preventing the measurement of the noise in the pulse profile, which in turn prevents an accurate measurement of the S/N ratio because it artificially increases the baseline of the profile. This frequency-dependent reduction can cause a low-frequency turn-over that is not caused by the absorption of the surrounding medium. By analysing the pulse profile, it will be apparent if the scattering is significant enough to affect the apparent flux density. Suppose we clarify which flux density measurements are significantly affected by scattering. In that case, we can easily distinguish which low-frequency turn-overs are caused by scattering and which are caused by the absorption of the surrounding medium.

7.3 Future improvements of the spectral fitting method

The current spectral fitting method provides good-fitting models for most of the pulsars in our sample, but there are several examples where the method needs to be improved. Some of the weaknesses in our current method have already been discussed in §6.3.4 and §6.4.2.1. In the following sections, we will discuss potential ways to improve our spectral fitting method.

7.3.1 Other potential spectral models

In this work, we added the double turn-over spectrum model, but there are still other models in the literature. One such model that has been suggested is the flicker noise model (Löhmer et al., 2008). This model suggests that pulsar emission is the coherent superposition of a number of powerful nano-pulses. This

theory is supported by the observations of giant pulses varying on nano-second timescales (Hankins et al., 2003; Jessner et al., 2005). A random superposition of nano-pulses has a simple spectrum

$$S_\nu = \frac{c}{1 + (2\pi\nu)^2 \tau_e^2}, \tag{7.1}$$

where τ_e is the timescale of the nano-pulses. This results in a flattening spectrum at low frequencies, as shown in Figure 7.2.

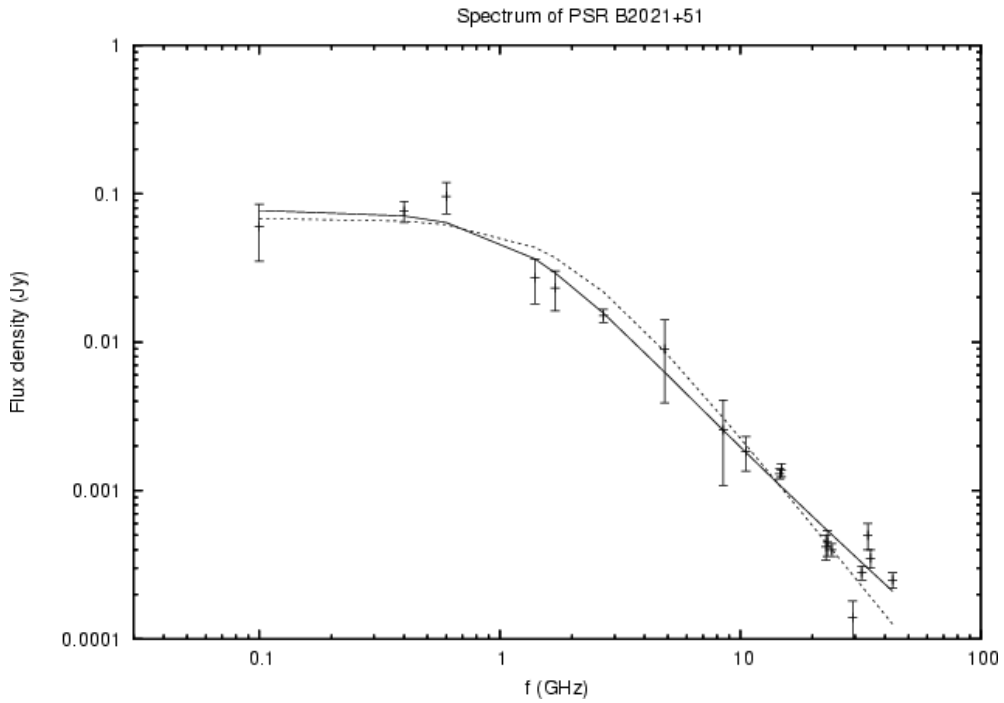

Figure 7.2: The spectral fit of PSR B2021+51 using the flicker noise model. The dashed fit used Equation 7.1 with $c = 68$ mJy and $\tau_e = 0.09$ ns. Image credit Löhmer et al. (2008).

This spectrum is similar to the power law with low-frequency turn-over model, so it may replace the spectrum for pulsars whose spectra are flattening rather than turning over (PSRs J0030+0451 and J1300+1240 from Figure 6.17 (e) and (f) for example). This also implies that the current low-frequency turn-overs may not be caused by absorption but rather an intrinsic property of the emission. The future incorporation of this model may lead to insight into nano-pulses and constrain their effect on emission.

7.3.2 Using flux density upper limits

Accurately sampling the low-frequency turn-over and the high-frequency cut-off curves is difficult due to requiring measurements of the curve at several frequencies before the flux falls below the detection limit. It is often the case that low-frequency turn-overs and high-frequency cut-offs are only assumed to be present due to a single constraining flux density measurement. However, these can easily be a pulsar scintillating down (PSRs J0024−7204C and J2124−3358 in Figure 6.17 (a) and (b) for example). A more robust method would ensure a non-detection past the turn-over or cut-off frequency to confirm the lack of emission.

Some publications include upper limits of flux density when they make non-detections of pulsars (e.g. Murphy et al., 2017; Sieber, 1973; Bilous et al., 2016, 2020), which could be included in the catalogue. These upper limits could be included in the fitting method using the Tobit model (Tobin, 1958), which modifies the likelihood function to reflect the unequal probability. If the non-detection upper limits were included in the database and the fitting process, we would be more confident that turn-overs are not due to scintillation or other fluctuations in measurements.

7.3.3 Calculating more accurate uncertainties with MCMC

The uncertainties of the spectral model parameters are calculated from their covariance matrix, which assumes that the likelihood is symmetric (i.e. normally distributed) around the best-fit value. This method can lead to underestimated and inaccurate uncertainties. A more robust method would be to use a Markov Chain Monte Carlo (MCMC) algorithm to sample the probability distributions of the model parameters. This method could be added to `pulsar_spectra` as an alternative and provide more robust spectral parameter uncertainties.

7.3.4 Further analysis of pulsar spectra

As introduced in §1.7.2 and §1.7.3, the measurement spectral parameters can infer properties about the pulsar and the surrounding medium. The low-frequency turn-over frequency can be used to estimate the optical depth of gigahertz-peaked spectra, and the high-frequency cut-off frequency can be used to estimate the pulsar's emission height. These calculations can easily be automated by creating functions in `pulsar_spectra` to calculate them, which has already been done for the emission height calculation[4]. This method has already been used by several authors (e.g. Jankowski et al., 2018; Lee et al., 2022) and can be used in future work at a larger scale thanks to `pulsar_spectra`.

7.3.5 Robust luminosity investigation

The luminosity correlation investigations performed in §6.3 used a simplified approach of only investigating correlations at two set frequencies (400 and 1400 MHz). A more robust method would be to investigate the integrated luminosity over an extensive frequency range, but this was not possible due to the inconsistent frequency range of our data set. To complete such an investigation would require several telescopes to measure a large number of pulsars to get a large enough sample to investigate potential luminosity correlations, which is out of the scope of this thesis.

7.3.6 Effect of profile evolution

To study the emission process, we must investigate the intrinsic spectral index, which is how the total luminosity of the pulsar beam changes with frequency, as opposed to the apparent spectral index, which is what we have been reporting as the spectral index in this thesis. As introduced in §1.3, the profile evolution of pulsars over a range of frequencies may affect the apparent spectral index.

[4] https://pulsar-spectra.readthedocs.io/en/latest/modules.html#module-pulsar_spectra.analysis

This is due to the emission beam often being wider at low frequencies, which in turn makes the pulse profile wider. Because it is standard practice to report the average flux density over the pulse profile, this can cause the apparent spectral index to differ from the intrinsic spectral index (often steeper if the pulsar follows the RFM).

To estimate the total luminosity of the beam, we must first model how the beam evolves over frequency. This can be done by investigating how the profile changes. For example, a filled conal beam is often sufficient for single-component pulse profiles that gets wider at low frequencies. The flux density along the line of sight for each frequency can then be extrapolated to estimate the flux density of the entire emission beam (e.g. Erkut, 2022). Once intrinsic spectral indices have been worked out by this method (or other suitable methods), we can begin to investigate the pulsar emission mechanism.

It can be difficult to model the beam shape of pulsars with profiles that evolve in unexpected ways. In these cases, a proper characterisation of the pulsar beam requires modelling of the individual components in the profile. For example, Zhao et al. (2017) found several pulsars with components that had different spectral indices and found that central components often had steeper spectra compared to outer components. Having a complete catalogue of component spectra that accurately describe the profile evolution is vital for future studies of the intrinsic spectral index for this class of pulsars.

To perform this analysis we must incorporate a database of pulse profiles that have been calibrated so they are in flux density units, such as the EPN database[5]. As it may be challenging to collect and analyse such data, a more straightforward but approximate method would be to record the maximum flux density of the pulse profile. This will yield an estimate of the spectral index along the maximum point of the profile, which would provide a good approximation for the component spectral index of pulsars with only a single pulse component.

[5] http://www.epta.eu.org/epndb/

7.3.7 Causes of absorption other than the surrounding medium

In this thesis, it has been assumed that the medium surrounding a pulsar is the cause of the absorption observed in low-frequency turn-overs. While it is most likely that this is the most dense medium, it is also possible that there are other dense regions along the line of sight that could cause the observed absorption. HII regions, for example, could have sufficient density to cause a low-frequency turn-over.

To test if dense regions along the line of sight are causing absorption, the medium along the line of sight could be investigated using electron density and HII region maps. The population of pulsars with low-frequency turn-overs that are caused by dense regions along the line of sight could then be separated from those that are caused by the surrounding medium. The two pulsar populations could be analysed again with this method to investigate if these dense regions are the cause of the correlation between DM and the $\nu_{\rm peak}$.

7.4 Pulsar population simulations

Understanding pulsars' spectra and their evolution will allow more accurate population simulation. Current pulsar population simulations only use a simple spectral index to estimate the flux density of pulsars at different observing frequencies. This work has shown that spectra are often more complex than can be explained by only a spectral index and that spectra of pulsars evolve as they age.

This work has shown that $\sim$14% of the 893 pulsars in our sample show a low-frequency turn-over. This may be an underestimation of the true fraction of pulsars that have turn-overs, as 462 pulsars in our sample have no flux density measurements below 300 MHz. The spectra of pulsars at low frequencies must be investigated further to accurately be accounted for in pulsar population simulations and predictions of the detectable pulsar population with SKA-Low.

It has been shown in this work that both $\nu_{\rm peak}$ and ν_c have a strong negative correlation with τ (see Figure 6.14). This implies that pulsars emit over a lower frequency range as they age. As the majority of pulsars have been discovered at high frequencies, our current pulsar population is likely biased towards young pulsars. This bias may contribute to the overestimation of the pulsar birth rate compared to the core-collapse supernova rate (e.g. Keane & Kramer, 2008). Future pulsar population surveys should include the evolution of $\nu_{\rm peak}$ and ν_c with τ to improve their accuracy.

7.5 Conclusion

The primary goal of this research was to study the spectra of pulsars to uncover clues about their emission mechanism. The SMART pulsar survey was developed to investigate the low-frequency properties of pulsar spectra. The SMART survey was made possible by the improvement in the efficiency of the beamformer software and the method to mitigate ionospheric offsets. The development of the SMART survey and search pipeline led to the discovery of the first new pulsars with the MWA and 120 flux density measurements of already known pulsars.

The `pulsar_spectra` repository was developed to create a pulsar flux density catalogue that makes published measurements more accessible to the astronomical community and provides a suite of tools for measuring spectra. `pulsar_spectra` implements a new spectral model called the double turn-over spectrum, and the bandwidth integration method, which accurately fits the spectral of flux density measurement with a large fractional bandwidth. The repository is open source and well documented to make it easier for this work to continue and improve.

The spectra of 893 pulsars were analysed by comparing the spectral fit parameters with pulsar parameters to investigate possible correlations that may give clues about pulsar emission. The vast majority of pulsars (68%) have a simple power law spectrum, which suggests that the majority of pulsars in our sample have insufficient flux data below 300 MHz and above 5 GHz. To improve this

sample, we have suggested pulsars that can likely be detected at these high and low frequencies (see Appendix C).

We made several findings relating to pulsar spectra, including normal pulsars and MSPs appear to have similar spectral model distribution and mean spectral index; the theoretical estimation of $\nu_{\rm c}$ based on $\tilde{\nu}$ is underestimated; and that as pulsars age, their peak emission region (both $\nu_{\rm peak}$ and $\nu_{\rm c}$) decreases to lower frequencies.

Our current pulsar spectral sample is still lacking (less than a third of currently known pulsars) and can be significantly improved. This work describes how to further improve the pulsar spectra sample by improving the number and quality of flux density measurements and ways to make the spectral fitting method more robust. The spectra of pulsars and how they constrain the pulsar emission mechanism is still an area ripe for further investigation.

Appendices

Appendix A

The SMART flux density measurements

The development of the processing pipelines in this thesis allowed the measurement of the 120 known pulsars detected in the SMART survey Bhat et al. (2023a,b), as shown in Table A.1.

Table A.1: Known pulsars detected in SMART survey observations where "Offset" is the target offset from the observation centre.

Pulsar	Period (ms)	DM ($pc\,cm^{-3}$)	Offset (deg)	S/N	Mean flux density (mJy)	Obs ID
J0030+0451	4.865	4.33	4.3	6.3	37±8	1255444104
J0034−0534	1.877	13.77	7.3	3.6	260±85	1255444104
J0034−0721	942.951	10.92	9.0	64.0	692±42	1255444104
J0038−2501	256.926	5.71	8.5	24.6	44±6	1226062160
J0051+0423	354.732	13.93	14.6	26.4	59±17	1225118240
J0133−6957	463.474	22.95	7.7	25.1	12±4	1227009976
J0134−2937	136.962	21.81	20.7	10.6	11±3	1226062160
J0151−0635	1464.665	25.66	17.3	13.9	8±3	1252177744
J0152−1637	832.742	11.93	11.5	74.4	131±17	1225462936

Continued on next page

Pulsar	Period (ms)	DM ($pc\,cm^{-3}$)	Offset (deg)	S/N	Mean flux density (mJy)	Obs ID
J0206−4028	630.551	12.9	11.1	68.2	1289±16	1224859816
J0255−5304	447.708	15.9	4.4	9.7	67±10	1253471952
J0304+1932	1387.584	15.66	12.7	22.3	35±9	1254594264
J0401−7608	545.254	21.7	4.9	52.0	74±18	1255803168
J0418−4154	757.119	24.33	3.9	42.3	38±11	1253991112
J0437−4715	5.757	2.64	15.4	6.2	1179±238	1257617424
J0450−1248	438.014	37.04	14.8	81.3	131±33	1256407632
J0452−1759	548.939	39.9	9.1	37.0	186±14	1257010784
J0459−0210	1133.076	21.02	3.9	81.5	68±22	1256407632
J0514−4408	320.271	15.12	13.3	13.2	91±8	1257617424
J0520−2553	241.642	33.77	3.8	20.5	18±5	1257010784
J0525+1115	354.438	79.42	12.8	8.7	44±6	1259685792
J0528+2200	3745.539	50.87	10.0	31.6	38±7	1259685792
J0600−5756	2261.365	30.0	2.9	8.6	27±3	1257617424
J0601−0527	395.969	80.54	7.7	19.7	72±12	1259427304
J0614+2229	334.96	96.91	4.0	9.7	33±6	1259685792
J0624−0424	1039.076	70.84	16.3	13.4	26±8	1260638120
J0630−2834	1244.419	34.43	12.2	126.3	1353±91	1261241272
J0636−4549	1984.597	26.31	7.3	7.1	19±6	1258221008
J0729−1448	251.659	91.89	12.6	12.9	64±11	1266155952
J0729−1836	510.16	61.29	13.6	12.4	72±11	1266155952
J0737−3039A	22.699	48.92	4.9	22.2	173±28	1261241272
J0742−2822	166.762	73.73	23.0	11.1	362±40	1265470568
J0758−1528	682.265	63.33	6.0	21.2	39±9	1266155952
J0820−1350	1238.13	40.94	0.9	112.7	411±48	1266155952
J0820−3921	1073.567	179.4	1.0	5.8	51±11	1265983624

Continued on next page

Pulsar	Period (ms)	DM ($pc\,cm^{-3}$)	Offset (deg)	S/N	Mean flux density (mJy)	Obs ID
J0820−4114	545.446	113.4	20.0	7.3	34±7	1265470568
J0823+0159	864.873	23.73	14.9	11.1	37±10	1266155952
J0826+2637	530.661	19.48	8.1	51.0	194±19	1265725128
J0835−4510	89.328	67.77	21.8	23.0	1121±55	1266680784
J0837+0610	1273.768	12.86	13.2	61.2	138±17	1265725128
J0837−4135	751.625	147.2	13.4	24.4	144±12	1266329600
J0842−4851	644.354	196.85	6.1	6.4	43±8	1266329600
J0855−3331	1267.536	86.64	9.6	15.7	76±9	1265470568
J0856−6137	962.511	95.0	10.4	32.9	93±9	1266932744
J0902−6325	660.313	72.72	8.7	22.7	23±5	1266932744
J0904−7459	549.554	51.1	3.4	6.9	13±4	1266932744
J0905−6019	340.854	91.4	11.8	14.8	32±5	1266932744
J0907−5157	253.558	103.72	4.7	7.1	89±13	1266329600
J0908−1739	401.626	15.88	20.6	20.2	62±6	1267283936
J0922+0638	430.627	27.3	5.0	45.0	184±17	1264867416
J0924−5302	746.338	152.9	17.1	14.1	64±9	1266680784
J0924−5814	739.505	57.4	14.4	10.2	30±5	1266932744
J0942−5552	664.389	180.16	17.2	14.4	37±5	1266932744
J0942−5657	808.164	159.74	16.2	44.4	95±11	1266932744
J0943+1631	1087.418	20.34	11.7	11.1	34±7	1267111608
J0944−1354	570.264	12.5	11.6	24.8	27±5	1267283936
J0946+0951	1097.706	15.32	14.2	53.4	182±18	1267111608
J0953+0755	253.065	2.97	14.3	96.9	775±51	1267111608
J0955−5304	862.122	156.9	14.2	35.3	49±13	1266680784
J0959−4809	670.086	92.7	9.8	19.0	110±8	1266680784
J1003−4747	307.074	98.49	9.1	17.6	29±7	1266680784

Continued on next page

Pulsar	Period (ms)	DM ($pc\,cm^{-3}$)	Offset (deg)	S/N	Mean flux density (mJy)	Obs ID
J1012−2337	2517.945	22.51	19.4	14.3	39±5	1268321832
J1018−1642	1804.695	48.82	20.8	13.1	16±5	1268321832
J1022+1001	16.453	10.25	16.4	10.7	68±10	1264867416
J1034−3224	1150.59	50.75	14.9	12.9	73±7	1268321832
J1041−1942	1386.368	33.78	14.6	24.5	49±7	1268321832
J1057−5226	197.115	29.69	4.5	19.1	287±15	1267459328
J1059−5742	1185.003	108.7	17.5	21.6	49±10	1301240224
J1112−6926	820.488	148.4	7.5	21.5	38±8	1301240224
J1116−4122	943.158	40.53	13.6	16.7	54±8	1267459328
J1121−5444	535.787	204.7	0.3	10.1	79±9	1267459328
J1123−4844	244.838	92.92	6.2	6.2	16±5	1267459328
J1123−6651	232.976	111.2	8.3	11.3	40±8	1301240224
J1136+1551	1187.913	4.84	14.1	151.6	318±37	1268063336
J1136−5525	364.713	85.11	1.9	7.4	34±6	1267459328
J1141−6545	393.899	116.08	8.1	14.1	55±10	1301240224
J1146−6030	273.375	111.68	6.4	9.4	24±6	1267459328
J1202−5820	452.803	145.41	14.1	13.9	88±11	1301240224
J1224−6407	216.48	97.69	7.9	18.1	89±9	1301240224
J1225−5556	1018.453	125.84	8.9	12	15±5.6	1267459328
J1239−6832	1301.923	94.3	3.4	20.8	26±7	1301240224
J1240−4124	512.242	44.1	1.1	22.2	34±9	1301412552
J1257−1027	617.308	29.63	5.0	18.0	29±9	1300809400
J1300+1240	6.219	10.17	15.6	9.4	34±9	1301847296
J1311−1228	447.518	36.21	16.4	26.1	51±9	1301847296
J1312−5402	728.154	133.0	15.8	8.5	26±6	1267459328
J1313+0931	848.933	12.04	11.1	23.3	37±8	1301847296

Continued on next page

Pulsar	Period (ms)	DM ($pc\,cm^{-3}$)	Offset (deg)	S/N	Mean flux density (mJy)	Obs ID
J1320−5359	279.738	97.1	15.4	10.7	36±9	1301412552
J1328−4357	532.699	42.0	9.7	20.6	55±9	1301412552
J1332−3032	650.434	15.1	4.7	12.1	51±9	1301674968
J1335−3642	399.192	41.82	11.6	13.2	49±9	1301412552
J1340−6456	378.622	76.99	8.9	12.1	24±7	1301240224
J1355−5153	644.305	112.1	3.0	28.7	146±16	1302106648
J1358−2533	912.971	16.05	3.3	26.0	27±8	1301674968
J1418−3921	1096.806	60.49	15.9	17.3	53±12	1302106648
J1430−6623	785.443	65.1	12.1	34.7	112±15	1302106648
J1440−6344	459.607	124.2	10.3	17.7	60±12	1302106648
J1453−6413	179.487	71.25	11.5	110.0	590±64	1302106648
J1455−3330	7.987	13.57	6.9	7.8	58±14	1302282040
J1456−6843	263.377	8.61	15.3	51.1	433±36	1302106648
J1507−4352	286.758	48.7	4.8	25.1	125±16	1302282040
J1510−4422	943.871	84.0	5.5	13.2	51±13	1302282040
J1527−3931	2417.605	48.8	7.3	24.0	31±13	1302282040
J1534−5334	1368.882	24.82	15.2	30.5	95±17	1302282040
J1536−4948	3.08	38.0	12.5	8.7	13±12	1302282040
J1543+0929	748.448	34.98	15.8	26.5	426±28	1302540536
J1543−0620	709.064	18.3	14.6	69.0	270±35	1302712864
J2048−1616	1961.572	11.46	17.6	32.1	69±10	1222435400
J2108−3429	1423.102	30.22	11.7	7.5	13±5	1222435400
J2145−0750	16.052	9.0	17.7	9.2	61±11	1222697776
J2155−3118	1030.002	14.85	4.7	109.9	223±28	1222435400
J2222−0137	32.818	3.27	8.6	13.3	31±7	1221832280
J2234+2114	1358.745	35.08	5.5	5.2	9±7	1223042480

Continued on next page

Pulsar	Period (ms)	DM ($pc\,cm^{-3}$)	Offset (deg)	S/N	Mean flux density (mJy)	Obs ID
J2241−5236	2.187	11.41	12.0	27.9	705±37	1224252736
J2317+2149	1444.653	20.87	6.2	24.0	52±7	1223042480
J2324−6054	2347.488	14.0	11.8	17.0	12±4	1227009976
J2325−0530	868.735	14.97	10.7	10.7	15±4	1222697776
J2330−2005	1643.622	8.46	9.7	112.4	87±14	1226062160
J2336−01	1029.8	19.6	15.3	11.7	53±10	1222697776
J2354−22	557.996	9.9	4.2	25.2	16±3	1226062160

Appendix B

Changes in the spectral model after the addition of the SMART flux density measurements

Of the 120 pulsars detected in the SMART observations, only 23 pulsars' spectral fit model changed after the addition of the flux density measurements, see Table 6.2. The changes to these fits are shown in Figures B.1, B.2 and B.3.

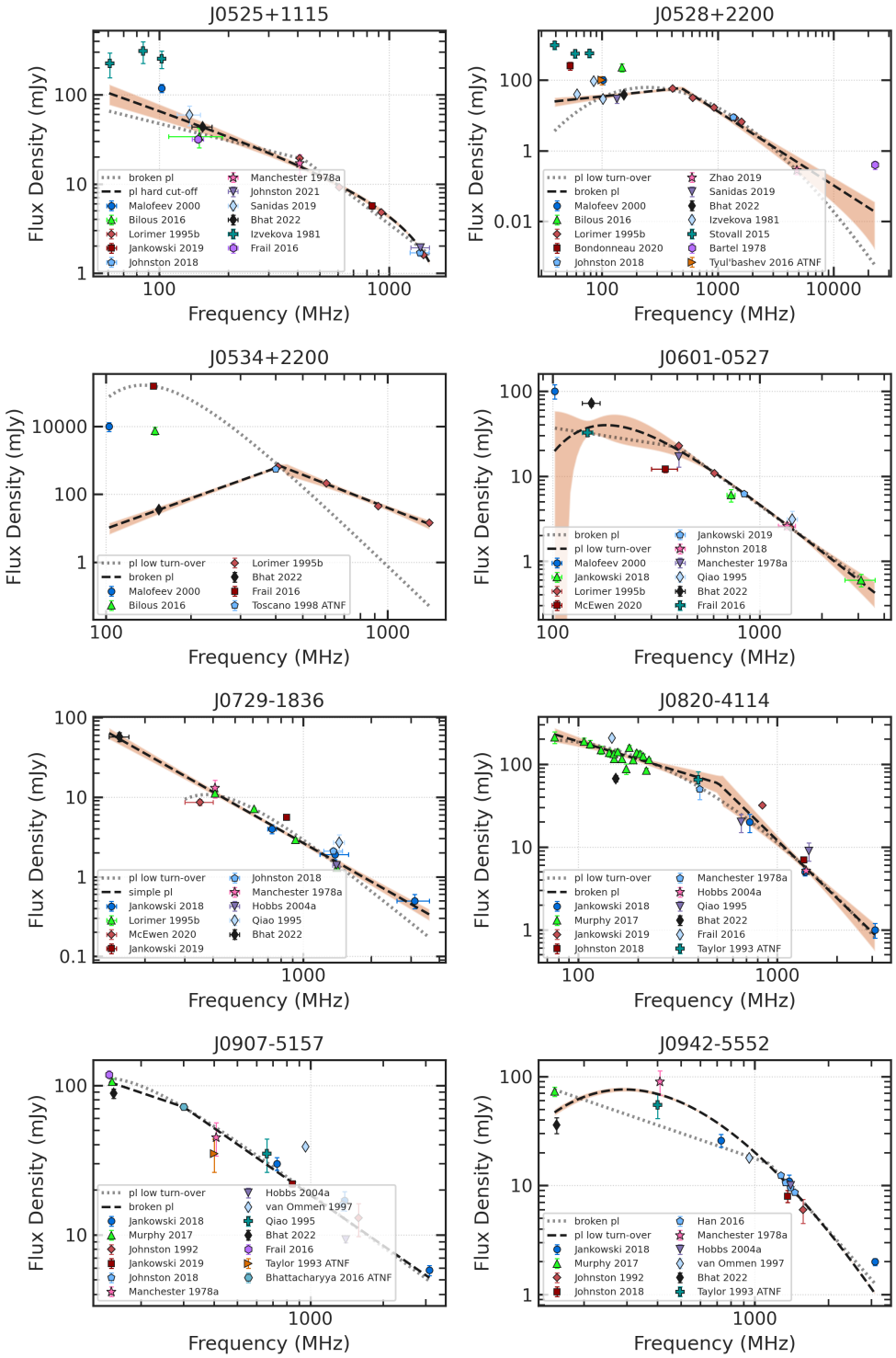

Figure B.1: The spectrum before the addition of SMART data (dotted line) and after (dashed line) for PSR J0525+1115, J0528+2200, J0534+2200, J0601−0527, J0729−1836, J0820−4114, J0907−5157 and J0942−5552.

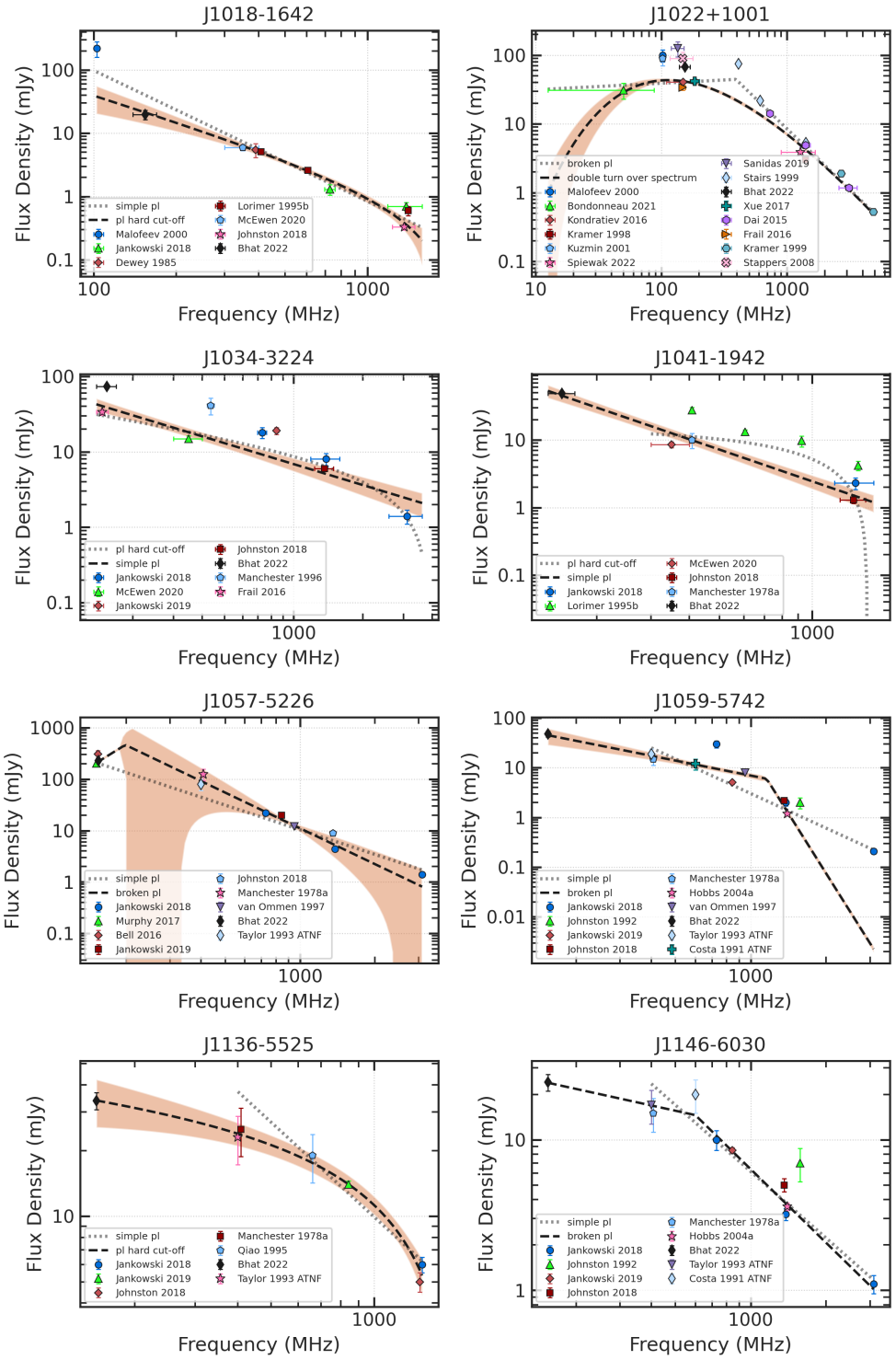

Figure B.2: The spectrum before the addition of SMART data (dotted line) and after (dashed line) for PSR J1018−1642, J1022+1001, J1034−3224, J1041−1942, J1057−5226, J1059−5742, J1136−5525 and J1146−6030.

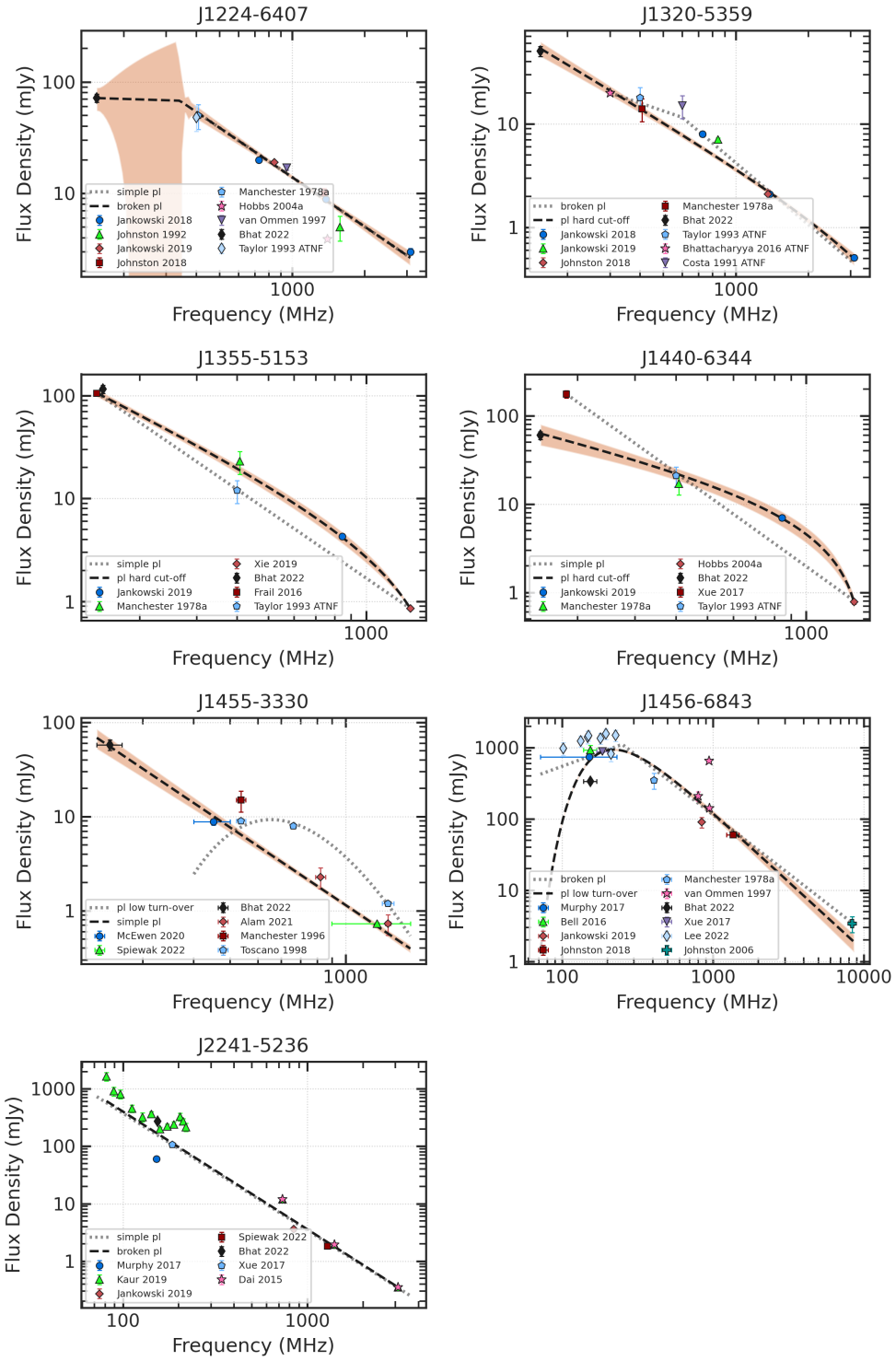

Figure B.3: The spectrum before the addition of SMART data (dotted line) and after (dashed line) for PSR J1224−6407, J1320−5359, J1355−5153, J1440−6344, J1455−3330, J1456−6843 and J2241−5236.

Appendix C

Recommended pulsar flux density campaigns

The spectral fits of the 898 pulsars from §6 can be used to estimate flux density at a range of frequencies. This and the `pulsar_spectra` flux density catalogue can be used to estimate which pulsars are detectable at frequencies that have not yet been observed. We do this in the following sections for both low and high frequencies.

C.1 Low-frequency flux density campaign

We recommend the 391 pulsars in Table C.1 as they have no flux density measurements below 300 MHz and an estimated flux density of greater than 1 mJy at both 150 or 300 MHz. The best spectral model for these pulsars are simple power law or power law with high-frequency cut-off so their spectral turn over has not yet been discovered, so they would benefit from further investigation at low frequencies.

Pulsar	Model	Min freq (MHz)	S150 (mJy)	S300 (mJy)
J0215+6218	SPL	350	16.2 ± 17.0	11.9± 11.9
J0340+4130	SPL	400	8.6 ± 7.7	3.6± 3.6
J0536−7543	SPL	400	354.4 ± 168.9	112.2± 112.2

Continued on next page

Pulsar	Model	Min freq	S150	S300
J0656−2228	SPL	350	1.3 ± 0.6	1.0± 1.0
J0719−2545	SPL	350	13.1 ± 4.1	5.6± 5.6
J0721−2038	SPL	350	8.4 ± 3.6	2.7± 2.7
J0745−5353	HFCO	400	82.9 ± 29.2	36.4± 36.4
J0820−3826	SPL	350	20.5 ± 4.2	6.0± 6.0
J0821−4221	SPL	1276	512.3 ± 691.5	60.1± 60.1
J0831−4406	SPL	1276	9.6 ± 15.2	4.1± 4.1
J0834−4159	SPL	728	10.2 ± 3.9	3.3± 3.3
J0838−2621	HFCO	350	3.5 ± 2.0	2.7± 2.7
J0855−4644	SPL	728	3.6 ± 0.9	1.6± 1.6
J0900−3144	SPL	728	68.8 ± 35.2	26.6± 26.6
J0901−4624	SPL	728	4.7 ± 2.8	2.3± 2.3
J0904−4246	SPL	400	52.1 ± 43.0	13.1± 13.1
J0909−7212	SPL	400	26.0 ± 20.3	9.9± 9.9
J0931−1902	SPL	350	3.8 ± 2.1	2.0± 2.0
J0932−3217	SPL	350	7.4 ± 2.0	2.9± 2.9
J0940−5428	SPL	728	5.9 ± 2.5	2.9± 2.9
J0945−4833	SPL	1278	164.1 ± 275.9	24.4± 24.4
J1001−5559	SPL	728	138.8 ± 125.1	26.3± 26.3
J1012−5857	SPL	400	94.2 ± 18.9	27.8± 27.8
J1013−5934	SPL	728	16.5 ± 7.3	8.6± 8.6
J1015−5719	SPL	728	3.3 ± 1.8	2.8± 2.8
J1016−5345	SPL	400	22.8 ± 12.6	7.3± 7.3
J1016−5819	SPL	728	31.9 ± 7.4	7.6± 7.6
J1016−5857	SPL	728	13.8 ± 4.6	5.7± 5.7
J1017−7156	SPL	728	42.0 ± 7.7	12.5± 12.5
J1032−5911	SPL	400	162.1 ± 83.0	31.6± 31.6
J1038−5831	SPL	640	16.8 ± 32.3	6.8± 6.8
J1042−5521	SPL	400	160.5 ± 115.9	29.0± 29.0
J1043−6116	SPL	728	16.9 ± 4.0	7.5± 7.5
J1046−5813	SPL	400	149.5 ± 56.5	34.3± 34.3
J1047−6709	SPL	400	10.1 ± 5.2	6.6± 6.6
J1048−5832	HFCO	640	26.2 ± 7.1	19.1± 19.1
J1055−6028	SPL	728	20.0 ± 8.1	6.4± 6.4
J1057−7914	SPL	400	59.3 ± 45.9	14.0± 14.0
J1058−5957	SPL	1277	181.8 ± 179.0	30.7± 30.7
J1105−6107	SPL	728	16.7 ± 4.5	7.3± 7.3
J1107−5947	SPL	400	27.1 ± 19.3	9.4± 9.4
J1107−6143	SPL	1342	21.8 ± 13.7	7.5± 7.5
J1110−5637	HFCO	640	15.2 ± 6.7	10.1± 10.1
J1112−6103	SPL	1360	18.5 ± 6.5	9.5± 9.5
J1112−6613	SPL	400	141.1 ± 43.2	35.3± 35.3
J1114−6100	HFCO	640	7.8 ± 0.6	7.5± 7.5
J1115−6052	SPL	728	5.7 ± 1.4	2.6± 2.6
J1119−6127	SPL	728	23.5 ± 8.7	8.9± 8.9
J1119−7936	SPL	400	64.1 ± 51.5	15.5± 15.5
J1123−6259	SPL	400	50.4 ± 13.1	12.1± 12.1
J1125+7819	SPL	350	32.2 ± 18.7	10.9± 10.9
J1126−6054	SPL	640	43.0 ± 65.5	13.6± 13.6
J1130−6807	SPL	400	90.1 ± 82.5	18.8± 18.8
J1133−6250	SPL	640	207.7 ± 213.6	65.9± 65.9

Continued on next page

Pulsar	Model	Min freq	S150	S300
J1138−6207	SPL	1360	4.1 ± 1.6	2.2± 2.2
J1141−3322	SPL	350	3.6 ± 1.5	2.9± 2.9
J1156−5707	SPL	728	3.3 ± 1.1	1.6± 1.6
J1157−6224	SPL	400	1932.9 ± 728.9	379.7± 379.7
J1210−5559	SPL	436	593.9 ± 292.0	86.1± 86.1
J1216−6223	SPL	1360	8.2 ± 3.7	2.7± 2.7
J1220−6318	SPL	1277	546.7 ± 555.6	72.0± 72.0
J1225−6035	SPL	1278	13.3 ± 26.0	4.1± 4.1
J1225−6408	HFCO	400	22.9 ± 0.3	20.2± 20.2
J1237−6725	SPL	1277	12787.1 ± 13960.4	597.8± 597.8
J1243−6423	BPL	408	70.0 ± nan	95.3± 95.3
J1253−5820	SPL	436	115.0 ± 66.6	39.8± 39.8
J1259−6741	SPL	400	24.4 ± 12.2	9.6± 9.6
J1301−6305	SPL	728	3.4 ± 1.1	1.8± 1.8
J1302−6350	HFCO	640	3.3 ± 0.6	3.2± 3.2
J1303−6305	SPL	1277	480.2 ± 1240.7	47.0± 47.0
J1305−6203	SPL	728	12.3 ± 5.3	4.9± 4.9
J1305−6455	SPL	400	423.7 ± 293.5	83.1± 83.1
J1306−6617	SPL	640	236.7 ± 186.7	70.1± 70.1
J1312−5516	SPL	400	181.1 ± 78.1	50.3± 50.3
J1314−6101	SPL	1277	525.6 ± 643.1	63.1± 63.1
J1317−6302	SPL	728	90.8 ± 38.9	22.9± 22.9
J1319−6056	SPL	640	215.0 ± 98.6	44.7± 44.7
J1319−6105	SPL	728	18.8 ± 7.6	8.2± 8.2
J1326−5859	BPL	400	14.9 ± 42.5	28.4± 28.4
J1326−6408	SPL	400	395.5 ± 134.7	78.6± 78.6
J1326−6700	SPL	400	125.5 ± 64.0	59.6± 59.6
J1327−6301	SPL	640	274.3 ± 154.0	72.7± 72.7
J1327−6400	SPL	728	3.4 ± 1.8	1.4± 1.4
J1338−6204	SPL	640	79.3 ± 57.4	30.7± 30.7
J1341−6220	SPL	1360	18.8 ± 5.9	10.1± 10.1
J1348−6307	SPL	1277	767.9 ± 1783.3	79.4± 79.4
J1349−6130	SPL	1360	7.1 ± 2.6	3.5± 3.5
J1352−6803	SPL	1278	1016.6 ± 710.5	132.8± 132.8
J1355−5925	SPL	1342	21.0 ± 24.5	7.3± 7.3
J1357−62	SPL	728	462.6 ± 259.2	137.6± 137.6
J1357−6429	SPL	728	13.0 ± 6.2	4.7± 4.7
J1401−6357	SPL	400	557.0 ± 207.5	142.8± 142.8
J1410−6132	SPL	1360	10.5 ± 2.5	6.2± 6.2
J1412−6111	SPL	1275	78.9 ± 172.0	16.4± 16.4
J1412−6145	SPL	1360	17.4 ± 6.2	6.2± 6.2
J1413−6141	SPL	1360	3.0 ± 1.1	2.0± 2.0
J1413−6307	SPL	640	11.9 ± 10.9	5.5± 5.5
J1415−6621	SPL	728	17.8 ± 11.4	5.8± 5.8
J1420−5416	SPL	400	112.9 ± 73.7	23.9± 23.9
J1420−6048	SPL	1360	2.2 ± 0.8	1.8± 1.8
J1424−5556	SPL	1277	35.2 ± 64.4	9.1± 9.1
J1424−5822	SPL	728	78.5 ± 53.3	21.1± 21.1
J1428−5530	SPL	400	174.3 ± 62.0	65.5± 65.5
J1444−5941	SPL	1277	250.8 ± 450.9	38.8± 38.8
J1446−4701	SPL	730	44.8 ± 15.5	10.7± 10.7

Continued on next page

Pulsar	Model	Min freq	S150	S300
J1452−5851	SPL	728	3.9 ± 1.6	1.8± 1.8
J1452−6036	HFCO	728	2.4 ± 0.1	2.3± 2.3
J1502−6128	SPL	1277	977.3 ± 1648.0	99.1± 99.1
J1507−6640	HFCO	400	43.3 ± 27.6	17.1± 17.1
J1511−5835	SPL	1277	1134.2 ± 1837.7	113.7± 113.7
J1512−5759	HFCO	640	97.2 ± 34.9	47.0± 47.0
J1513−5908	HFCO	400	3.8 ± 6.0	3.0± 3.0
J1515−5720	SPL	728	32.7 ± 13.0	7.1± 7.1
J1522−5829	SPL	640	339.4 ± 184.8	90.3± 90.3
J1524−5625	SPL	728	9.8 ± 3.2	5.1± 5.1
J1527−5552	SPL	400	409.6 ± 256.8	61.1± 61.1
J1530−5327	SPL	728	6.7 ± 3.9	3.5± 3.5
J1531−5610	SPL	1360	2.0 ± 0.7	1.5± 1.5
J1534−5405	SPL	640	352.1 ± 158.3	63.7± 63.7
J1537−5645	SPL	1277	12.0 ± 19.7	5.9± 5.9
J1538−5551	SPL	1360	8.0 ± 4.1	2.9± 2.9
J1539−5626	SPL	640	43.9 ± 9.6	21.9± 21.9
J1543−5459	SPL	1360	28.6 ± 13.1	9.3± 9.3
J1548−4927	SPL	728	59.6 ± 51.7	14.3± 14.3
J1548−5607	SPL	728	47.5 ± 16.6	14.9± 14.9
J1549−4848	SPL	436	93.6 ± 54.1	23.6± 23.6
J1551−5310	SPL	1360	12.6 ± 4.3	5.1± 5.1
J1553−5456	HFCO	400	77.1 ± 70.6	25.7± 25.7
J1555−2341	SPL	350	39.3 ± 8.8	12.5± 12.5
J1555−3134	SPL	350	62.6 ± 11.1	26.9± 26.9
J1557−4258	SPL	436	697.9 ± 251.7	127.8± 127.8
J1600−5751	SPL	400	191.3 ± 46.9	49.2± 49.2
J1601−5335	SPL	728	6.5 ± 3.1	2.3± 2.3
J1602−5100	SPL	400	357.9 ± 110.3	109.7± 109.7
J1603−5657	SPL	400	51.4 ± 58.2	14.6± 14.6
J1605−5257	SPL	400	148.1 ± 95.9	71.4± 71.4
J1611−5209	SPL	640	15.5 ± 4.3	7.2± 7.2
J1614−2230	SPL	350	16.5 ± 6.1	6.9± 6.9
J1614−3937	SPL	350	75.0 ± 16.9	15.3± 15.3
J1615−2940	SPL	350	30.1 ± 39.7	6.8± 6.8
J1615−5537	SPL	400	92.6 ± 60.4	22.0± 22.0
J1622−4802	SPL	1277	9.7 ± 5.5	4.5± 4.5
J1623−4256	SPL	400	104.5 ± 72.1	32.8± 32.8
J1624−4411	SPL	1277	13.2 ± 28.2	4.7± 4.7
J1626−4537	SPL	728	28.6 ± 17.1	9.9± 9.9
J1627−4706	SPL	1360	3.4 ± 1.4	1.3± 1.3
J1627−4845	SPL	1277	8.3 ± 23.8	3.7± 3.7
J1627−5547	SPL	1342	75.8 ± 103.0	16.9± 16.9
J1628−4804	SPL	1274	50.6 ± 87.3	15.7± 15.7
J1630−4733	SPL	1360	7.1 ± 4.5	6.0± 6.0
J1632−4621	SPL	1278	60.2 ± 24.9	16.1± 16.1
J1632−4757	SPL	1360	5.8 ± 2.1	2.7± 2.7
J1632−4818	SPL	1360	29.1 ± 11.8	7.9± 7.9
J1633−4453	SPL	640	68.9 ± 86.0	25.1± 25.1
J1636−4803	SPL	1278	177.1 ± 73.8	42.6± 42.6
J1636−4933	SPL	1277	3098.8 ± 8699.2	204.9± 204.9

Continued on next page

Pulsar	Model	Min freq	S150	S300
J1637−4553	SPL	400	31.0 ± 10.4	11.4± 11.4
J1637−4642	SPL	1360	3.8 ± 1.3	2.4± 2.4
J1637−4721	SPL	1277	141.8 ± 289.6	27.0± 27.0
J1638−3815	SPL	350	2.4 ± 1.0	1.6± 1.6
J1638−4417	SPL	1360	14.6 ± 18.0	4.2± 4.2
J1638−4608	SPL	1360	14.8 ± 5.5	4.9± 4.9
J1638−5226	SPL	1277	106.1 ± 147.7	21.3± 21.3
J1639−4604	SPL	400	161.3 ± 94.8	31.8± 31.8
J1640−4715	SPL	728	19.1 ± 6.3	8.6± 8.6
J1643−4505	SPL	1360	1.7 ± 0.6	1.1± 1.1
J1646−4346	SPL	1360	25.4 ± 13.3	9.7± 9.7
J1646−6831	SPL	400	93.7 ± 52.7	34.9± 34.9
J1648−4458	SPL	1276	58.0 ± 196.1	13.5± 13.5
J1648−4611	SPL	1360	1.3 ± 0.4	1.0± 1.0
J1649−3805	SPL	1277	200.1 ± 229.7	41.3± 41.3
J1649−4653	SPL	1277	5.2 ± 1.9	2.2± 2.2
J1650−4502	SPL	1360	4.2 ± 2.3	2.2± 2.2
J1651−5222	SPL	400	230.2 ± 140.0	61.7± 61.7
J1652−2404	SPL	350	45.0 ± 6.5	15.3± 15.3
J1653−3838	SPL	640	7.6 ± 5.5	4.5± 4.5
J1654−2713	SPL	350	15.8 ± 6.1	4.5± 4.5
J1658−4958	SPL	728	320.3 ± 165.0	62.7± 62.7
J1659−4439	SPL	1277	4.5 ± 10.6	2.2± 2.2
J1700−3312	SPL	350	16.1 ± 4.2	7.1± 7.1
J1700−3611	HFCO	350	4.1 ± 2.0	3.4± 3.4
J1701−3726	SPL	640	471.4 ± 278.5	100.6± 100.6
J1701−4533	SPL	640	57.7 ± 22.0	20.8± 20.8
J1702−4128	SPL	1360	2.5 ± 0.7	2.0± 2.0
J1702−4217	SPL	1276	40.7 ± 131.5	13.4± 13.4
J1702−4310	SPL	1360	6.2 ± 4.6	3.3± 3.3
J1703−4851	SPL	436	275.2 ± 196.8	50.1± 50.1
J1707−4341	SPL	1342	22.8 ± 42.0	7.1± 7.1
J1707−4729	SPL	1278	48.5 ± 31.3	19.5± 19.5
J1708−3426	SPL	350	204.3 ± 117.7	45.2± 45.2
J1708−3827	SPL	1276	104.5 ± 272.9	19.2± 19.2
J1709−3626	SPL	1276	4.2 ± 9.2	2.3± 2.3
J1709−4429	SPL	400	72.0 ± 26.1	40.4± 40.4
J1711−5350	SPL	400	68.4 ± 38.0	17.2± 17.2
J1715−3903	SPL	1360	3.6 ± 2.1	2.1± 2.1
J1715−4034	SPL	728	209.1 ± 102.0	48.5± 48.5
J1716−3720	SPL	1276	2155.6 ± 4820.3	149.7± 149.7
J1717−3953	SPL	1277	2206.7 ± 3032.1	220.2± 220.2
J1717−4054	SPL	400	197.8 ± 176.1	40.9± 40.9
J1718−3718	SPL	1276	17487922.9 ± 5809334.1	68312.2± 68312.2
J1718−3825	SPL	1360	4.8 ± 3.7	3.4± 3.4
J1719−4006	SPL	640	32.8 ± 19.4	11.8± 11.8
J1719−4302	SPL	1276	559.4 ± 1333.2	58.3± 58.3
J1721−3532	HFCO	1360	83.8 ± 34.8	50.0± 50.0
J1722−3632	SPL	640	28.5 ± 26.3	13.9± 13.9
J1722−3712	SPL	350	175.4 ± 43.9	50.9± 50.9
J1723−3659	HFCO	325	3.0 ± 0.2	2.9± 2.9

Continued on next page

Pulsar	Model	Min freq	S150	S300
J1724−3149	SPL	1278	15.2 ± 41.4	5.0± 5.0
J1725−3546	SPL	1276	5391.9 ± 10199.1	337.9± 337.9
J1726−3530	SPL	1360	2.7 ± 3.7	1.5± 1.5
J1727−2739	BPL	350	4.5 ± 3.1	5.5± 5.5
J1728−4028	SPL	1277	414.9 ± 566.0	61.6± 61.6
J1730−3350	SPL	1360	140.2 ± 90.4	44.6± 44.6
J1730−3353	SPL	1278	3644.8 ± 9165.7	209.5± 209.5
J1732−4128	SPL	400	72.8 ± 43.9	19.3± 19.3
J1733−2228	HFCO	350	28.5 ± 3.1	25.5± 25.5
J1733−3322	SPL	1342	279.8 ± 624.0	50.2± 50.2
J1733−3716	SPL	640	12.8 ± 6.8	8.5± 8.5
J1733−4005	SPL	1276	942.4 ± 1112.5	95.3± 95.3
J1734−3333	SPL	1360	2.2 ± 1.1	1.4± 1.4
J1736−2457	HFCO	350	8.1 ± 4.6	5.5± 5.5
J1736−2843	SPL	1277	457.6 ± 844.9	50.1± 50.1
J1737−3102	SPL	1275	139.1 ± 231.0	25.5± 25.5
J1737−3137	SPL	1278	84.8 ± 34.2	21.2± 21.2
J1737−3555	SPL	606	11.8 ± 6.0	5.0± 5.0
J1738−2330	HFCO	350	11.8 ± 21.7	7.9± 7.9
J1738−2647	SPL	1277	270.9 ± 526.6	38.4± 38.4
J1738−2955	SPL	1360	30.4 ± 31.6	6.6± 6.6
J1738−3211	SPL	350	11.0 ± 4.0	6.0± 6.0
J1738−3316	SPL	1275	4213.7 ± 10929.8	269.7± 269.7
J1739−2903	SPL	350	43.7 ± 33.5	20.3± 20.3
J1739−3159	SPL	1277	133.2 ± 228.5	28.7± 28.7
J1740−3015	HFCO	350	69.0 ± 10.9	34.6± 34.6
J1740−3052	SPL	1278	1345.1 ± 2173.3	134.5± 134.5
J1741−2733	HFCO	350	34.7 ± 9.6	18.9± 18.9
J1741−3927	SPL	350	87.8 ± 16.8	37.1± 37.1
J1744−2335	SPL	350	240.7 ± 234.6	27.4± 27.4
J1744−3130	SPL	610	8.6 ± 4.9	3.9± 3.9
J1745−3040	BPL	350	147.0 ± nan	87.3± 87.3
J1746−2849	SPL	1400	10.7 ± 16.4	3.8± 3.8
J1746−2850	SPL	1400	1.5 ± 2.4	1.2± 1.2
J1748−2021A	SPL	400	115.0 ± 129.2	19.6± 19.6
J1749−2629	SPL	1342	146.3 ± 279.7	27.8± 27.8
J1749−3002	SPL	606	101.8 ± 45.9	35.9± 35.9
J1750−2438	SPL	1275	2893.7 ± 3714.6	202.9± 202.9
J1750−3157	SPL	606	23.0 ± 12.6	9.5± 9.5
J1755−2725	SPL	350	23.4 ± 14.0	8.6± 8.6
J1756−2251	SPL	1276	61.2 ± 26.7	16.2± 16.2
J1756−2435	HFCO	606	6.3 ± 2.8	4.8± 4.8
J1757−2223	HFCO	600	1.9 ± 0.1	1.9± 1.9
J1758−2206	SPL	1276	826.6 ± 2464.0	80.1± 80.1
J1758−2630	SPL	1276	4.2 ± 13.5	1.7± 1.7
J1759−1940	SPL	1276	368.1 ± 702.5	61.5± 61.5
J1759−2922	SPL	350	101.7 ± 47.1	20.2± 20.2
J1759−3107	HFCO	350	17.7 ± 6.7	8.9± 8.9
J1801−1909	SPL	1277	6071.8 ± 10384.1	331.3± 331.3
J1801−2154	SPL	1360	4.1 ± 2.7	1.6± 1.6
J1802−2426	SPL	1276	16.1 ± 38.7	5.2± 5.2

Continued on next page

Pulsar	Model	Min freq	S150	S300
J1803−1857	SPL	1277	13.3 ± 19.0	4.4± 4.4
J1803−2712	SPL	640	13.6 ± 26.3	6.0± 6.0
J1803−3002A	SPL	900	78.9 ± 26.7	18.4± 18.4
J1804−0735	SPL	606	1.9 ± 1.2	1.5± 1.5
J1804−2717	HFCO	350	12.5 ± 1.9	11.1± 11.1
J1805−1504	SPL	728	293.5 ± 295.2	79.8± 79.8
J1806−2125	SPL	1170	71.7 ± 39.4	17.6± 17.6
J1807−2715	SPL	350	198.0 ± 107.7	36.6± 36.6
J1808−2057	SPL	606	51.7 ± 16.0	20.8± 20.8
J1809−1429	SPL	728	65.3 ± 37.9	17.0± 17.0
J1809−2109	SPL	606	84.8 ± 114.2	20.9± 20.9
J1810−1820	SPL	1275	16.0 ± 40.9	6.0± 6.0
J1810−5338	SPL	400	88.6 ± 52.7	28.0± 28.0
J1812−1718	SPL	1278	165.3 ± 97.0	36.1± 36.1
J1812−1733	HFCO	728	54.9 ± 20.7	28.0± 28.0
J1812−2102	SPL	1278	124.3 ± 44.9	31.9± 31.9
J1813−2113	SPL	1275	274.6 ± 606.6	38.5± 38.5
J1814−1649	SPL	1278	33.7 ± 45.5	12.3± 12.3
J1814−1744	SPL	1276	1069.7 ± 2333.5	105.3± 105.3
J1815−1738	SPL	1360	5.9 ± 4.1	2.5± 2.5
J1816−2650	HFCO	350	55.7 ± 17.9	26.9± 26.9
J1817−3618	HFCO	350	29.3 ± 7.6	17.1± 17.1
J1817−3837	HFCO	350	9.7 ± 2.8	6.4± 6.4
J1819−0925	SPL	1278	645.8 ± 686.3	80.3± 80.3
J1819−1510	SPL	1275	1315.0 ± 2313.7	129.4± 129.4
J1820−1346	SPL	606	131.1 ± 170.3	36.6± 36.6
J1820−1529	SPL	1278	46.6 ± 18.8	13.7± 13.7
J1820−1818	SPL	640	11.6 ± 19.9	5.7± 5.7
J1822−2256	BPL	350	78.9 ± 26.8	34.9± 34.9
J1822−4209	SPL	436	26.4 ± 26.0	9.2± 9.2
J1823−1347	SPL	1277	6.9 ± 22.5	2.9± 2.9
J1823−1526	SPL	1277	76.7 ± 155.8	15.1± 15.1
J1823−3021B	SPL	350	20.5 ± 4.5	4.4± 4.4
J1824−1118	SPL	606	109.4 ± 48.6	29.9± 29.9
J1824−1423	SPL	1278	17.0 ± 18.0	7.3± 7.3
J1826−1131	SPL	606	272.4 ± 67.4	48.2± 48.2
J1826−1526	SPL	1277	38.3 ± 92.3	8.8± 8.8
J1827−0750	SPL	728	154.4 ± 69.0	44.3± 44.3
J1827−0958	SPL	1278	725.4 ± 615.8	120.0± 120.0
J1828−0611	SPL	728	47.8 ± 17.1	16.7± 16.7
J1828−1101	HFCO	1360	4.4 ± 3.1	3.9± 3.9
J1829+0000	SPL	350	19.7 ± 10.3	6.5± 6.5
J1830−1135	SPL	843	206.8 ± 247.5	41.5± 41.5
J1831−1223	SPL	728	101.8 ± 44.3	25.7± 25.7
J1831−1329	SPL	1276	900.4 ± 1059.0	92.0± 92.0
J1832−0836	SPL	820	12.0 ± 4.2	5.2± 5.2
J1833−0559	SPL	1277	21.4 ± 45.2	8.1± 8.1
J1833−1055	SPL	1275	168.8 ± 284.9	38.0± 38.0
J1834−0602	SPL	1278	64.4 ± 89.7	17.3± 17.3
J1834−0731	SPL	610	45.8 ± 11.4	14.6± 14.6
J1834−1202	SPL	1277	6.7 ± 11.1	3.5± 3.5

Continued on next page

Pulsar	Model	Min freq	S150	S300
J1834−1710	SPL	728	25.8 ± 18.5	8.5± 8.5
J1834−1855	SPL	1276	71.2 ± 123.9	14.3± 14.3
J1835−0924	SPL	1277	5.3 ± 17.1	2.4± 2.4
J1835−0944	SPL	1276	41.1 ± 104.4	10.8± 10.8
J1836−0436	SPL	606	51.3 ± 25.1	19.0± 19.0
J1837−0045	SPL	350	22.4 ± 4.9	7.2± 7.2
J1837−0559	SPL	1342	41.1 ± 24.0	11.1± 11.1
J1837−0604	SPL	1360	5.2 ± 2.9	2.9± 2.9
J1837−1837	SPL	1278	104.2 ± 202.6	17.9± 17.9
J1838−0453	SPL	1360	20.2 ± 13.4	5.8± 5.8
J1838−0549	SPL	1360	4.3 ± 3.4	1.9± 1.9
J1838−1046	SPL	350	36.3 ± 17.0	9.0± 9.0
J1839−0321	SPL	1360	10.2 ± 7.1	3.2± 3.2
J1839−0643	SPL	1278	55.0 ± 33.6	18.9± 18.9
J1840−0809	SPL	728	71.9 ± 26.6	25.7± 25.7
J1840−0815	SPL	728	318.4 ± 162.5	64.7± 64.7
J1840−0840	SPL	350	143.6 ± 69.3	36.6± 36.6
J1841−0157	SPL	1278	21.8 ± 38.8	9.9± 9.9
J1841−0345	SPL	325	11.3 ± 1.7	6.2± 6.2
J1841−0500	SPL	2000	1040.3 ± 626.4	259.8± 259.8
J1841−0524	SPL	1360	11.7 ± 9.2	3.3± 3.3
J1842−0153	HFCO	728	3.2 ± 2.1	2.4± 2.4
J1842−0415	SPL	1277	2.4 ± 6.7	1.4± 1.4
J1842−0905	SPL	610	16.8 ± 7.9	6.9± 6.9
J1843−0211	HFCO	728	6.3 ± 3.8	4.2± 4.2
J1843−0355	SPL	1360	3.4 ± 1.8	2.2± 2.2
J1843−0806	SPL	1277	352.1 ± 764.9	43.6± 43.6
J1844−0030	SPL	1276	172.4 ± 426.4	26.8± 26.8
J1844−0256	SPL	1360	2.1 ± 1.2	1.4± 1.4
J1844−0310	SPL	1277	256.5 ± 911.2	42.3± 42.3
J1844−0433	SPL	350	65.1 ± 9.6	19.0± 19.0
J1844−0538	SPL	606	155.4 ± 37.9	43.1± 43.1
J1845−0316	SPL	1277	441.7 ± 1896.9	50.0± 50.0
J1845−0434	HFCO	606	5.4 ± 0.7	5.1± 5.1
J1846+0051	SPL	1275	922.2 ± 3241.3	72.7± 72.7
J1847−0438	SPL	1276	27.1 ± 18.6	8.2± 8.2
J1847−0605	SPL	1278	232.5 ± 305.2	42.9± 42.9
J1848−1414	SPL	436	100.6 ± 67.4	19.9± 19.9
J1848−1952	SPL	408	83.5 ± 32.5	26.4± 26.4
J1849−0614	SPL	350	67.8 ± 38.3	16.1± 16.1
J1850+0026	HFCO	350	20.1 ± 6.7	10.9± 10.9
J1852+0305	SPL	1276	435.4 ± 2118.6	39.4± 39.4
J1852−2610	SPL	350	103.7 ± 46.6	24.5± 24.5
J1853+0545	SPL	1278	24.8 ± 9.2	12.7± 12.7
J1853−0004	SPL	1278	127.9 ± 67.4	27.7± 27.7
J1854−1421	SPL	408	39.9 ± 9.3	14.9± 14.9
J1855+0307	SPL	728	24.6 ± 12.0	7.9± 7.9
J1855−0941	HFCO	350	14.7 ± 7.7	9.2± 9.2
J1856+0404	SPL	1278	201.3 ± 660.0	28.7± 28.7
J1857+0143	SPL	1170	41.4 ± 46.5	10.5± 10.5
J1900−0051	SPL	1278	118.9 ± 269.4	20.8± 20.8

Continued on next page

Pulsar	Model	Min freq	S150	S300
J1900−7951	SPL	400	48.0 ± 37.0	14.0± 14.0
J1901+0254	SPL	1277	38.8 ± 57.8	12.7± 12.7
J1901+0413	SPL	1278	75.3 ± 99.1	20.1± 20.1
J1901+0716	SPL	606	74.5 ± 27.7	19.7± 19.7
J1901−0906	HFCO	350	11.6 ± 4.2	9.2± 9.2
J1902+0615	HFCO	408	129.7 ± 50.5	41.1± 41.1
J1903+0327	SPL	1284	8.6 ± 3.2	3.6± 3.6
J1904+0004	SPL	350	22.9 ± 5.2	10.5± 10.5
J1904+0800	SPL	1278	1.7 ± 4.9	1.2± 1.2
J1904+1011	SPL	400	24.4 ± 4.3	7.3± 7.3
J1904−1224	SPL	400	90.5 ± 67.9	15.3± 15.3
J1905+0709	SPL	606	38.9 ± 10.6	15.0± 15.0
J1906+0641	SPL	408	8.0 ± 1.9	5.1± 5.1
J1906+0746	SPL	400	3.7 ± 1.3	1.6± 1.6
J1907+0918	SPL	400	2.2 ± 2.4	1.0± 1.0
J1908+0500	SPL	430	40.3 ± 44.3	12.2± 12.2
J1909−3744	SPL	350	16.9 ± 3.7	8.3± 8.3
J1910+1256	SPL	1284	14.0 ± 30.4	5.1± 5.1
J1915+1606	SPL	408	26.3 ± 16.8	7.6± 7.6
J1932−3655	SPL	350	5.5 ± 1.8	2.4± 2.4
J1944−1750	SPL	408	95.1 ± 25.7	16.5± 16.5
J1946−2913	HFCO	350	16.4 ± 7.2	9.6± 9.6
J1949−2524	SPL	350	30.6 ± 8.8	8.5± 8.5
J2004+3137	HFCO	350	19.3 ± 3.8	16.0± 16.0
J2007+2722	HFCO	610	2.6 ± 0.1	2.6± 2.6
J2010−1323	SPL	350	8.1 ± 3.6	3.6± 3.6
J2038−3816	SPL	350	12.0 ± 4.9	3.9± 3.9
J2129−5721	SPL	436	161.8 ± 58.7	35.6± 35.6
J2144−3933	SPL	350	5.6 ± 3.0	3.5± 3.5
J2234+0611	SPL	400	2.4 ± 2.3	1.4± 1.4
J2256−1024	SPL	350	121.3 ± 72.0	24.6± 24.6

Table C.1: The 391 pulsars that had no flux density measurements below 300 MHz and an estimated flux density of greater than 1 mJy at both 150 or 300 MHz. CSV of this data can be found here: https://github.com/NickSwainston/all_pulsar_spectra/blob/2.0.2/low_freq_camp.csv.

C.2 High-frequency flux density campaign

We recommend the 524 pulsars in Table C.2 as they have no flux density measurements above 5 GHz and an estimated flux density of greater than 0.01 mJy at both 5 and 10 GHz. The best spectral model for these pulsars are simple power law or power law with low-frequency turn-over, so their spectral cut-off has not yet been discovered, so they would benefit from further investigation at

high frequencies.

Pulsar	Model	Max freq (MHz)	S5000 (mJy)	S10000 (mJy)
J0014+4746	SPL	1408	0.42 ± 1.11	0.21± 0.21
J0026+6320	SPL	1400	0.24 ± 0.19	0.11± 0.11
J0040+5716	SPL	1606	0.11 ± 0.03	0.04± 0.04
J0051+0423	SPL	1360	0.12 ± 0.05	0.06± 0.06
J0055+5117	SPL	1408	0.95 ± 0.53	0.72± 0.72
J0056+4756	SPL	408	0.28 ± 0.13	0.15± 0.15
J0102+6537	SPL	1606	0.42 ± 0.15	0.25± 0.25
J0108+6905	SPL	1408	0.09 ± 0.08	0.05± 0.05
J0134−2937	SPL	1360	2.80 ± 1.31	2.18± 2.18
J0139+5814	BPL	1606	1.00 ± nan	0.41± 0.41
J0141+6009	LFTO	1408	0.64 ± 0.48	0.20± 0.20
J0147+5922	BPL	4920	0.91 ± 0.04	0.61± 0.61
J0152−1637	LFTO	1440	0.27 ± 0.09	0.08± 0.08
J0156+3949	SPL	408	2.38 ± 4.01	2.16± 2.16
J0157+6212	SPL	1408	0.94 ± 0.37	0.64± 0.64
J0212+5222	SPL	1400	0.40 ± 0.71	0.28± 0.28
J0215+6218	SPL	1400	3.38 ± 4.67	2.48± 2.48
J0231+7026	SPL	1408	0.06 ± 0.03	0.02± 0.02
J0255−5304	SPL	1360	1.57 ± 0.71	0.81± 0.81
J0304+1932	LFTO	1408	0.29 ± nan	0.04± 0.04
J0335+4555	SPL	1408	0.20 ± 0.08	0.09± 0.09
J0340+4130	SPL	1400	0.10 ± 0.06	0.04± 0.04
J0343+5312	SPL	1408	0.05 ± 0.02	0.02± 0.02
J0348+0432	SPL	1284	0.19 ± 0.08	0.10± 0.10
J0401−7608	SPL	3100	0.60 ± 0.26	0.24± 0.24
J0415+6954	SPL	1408	0.05 ± 0.02	0.02± 0.02
J0418−4154	SPL	843	0.08 ± 0.03	0.02± 0.02
J0421−0345	SPL	1400	0.09 ± 0.13	0.03± 0.03
J0435+2749	SPL	1400	0.03 ± 0.01	0.01± 0.01
J0448−2749	SPL	1360	3.83 ± 2.27	5.36± 5.36
J0454+5543	LFTO	4820	1.76 ± nan	0.46± 0.46
J0517+2212	SPL	1400	0.08 ± 0.03	0.03± 0.03
J0520−2553	SPL	1360	0.16 ± 0.15	0.07± 0.07
J0534+2200	BPL	1408	0.22 ± 0.21	0.02± 0.02
J0536−7543	SPL	3100	1.05 ± 0.29	0.33± 0.33
J0538+2817	SPL	4820	0.43 ± 0.07	0.19± 0.19
J0543+2329	BPL	4820	1.48 ± 0.18	0.51± 0.51
J0601−0527	LFTO	3100	0.23 ± 0.11	0.06± 0.06
J0612+3721	SPL	1408	2.43 ± 1.48	1.58± 1.58
J0613+3731	SPL	1400	0.04 ± 0.02	0.02± 0.02
J0613−0200	LFTO	3100	0.13 ± 0.01	0.03± 0.03
J0614+2229	LFTO	3100	0.14 ± 0.02	0.03± 0.03
J0624−0424	SPL	1408	0.39 ± 0.19	0.19± 0.19
J0627+0706	SPL	3100	0.17 ± 0.02	0.06± 0.06
J0629+2415	SPL	1408	0.46 ± 0.15	0.15± 0.15
J0631+1036	SPL	1400	0.09 ± 0.01	0.02± 0.02
J0636+5128	SPL	1400	0.42 ± 0.27	0.28± 0.28
J0645+5158	SPL	1400	0.08 ± 0.04	0.03± 0.03

Continued on next page

Pulsar	Model	Max freq	S5000	S10000
J0656−2228	SPL	3100	0.36 ± 0.16	0.28± 0.28
J0711−6830	LFTO	3100	0.28 ± 0.05	0.07± 0.07
J0719−2545	SPL	1459	0.17 ± 0.03	0.07± 0.07
J0729−1448	SPL	3100	0.10 ± 0.02	0.03± 0.03
J0729−1836	SPL	3100	0.20 ± 0.04	0.07± 0.07
J0740+6620	SPL	1400	0.70 ± 0.44	0.49± 0.49
J0751+1807	SPL	2695	0.54 ± 0.09	0.34± 0.34
J0754+3231	SPL	1408	0.24 ± 0.13	0.11± 0.11
J0758−1528	SPL	3100	0.83 ± 0.46	0.51± 0.51
J0809−4753	LFTO	3100	0.12 ± 0.03	0.02± 0.02
J0815+4611	SPL	400	0.07 ± 0.12	0.03± 0.03
J0820−1350	BPL	4820	0.39 ± 0.15	0.08± 0.08
J0820−3826	SPL	3100	0.04 ± 0.01	0.01± 0.01
J0820−3921	SPL	1460	0.04 ± 0.01	0.01± 0.01
J0820−4114	BPL	3100	0.29 ± 0.16	0.06± 0.06
J0823+0159	SPL	3100	0.39 ± 0.18	0.16± 0.16
J0831−4406	SPL	1461	0.12 ± 0.12	0.05± 0.05
J0834−4159	SPL	3100	0.03 ± 0.01	0.01± 0.01
J0842−4851	SPL	1400	0.11 ± 0.01	0.03± 0.03
J0846−3533	BPL	3100	0.21 ± 0.09	0.04± 0.04
J0849+8028	SPL	390	0.09 ± 0.15	0.04± 0.04
J0855−4644	SPL	3100	0.06 ± 0.01	0.03± 0.03
J0857−4424	SPL	3100	0.07 ± 0.01	0.02± 0.02
J0900−3144	SPL	3100	0.57 ± 0.20	0.22± 0.22
J0901−4624	SPL	3100	0.12 ± 0.03	0.06± 0.06
J0902−6325	SPL	1360	0.35 ± 0.21	0.15± 0.15
J0904−4246	SPL	1400	0.05 ± 0.03	0.01± 0.01
J0904−7459	SPL	3100	0.24 ± 0.07	0.10± 0.10
J0905−5127	SPL	3100	0.10 ± 0.01	0.03± 0.03
J0907−5157	BPL	3100	3.02 ± nan	1.38± 1.38
J0908−1739	LFTO	3100	0.50 ± 0.18	0.19± 0.19
J0909−7212	SPL	1382	0.20 ± 0.14	0.08± 0.08
J0924−5302	SPL	3100	0.09 ± 0.02	0.02± 0.02
J0924−5814	SPL	3100	1.20 ± 0.25	0.58± 0.58
J0931−1902	SPL	1400	0.15 ± 0.06	0.08± 0.08
J0932−3217	SPL	1459	0.06 ± 0.01	0.02± 0.02
J0934−5249	SPL	3100	0.06 ± 0.02	0.01± 0.01
J0940−5428	SPL	3100	0.18 ± 0.03	0.09± 0.09
J0942−5552	LFTO	3100	0.22 ± 0.01	0.02± 0.02
J0942−5657	SPL	3100	0.05 ± 0.01	0.01± 0.01
J0943+1631	LFTO	3100	0.09 ± 0.08	0.02± 0.02
J0943+2253	SPL	1400	0.08 ± 0.03	0.03± 0.03
J0944−1354	SPL	1408	0.09 ± 0.05	0.03± 0.03
J0954−5430	SPL	3100	0.30 ± 0.07	0.23± 0.23
J0959−4809	SPL	3100	0.25 ± 0.07	0.08± 0.08
J1001−5507	BPL	3100	0.26 ± 0.12	0.04± 0.04
J1012−5857	SPL	3100	0.19 ± 0.02	0.06± 0.06
J1013−5934	SPL	3100	0.60 ± 0.19	0.31± 0.31
J1015−5719	SPL	3100	1.50 ± 0.21	1.28± 1.28
J1016−5345	SPL	3100	0.07 ± 0.03	0.02± 0.02
J1016−5857	SPL	3100	0.16 ± 0.02	0.06± 0.06

Continued on next page

Pulsar	Model	Max freq	S5000	S10000
J1017−5621	LFTO	3100	0.08 ± 0.02	0.01± 0.01
J1017−7156	SPL	3100	0.09 ± 0.01	0.03± 0.03
J1019−5749	SPL	3100	4.36 ± 0.55	10.40± 10.40
J1022+1001	DTOS	4850	0.47 ± 0.03	0.11± 0.11
J1024−0719	BPL	4850	0.33 ± 0.03	0.17± 0.17
J1028−5819	SPL	3100	0.15 ± 0.11	0.12± 0.12
J1034−3224	SPL	3100	1.55 ± 0.62	0.82± 0.82
J1036−4926	SPL	1382	0.11 ± 0.05	0.04± 0.04
J1038−5831	SPL	3100	0.17 ± 0.19	0.07± 0.07
J1041−1942	SPL	1408	0.20 ± 0.09	0.07± 0.07
J1043−6116	SPL	3100	0.28 ± 0.03	0.12± 0.12
J1046−5813	SPL	3100	0.09 ± 0.02	0.02± 0.02
J1047−3032	SPL	1360	0.16 ± 0.08	0.06± 0.06
J1047−6709	SPL	3100	1.17 ± 0.37	0.76± 0.76
J1052−5954	SPL	3100	0.05 ± 0.01	0.02± 0.02
J1055−6028	SPL	3100	0.06 ± 0.01	0.02± 0.02
J1057−5226	BPL	3100	0.27 ± 0.46	0.05± 0.05
J1105−6107	SPL	3100	0.25 ± 0.04	0.11± 0.11
J1107−5947	SPL	1460	0.12 ± 0.05	0.04± 0.04
J1107−6143	SPL	1522	0.10 ± 0.04	0.03± 0.03
J1112−6103	SPL	3100	0.65 ± 0.10	0.33± 0.33
J1112−6613	SPL	3100	0.13 ± 0.03	0.03± 0.03
J1112−6926	SPL	3100	0.10 ± 0.05	0.03± 0.03
J1115−6052	SPL	3100	0.12 ± 0.01	0.05± 0.05
J1119−6127	SPL	3100	0.17 ± 0.03	0.07± 0.07
J1119−7936	SPL	1360	0.05 ± 0.03	0.01± 0.01
J1121−5444	SPL	3100	0.11 ± 0.02	0.03± 0.03
J1123−4844	SPL	3100	0.23 ± 0.08	0.10± 0.10
J1125+7819	SPL	1400	0.13 ± 0.15	0.04± 0.04
J1126−6054	SPL	3100	0.13 ± 0.11	0.04± 0.04
J1133−6250	SPL	3100	0.62 ± 0.27	0.20± 0.20
J1138−6207	SPL	3100	0.17 ± 0.03	0.09± 0.09
J1141−3322	SPL	1382	1.26 ± 0.65	1.02± 1.02
J1146−6030	BPL	3100	0.47 ± nan	0.15± 0.15
J1156−5707	SPL	3100	0.07 ± 0.01	0.03± 0.03
J1157−6224	SPL	3100	0.51 ± 0.19	0.10± 0.10
J1202−5820	SPL	3100	0.29 ± 0.09	0.09± 0.09
J1224−6407	BPL	3100	1.31 ± 0.28	0.47± 0.47
J1225−6035	SPL	1459	0.04 ± 0.04	0.01± 0.01
J1231−1411	SPL	1284	0.04 ± 0.01	0.01± 0.01
J1239−6832	SPL	3100	0.12 ± 0.03	0.04± 0.04
J1240−4124	SPL	1360	0.06 ± 0.03	0.02± 0.02
J1246+2253	SPL	1400	0.09 ± 0.02	0.04± 0.04
J1253−5820	SPL	3100	0.54 ± 0.25	0.19± 0.19
J1257−1027	SPL	1606	0.24 ± 0.08	0.09± 0.09
J1259−6741	SPL	3100	0.21 ± 0.07	0.08± 0.08
J1301−6305	SPL	3100	0.14 ± 0.02	0.08± 0.08
J1305−6203	SPL	3100	0.12 ± 0.02	0.05± 0.05
J1305−6455	SPL	3100	0.11 ± 0.08	0.02± 0.02
J1306−6617	SPL	3100	0.50 ± 0.23	0.15± 0.15
J1311−1228	SPL	1408	0.05 ± 0.03	0.02± 0.02

Continued on next page

Pulsar	Model	Max freq	S5000	S10000
J1312−5402	SPL	3100	0.09 ± 0.01	0.03± 0.03
J1312−5516	SPL	3100	0.28 ± 0.07	0.08± 0.08
J1317−6302	SPL	3100	0.09 ± 0.02	0.02± 0.02
J1319−6056	SPL	3100	0.08 ± 0.03	0.02± 0.02
J1319−6105	SPL	3100	0.28 ± 0.07	0.12± 0.12
J1321+8323	SPL	606	8.44 ± 3.98	8.35± 8.35
J1326−6408	SPL	3100	0.11 ± 0.02	0.02± 0.02
J1326−6700	SPL	3100	2.91 ± 0.85	1.38± 1.38
J1327−6301	SPL	3100	0.33 ± 0.14	0.09± 0.09
J1327−6400	SPL	3100	0.04 ± 0.01	0.02± 0.02
J1328−4357	SPL	1360	0.96 ± 0.33	0.43± 0.43
J1338−6204	SPL	3100	0.65 ± 0.21	0.25± 0.25
J1340−6456	SPL	1400	0.17 ± 0.05	0.06± 0.06
J1349−6130	SPL	3100	0.19 ± 0.03	0.10± 0.10
J1355−5925	SPL	1522	0.10 ± 0.07	0.03± 0.03
J1357−62	SPL	3100	1.00 ± 0.32	0.30± 0.30
J1357−6429	SPL	3100	0.08 ± 0.02	0.03± 0.03
J1400−6325	SPL	3000	0.06 ± 0.06	0.03± 0.03
J1401−6357	SPL	3100	0.57 ± 0.18	0.15± 0.15
J1412−6145	SPL	3100	0.10 ± 0.01	0.03± 0.03
J1413−6141	SPL	3100	0.37 ± 0.05	0.24± 0.24
J1413−6307	SPL	3100	0.25 ± 0.12	0.12± 0.12
J1415−6621	SPL	1459	0.06 ± 0.02	0.02± 0.02
J1418−3921	SPL	1369	0.07 ± 0.01	0.02± 0.02
J1420−6048	SPL	3100	0.78 ± 0.10	0.63± 0.63
J1424−5556	SPL	1459	0.04 ± 0.04	0.01± 0.01
J1424−5822	SPL	3100	0.10 ± 0.04	0.03± 0.03
J1428−5530	SPL	1400	1.23 ± 0.26	0.46± 0.46
J1452−5851	SPL	3100	0.07 ± 0.01	0.03± 0.03
J1509+5531	LFTO	4820	0.13 ± 0.08	0.02± 0.02
J1514−5925	SPL	3100	0.11 ± 0.02	0.07± 0.07
J1518+4904	SPL	4850	0.28 ± 0.07	0.11± 0.11
J1524−5625	SPL	3100	0.35 ± 0.04	0.18± 0.18
J1527−3931	SPL	843	0.19 ± 0.10	0.06± 0.06
J1530−5327	SPL	3100	0.26 ± 0.08	0.14± 0.14
J1532+2745	LFTO	1408	0.10 ± 0.08	0.03± 0.03
J1534−5334	SPL	1577	0.81 ± 0.47	0.26± 0.26
J1534−5405	SPL	3100	0.06 ± 0.02	0.01± 0.01
J1537−5645	SPL	1460	0.35 ± 0.33	0.17± 0.17
J1538−5551	SPL	3100	0.05 ± 0.01	0.02± 0.02
J1541−5535	SPL	3100	0.13 ± 0.02	0.08± 0.08
J1543+0929	DTOS	1408	0.24 ± 0.12	0.02± 0.02
J1543−5459	SPL	3100	0.09 ± 0.02	0.03± 0.03
J1544−5308	SPL	1577	0.96 ± 0.12	0.36± 0.36
J1548−4927	SPL	3100	0.04 ± 0.02	0.01± 0.01
J1548−5607	SPL	3100	0.13 ± 0.02	0.04± 0.04
J1549−4848	SPL	3100	0.09 ± 0.03	0.02± 0.02
J1551−5310	SPL	3100	0.13 ± 0.01	0.05± 0.05
J1555−2341	SPL	1408	0.12 ± 0.04	0.04± 0.04
J1555−3134	SPL	1408	0.87 ± 0.09	0.37± 0.37
J1557−4258	SPL	1369	0.13 ± 0.03	0.02± 0.02

Continued on next page

Pulsar	Model	Max freq	S5000	S10000
J1600−3053	LFTO	4820	0.30 ± nan	0.04± 0.04
J1600−5751	SPL	3100	0.20 ± 0.03	0.05± 0.05
J1601−5335	SPL	3100	0.03 ± 0.01	0.01± 0.01
J1603−2712	SPL	1408	0.25 ± 0.09	0.08± 0.08
J1603−5657	SPL	1400	0.09 ± 0.06	0.03± 0.03
J1603−7202	LFTO	3100	0.10 ± 0.03	0.01± 0.01
J1604−4909	BPL	3100	0.25 ± nan	0.04± 0.04
J1605−5257	SPL	1577	3.71 ± 1.76	1.79± 1.79
J1610−1322	SPL	1369	0.07 ± 0.01	0.02± 0.02
J1611−5209	SPL	3100	0.32 ± 0.06	0.15± 0.15
J1613−4714	SPL	3100	0.18 ± 0.04	0.05± 0.05
J1614+0737	LFTO	1408	0.07 ± 0.03	0.02± 0.02
J1614−2230	SPL	1400	0.20 ± 0.05	0.08± 0.08
J1614−5048	SPL	3100	0.25 ± 0.02	0.06± 0.06
J1615−5537	SPL	3100	0.06 ± 0.02	0.02± 0.02
J1622−4802	SPL	3100	0.20 ± 0.07	0.09± 0.09
J1623−0908	SPL	1408	0.08 ± 0.02	0.02± 0.02
J1623−4256	SPL	1460	0.30 ± 0.12	0.09± 0.09
J1624−4411	SPL	1460	0.07 ± 0.09	0.03± 0.03
J1626−4537	SPL	3100	0.13 ± 0.05	0.05± 0.05
J1626−4807	SPL	3100	0.21 ± 0.04	0.15± 0.15
J1627+1419	SPL	400	0.08 ± 0.07	0.02± 0.02
J1627−4706	SPL	3100	0.03 ± 0.01	0.01± 0.01
J1627−4845	SPL	1459	0.13 ± 0.22	0.06± 0.06
J1628−4804	SPL	1460	0.13 ± 0.14	0.04± 0.04
J1632−4621	SPL	3100	0.08 ± 0.02	0.02± 0.02
J1632−4757	SPL	3100	0.12 ± 0.01	0.05± 0.05
J1632−4818	SPL	3100	0.04 ± 0.01	0.01± 0.01
J1633−4453	SPL	3100	0.42 ± 0.31	0.15± 0.15
J1633−5015	LFTO	3100	0.31 ± 0.10	0.06± 0.06
J1636−4803	SPL	3100	0.13 ± 0.03	0.03± 0.03
J1637−4553	SPL	3100	0.19 ± 0.03	0.07± 0.07
J1637−4642	SPL	3100	0.39 ± 0.05	0.25± 0.25
J1638−3815	SPL	1460	0.33 ± 0.08	0.22± 0.22
J1638−4608	SPL	3100	0.06 ± 0.01	0.02± 0.02
J1640+2224	SPL	2695	0.05 ± 0.01	0.02± 0.02
J1640−4715	SPL	3100	0.34 ± 0.04	0.15± 0.15
J1643−1224	SPL	4850	0.47 ± 0.03	0.15± 0.15
J1643−4505	SPL	3100	0.20 ± 0.03	0.13± 0.13
J1646−4346	SPL	3100	0.20 ± 0.05	0.08± 0.08
J1646−6831	SPL	3100	0.63 ± 0.41	0.23± 0.23
J1648−4611	SPL	3100	0.39 ± 0.06	0.31± 0.31
J1649+2533	SPL	400	13897.16 ± 1104.86	111177.30± 111177.30
J1649−3805	SPL	1460	0.07 ± 0.05	0.01± 0.01
J1649−4653	SPL	3100	0.07 ± 0.01	0.03± 0.03
J1650−4502	SPL	3100	0.17 ± 0.04	0.09± 0.09
J1650−4921	SPL	3100	0.33 ± 0.07	0.36± 0.36
J1651−5222	SPL	3100	0.29 ± 0.13	0.08± 0.08
J1652−2404	SPL	1408	0.19 ± 0.02	0.06± 0.06
J1653−3838	SPL	3100	0.57 ± 0.24	0.34± 0.34
J1653−4249	SPL	3100	10.92 ± 7.39	36.94± 36.94

Continued on next page

Pulsar	Model	Max freq	S5000	S10000
J1658−4958	SPL	3100	0.08 ± 0.03	0.02± 0.02
J1659−1305	SPL	1369	0.09 ± 0.01	0.03± 0.03
J1659−4439	SPL	1460	0.11 ± 0.16	0.06± 0.06
J1700−3312	SPL	3100	0.26 ± 0.08	0.11± 0.11
J1701−3726	SPL	3100	0.19 ± 0.09	0.04± 0.04
J1701−4533	SPL	3100	0.33 ± 0.08	0.12± 0.12
J1702−4217	SPL	1460	0.15 ± 0.28	0.05± 0.05
J1702−4310	SPL	3100	0.27 ± 0.10	0.15± 0.15
J1705−3423	SPL	4920	1.12 ± 0.17	0.54± 0.54
J1705−3950	LFTO	3100	0.57 ± 0.29	0.26± 0.26
J1707−4341	SPL	1522	0.06 ± 0.06	0.02± 0.02
J1707−4729	SPL	3100	0.48 ± 0.18	0.19± 0.19
J1708−3426	SPL	3100	0.10 ± 0.03	0.02± 0.02
J1709−3626	SPL	1460	0.19 ± 0.25	0.10± 0.10
J1711−1509	SPL	1408	0.05 ± 0.04	0.01± 0.01
J1711−5350	SPL	3100	0.06 ± 0.02	0.02± 0.02
J1713+0747	BPL	4850	0.82 ± 0.26	0.17± 0.17
J1715−3903	SPL	3100	0.22 ± 0.06	0.13± 0.13
J1715−4034	SPL	3100	0.13 ± 0.04	0.03± 0.03
J1717−3425	LFTO	3100	0.15 ± 0.05	0.03± 0.03
J1717−4054	SPL	3100	0.07 ± 0.04	0.01± 0.01
J1718−3825	SPL	3100	0.87 ± 0.36	0.62± 0.62
J1719−4006	SPL	3100	0.19 ± 0.06	0.07± 0.07
J1720−1633	SPL	1408	0.21 ± 0.06	0.07± 0.07
J1720−2933	SPL	1408	0.08 ± 0.00	0.01± 0.01
J1722−3207	LFTO	3100	0.19 ± 0.06	0.03± 0.03
J1722−3632	SPL	3100	0.75 ± 0.41	0.37± 0.37
J1722−3712	SPL	3100	0.34 ± 0.08	0.10± 0.10
J1724−3149	SPL	1460	0.05 ± 0.08	0.02± 0.02
J1726−3530	SPL	3100	0.12 ± 0.09	0.06± 0.06
J1727−2739	BPL	3100	0.24 ± 0.06	0.06± 0.06
J1728−0007	SPL	1369	0.05 ± 0.01	0.01± 0.01
J1731−4744	LFTO	3100	1.67 ± 0.42	0.39± 0.39
J1732−4128	SPL	1459	0.09 ± 0.03	0.02± 0.02
J1733−3716	SPL	3100	1.63 ± 0.45	1.08± 1.08
J1734−3333	SPL	3100	0.25 ± 0.02	0.16± 0.16
J1735−3258	SPL	3100	0.38 ± 0.12	0.36± 0.36
J1737−3137	SPL	3100	0.08 ± 0.02	0.02± 0.02
J1737−3555	SPL	3100	0.15 ± 0.06	0.06± 0.06
J1738−3211	SPL	3100	0.51 ± 0.14	0.27± 0.27
J1739−2903	SPL	4920	0.91 ± 0.25	0.42± 0.42
J1739−3159	SPL	1459	0.06 ± 0.06	0.01± 0.01
J1741+2758	SPL	400	0.56 ± 0.30	0.36± 0.36
J1741−0840	SPL	1408	0.17 ± 0.08	0.05± 0.05
J1741−3927	SPL	3100	1.13 ± 0.31	0.48± 0.48
J1743−1351	SPL	1408	0.07 ± 0.05	0.02± 0.02
J1744−1134	DTOS	4850	0.31 ± 0.02	0.09± 0.09
J1744−3130	SPL	3100	0.15 ± 0.05	0.07± 0.07
J1745−3040	BPL	4820	1.64 ± nan	0.45± 0.45
J1746+2540	SPL	400	0.04 ± 0.07	0.02± 0.02
J1748−1300	SPL	3100	0.16 ± 0.06	0.04± 0.04

Continued on next page

Pulsar	Model	Max freq	S5000	S10000
J1749−3002	SPL	3100	0.52 ± 0.14	0.19± 0.19
J1750−3157	SPL	3100	0.27 ± 0.09	0.11± 0.11
J1751−3323	LFTO	3100	0.46 ± 0.18	0.18± 0.18
J1751−4657	LFTO	3100	0.16 ± 0.06	0.02± 0.02
J1752+2359	SPL	400	0.79 ± 1.17	0.53± 0.53
J1753−2501	SPL	1606	1.91 ± 0.73	1.94± 1.94
J1754+5201	SPL	1408	1.27 ± 0.62	1.07± 1.07
J1755−2725	SPL	1459	0.15 ± 0.05	0.06± 0.06
J1756−2251	SPL	1459	0.07 ± 0.02	0.02± 0.02
J1758+3030	SPL	900	0.51 ± 0.34	0.24± 0.24
J1758−2540	SPL	1460	2.48 ± 4.25	5.05± 5.05
J1758−2630	SPL	1460	0.04 ± 0.08	0.02± 0.02
J1759−2205	SPL	3100	0.11 ± 0.02	0.03± 0.03
J1801−0357	SPL	1408	0.08 ± 0.05	0.02± 0.02
J1801−2154	SPL	3100	0.04 ± 0.01	0.01± 0.01
J1801−2920	LFTO	3100	0.13 ± 0.06	0.03± 0.03
J1802−2124	SPL	1521	0.78 ± 0.41	0.80± 0.80
J1802−2426	SPL	1460	0.05 ± 0.08	0.02± 0.02
J1803−1857	SPL	1460	0.05 ± 0.04	0.02± 0.02
J1803−2712	SPL	1577	0.22 ± 0.25	0.10± 0.10
J1803−3002A	SPL	4000	0.05 ± 0.01	0.01± 0.01
J1804−0735	SPL	1459	0.53 ± 0.19	0.42± 0.42
J1805+0306	SPL	400	0.10 ± 0.27	0.04± 0.04
J1805−1504	SPL	1460	0.40 ± 0.25	0.11± 0.11
J1806−2125	SPL	3100	0.06 ± 0.02	0.01± 0.01
J1807−0847	BPL	4820	1.78 ± 0.12	0.55± 0.55
J1808−2057	SPL	3100	0.51 ± 0.10	0.21± 0.21
J1809−1429	SPL	3100	0.07 ± 0.02	0.02± 0.02
J1809−2109	SPL	3100	0.07 ± 0.06	0.02± 0.02
J1810−1820	SPL	1460	0.11 ± 0.16	0.04± 0.04
J1810−5338	SPL	3100	0.26 ± 0.15	0.08± 0.08
J1812+0226	SPL	1408	0.05 ± 0.04	0.01± 0.01
J1812−1718	SPL	3100	0.07 ± 0.03	0.02± 0.02
J1812−2102	SPL	4850	0.13 ± 0.03	0.03± 0.03
J1814−1649	SPL	1459	0.21 ± 0.16	0.08± 0.08
J1815−1738	SPL	3100	0.08 ± 0.03	0.03± 0.03
J1820−0427	LFTO	4920	0.46 ± 0.02	0.09± 0.09
J1820−1346	SPL	1606	0.21 ± 0.16	0.06± 0.06
J1820−1529	SPL	3100	0.10 ± 0.02	0.03± 0.03
J1820−1818	SPL	3100	0.32 ± 0.31	0.16± 0.16
J1822−1400	SPL	2640	0.27 ± 0.03	0.13± 0.13
J1822−2256	BPL	3100	0.21 ± 0.07	0.05± 0.05
J1822−4209	SPL	3100	0.13 ± 0.08	0.05± 0.05
J1823+0550	SPL	1408	0.18 ± 0.06	0.05± 0.05
J1823−0154	SPL	1400	0.09 ± 0.04	0.03± 0.03
J1823−1115	LFTO	3100	0.39 ± 0.10	0.11± 0.11
J1823−1347	SPL	1459	0.09 ± 0.18	0.04± 0.04
J1823−3106	SPL	3100	0.56 ± 0.19	0.18± 0.18
J1824−1118	SPL	3100	0.16 ± 0.05	0.04± 0.04
J1824−1423	SPL	1459	0.24 ± 0.15	0.10± 0.10
J1824−1945	LFTO	3100	0.40 ± 0.05	0.09± 0.09

Continued on next page

Pulsar	Model	Max freq	S5000	S10000
J1824−2452A	SPL	3100	0.12 ± 0.01	0.03± 0.03
J1825−0935	LFTO	4820	2.93 ± 0.29	1.39± 1.39
J1826−1334	LFTO	4920	2.64 ± 0.52	1.75± 1.75
J1827−0750	SPL	3100	0.28 ± 0.07	0.08± 0.08
J1827−0958	SPL	1459	0.08 ± 0.04	0.01± 0.01
J1828−0611	SPL	3100	0.24 ± 0.05	0.08± 0.08
J1828−1057	SPL	3100	0.12 ± 0.05	0.08± 0.08
J1829+0000	SPL	1460	0.07 ± 0.02	0.02± 0.02
J1830−1135	SPL	1460	0.06 ± 0.04	0.01± 0.01
J1831−0823	LFTO	3100	0.07 ± 0.03	0.02± 0.02
J1831−1223	SPL	3100	0.10 ± 0.02	0.02± 0.02
J1832−0836	SPL	3100	0.18 ± 0.04	0.08± 0.08
J1833−0559	SPL	1460	0.16 ± 0.19	0.06± 0.06
J1833−0827	BPL	4920	0.92 ± nan	0.34± 0.34
J1833−1055	SPL	1460	0.09 ± 0.09	0.02± 0.02
J1834−0426	SPL	1408	3.04 ± 0.07	1.13± 1.13
J1834−0602	SPL	1459	0.08 ± 0.07	0.02± 0.02
J1834−0731	SPL	4850	0.14 ± 0.01	0.04± 0.04
J1834−1202	SPL	1461	0.25 ± 0.25	0.13± 0.13
J1834−1710	SPL	3100	0.09 ± 0.04	0.03± 0.03
J1835−0924	SPL	1459	0.10 ± 0.18	0.04± 0.04
J1835−0944	SPL	1460	0.05 ± 0.07	0.01± 0.01
J1835−1020	LFTO	4850	0.23 ± 0.03	0.05± 0.05
J1835−1106	SPL	4920	0.26 ± 0.02	0.08± 0.08
J1836−0436	SPL	3100	0.33 ± 0.10	0.12± 0.12
J1837−0045	SPL	1400	0.07 ± 0.02	0.02± 0.02
J1837−0559	SPL	3100	0.05 ± 0.02	0.01± 0.01
J1837−0604	SPL	3100	0.25 ± 0.06	0.14± 0.14
J1838−0453	SPL	3100	0.04 ± 0.01	0.01± 0.01
J1838−0549	SPL	3100	0.08 ± 0.03	0.04± 0.04
J1839−0643	SPL	3100	0.25 ± 0.09	0.08± 0.08
J1839−0905	SPL	3100	0.08 ± 0.03	0.04± 0.04
J1840+5640	LFTO	1408	0.64 ± 0.53	0.24± 0.24
J1840−0809	SPL	3100	0.39 ± 0.08	0.14± 0.14
J1840−0815	SPL	3100	0.10 ± 0.03	0.02± 0.02
J1840−0840	SPL	1460	0.14 ± 0.04	0.04± 0.04
J1841−0157	SPL	1459	0.39 ± 0.41	0.18± 0.18
J1841−0345	SPL	4850	0.56 ± 0.01	0.31± 0.31
J1842−0359	BPL	3100	0.12 ± nan	1.00± 1.00
J1842−0415	SPL	1460	0.13 ± 0.20	0.07± 0.07
J1842−0905	SPL	3100	0.19 ± 0.05	0.08± 0.08
J1843−0355	SPL	3100	0.40 ± 0.09	0.26± 0.26
J1844+1454	SPL	1408	0.17 ± 0.04	0.05± 0.05
J1844−0256	SPL	3100	0.26 ± 0.06	0.17± 0.17
J1844−0433	SPL	3100	0.13 ± 0.02	0.04± 0.04
J1844−0538	SPL	3100	0.24 ± 0.04	0.07± 0.07
J1845−0743	BPL	3100	0.37 ± 0.06	0.11± 0.11
J1847−0402	BPL	3100	0.66 ± 0.22	0.23± 0.23
J1847−0438	SPL	3100	0.06 ± 0.03	0.02± 0.02
J1848−1952	SPL	950	0.25 ± 0.13	0.08± 0.08
J1849+2423	SPL	400	0.06 ± 0.11	0.02± 0.02

Continued on next page

Pulsar	Model	Max freq	S5000	S10000
J1849−0614	SPL	1460	0.05 ± 0.02	0.01± 0.01
J1849−0636	BPL	3100	0.08 ± 0.02	0.02± 0.02
J1851+0418	SPL	1460	0.23 ± 0.02	0.07± 0.07
J1851+1259	SPL	1606	0.08 ± 0.03	0.03± 0.03
J1851−0053	SPL	1400	0.49 ± 0.14	0.34± 0.34
J1852+0031	SPL	1606	2.33 ± 0.31	1.46± 1.46
J1852−2610	SPL	1360	0.07 ± 0.06	0.02± 0.02
J1853+0545	SPL	4920	0.83 ± 0.18	0.43± 0.43
J1853+1303	SPL	1400	0.05 ± 0.01	0.02± 0.02
J1853−0004	SPL	3100	0.06 ± 0.02	0.01± 0.01
J1854−1421	SPL	3100	0.28 ± 0.08	0.10± 0.10
J1855+0307	SPL	3100	0.08 ± 0.02	0.02± 0.02
J1857+0057	SPL	1400	0.10 ± 0.04	0.03± 0.03
J1857+0143	SPL	4850	0.04 ± 0.02	0.01± 0.01
J1857+0212	SPL	3100	0.20 ± 0.09	0.06± 0.06
J1857+0943	BPL	4850	0.94 ± 0.28	0.40± 0.40
J1900−2600	LFTO	4820	0.79 ± 0.17	0.16± 0.16
J1900−7951	SPL	1369	0.09 ± 0.04	0.03± 0.03
J1901+0254	SPL	1460	0.14 ± 0.12	0.04± 0.04
J1901+0413	SPL	1459	0.09 ± 0.07	0.03± 0.03
J1901+0716	SPL	1606	0.09 ± 0.03	0.02± 0.02
J1902+0556	SPL	3100	0.22 ± 0.06	0.07± 0.07
J1903+0135	LFTO	3100	0.31 ± 0.10	0.06± 0.06
J1904+0004	SPL	3100	0.45 ± 0.13	0.21± 0.21
J1904+0800	SPL	1460	0.21 ± 0.35	0.14± 0.14
J1904+1011	SPL	1459	0.05 ± 0.01	0.02± 0.02
J1905+0616	SPL	4850	0.18 ± 0.02	0.12± 0.12
J1905+0709	SPL	2600	0.31 ± 0.07	0.12± 0.12
J1906+0641	SPL	2600	0.81 ± 0.07	0.51± 0.51
J1907+0918	SPL	2640	0.04 ± 0.03	0.02± 0.02
J1908+0500	SPL	3100	0.09 ± 0.07	0.03± 0.03
J1909+1102	LFTO	4920	0.08 ± 0.02	0.01± 0.01
J1909−3744	SPL	3100	0.45 ± 0.05	0.22± 0.22
J1910+1256	SPL	2100	0.09 ± 0.13	0.03± 0.03
J1912+2104	SPL	1408	0.22 ± 0.07	0.10± 0.10
J1913+1400	SPL	1408	0.21 ± 0.05	0.08± 0.08
J1913−0440	LFTO	3100	0.31 ± nan	0.04± 0.04
J1915+1009	SPL	3100	0.12 ± 0.03	0.03± 0.03
J1915+1606	SPL	1408	0.05 ± 0.02	0.01± 0.01
J1916+1312	SPL	3100	0.20 ± 0.06	0.06± 0.06
J1917+2224	SPL	400	0.14 ± 0.23	0.06± 0.06
J1918+1444	SPL	2600	4.23 ± 0.65	8.73± 8.73
J1918−0642	SPL	1400	0.06 ± 0.01	0.02± 0.02
J1920+2650	SPL	408	0.54 ± 0.48	0.26± 0.26
J1921+1419	SPL	1408	0.10 ± 0.04	0.03± 0.03
J1926+0431	SPL	843	0.39 ± 0.16	0.16± 0.16
J1926+1648	SPL	1408	0.18 ± 0.10	0.06± 0.06
J1932+2020	SPL	1408	0.14 ± 0.08	0.04± 0.04
J1932+2220	SPL	1606	0.22 ± 0.06	0.08± 0.08
J1932−3655	SPL	3100	0.07 ± 0.04	0.03± 0.03
J1937+2544	SPL	4920	0.41 ± 0.17	0.19± 0.19

Continued on next page

Pulsar	Model	Max freq	S5000	S10000
J1943−1237	LFTO	1408	0.06 ± 0.02	0.01± 0.01
J1944+0907	SPL	1400	0.20 ± 0.04	0.06± 0.06
J1945−0040	SPL	1408	0.09 ± 0.03	0.03± 0.03
J1946+1805	LFTO	4920	2.58 ± nan	0.75± 0.75
J1949−2524	SPL	1408	0.05 ± 0.02	0.01± 0.01
J1952+3252	SPL	1606	0.13 ± 0.04	0.04± 0.04
J1955+2908	SPL	1400	0.09 ± 0.01	0.03± 0.03
J1955+5059	LFTO	4920	0.72 ± 0.17	0.26± 0.26
J2002+3217	SPL	1606	0.30 ± 0.07	0.13± 0.13
J2002+4050	BPL	1606	0.48 ± 0.06	0.13± 0.13
J2005−0020	SPL	1360	0.11 ± 0.05	0.04± 0.04
J2006−0807	SPL	1408	0.48 ± 0.17	0.17± 0.17
J2008+2513	SPL	430	0.15 ± 0.31	0.07± 0.07
J2010−1323	SPL	1400	0.14 ± 0.04	0.06± 0.06
J2013+3845	SPL	1606	1.97 ± 0.26	0.98± 0.98
J2017+2043	SPL	400	0.05 ± 0.07	0.02± 0.02
J2019+2425	SPL	1284	0.03 ± 0.01	0.01± 0.01
J2023+5037	SPL	1606	0.63 ± 0.30	0.34± 0.34
J2027+4557	SPL	1400	0.27 ± 0.07	0.11± 0.11
J2030+2228	SPL	400	0.39 ± 0.56	0.21± 0.21
J2037+1942	SPL	400	0.42 ± 0.75	0.24± 0.24
J2037+3621	SPL	1408	0.18 ± 0.09	0.07± 0.07
J2038+5319	SPL	1408	0.06 ± 0.04	0.02± 0.02
J2038−3816	SPL	1360	0.04 ± 0.02	0.01± 0.01
J2046+1540	SPL	1408	0.31 ± 0.12	0.12± 0.12
J2051−0827	HFCO	2695	0.22 ± 0.03	0.06± 0.06
J2055+2209	SPL	606	0.93 ± 0.67	0.50± 0.50
J2108−3429	SPL	1360	0.09 ± 0.05	0.04± 0.04
J2113+2754	LFTO	1408	0.11 ± 0.05	0.03± 0.03
J2113+4644	BPL	1606	1.37 ± 0.38	0.33± 0.33
J2124+1407	SPL	390	1.61 ± 5.01	1.27± 1.27
J2124−3358	LFTO	3100	0.34 ± 0.02	0.10± 0.10
J2129−5721	SPL	3100	0.08 ± 0.02	0.02± 0.02
J2139+2242	SPL	900	8.34 ± 6.82	6.70± 6.70
J2144−3933	SPL	1400	0.52 ± 0.38	0.32± 0.32
J2150+5247	SPL	1606	0.89 ± 0.12	0.48± 0.48
J2155+2813	SPL	400	4014.26 ± 276.22	32114.11± 32114.11
J2156+2618	SPL	430	0.28 ± 0.60	0.17± 0.17
J2205+1444	SPL	430	0.08 ± 0.13	0.04± 0.04
J2208+5500	SPL	1400	0.06 ± 0.03	0.02± 0.02
J2212+2933	SPL	1408	0.23 ± 0.10	0.10± 0.10
J2214+3000	SPL	2100	0.12 ± 0.06	0.06± 0.06
J2215+1538	SPL	430	0.32 ± 0.90	0.16± 0.16
J2217+5733	SPL	1400	0.06 ± 0.03	0.02± 0.02
J2222−0137	SPL	3100	0.17 ± 0.05	0.07± 0.07
J2227+3038	SPL	400	0.83 ± 0.62	0.55± 0.55
J2229+2643	SPL	1400	0.07 ± 0.02	0.02± 0.02
J2234+0611	SPL	1400	0.15 ± 0.13	0.09± 0.09
J2234+2114	SPL	430	0.11 ± 0.14	0.04± 0.04
J2235+1506	SPL	400	0.39 ± 1.10	0.23± 0.23
J2241−5236	BPL	3100	0.13 ± nan	0.04± 0.04

Continued on next page

Pulsar	Model	Max freq	S5000	S10000
J2242+6950	SPL	1408	0.12 ± 0.12	0.06± 0.06
J2248−0101	SPL	1360	0.07 ± 0.03	0.02± 0.02
J2253+1516	SPL	430	0.44 ± 0.70	0.25± 0.25
J2257+5909	LFTO	4820	0.39 ± 0.04	0.06± 0.06
J2302+4442	SPL	1400	0.64 ± 0.29	0.38± 0.38
J2302+6028	SPL	900	0.16 ± 0.15	0.05± 0.05
J2305+3100	LFTO	1408	0.21 ± 0.07	0.07± 0.07
J2305+4707	SPL	1060	0.18 ± 0.19	0.08± 0.08
J2307+2225	SPL	430	1.45 ± 3.47	1.46± 1.46
J2317+1439	SPL	1400	0.04 ± 0.01	0.01± 0.01
J2322+2057	SPL	2100	0.10 ± 0.04	0.06± 0.06
J2324−6054	SPL	1360	0.30 ± 0.12	0.14± 0.14
J2326+6113	SPL	1408	1.51 ± 0.49	0.83± 0.83
J2330−2005	LFTO	4920	0.15 ± 0.04	0.04± 0.04
J2337+6151	SPL	1408	0.24 ± 0.12	0.09± 0.09
J2346−0609	SPL	1360	0.61 ± 0.32	0.31± 0.31
J2354+6155	SPL	4920	1.26 ± 0.31	0.81± 0.81

Table C.2: The 524 pulsars that had no flux density measurements below 5000 MHz and an estimated flux density of greater than 0.01 mJy at both 5 or 10 GHz. CSV of this data can be found here :https://github.com/NickSwainston/all_pulsar_spectra/blob/2.0.2/high_freq_camp.csv.

Appendix D

Copyright Information

D.1 MWA Tied-Array Processing IV: A Multi-Pixel Beamformer for Pulsar Surveys and Ionospheric Corrected Localisation

I, Nicholas Swainston, have outlined in the table below the contribution of the co-authors to Chapter 3 of this thesis, "MWA Tied-Array Processing IV: A Multi-Pixel Beamformer for Pulsar Surveys and Ionospheric Corrected Localisation", which is a reproduction of an already published work by Swainston et al. (2020) (accepted in Publications of the Astronomical Society of Australia, DOI: 10.1017/pasa.2022.14).

	Conception and Design	Acquisition of Data and Method	Data Conditioning and Manipulation	Analysis and Statistical Method	Interpretation and Discussion
N.A. Swainston	✔	✔	✔	✔	✔
N.A. Swainston Acknowledgment: I acknowledge that these represent my contribution to the above research output and I have approved the final version. Signed:					
N.D.R.Bhat	✔			✔	✔
N.D.R.Bhat Acknowledgment: I acknowledge that these represent my contribution to the above research output and I have approved the final version. Signed:					
I. S. Morrison	✔			✔	✔
I. S. Morrison Acknowledgment: I acknowledge that these represent my contribution to the above research output and I have approved the final version. Signed:					
S. J. McSweeney	✔	✔		✔	✔
S. J. McSweeney Acknowledgment: I acknowledge that these represent my contribution to the above research output and I have approved the final version. Signed:					
S.M.Ord	✔				
S.M.Ord Acknowledgment: I acknowledge that these represent my contribution to the above research output and I have approved the final version. Signed:					
S.E.Tremblay	✔				
S.E.Tremblay Acknowledgment: I acknowledge that these represent my contribution to the above research output and I have approved the final version.					

Signed:					
M. Sokolowski		✔			
M. Sokolowski Acknowledgment: I acknowledge that these represent my contribution to the above research output and I have approved the final version. Signed:					

D.2 Discovery of a steep-spectrum low-luminosity pulsar with the Murchison Widefield Array

I, Nicholas Swainston, have outlined in the table below the contribution of the co-author to Chapter 4 of this thesis, "Discovery of a Steep-spectrum Low-luminosity Pulsar with the Murchison Widefield Array", which is a reproduction of an already published work by Swainston et al. (2021) (accepted in The Astrophysical Journal Letters, DOI: 10.3847/2041-8213/abec7b).

	Conception and Design	Acquisition of Data and Method	Data Conditioning and Manipulation	Analysis and Statistical Method	Interpretation and Discussion
N.A. Swainston	✔	✔	✔	✔	✔
N.A. Swainston Acknowledgment: I acknowledge that these represent my contribution to the above research output and I have approved the final version. Signed:					
N.D.R.Bhat	✔	✔	✔	✔	✔
N.D.R.Bhat Acknowledgment: I acknowledge that these represent my contribution to the above research output and I have approved the final version. Signed:					
M. Sokolowski		✔	✔	✔	✔
M. Sokolowski Acknowledgment: I acknowledge that these represent my contribution to the above research output and I have approved the final version. Signed:					
S. J. McSweeney	✔	✔		✔	✔
S. J. McSweeney Acknowledgment: I acknowledge that these represent my contribution to the above research output and I have approved the final version. Signed:					
S. Kudale		✔	✔	✔	
S. Kudale Acknowledgment: I acknowledge that these represent my contribution to the above research output and I have approved the final version. Signed:					
S. Dai		✔	✔	✔	
S. Dai Acknowledgment: I acknowledge that these represent my contribution to the above research output and I have approved the final version. Signed:					

K. R. Smith	✔	✔			
K. R. Smith Acknowledgment: I acknowledge that these represent my contribution to the above research output and I have approved the final version. Signed:					
I. S. Morrison		✔			✔
I. S. Morrison Acknowledgment: I acknowledge that these represent my contribution to the above research output and I have approved the final version. Signed:					
R. M. Shannon			✔	✔	
R. M. Shannon Acknowledgment: I acknowledge that these represent my contribution to the above research output and I have approved the final version. Signed:					
W. van Straten			✔	✔	
W. van Straten Acknowledgment: I acknowledge that these represent my contribution to the above research output and I have approved the final version. Signed:					
M. Xue		✔		✔	
M. Xue Acknowledgment: I acknowledge that these represent my contribution to the above research output and I have approved the final version. Signed:					
S. M. Ord		✔			
S. M. Ord Acknowledgment: I acknowledge that these represent my contribution to the above research output and I have approved the final version. Signed:					
S. E. Tremblay	✔	✔			
S. E. Tremblay Acknowledgment:					

I acknowledge that these represent my contribution to the above research output and I have approved the final version. Signed:					
B. W. Meyers	✔				
B. W. Meyers Acknowledgment: I acknowledge that these represent my contribution to the above research output and I have approved the final version. Signed:					
A. Williams		✔			
A. Williams Acknowledgment: I acknowledge that these represent my contribution to the above research output and I have approved the final version. Signed:					
G. Sleap		✔			
G. Sleap Acknowledgment: I acknowledge that these represent my contribution to the above research output and I have approved the final version. Signed:					
M. Johnston-Hollitt		✔			
M. Johnston-Hollitt Acknowledgment: I acknowledge that these represent my contribution to the above research output and I have approved the final version. Signed:					
D. L. Kaplan		✔			
D. L. Kaplan Acknowledgment: I acknowledge that these represent my contribution to the above research output and I have approved the final version. Signed:					
S. J. Tingay		✔			
S. J. Tingay Acknowledgment: I acknowledge that these represent my contribution to the above research output and I have approved the final version.					

Signed:					
R. B. Wayth		✔			
R. B. Wayth Acknowledgment: I acknowledge that these represent my contribution to the above research output and I have approved the final version. Signed:					

D.3 pulsar_spectra: A pulsar flux density catalogue and spectrum fitting repository

I, Nicholas Swainston, have outlined in the table below the contribution of the co-author to Chapter 5 of this thesis, "pulsar_spectra: A pulsar flux density catalogue and spectrum fitting repository", which is a reproduction of an already published work by Swainston et al. (2022b) (accepted in Publications of the Astronomical Society of Australia, DOI: 10.1017/pasa.2022.52).

	Conception and Design	Acquisition of Data and Method	Data Conditioning and Manipulation	Analysis and Statistical Method	Interpretation and Discussion
N.A. Swainston	✔	✔	✔	✔	✔
N.A. Swainston Acknowledgment: I acknowledge that these represent my contribution to the above research output and I have approved the final version. Signed:					
C.P.Lee	✔	✔	✔	✔	
C.P.Lee Acknowledgment: I acknowledge that these represent my contribution to the above research output and I have approved the final version. Signed:					
S. J. McSweeney	✔			✔	✔
S. J. McSweeney Acknowledgment: I acknowledge that these represent my contribution to the above research output and I have approved the final version. Signed:					
N. D. R. Bhat	✔			✔	✔
N. D. R. Bhat Acknowledgment: I acknowledge that these represent my contribution to the above research output and I have approved the final version. Signed:					

Bibliography

B. P. Abbott, et al. (2016). 'Observation of gravitational waves from a binary black hole merger'. *Physical Review Letters* **116**(6):1–16.

E. Aliu, et al. (2008). 'Observation of Pulsed γ-Rays Above 25 GeV from the Crab Pulsar with MAGIC'. *Science* **322**(5905):1221–1224.

M. A. Alpar, et al. (1982). 'A new class of radio pulsars'. *Nature* **300**(5894):728–730.

A. M. Archibald, et al. (2009). 'A Radio Pulsar/X-ray Binary Link'. *Science* **324**(5933):1411–1414.

B. S. Arora, et al. (2015). 'Ionospheric Modelling using GPS to Calibrate the MWA. I: Comparison of First Order Ionospheric Effects between GPS Models and MWA Observations'. *Publications of the Astronomical Society of Australia* **32**:e029.

J. W. M. Baars, et al. (1977). 'The absolute spectrum of Cas A; an accurate flux density scale and a set of secondary calibrators.'. *Astronomy and Astrophysics* **500**:135–142.

D. C. Backer (1973). 'Pulsar Fluctuation Spectra and the Generalized Drifting-Subpulse Phenomenon'. *The Astrophysical Journal* **182**:245.

D. C. Backer, et al. (1982). 'A millisecond pulsar'. *Nature* **300**:615–618.

K. W. Bannister, et al. (2017). 'The Detection of an Extremely Bright Fast Radio Burst in a Phased Array Feed Survey'. *The Astrophysical Journal* **841**(1):L12.

M. G. Baring (2004). 'High-energy emission from pulsars: the polar cap scenario'. *Advances in Space Research* **33**(4):552–560.

N. Bartel, et al. (1978). 'Observations of pulsars at 14.8 and 22.7 GHz.'. *aap* **68**:361–365.

C. Bassa, et al. (2017a). 'Enabling pulsar and fast transient searches using coherent dedispersion'. *Astronomy and Computing* **18**:40–46.

C. G. Bassa, et al. (2014). 'A state change in the low-mass X-ray binary XSS J12270-4859'. *Monthly Notices of the Royal Astronomical Society* **441**(2):1825–1830.

C. G. Bassa, et al. (2017b). 'LOFAR Discovery of the Fastest-spinning Millisecond Pulsar in the Galactic Field'. *The Astrophysical Journal* **846**(2):L20.

R. Basu, et al. (2016). 'Time variation in the low-frequency spectrum of Vela-like pulsar B180021'. *Monthly Notices of the Royal Astronomical Society* **458**(3):2509–2515.

S. D. Bates, et al. (2011). 'A 6.5-GHz multibeam pulsar survey'. *Monthly Notices of the Royal Astronomical Society* **411**(3):1575–1584.

S. D. Bates, et al. (2014a). 'PSRPOPPY: An open-source package for pulsar population simulations'. *Monthly Notices of the Royal Astronomical Society* **439**(3):2893–2902.

S. D. Bates, et al. (2013). 'The pulsar spectral index distribution'. *Monthly Notices of the Royal Astronomical Society* **431**(2):1352–1358.

S. D. Bates, et al. (2014b). 'The High Time Resolution Universe survey - XI. Discovery of five recycled pulsars and the optical detectability of survey

white dwarf companions'. *Monthly Notices of the Royal Astronomical Society* **446**(4):4019–4028.

M. E. Bell, et al. (2016). 'Time-domain and spectral properties of pulsars at 154MHz'. *Monthly Notices of the Royal Astronomical Society* **461**(1):908–921.

N. D. R. Bhat, et al. (2004). 'Multifrequency Observations of Radio Pulse Broadening and Constraints on Interstellar Electron Density Microstructure'. *The Astrophysical Journal* **605**(2):759–783.

N. D. R. Bhat, et al. (2016). 'SCINTILLATION ARCS IN LOW-FREQUENCY OBSERVATIONS OF THE TIMING-ARRAY MILLISECOND PULSAR PSR J04374715'. *The Astrophysical Journal* **818**(1):86.

N. D. R. Bhat, et al. (2023a). 'The Southern-sky MWA Rapid Two-metre (SMART) pulsar surveyI. Survey design and processing pipeline'. *Publications of the Astronomical Society of Australia* **40**:e021.

N. D. R. Bhat, et al. (2023b). 'The Southern-sky MWA Rapid Two-metre (SMART) pulsar surveyII. Survey status, pulsar census, and first pulsar discoveries'. *Publications of the Astronomical Society of Australia* **40**:e020.

N. D. R. Bhat, et al. (2018). 'Observations of Low-frequency Radio Emission from Millisecond Pulsars and Multipath Propagation in the Interstellar Medium'. *The Astrophysical Journal Supplement Series* **238**(1):1.

B. Bhattacharyya, et al. (2016). 'THE GMRT HIGH RESOLUTION SOUTHERN SKY SURVEY FOR PULSARS AND TRANSIENTS. I. SURVEY DESCRIPTION AND INITIAL DISCOVERIES'. *The Astrophysical Journal* **817**(2):130.

A. V. Bilous, et al. (2020). 'A LOFAR census of non-recycled pulsars: extending to frequencies below 80 MHz'. *Astronomy & Astrophysics* **635**:A75.

A. V. Bilous, et al. (2016). 'A LOFAR census of non-recycled pulsars: Average profiles, dispersion measures, flux densities, and spectra'. *Astronomy and Astrophysics* **591**:1–34.

L. Bondonneau, et al. (2020). 'A census of the pulsar population observed with the international LOFAR station FR606 at low frequencies (25-80 MHz)'. *Astronomy and Astrophysics* **635**:1–17.

J. D. Bowman, et al. (2007). 'Field Deployment of Prototype Antenna Tiles for the Mileura Widefield Array Low Frequency Demonstrator'. *The Astronomical Journal* **133**(4):1505–1518.

J. D. Bowman & M. W. A. M. Collaboration (2015). 'Murchison Widefield Array (MWA) - 1st Year Science Results'. *American Astronomical Society* **225**.

R. Bracewell (1999). *The Fourier Transform and its Applications*. New York: McGrawHill, 3rd edn.

M. A. Brentjens & A. G. de Bruyn (2005). 'Faraday rotation measure synthesis'. *Astronomy & Astrophysics* **441**(3):1217–1228.

P. C. Broekema, et al. (2018). 'Cobalt: A GPU-based correlator and beamformer for LOFAR'. *Astronomy and Computing* **23**:180–192.

A. D. Cameron, et al. (2017). 'An investigation of pulsar searching techniques with the fast folding algorithm'. *Monthly Notices of the Royal Astronomical Society* **468**(2):1994–2010.

F. Camilo & D. J. Nice (1995). 'Timing parameters of 29 pulsars'. *The Astrophysical Journal* **445**:756.

K. Chen & M. Ruderman (1993). 'Pulsar death lines and death valley'. *The Astrophysical Journal* **402**:264.

A. Chokshi, et al. (2021). 'Dual polarization measurements of MWA beam-patterns at 137 MHz'. *Monthly Notices of the Royal Astronomical Society* **502**(2):1990–2004.

J. M. Cordes (1978). 'Observational limits on the location of pulsar emission regions'. *The Astrophysical Journal* **222**:1006–1011.

J. M. Cordes, et al. (2006). 'Arecibo Pulsar Survey Using ALFA. I. Survey Strategy and First Discoveries'. *The Astrophysical Journal* **637**(1):446–455.

J. M. Cordes & T. J. W. Lazio (2002). 'NE2001.I. A New Model for the Galactic Distribution of Free Electrons and its Fluctuations'. *Spectrum* p. 21.

J. M. Cordes, et al. (1985). 'Small-scale electron density turbulence in the interstellar medium'. *The Astrophysical Journal* **288**:221.

S. Dai, et al. (2015). 'A study of multifrequency polarization pulse profiles of millisecond pulsars'. *Monthly Notices of the Royal Astronomical Society* **449**(3):3223–3262.

S. Dai, et al. (2020). 'Discovery of Millisecond Pulsars in the Globular Cluster Omega Centauri'. *The Astrophysical Journal* **888**(2):L18.

J. K. Daugherty & A. K. Harding (1982). 'Electromagnetic cascades in pulsars'. *The Astrophysical Journal* **252**:337.

A. de Oliveira-Costa, et al. (2008). 'A model of diffuse Galactic radio emission from 10 MHz to 100 GHz'. *Monthly Notices of the Royal Astronomical Society* **388**(1):247–260.

A. T. Deller, et al. (2009). 'Implications of a VLBI Distance to the Double Pulsar J0737-3039A/B'. *Science* **323**(5919):1327–1329.

A. T. Deller, et al. (2019). 'Microarcsecond VLBI Pulsar Astrometry with PSR π II. Parallax Distances for 57 Pulsars'. *The Astrophysical Journal* **875**(2):100.

M. Dembska, et al. (2015). 'Flux density measurements of gigahertz-peaked spectra candidate pulsars at 610MHz using an interferometric imaging technique'. *Monthly Notices of the Royal Astronomical Society* **449**(2):1869–1875.

M. Dembska, et al. (2014). 'Flux-density spectral analysis for several pulsars and two newly identified gigahertz-peaked spectra pulsars'. *Monthly Notices of the Royal Astronomical Society* **445**(3):3105–3114.

J. S. Deneva, et al. (2009). 'Arecibo pulsar survey using ALPHA: Probing radio pulsar intermittency and transients'. *Astrophysical Journal* **703**(2):2259–2274.

R. J. Dewey, et al. (1985). 'A search for low-luminosity pulsars'. *The Astrophysical Journal* **294**:L25.

P. Di Tommaso, et al. (2017). 'Nextflow enables reproducible computational workflows'. *Nature Biotechnology* **35**(4):316–319.

M. H. Erkut (2022). 'Radio luminosity of GLEAM-X J162759.5523504.3: does it really exceed the spin-down power of the pulsar?'. *Monthly Notices of the Royal Astronomical Society: Letters* **514**(1):L41–L45.

D. A. Frail, et al. (2016). 'KNOWN PULSARS IDENTIFIED IN THE GMRT 150 MHz ALL-SKY SURVEY'. *The Astrophysical Journal* **829**(2):119.

P. Goldreich & W. H. Julian (1969). 'Pulsar Electrodynamics'. *The Astrophysical Journal* **157**(August):869.

D. C. Good, et al. (2021). 'First Discovery of New Pulsars and RRATs with CHIME/FRB'. *The Astrophysical Journal* **922**(1):43.

D. M. Gould & A. G. Lyne (1998). 'Multifrequency polarimetry of 300 radio pulsars'. *Monthly Notices of the Royal Astronomical Society* **301**:235–260.

Q. Guojun, et al. (1995). 'Polarization and Faraday rotation measurements of southern pulsars'. *Monthly Notices of the Royal Astronomical Society* **274**(2):572–588.

Y. Gupta, et al. (2017). 'The Upgraded GMRT:Opening New Windows on the Radio Universe'. *Current Science* **113**(04):707.

Y. Gupta, et al. (2005). 'The discovery of PSR J1833 1034 : the pulsar associated with the supernova remnant'. *Current science* **89**:853.

J. D. Hamaker, J. P.; Bregman (1996). 'Understanding radio polarimetry. III. Interpreting the IAU/IEEE definitions of the Stokes parameters.'. *Astronomy and Astrophysics Supplement* **117**:161–165.

J. P. Hamaker (2000). 'Understanding radio polarimetry. IV. The full-coherency analogue of scalar self-calibration: Self-alignment, dynamic range and polarimetric fidelity'. *Astronomy and Astrophysics Supplement Series* **143**(3):515–534.

J. P. Hamaker, et al. (1996). 'Understanding radio polarimetry. I. Mathematical foundations'. *Astronomy and Astrophysics Supplement Series* **117**(1):137–147.

J. Han, et al. (2016a). 'Spectral indices for radio emission of 228 pulsars'. *Research in Astronomy and Astrophysics* **16**(10):159.

J. Han, et al. (2016b). 'Spectral indices for radio emission of 228 pulsars'. *Research in Astronomy and Astrophysics* **16**(10):159.

J. L. Han, et al. (2021). 'The FAST Galactic Plane Pulsar Snapshot survey: I. Project design and pulsar discoveries'. *Research in Astronomy and Astrophysics* **21**(5):107.

P. J. Hancock, et al. (2019). 'Refractive Interstellar Scintillation of Extra-galactic Radio Sources I: Expectations' .

T. H. Hankins, et al. (2003). 'Nanosecond radio bursts from strong plasma turbulence in the Crab pulsar'. *Nature* **422**(6928):141–143.

A. Hewish, et al. (1968). 'Observation of a Rapidly Pulsating Radio Source'. *Nature* **217**:709–713.

G. Hobbs, et al. (2004a). 'The Parkes multibeam pulsar survey - IV. Discovery of 180 pulsars and parameters for 281 previously known pulsars'. *Monthly Notices of the Royal Astronomical Society* **352**(4):1439–1472.

G. Hobbs, et al. (2004b). 'The ATNF Pulsar Catalog'. In F. Camilo & B. M. Gaensler (eds.), *Young Neutron Stars and Their Environments*, vol. 218, p. 139.

G. Hobbs, et al. (2020). 'An ultra-wide bandwidth (704 to 4032MHz) receiver for the Parkes radio telescope'. *Publications of the Astronomical Society of Australia* **37**:e012.

A. W. Hotan, et al. (2004). '¡scp¿psrchive¡/scp¿ and ¡scp¿psrfits¡/scp¿ : An Open Approach to Radio Pulsar Data Storage and Analysis'. *Publications of the Astronomical Society of Australia* **21**(3):302–309.

P. J. Huber (1964). 'Robust Estimation of a Location Parameter'. *The Annals of Mathematical Statistics* **35**(1):73–101.

R. a. Hulse & J. H. Taylor (1974). 'A High-Sensitivity Pulsar Survey'. *The Astrophysical Journal* **191**:L59.

N. Hurley-Walker, et al. (2017). 'GaLactic and Extragalactic All-sky Murchison Widefield Array (GLEAM) survey I. A low-frequency extragalactic catalogue'. *Monthly Notices of the Royal Astronomical Society* **464**(1):1146–1167.

H. T. Intema, et al. (2017). 'The GMRT 150 MHz all-sky radio survey'. *Astronomy & Astrophysics* **598**:A78.

V. A. Izvekova, et al. (1981). 'Radio spectra of pulsars'. *Astrophysics and Space Science* **78**(1):45–72.

F. James & M. Roos (1975). 'Minuit - a system for function minimization and analysis of the parameter errors and correlations'. *Computer Physics Communications* **10**(6):343–367.

P. Janagal, et al. (2021). 'Revisiting the subpulse drifting phenomenon in PSR J18222256: drift modes, sparks, and emission heights'. *Monthly Notices of the Royal Astronomical Society* **509**(3):4573–4584.

P. Janagal, et al. (2023). 'PSR J00261955: A curious case of evolutionary subpulse drifting and nulling'. *Monthly Notices of the Royal Astronomical Society* **524**(2):2684–2697.

F. Jankowski, et al. (2019). 'The UTMOST pulsar timing programme I: Overview and first results'. *Monthly Notices of the Royal Astronomical Society* **484**(3):3691–3712.

F. Jankowski, et al. (2018). 'Spectral properties of 441 radio pulsars'. *Monthly Notices of the Royal Astronomical Society* **473**(4):4436–4458.

G. Janssen, et al. (2015). 'Gravitational Wave Astronomy with the SKA'. In *Proceedings of Advancing Astrophysics with the Square Kilometre Array PoS(AASKA14)*, p. 037, Trieste, Italy. Sissa Medialab.

A. Jessner, et al. (2005). 'Giant radio pulses from the Crab pulsar'. *Advances in Space Research* **35**(6):1166–1171.

S. Johnston & A. Karastergiou (2017). 'Pulsar braking and the P- P diagram'. *Monthly Notices of the Royal Astronomical Society* **467**(3):3493–3499.

S. Johnston, et al. (2008). 'Multifrequency integrated profiles of pulsars'. *Monthly Notices of the Royal Astronomical Society* **388**(1):261–274.

S. Johnston, et al. (2006). 'High-frequency observations of southern pulsars'. *Monthly Notices of the Royal Astronomical Society* **369**(4):1916–1928.

S. Johnston & M. Kerr (2018). 'Polarimetry of 600 pulsars from observations at 1.4GHz with the Parkes radio telescope'. *Monthly Notices of the Royal Astronomical Society* **474**(4):4629–4636.

S. Johnston, et al. (1993). 'Discovery of a very bright, nearby binary millisecond pulsar'. *nat* **361**(6413):613–615.

S. Johnston, et al. (1992). 'A high-frequency survey ofthe southern Galactic plane for pulsars'. *Monthly Notices of the Royal Astronomical Society* **255**:401–411.

S. Johnston, et al. (2021). 'Two years of pulsar observations with the ultra-wide-band receiver on the Parkes radio telescope'. *Monthly Notices of the Royal Astronomical Society* **502**(1):1253–1262.

C. H. Jordan, et al. (2017). 'Characterization of the ionosphere above the Murchison Radio Observatory using the Murchison Widefield Array'. *Monthly Notices of the Royal Astronomical Society* **471**(4):3974–3987.

A. Karastergiou, et al. (2005). 'Polarization profiles of southern pulsars at 3.1 GHz'. *Monthly Notices of the Royal Astronomical Society* **359**(2):481–492.

N. E. Kassim, et al. (2007). 'The 74 MHz System on the Very Large Array'. *The Astrophysical Journal Supplement Series* **172**(2):686–719.

D. Kaur, et al. (2019). 'A High Time-resolution Study of the Millisecond Pulsar J22415236 at Frequencies Below 300 MHz'. *The Astrophysical Journal* **882**(2):133.

E. Keane, et al. (2015a). 'A Cosmic Census of Radio Pulsars with the SKA'. In *Proceedings of Advancing Astrophysics with the Square Kilometre Array PoS(AASKA14)*, p. 040, Trieste, Italy. Sissa Medialab.

E. Keane, et al. (2015b). 'A Cosmic Census of Radio Pulsars with the SKA'. In *Proceedings of Advancing Astrophysics with the Square Kilometre Array PoS(AASKA14)*, p. 040, Trieste, Italy. Sissa Medialab.

E. F. Keane & M. Kramer (2008). 'On the birthrates of Galactic neutron stars'. *Monthly Notices of the Royal Astronomical Society* **391**(4):2009–2016.

M. J. Keith, et al. (2010). 'The High Time Resolution Universe Pulsar Survey - I. System configuration and initial discoveries'. *Monthly Notices of the Royal Astronomical Society* **409**(2):619–627.

M. J. Keith, et al. (2008). 'A high-frequency search for radio pulsars in three EGRET error boxes'. *Monthly Notices of the Royal Astronomical Society* **389**(4):1881–1884.

M. J. Keith, et al. (2011). '17- and 24-GHz observations of southern pulsars'. *Monthly Notices of the Royal Astronomical Society* **416**(1):no–no.

J. Kijak, et al. (2017). 'Gigahertz-peaked Spectra Pulsars and Thermal Absorption Model'. *The Astrophysical Journal* **840**(2):108.

J. Kijak, et al. (2007). 'Turn-over in pulsar spectra around 1 GHz'. *Astronomy & Astrophysics* **462**(2):699–702.

J. Kijak, et al. (2011). 'Pulsars with gigahertz-peaked spectra'. *Astronomy & Astrophysics* **531**:A16.

F. Kirsten, et al. (2019). 'Probing Pulsar Scattering between 120 and 280 MHz with the MWA'. *The Astrophysical Journal* **874**(2):179.

I. M. Kloumann & J. M. Rankin (2010). 'On the long and short nulls, modes and interpulse emission of radio pulsar B1944+17'. *Monthly Notices of the Royal Astronomical Society* **408**(1):40–52.

V. I. Kondratiev, et al. (2016). 'A LOFAR census of millisecond pulsars'. *Astronomy and Astrophysics* **585**(128):1–27.

V. M. Kontorovich & A. B. Flanchik (2013). 'High-frequency cutoff and change of radio emission mechanism in pulsars'. *Astrophysics and Space Science* **345**(1):169–175.

M. Kramer, et al. (2003a). 'The Parkes Multibeam Pulsar Survey - III. Young pulsars and the discovery and timing of 200 pulsars'. *Monthly Notices of the Royal Astronomical Society* **342**(4):1299–1324.

M. Kramer, et al. (1999). 'The Characteristics of Millisecond Pulsar Emission. III. From Low to High Frequencies'. *The Astrophysical Journal* **526**(2):957–975.

M. Kramer, et al. (2003b). 'The Proper Motion, Age, and Initial Spin Period of PSR J0538+2817 in S147'. *The Astrophysical Journal* **593**(1):L31–L34.

M. Kramer, et al. (2021a). 'Strong-Field Gravity Tests with the Double Pulsar'. *Physical Review X* **11**(4):041050.

M. Kramer, et al. (2021b). 'Strong-Field Gravity Tests with the Double Pulsar'. *Physical Review X* **11**(4):041050.

M. Kramer, et al. (2006). 'Tests of General Relativity from Timing the Double Pulsar'. *Science* **314**(5796):97–102.

M. Kuniyoshi, et al. (2015). 'Low-frequency spectral turn-overs in millisecond pulsars studied from imaging observations'. *Monthly Notices of the Royal Astronomical Society* **453**(1):828–836.

A. D. Kuzmin & B. Y. Losovsky (2001). 'No low-frequency turn-over in the spectra of millisecond pulsars'. *Astronomy and Astrophysics* **368**(1):230–238.

C. P. Lee, et al. (2022). 'Spectral analysis of 22 radio pulsars using SKA-Low precursor stations'. *Publications of the Astronomical Society of Australia* **39**:e042.

L. C. Lee & J. R. Jokipii (1975). 'Strong Scintillations in Astrophysics. II - A Theory of Temporal Broadening of Pulses'. *The Astrophysical Journal* **201**:532–543.

L. Levin, et al. (2013). 'The high time resolution universe pulsar survey -VIII. The galactic millisecond pulsar population'. *Monthly Notices of the Royal Astronomical Society* **434**(2):1387–1397.

W. Lewandowski, et al. (2015). 'The study of multi-frequency scattering of 10 radio pulsars'. *Monthly Notices of the Royal Astronomical Society* **454**(3):2517–2528.

W. Li, et al. (2018). 'Comparing Redundant and Sky-model-based Interferometric Calibration: A First Look with Phase II of the MWA'. *The Astrophysical Journal* **863**(2):170.

J. L. B. Line, et al. (2018). 'In situ measurement of MWA primary beam variation using ORBCOMM'. *Publications of the Astronomical Society of Australia* **35**:e045.

O. Löhmer, et al. (2008). 'Observations of pulsars at 9 millimetres'. *Astronomy and Astrophysics* **480**(3):623–628.

C. Lonsdale, et al. (2009). 'The Murchison Widefield Array: Design Overview'. *Proceedings of the IEEE* **97**(8):1497–1506.

D. Lorimer & M. Kramer (2005). 'Handbook of Pulsar Astronomy'. Cambridge University Press.

D. R. Lorimer, et al. (1993). 'Pulsar statistics: the birthrate and initial spin periods of radio pulsars'. *Royal Astronomical Society* **415**:403–415.

D. R. Lorimer, et al. (2006). 'The Parkes Multibeam Pulsar Survey VI. Discovery and timing of 142 pulsars and a Galactic population analysis'. *Monthly Notices of the Royal Astronomical Society* **372**(2):777–800.

D. R. Lorimer, et al. (1995). 'Multifrequency flux density measurements of 280 pulsars'. *Monthly Notices of the Royal Astronomical Society* **273**(2):411–421.

S. C. Lundgren, et al. (1995). 'A Millisecond Pulsar in a 6 Hour Orbit: PSR J0751+1807'. *The Astrophysical Journal* **453**:419.

A. G. Lyne (2009). 'Intermittent Pulsars'. In *Neutron Stars and Pulsars*, pp. 67–72. Springer Berlin Heidelberg, Berlin, Heidelberg.

A. G. Lyne & B. J. Rickett (1968). 'Radio Observations of Five Pulsars'. *Nature* **219**(5161):1339–1342.

R. J. Lyon, et al. (2016). 'Fifty years of pulsar candidate selection: from simple filters to a new principled real-time classification approach'. *Monthly Notices of the Royal Astronomical Society* **459**(1):1104–1123.

I. F. Malofeev, V. M. ; Malov (1980). 'Mean spectra for 39 pulsars, and the interpretation of their characteristic features.'. *Sov. Astron.* **24**(February):54–63.

V. M. Malofeev (1996). 'Pulsar Radio Spectra'. In S. Johnston, M. A. Walker, & M. Bailes (eds.), *IAU Colloq. 160: Pulsars: Problems and Progress*, vol. 105 of *Astronomical Society of the Pacific Conference Series*, p. 271.

V. M. Malofeev, et al. (2000). 'Flux Densities of 235 Pulsars at 102.5 MHz'. *Astronomy Reports* **44**(7):436–445.

R. N. Manchester, et al. (2005). 'VizieR Online Data Catalog: ATNF Pulsar Catalog'. *VizieR On-line Data Catalog* **2**:245.

R. N. Manchester, et al. (2001). 'The Parkes multi-beam pulsar survey - I. Observing and data analysis systems, discovery and timing of 100 pulsars'. *Monthly Notices of the Royal Astronomical Society* **328**(1):17–35.

R. N. Manchester, et al. (1996). 'The Parkes Southern Pulsar Survey - I. Observing and data analysis systems and initial results'. *Monthly Notices of the Royal Astronomical Society* **279**(4):1235–1250.

R. N. Manchester, et al. (1978). 'The second Molonglo pulsar survey - discovery of 155 pulsars'. *Monthly Notices of the Royal Astronomical Society* **185**(2):409–421.

R. N. Manchester, et al. (1993). 'Radio detection of PSR B0540-69'. *The Astrophysical Journal* **403**:L29.

R. N. Manchester, et al. (1973). 'Frequency Dependence of Pulsar Polarization'. *The Astrophysical Journal* **179**:L7.

O. Maron, et al. (2000). 'Pulsar spectra of radio emission'. *Astronomy and Astrophysics Supplement Series* **147**(2):195–203.

D. McConnell, et al. (1991). 'Radio pulsars in the Magellanic Clouds'. *Monthly Notices of the Royal Astronomical Society* **249**(4):654–657.

A. E. McEwen, et al. (2020). 'The Green Bank North Celestial Cap Pulsar Survey. V. Pulsar Census and Survey Sensitivity'. *The Astrophysical Journal* **892**(2):76.

S. J. McSweeney, et al. (2022). 'Independent Discovery of a Nulling Pulsar with Unusual Subpulse Drifting Properties with the Murchison Widefield Array'. *The Astrophysical Journal* **933**(2):210.

S. J. Mcsweeney, et al. (2017). 'Low-frequency Observations of the Subpulse Drifter PSR J0034 0721 with the Murchison Wide fi eld Array'. *The Astrophysical Journal* **836**(2):1–9.

S. J. McSweeney, et al. (2019). 'The Frequency-dependent Behavior of Subpulse Drifting. I. Carousel Geometry and Emission Heights of PSR B003107'. *The Astrophysical Journal* **883**(1):28.

S. J. McSweeney, et al. (2020). 'MWA tied-array processing III: Microsecond time resolution via a polyphase synthesis filter'. *Publications of the Astronomical Society of Australia* **37**:e034.

D. B. Melrose (2017). 'Coherent emission mechanisms in astrophysical plasmas'. *Reviews of Modern Plasma Physics* **1**(1):5.

D. B. Melrose & R. Yuen (2016). 'Pulsar electrodynamics: an unsolved problem'. *Journal of Plasma Physics* **82**(02):635820202.

B. W. Meyers, et al. (2018). 'Hunting for Radio Emission from the Intermittent Pulsar J1107-5907 at Low Frequencies'. *The Astrophysical Journal* **869**(2):134.

B. W. Meyers, et al. (2017). 'Spectral Flattening at Low Frequencies in Crab Giant Pulses'. *The Astrophysical Journal* **851**(1):1–21.

B. W. Meyers, et al. (2019). 'The emission and scintillation properties of RRAT' (2016).

P. G. Mezger & A. P. Henderson (1967). 'Galactic H II Regions. I. Observations of Their Continuum Radiation at the Frequency 5 GHz'. *The Astrophysical Journal* **147**:471.

D. Michilli, et al. (2018). 'Single-pulse classifier for the LOFAR Tied-Array All-sky Survey'. *Monthly Notices of the Royal Astronomical Society* **480**(3):3457–3467.

R. P. Mignani, et al. (2017). 'The First Detection of a Pulsar with ALMA'. *The Astrophysical Journal* **851**(1):L10.

D. A. Mitchell, et al. (2008). 'Real-time calibration of the Murchison Widefield Array'. *IEEE Journal on Selected Topics in Signal Processing* **2**(5):707–717.

N. Mohan & D. Rafferty (2015). 'PyBDSF: Python Blob Detection and Source Finder'.

V. Morello, et al. (2020). 'Optimal periodicity searching: revisiting the fast folding algorithm for large-scale pulsar surveys'. *Monthly Notices of the Royal Astronomical Society* **497**(4):4654–4671.

I. S. Morrison, et al. (2023). 'MWAX: A New Correlator for the Murchison Widefield Array'. *Publications of the Astronomical Society of Australia* .

T. Murphy, et al. (2017). 'Low-Frequency Spectral Energy Distributions of Radio Pulsars Detected with the Murchison Widefield Array'. *Publications of the Astronomical Society of Australia* **34**.

L. Nicastro, et al. (1995). 'PSR:J1012+5307:a 5.26-ms pulsar in a 14.5-h binary system'. *Monthly Notices of the Royal Astronomical Society* **273**(1):L68–L70.

L. Nieder, et al. (2020). 'Exploiting Orbital Constraints from Optical Data to Detect Binary Gamma-Ray Pulsars'. *The Astrophysical Journal* **901**(2):156.

Ochsenbein F. (2019). 'The VizieR database of astronomical catalogues'.

A. R. Offringa, et al. (2014). 'wsclean: an implementation of a fast, generic wide-field imager for radio astronomy'. *Monthly Notices of the Royal Astronomical Society* **444**(1):606–619.

S. M. Ord, et al. (2015). 'The Murchison Widefield Array Correlator'. *Publications of the Astronomical Society of Australia* **32**.

S. M. Ord, et al. (2019). 'MWA tied-array processing I: Calibration and beamformation'. *Publications of the Astronomical Society of Australia* **36**:e030.

S. I. Oronsaye, et al. (2015). 'SIMULTANEOUS OBSERVATIONS OF GIANT PULSES FROM THE CRAB PULSAR, WITH THE MURCHISON WIDEFIELD ARRAY AND PARKES RADIO TELESCOPE: IMPLICATIONS FOR THE GIANT PULSE EMISSION MECHANISM'. *The Astrophysical Journal* **809**(1):51.

A. Papitto, et al. (2013). 'Swings between rotation and accretion power in a binary millisecond pulsar'. *Nature* **501**(7468):517–520.

A. R. Parsons, et al. (2012). 'A per-baseline, delay-spectrum technique for accessing the 21cm cosmic reionization signature'. *Astrophysical Journal* **756**(2).

B. B. P. Perera, et al. (2019). 'The International Pulsar Timing Array: second data release'. *Monthly Notices of the Royal Astronomical Society* **490**(4):4666–4687.

M. Pilia, et al. (2016). 'Wide-band, low-frequency pulse profiles of 100 radio pulsars with LOFAR'. *Astronomy & Astrophysics* **586**:A92.

T. Prabu, et al. (2015). 'A digital-receiver for the MurchisonWidefield Array'. *Experimental Astronomy* **39**(1):73–93.

J. Prasad & J. Chengalur (2012). 'FLAGCAL: a flagging and calibration package for radio interferometric data'. *Experimental Astronomy* **33**(1):157–171.

V. Radhakrishnan & D. J. Cooke (1969). 'Magnetic Poles and the Polarization Structure of Pulsar Radiation'. *Astrophysical Letters* **3**:225.

V. Radhakrishnan & G. Srinivasan (1982). 'On the origin of the recently discovered ultra-rapid pulsar'. *Current Science* **51**:1096.

K. Rajwade, et al. (2016). 'On gigahertz spectral turnovers in pulsars'. *Monthly Notices of the Royal Astronomical Society* **455**(1):493–498.

J. M. Rankin (1986). 'Toward an empirical theory of pulsar emission. III - Mode changing, drifting subpulses, and pulse nulling'. *The Astrophysical Journal* **301**(April):901.

S. M. Ransom (2001). *New search techniques for binary pulsars*. Ph.D. thesis, Harvard University.

S. H. Reddy, et al. (2017). 'A Wideband Digital Back-End for the Upgraded GMRT'. *Journal of Astronomical Instrumentation* **06**(01).

J. P. Ridley & D. R. Lorimer (2010). 'Isolated pulsar spin evolution on the diagram'. *Monthly Notices of the Royal Astronomical Society* **404**(2):1081–1088.

C. Robinson, et al. (1995). 'Millisecond pulsars in the globular cluster 47 Tucanae'. *Monthly Notices of the Royal Astronomical Society* **274**(2):547–554.

J. Roy, et al. (2012). 'A multi-pixel beamformer using an interferometric array and its application to the localization of newly discovered pulsars'. *Monthly Notices of the Royal Astronomical Society: Letters* **427**(1):90–94.

M. A. Ruderman & P. G. Sutherland (1975). 'Theory of pulsars - Polar caps, sparks, and coherent microwave radiation'. *The Astrophysical Journal* **196**:51–72.

A. J. Ruiter, et al. (2019). 'On the formation of neutron stars via accretion-induced collapse in binaries'. *Monthly Notices of the Royal Astronomical Society* **484**(1):698–711.

F. Ryde (1999). 'Smoothly Broken Power Law Spectra of Gamma-Ray Bursts'. *Astrophysical Letters and Communications* **39**:281.

S. Sanidas, et al. (2019). 'The LOFAR Tied-Array All-Sky Survey (LOTAAS): Survey overview and initial pulsar discoveries'. *Astronomy & Astrophysics* **626**:A104.

R. Sault, et al. (1996). 'Understanding radio polarimetry. II. Instrumental calibration of an interferometer array.'. *Astronomy and Astrophysics Supplement* **117**:149–159.

P. A. G. Scheuer (1968). 'Amplitude Variations in Pulsed Radio Sources'. *Nature* **218**(5145):920–922.

J. Seiradakis, et al. (1995). 'Pulsar profiles at high frequencies. I. The data.'. *Astronomy and Astrophysics Supplement* **111**:205.

R. Sengar, et al. (2023). 'Discovery of 37 new pulsars through GPU-accelerated reprocessing of archival data of the Parkes Multibeam Pulsar Survey'. *Monthly Notices of the Royal Astronomical Society* .

R. M. Shannon, et al. (2018). 'The dispersionbrightness relation for fast radio bursts from a wide-field survey'. *Nature* **562**(7727):386–390.

W. Sieber (1973). 'Pulsar Spectra'. *Astronomy and Astrophysics* **28**:237.

M. Sokolowski, et al. (2017). 'Calibration and Stokes Imaging with Full Embedded Element Primary Beam Model for the Murchison Widefield Array'. *Publications of the Astronomical Society of Australia* **34**:e062.

R. Spiewak, et al. (2022). 'The MeerTime Pulsar Timing Array: A census of emission properties and timing potential'. *Publications of the Astronomical Society of Australia* **39**:e027.

D. H. Staelin & E. C. Reifenstein (1968). 'Pulsating Radio Sources near the Crab Nebula.'. *Science (New York, N.Y.)* **162**(3861):1481–1483.

B. W. Stappers, et al. (2008). 'Low Frequency Observations of Millisecond Pulsars with the WSRT'. In C. Bassa, Z. Wang, A. Cumming, & V. M. Kaspi (eds.), *40 Years of Pulsars: Millisecond Pulsars, Magnetars and More*, vol. 983 of *American Institute of Physics Conference Series*, pp. 593–597.

J. J. Stickel (2010). 'Data smoothing and numerical differentiation by a regularization method'. *Computers & Chemical Engineering* **34**(4):467–475.

D. R. Stinebring, et al. (2022). 'A Scintillation Arc Survey of 22 Pulsars with Low to Moderate Dispersion Measures'. *The Astrophysical Journal* **941**(1):34.

K. Stovall, et al. (2014). 'The Green Bank Northern Celestial Cap Pulsar Survey. I. Survey Descripton, Data Analaysis, and Initial Results'. *The Astrophysical Journal* **791**(1):67.

K. Stovall, et al. (2015). 'Pulsar Observations Using the First Station of the Long Wavelength Array and the LWA Pulsar Data Archive'. *The Astrophysical Journal* **808**(2):156.

S. M. Straal & J. van Leeuwen (2019). 'A LOFAR search for steep-spectrum pulsars in supernova remnants and pulsar wind nebulae'. *Astronomy & Astrophysics* **623**:A90.

N. Swainston (2022). 'NickSwainston/all_pulsar_spectra: Thesis version'.

N. Swainston, et al. (2020). 'CIRA-Pulsars-and-Transients-Group/vcstools: v2.0'. *Zenodo* .

N. Swainston, et al. (2023). 'CIRA-Pulsars-and-Transients-Group/mwa_search'.

N. A. Swainston, et al. (2022a). 'MWA tied-array processing IV: A multi-pixel beamformer for pulsar surveys and ionospheric corrected localisation'. *Publications of the Astronomical Society of Australia* **39**.

N. A. Swainston, et al. (2021). 'Discovery of a Steep-spectrum Low-luminosity Pulsar with the Murchison Widefield Array'. *The Astrophysical Journal Letters* **911**(2):L26.

N. A. Swainston, et al. (2022b). 'pulsar_spectra: A pulsar flux density catalogue and spectrum fitting repository'. *Publications of the Astronomical Society of Australia* **39**.

C. M. Tan, et al. (2018a). 'LOFAR Discovery of a 23.5 s Radio Pulsar'. *The Astrophysical Journal* **866**(1):54.

C. M. Tan, et al. (2020). 'The LOFAR Tied-Array all-sky survey: Timing of 21 pulsars including the first binary pulsar discovered with LOFAR'. *Monthly Notices of the Royal Astronomical Society* **492**(4):5878–5896.

C. M. Tan, et al. (2018b). 'Ensemble candidate classification for the LOTAAS pulsar survey'. *Monthly Notices of the Royal Astronomical Society* **474**(4):4571–4583.

J. H. Taylor (1975). 'Discovery of a Pulsar in a Binary System'. *Annals of the New York Academy of Sciences* **262**(1):490–492.

J. H. Taylor, et al. (1993). 'Catalog of 558 pulsars'. *The Astrophysical Journal Supplement Series* **88**:529.

J. H. Taylor & J. M. Weisberg (1989). 'Further experimental tests of relativistic gravity using the binary pulsar PSR 1913 + 16'. *Astrophysical Journal* **345**:434.

S. J. Tingay, et al. (2013). 'The Murchison Widefield Array: The Square Kilometre Array Precursor at Low Radio Frequencies'. *Publications of the Astronomical Society of Australia* **30**(1):7.

J. Tobin (1958). 'Estimation of Relationships for Limited Dependent Variables'. *Econometrica* **26**(1):24.

M. Toscano, et al. (1998). 'Spectra of Southern Pulsars'. *The Astrophysical Journal* **506**(2):863–867.

S. E. Tremblay, et al. (2015). 'The High Time and Frequency Resolution Capabilities of the Murchison Widefield Array'. *Publications of the Astronomical Society of Australia* **32**(May):e005.

M. P. van Haarlem, et al. (2013). 'LOFAR: The LOw-Frequency ARray'. *Astronomy & Astrophysics* **556**(2):A2.

T. D. van Ommen, et al. (1997). 'Polarimetric observations of southern pulsars at 800 and 950 MHz'. *Monthly Notices of the Royal Astronomical Society* **287**(2):307–327.

W. van Straten & M. Bailes (2011). 'DSPSR: Digital Signal Processing Software for Pulsar Astronomy'. *Publications of the Astronomical Society of Australia* **28**(1):1–14.

J. P. W. Verbiest, et al. (2016). 'The International Pulsar Timing Array: First data release'. *Monthly Notices of the Royal Astronomical Society* **458**(2):1267–1288.

M. Vivekanand & B. C. Joshi (1997). 'The Drifting Behavior of PSR B003107'. *The Astrophysical Journal* **477**(1):431–438.

R. B. Wayth, et al. (2015). 'GLEAM: The GaLactic and Extragalactic All-Sky MWA Survey'. *Publications of the Astronomical Society of Australia* **32**(1):e025.

R. B. Wayth, et al. (2018). 'The Phase II Murchison Widefield Array: Design overview'. *Publications of the Astronomical Society of Australia* **35**:e033.

J. M. Weisberg & J. H. Taylor (2003). 'The Relativistic Binary Pulsar B1913+16'. *Radio Pulsars, ASP Conference Proceedings* **302**(August 2002):93.

A. Whitney, et al. (2009). 'VLBI data interchange format (VDIF)'. *Proceedings of Science* **82**:1–7.

I. P. Williamson (1972). 'Pulse Broadening due to Multiple Scattering in the Interstellar Medium'. *Monthly Notices of the Royal Astronomical Society* **157**(1):55–71.

A. Wolszczan & D. A. Frail (1992). 'A planetary system around the millisecond pulsar PSR1257 + 12'. *Nature* **355**(6356):145–147.

Y.-W. Xie, et al. (2019). 'Flux density measurements for 32 pulsars in the 20 cm observing band'. *Research in Astronomy and Astrophysics* **19**(7):103.

M. Xue (2019). *Characterising the Local Interstellar Medium using Low-Frequency Pulsar Polarimetry*. Ph.D. thesis, Curtin Institute of Radio Astronomy.

M. Xue, et al. (2017). 'A Census of Southern Pulsars at 185 MHz'. *Publications of the Astronomical Society of Australia* **34**:e070.

M. Xue, et al. (2019). 'MWA tied-array processing II: Polarimetric verification and analysis of two bright southern pulsars'. *Publications of the Astronomical Society of Australia* **36**.

J. M. Yao, et al. (2017). 'A NEW ELECTRON-DENSITY MODEL FOR ESTIMATION OF PULSAR AND FRB DISTANCES'. *The Astrophysical Journal* **835**(1):29.

V. V. Zakharenko, et al. (2013). 'Detection of decametre-wavelength pulsed radio emission of 40 known pulsars'. *Monthly Notices of the Royal Astronomical Society* **431**(4):3624–3641.

A. Zepka, et al. (1996). 'Discovery of Three Radio Pulsars from an X-Ray–selected Sample'. *The Astrophysical Journal* **456**:305.

R.-S. Zhao, et al. (2017). 'TMRT Observations of 26 Pulsars at 8.6 GHz'. *The Astrophysical Journal* **845**(2):156.

R.-S. Zhao, et al. (2019). '5.0 GHz TMRT Observations of 71 Pulsars'. *The Astrophysical Journal* **874**(1):64.